UNIVERSITÀ DEGLI STUDI DI MILANO BICOCCA

Scuola di Dottorato di Scienze
Corso di Dottorato di Ricerca in Fisica e Astronomia

**Stefano Freddi**
Matricola 043479

# Gold Nanorods Characterization for Nanomedical Applications

**Tutore**
**Prof. Maddalena Collini**

**Coordinatore**
**Prof. Giuseppe Chirico**

Ciclo XXIV 2009-2011

*To Bruno and my Family*

*A volte non ci si puó sottrarre al vento... si puó solo mettere a segno le vele e tirare dritto...*
L'Albatross, Oltre la Tempesta

# Contents

# Introduction

In recent years, researchers have exploited the unique optical properties of gold nanoparticles (NPs), for a wide range of diagnostic and therapeutic biomedical applications. In noble metals, the coherent collective oscillation of electrons in the conduction band (Surface Plasmon Resonance, SPR), induces large surface electric fields which greatly enhance the radiative properties of gold and silver NPs when they interact with resonant electromagnetic radiation. This makes the absorption cross section of this NPs orders of magnitude larger than that of the most strongly absorbing molecules and the light scattering cross section orders of magnitude more intense than that of organic dyes. These properties are directly related to the size and shape of the gold nanoparticles. Furthermore, the conjugation of gold NPs to probe molecules such antibodies or fluorophores has been thoroughly developed over the last several decades, allowing for reliable and specific targeting of the cellular lever. The use of NPs in medicine is one of the important directions that nanotechnology is taking at this time. Their applications in drug delivery, cancer cell diagnostics, and therapeutics have been active fields of research.
The coupling of the SPR with dye electronic levels becomes also particularly important under two-photon excitation (TPE), which consists in the simultaneous absorption of two photons, each carrying about half the energy necessary to excite the molecule. This excitation technique has been particularly useful in the context of this work because it induces a significant luminescence emission of non spherically symmetric NPs: due to non-linear phenomena such as the TPE, the two-photon luminescence (TPL) intensity is enhanced by many order of magnitude with respect to the single photon excitation, improving the usefulness of these nanoparticles for in-vivo imaging in the NIR region of the electromagnetic spectrum.

TPE offers a series of unique features for biological investigation both in vitro and in vivo. First, the two-photon absorption bands of the used dyes commonly in biological studies are wider than their one-photon analogous allowing the simultaneous excitation of multiple fluorophores with a single excitation wavelength. Second, the stimulating light beam has a high penetration depth because of the infra-red wavelengths used, allowing experiments in turbid media and biological tissues. Third, excitation takes place only in the focal plane, due to the superlinear scaling of the probability of simultaneous photon absorption with the light intensity.

According to these considerations I have developed our project on three lines related to the use of gold nanoparticles for sensing, non linear imaging and photothermal therapy. In the first part of this work I have introduced the materials and methods used: in Chapter 1 and 2, are presented the most relevant features of the surface plasmon resonance, the properties of spherical symmetric, asymmetric gold nanoparticles and magnetic nanoparticles and the basics of fluorescence emission and two-photon excitation.

In Chapter 3 I have studied the interaction of gold nanoparticles a few nanometers in size with fluorophores and to exploit the changes of the dye excited-state lifetime and brightness induced by ther interaction in solution under physiological conditions. I have investigated the system based on 5 and 10 nm gold NPs coupled (via a biotin-streptavidin linker) to a fluorophore (FITC) and to a specific protein antibody. The binding of protein to the gold NPs through antigen-antibody recognition modifies the dye excited-state lifetime, whose change can then be used to measure the protein concentration. In particular, I have tested this nanodevice measuring the change of the fluorophore excited-state lifetime after the binding of the model protein bovine serum albumine (BSA). The interaction with p53 protein, a marker for early cancer diagnosis and prognosis has been the focus of this application and the measurements has been performed both in standard solution and in total cell extracts.

In the second part of the project (Chapter 4) I focused on the exploitation of anisotropic gold nanoparticles as probes for cellular imaging. I have studied the optical properties of gold nanorods obtained by synthesis with the standard surfactant CTAB (cetyl trimethilammonium bromide). Moreover, a new NP shape, obtained using for the first time in the seed growth method approach a zwitterionic surfactant, laurylsulphobetaine (LSB), has been developed by the University of Pavia (Prof. P. Pallavicini, General Chemistry Department, University of Pavia). Using several structural techniques, I have characterized optical and diffusional properties of samples synthesized at increasing levels of surfactants. It has been shown that LSB concentration in the growth solution allows to control the dimension of the NPs and the SPR position, that can be tuned in the 700-1100 nm near infrared range. From the analysis of these data, I have reached information on the nanoparticles shapes, dimensions and aggregation. With these studies and using TPL of NPs, has been performed a study of cellular uptake and toxicity of the nanoparticles by different cell liner (macrophages, HEK and A549 cells).

In the last part of this work (Chapter 5), I have demonstrated the potential use of

NPs, gold nanorods and magnetic nanoparticles (MNPs), for selective thermal therapy of cancer cells using a near-infrared low energy laser and an AC magnetic field, respectively. Photothermal therapy for cancer have been widely investigated as a minimally invasive treatment modality in comparison with other methods. The appeal of gold NRs as contrast agents is amplified by their additional capability to absorb photons and to convert into heat by nonradiative processes (phonon-phonon interaction). Magnetic nanoparticles heat inductively due to magnetic losses associated with three mechanisms: hysteresis, Néel relaxation and Brownian relaxation. These two kinds of NPs (gold and magnetic nanoparticles) are delivered to cancer cells and heated to induce apoptosis (programmed cell death).

Within this last part of the project, I have first evaluated the increase in temperature of NR and MNP solutions, using a direct visualization by means of a sensitive thermocamera. Then I have developed a nano-sensor to measure the local temperature on the surface of the nanoparticles under excitation, in order to control locally the temperature change due to heating. The rationale is to bind an organic chromophore whose excited state lifetime is particularly sensitive to the temperature, and to refer to its lifetime which is an intensive parameter. Rhodamine B is such a fluorophore, with a temperature dependence of the excited state lifetime $\approx 0.029 \pm 0.001$ ns/°C, as we also measure here. Moreover this nanoconstruct can target tissues or single cells and used for imaging before the therapy.

Part of these experimental results have been successfully composed to numerical simulations of light induced heating of gold nanorods, using the Two Temperature Model in order to calculate raising in temperature due to laser irradiation. Finally, we have developed methods and knowledge in the field of the use of NPs made of gold or oxide in biological and medical research and applications.

Chapter 1

# Metal Nanoparticles

E lucevan le stelle, e olezzava la
terra, stridea l'uscio dell'orto...

G. Gicosa, Tosca
G. Puccini

Metal nanoparticles (MN), with diameters ranging roughly between 1 and 100 nanometers, are natural bridges between molecules and extended solids. They are complex many-electron systems, where reduced sizes and quantum confinement of electrons and phonons give birth to fascinating new effects, potentially tunable with particle size and shape. Metal nanoparticles attract strong interest both because they open up a new field in fundamental science and because of their potential technological applications. They are convenient components for sub-wavelength optical devices, for nonlinear optics, for optical data storage, for surface-enhanced spectroscopy, for biological labelling and sensing, and even for cancer therapy.

## 1.1 Nanoscaled materials

The general vision of nanoscience depends strongly on the ability of creating and manipulating matter at the nanoscale. Figure 1.1 shows the nanoscale in context illustrating the size of a football compared to a carbon 60 ($C_{60}$) molecole. Nanoscaled materials are ussually categorized as materials having structured components with at least one dimension less than 100 nm. The research in nanoscaled matter began to grow exponentially when it became recognized that the bulk properties of materials change drastically as their sizes decrease from the bulk material to small cluster of atoms. Suitable control of the properties of nanometer-scale structures can lead to new science as well as new products, devices and technologies. Two principal factors are responsible for causing the properties of nanoscaled materials to differ significantly from their behaviour in bulk condition. Firstly, there is the increased relative surface area and secondly size-dependent properties begin to dominate when matter is reduced to the nanoscale. Nanoparticles, in the 1-100 nm range can be said to bridge the gap between small molecules and bulk materials [14]. As a class of materials, NPs offer a variety of opportunities to investigate the evolution of material properties with particle dimensions. Metal NPs, especially Au, Ag and CU NPs, have been extensively investigated over the past decade due to their unique electronic, optical and catalystic properties [26] [16].

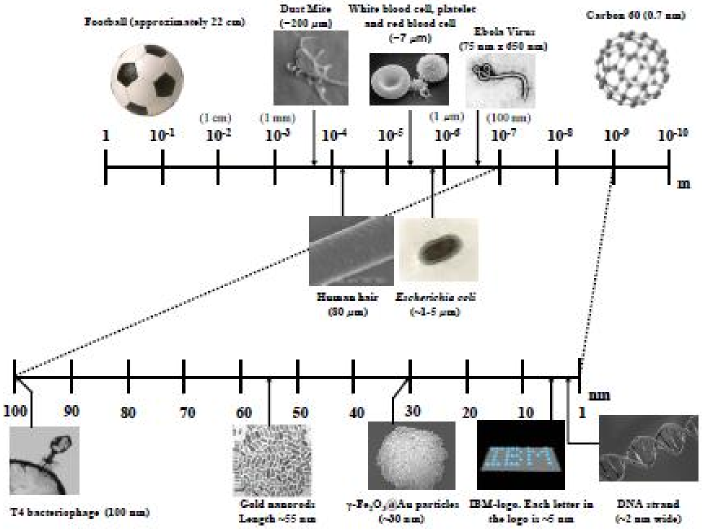

Figure 1.1: Nanoparticles in comparison with other biological entities.

These properties are neither those of bulk metal nor those of molecular compounds as has been widely demonstrated in both experimental and theoretical investigations, but they strongly depend on the particle size, shape and interparticle distance as well as the nature of the protecting organic shell [17]. The chemical stability of NPs is crucial to avoid degradation processes such as partial oxidation or undesired sintering of particles. The most striking phenomenon encountered in metal nanoparticles are electromagnetic resonances due to the collective oscillation of the conduction electrons. These so-called localized Surface Plasmon Resonance (SPR) have been widely investigated in the past decade, during which metal nanoparticles have been used for catalysis, sub-wavelength optical devices, surface enhanced Raman spectroscopy, diagnostic application, biological imaging, sensing and for cancer treatment. Moreover, the compatibility of NPs and biological systems, proteins and oligonucleotides is well established. Small particles of different sizes and shapes have been shown to be suitable markers, contrast and therapeutic agents applications [18] [19] [20]. For all these issues, it is advantageous to be able to tune the particle plasmon resonance to the near-infrared region between 650 and 900 nm, where water and hemoglobin have their lowest absorption coefficient [21] [22] [23]. This tunability is provided by engineering the shape and the dimension of the particles. In the following sections describe the properties and the origin of the plasmon resonances in spherical and ellipsoidal metal nanoparticles.

## 1.2 Historical Overview

Since ancient times, gold has been valued in every culture for its beauty as weel as for its unique physical and chemical properties. Gold is probably one of the first metals known to man. The ancient civilizations of Egypt and Mesopotamia developed a high degree of technical skill in metallurgy. Greeks and Romans used many colored pigments for the decoration of their buildings, ceramics and glass-ware [1].

Figure 1.2: The Lycurgus Cup. British Museum

The use of gold and silver particles in glass-blowing can be seen in the famous *Lycurgus Cup* exposed in the British Museum. The most unusual feature of this cup however is its color. When viewed in reflected light, for example in daylight, it appears to be green, but when light is transmitted from the inside of the vessel through the glass, it appears to be red [2]. Chemical analysis of the Lycurgus cup shows that it is similar to most other Roman glass, but it contains very small amounts of gold (about 40 parts per million) and silver (about 300 parts per million). The crystalline nature of the Ag/Au particles and their fine dispersion in the glass suggests that this colloidal metal was precipitated out from solution by heat treatment [3]. Roman glass makers were used to make red glass using copper, but this was nearly always opaque. They added scrap metal to color their glass and sometimes these materials contained small amounts of gold and silver. In the Middle Ages, chemistry developed mostly through the protoscience of Alchemy. Alchemical processes required the construction of scientific apparatus and the invention of many laboratory techniques like heating, refluxing, extraction, sublimation and distillation to treat metals with various chemical substances [4]. Gold was the only metal that did not corrode. It symbolized immortality and so it was recommended for medical use in a form that could be consumed internally as potable gold. In the middle of the nineteenth century a more scientific interest in colloidal systems arose. In the early thirteenth century the improvement of distillation methods resulted in the discovery of the mineral acids which greatly increased the power of the alchemist to dissolve substances and to carry out reactions in solutions. The *royal* solvent for gold was found to be *aqua regia*, created by adding salt ammoniac to aqua fortis $HNO_3$) [5].

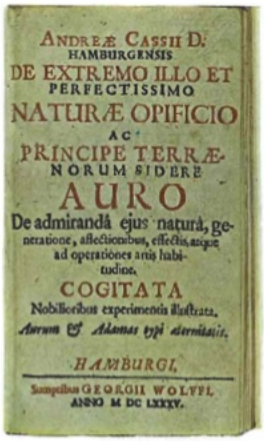

ANDREÆ CASSII D:
HAMBURGENSIS
DE EXTREMO ILLO ET
PERFECTISSIMO
NATURÆ OPIFICIO
AC
PRINCIPE TERRÆ-
NORUM SIDERE
AURO
De admirandâ ejus naturâ, generatione, affectionibus, effectis, atque
ad operationes artis habitudine.
COGITATA
Nobilioribus experimentis illustrata.
*Aurum & Adamas typi æternitatis.*
*HAMBURGI,*
Sumptibus GEORGII WOLFFI,
ANNO M DC LXXXV.

Figure 1.3: Title page of De Auro by Andreas Cassius published in Hamburg 1685 [1]

Paracelsus severely criticized the alchemists for their fascination for gold and in- sisted that they should be better spending their time in the preparation of drugs to relieve suffering. He recommended potable gold in the sixteenth century as a cure for heart disorders. Closely related to its use in medicine, the colloidal gold preparations were used to produce gold ruby glass; a first treatise on glass making appeared, written by the Florentine priest Antonio Neri. The purple precipitate of gold is mostly referred to as the Purple of Cassius. The reason is that in 1685 a doctor called Andreas Cassius published a basic alchemical work De Auro. In this book he described a method for the precipitation of gold [1].

Dr. Michael Faraday published a comprehensive paper about the preparation and properties of gold sols which can now be seen as the foundation of modern colloid science. He was the first to recognize that the red color of gold colloids was due to the minute size of the Au particles and that one could turn the preparation to blue by adding salt to the solution. Faraday's discovery that metals could form colloids was a breakthrough, although the importance of his observations was not fully realized at that time: today his studies are generally considered to mark the foundations of modern colloid science [6] [7]. Thomas Graham (1805-1869), who is referred to as "the father of colloid chemistry". The first theoretical description was given by Gustav Mie in the beginning of the twentieth century; he described the optical properties of small metal particles. In 1925 Richard Adolf Zsigmondy (1865-1929) was awarded by the Nobel price [8] for his demonstration of the heterogenous nature of colloid solutions and for the methods be used, which have since became fundamental in modern colloid chemistry. Finally, he showed that colloidal gold particles have a negative electrical charge, which largely determined their stability. An interesting investigation of various preparations of colloidal gold using the electron microscope as the main tool started in 1948 at Princeton University and the RCA Laboratories by John Turkevich and colleagues, who studied the reduction of gold salt with sodium citrate extensively. G. Frens used the citrate reduction method studied by Turkevich to control the size of gold particles ranging from 16 nm to 150 nm simply by varying the concentration of sodium citrate added to the solution during the nucleation of the particles [9]. The real renaissance of gold nanoparticles, however, started when M. Brust and coworkers reported a simple reductive method using the borohydride reduction of chloroauric acid in the presence of alkane thiols [10]; functionalized groups on gold colloids surface allow their incorporation in three dimensional networks and make then useful in a wide range of applications in the fields of sensors and molecular electronics.

## 1.3 Gold

Gold is a chemical element with symbol Au (from the Latin aurum), atomic number 79 and atomic weight of 196.967.

It is a soft, yellow metal (mp 1063 °C ) with the highest ductility and malleability of any element: a single gram can be beaten into a sheet of one square meter. The transmitted light appears greenish blue, because gold strongly reflects yellow and red. Gold is a good conductor of heat and electricity, and is not affected by air and most reagents. Heat, moisture, oxygen, sulfur and most corrosive agents have very little chemical effect on gold, making it weel-suited for use in coins; but reacts readily with alogens or with solutions containing or generating chlorine such as aqua regia, that dissolves it via formation of the chloraurate ion. In addition, gold is very dense, a cubic meter weighing 19300 Kg ; by comparison, the density of lead is 11340 $kg/m^3$. Gold is reactive with sulfur: in particular in the case of organic thiols, ligation to nanoparticles surface is particularly effective for the contemporary presence of a $\sigma$ type bound, in which sulfur is the electron density donor and the metal atom is the acceptor, and a $\pi$ type bound, in which metal electrons are partially delocalised in molecular orbitals formed between the filled d orbitals of the metal and the empty d orbitals of sulfur [11]. When nanoparticles size becomes comparable to the de Broglie's wavelength of an electron at the Fermi energy (0.5 nm for gold and silver), quantum size effects on the optical properties of metal nanoparticles induce fluorescence emission, due to transitions between discrete electronic states [12]. Finally, when a metal particle decreases in size to become a nanoparticle or a nanocrystal, a larger proportion of atoms is found at the surface. This observation together with the fact that catalytic chemical reactions occur at surfaces leads to much

Figure 1.4: Mask of Agamemnon. National Archaeological Museum of Athens

more pronounced reactivity when a given mass of gold is used in nanoparticulate from compared to the case in which microscope particles are used [13].

### 1.3.1 Stability and chemical reactivity

Gold is probably the most noble of the metals, being the only one which is not attacked in water by either oxygen or sulphur at any temperature. To understand this nobility of gold, it is useful to consider the redox potentials of gold in the absence of coordinating ligands. Thus, gold must be oxidized for a reaction to take place. For example,

$$\mathrm{Au} \longrightarrow \mathrm{Au}^{+}(\mathrm{aq}) + \mathrm{e}^{-}$$

The tendency for this reaction to take place is given by Nernst equation or the reduction potential:

$$E = E^{\ominus} - 2.303\frac{RT}{F}log_{10}\frac{[Au]}{[Au^{+}]} = 1.7 + 0.059log_{10}[Au^{+}] \tag{1.1}$$

where R is the gas constant, F the Faraday constant, T the absolute temperature and $E^{\ominus}$ the standard potential for the reaction ($\sim$ 1.7 V). Gold is the only metal with this property and therefore one can say that it is truly the most noble of the metallic elements.

However, gold can dissolve in aqueous solutions containing good ligands for gold and an oxidizing agent. For example, gold does not dissolve appreciably in hydrochloric or nitric acid separately, but dissolves readily in *aqua regia* to give tetrachloroauric(III)acid.

## 1.4 Optical properties of small metal particles

Metal colloids exhibit colors that often differ from the color of their bulk materials. For example, a dispersion of gold colloids is red and of silver colloids yellow. The origin of these color changes are explained by surface plasmon resonances, which are electrons oscillating collective in response to an applied field. For example, when a metal particle is decreased below the wavelength of visible light and when the visible light has a frequency close to that of the oscillating electrons, then the surface plasmon resonance absorbs energy. In this section a theoretical understanding of the optical response of small metal particles shall be given. The surface plasmon resoncances are explained by the Lorentz-Drude-Sommerfeld Model, which gives us an intuitive basis for the understanding of free electrons moving in response to an electric field. Furthermore, the absorption of light by metal colloids is explained by the application of the Mie theory.

### 1.4.1 Surface Plasmon Resonances

The optical response of metal colloids to an electric field of incident wavelength, with radius $r << \lambda$, is schematically shown in Figure 1.5. In the quasi-stati regime the positive charges in the metal colloids are assumed to be immobile, while the negative charges (the conduction electrons) are allowed to move under the influence of an external field. Hence, when metal colloids are placed in an electric field, a displacement of the negative charges from the positive ones occurs. These collective resonances from the negative electrons are denoted as Mie resonances or surface plasmon resonances.

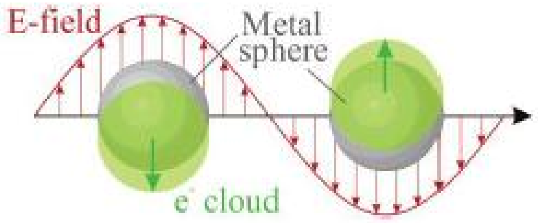

Figure 1.5: A scheme of surface plasmon absorption of spherical nanoparticles illustrating the excitation of the dipole surface plasmon oscillation

The optical properties of metal colloids are described by the optical material function or the dielectric function $\epsilon(\omega)$. For metal colloids with a diameter larger than 10 nm, the dielectric functions have the values of the bulk material. For smaller metal colloids, the dielectric functions vary as a function of particle size and for sub-nm nanoclusters.

### 1.4.2 Light absorption by spherical Metal Colloids

The optical properties of a metal particle in terms of absorption and scattering cross sections $\sigma_{abs}$ and $\sigma_{sca}$ are related to the intensity loss of the incident light due to absorption or elastic scattering. In practice, both absorption and scattering contribute, resulting in a total extinction cross section

$$\sigma_{ext} = \sigma_{abs} + \sigma_{sca} \tag{1.2}$$

The measured attenuation of a parallel beam of incident light with intensity $I_0$, over a path length x cm in a spectrophotometer is given by the Lambert-Beer law. For a colloidal solution containing N particles per unit volume, the transmitted light I(x) is

$$I(x) = I_0 e^{-N\sigma_{ext}x} \tag{1.3}$$

However, the Lambert-Beer law is usually expressed as

$$A = log_{10}(\frac{I_0}{I(x)}) = \frac{N\sigma_{ext}x}{2.303} \tag{1.4}$$

where A is the solution absorbance. The extinction cross section is calculated from Mie theory by series expansion of the involved fields into partial waves of different spherical symmetries. For spherical particles with a complex dielectric function, embedded in a medium of dielectric function $\epsilon_m$, the extinction cross section according to Bohren and Huffman, is written as

$$\sigma_{ext} = \frac{2\pi}{k^2}\sum_{n=1}^{\infty}(2n+1)\{a_n b_n\} \tag{1.5}$$

where $k = 2\pi\sqrt{\epsilon_m/\lambda}$. $a_n$ and $b_n$ are the scattering coefficients which are functions of the radius r and the wavelength $\lambda$ in terms of Ricatti-Bessel cylindrical functions. However, when the size of the metal particle is much smaller than the wavelength of the exciting radiation ($r << \lambda$), the effects of higher multipoles are neglected and only the first, electric dipole term is significant. Hence, the Mie formula (eq. 1.5) is simplified and given by

$$\sigma_{ext}(\omega) = 9\frac{\omega}{c}\epsilon_m^{3/2}V_0\frac{\epsilon_2(\omega)}{[\epsilon_1(\omega)+2\epsilon_m]^2+\epsilon_2^2(\omega)} \tag{1.6}$$

with $V_0 = 4/3\pi r^3$ the particle volume, $\epsilon_m$ the dielectric function of the embedding medium and $\epsilon(\omega)$ the dielectric function of the particle. Taking interband and core transitions into account, the real part of the dielectric function in the Drude model can be rewritten as

$$\epsilon_1(\omega) = \epsilon^{\infty} - \frac{\omega_p^2}{\omega^2+\omega_d^2} \tag{1.7}$$

with $\omega^{\infty}$ the high frequency dielectric constant. The cross section$\omega_{ext}(\omega)$ has a resonance at the frequency where the denominator $[\epsilon_1(\omega)+2\epsilon_m]^2+\epsilon_2^2(\omega)$ takes its minimum.

### 1.4.3 An exact solution

Solving the problem of absorption and scattering of light by a small particle involves solving Maxwell's equations with the correct boundary conditions. We use the general formulation of the problem as shown in figure 1.6. Assuming harmonic time dependence of the light source, we can rewrite Maxwell's equations into the vector wave equation

$$\begin{aligned} \nabla^2 E + k^2 E = 0 \\ \nabla^2 H + k^2 H = 0 \end{aligned} \tag{1.8}$$

where k is the wave number. Both the particle and the medium can be described by two non-dimensional parameters, the dielectric function $\epsilon$ and the magnetic permeability $\mu$, that enter in the wave number as $k^2 = \omega^2\epsilon\mu$. At the boundary between the particle and the medium, $\epsilon$ and $\mu$ are discontinuous. It follows from Maxwell's equations that the tangential components of the fields are continuous. For points x on the particle surface, we can write

$$\begin{aligned}[\mathbf{E_2}(\mathbf{x}) - \mathbf{E_1}(\mathbf{x})] \times \hat{\mathbf{n}} &= 0 \\ [\mathbf{H_2}(\mathbf{x}) - \mathbf{H_1}(\mathbf{x})] \times \hat{\mathbf{n}} &= 0 \end{aligned} \tag{1.9}$$

Only if we restrict ourselves to spherical particles, is this problem exactly solvable.

This was first shown in 1908 by Gustav Mie. A complete derivation of Mie theory is given by Bohren and Huffman. From Mie theory scattering matrices can be derived, from which information about, e.g., the direction and polarization dependence of the scattered light can be extracted. An important parameter that can be calculated with Mie theory is the cross section, a geometrical quantify that relates the incident light to the scattered, absorbed or excincted power.

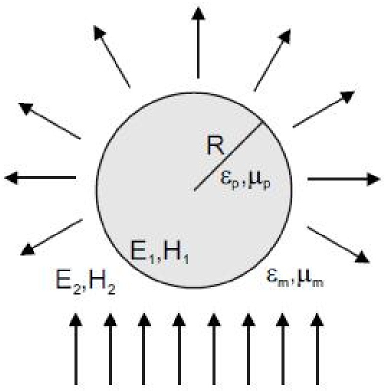

Figure 1.6: A particle is embedded in a medium and illuminated by a plane wave, which generates an electric and magnetic field inside the particle.

$$\sigma_{sca} = \frac{P_{sca}}{I_{inc}} \quad \sigma_{abs} = \frac{P_{abs}}{I_{inc}} \quad \sigma_{ext} = \frac{P_{ext}}{I_{inc}} \tag{1.10}$$

From Mie theory, absorption, scattering and extinction cross sections for an arbitrary spherical particle with dielectric function $\epsilon_p$ can be calculated. Since extincted power is the sum of the scattered and absorbed power, the absorption cross section is simply

$$\sigma_{abs} = \sigma_{ext} - \sigma_{sca} \tag{1.11}$$

while the scattering and extinction cross sections can be calculated from

$$\sigma_{sca} = \frac{2\pi}{k^2}\sum_{n=1}^{\infty}(2n+1)(|a_n|^2 + |b_n|^2) \tag{1.12}$$

$$\sigma_{ext} = \frac{2\pi}{k^2} Re(a_n + b_n) \tag{1.13}$$

The coefficients $a_n$ and $b_n$ in eq. 1.12 are given by

$$a_n = \frac{m\psi_n(mx)\psi_n'(x) - \psi_n(x)\psi_n'(mx)}{m\psi_n(mx)\xi_n'(x) - \xi_n(x)\psi_n'(mx)} \tag{1.14}$$

$$b_n = \frac{\psi_n(mx)\psi_n'(x) - m\psi_n(x)\psi_n'(mx)}{\psi_n(mx)\xi_n'(x) - m\xi_n(x)\psi_n'(mx)} \tag{1.15}$$

in which $\psi$ and $\xi$ are Ricatti-Bessel functions of order n, x = kR is a size parameter (R is the radius of the particle) and $m = \sqrt{\epsilon_p/\epsilon_m}$ is the square root of the ratio of the dielectric functions of the particle and of the medium. The prime indicates a derivation to the parameter in parentheses. The complex dielectric function $\epsilon = \epsilon_1 + i\epsilon_2$ is related to the particle's complex refractive index $\hat{n} = n + ik$, whose real andd imaginary parts describe the spatial varieties of respectively the phase and ampliutude of a wave in matter. Assuming the material is not magnetic ($\mu \approx 1$), the dielectric function and the refractive index are related by $\epsilon = \widetilde{n}^2$.

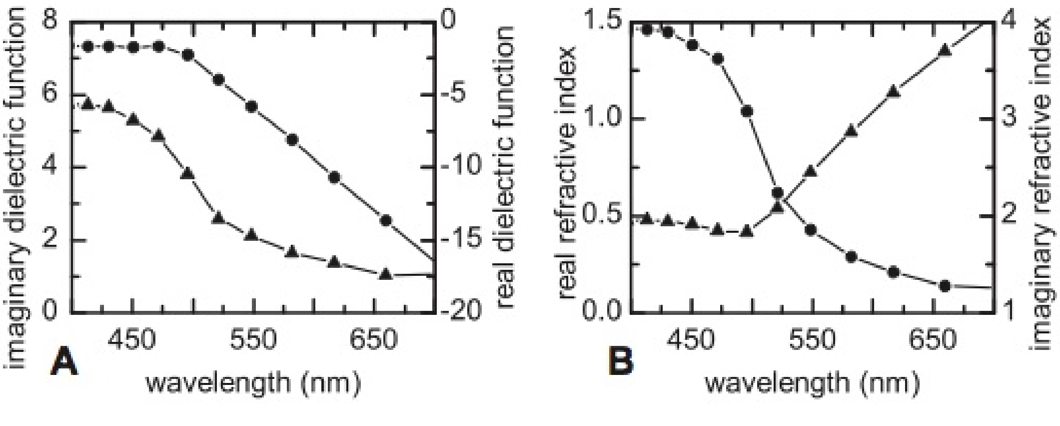

Figure 1.7: (A) Imaginary (circles) and real (triangles) part of the dielectric function of gold. (B) Imaginary (circle) and real (triangles) part of the refractive index of gold. Data measured by Johnson and Christy.

### 1.4.4 Size dependence of spherical metal nanoparticles on the plasmon absorption band

The Mie theory within the dipole approximation, which has been described in the previous section, has the advantage that it is conceptually easy to understand. However, there is no size dependence within this dipole approximation except for a varying intensity due to the dependence of the volume $V_0$ on the particle radius r. Furthermore, a strong dependence of spherical metal nanoparticles on the plasmon absorption bandwidth is experimentally observed. The position of the plasmon absorption maximum ($\lambda_{max}$) is also affected with decreasing particle size although both a blue-shift and a red-shift have been observed. The size effect on the plasmon absorption band was examined by Link et al. by studying colloidal gold nanoparticles with an average diameter between 9 and 99 nm [24]. The gold nanoparticles were prepared following the method introduced by Turkevich [25] and modified by Frens [9].

Figure 1.8 shows the absorption spectra of four different size gold nanoparticles where $\lambda_{max}$ of the plasmon absorption red-shift with increasing particle diameter. Furthermore, it is seen that the plasmon absorption bandwidth decreases with increasing particle size and then increases again with a minimum for the 22 nm nanoparticles. A modification to the Mie theory for small metal particles is the assumption that the dielectric function of the metal nanoparticles itself becomes size-dependent [$\epsilon = \epsilon(\omega, r)$] and this size dependence is introduced as the diameter of the particle becomes smaller than the mean free path of the conduction electrons. Moreover, this results in a size-dependent absorption cross section within the dipole approximation which is regarded as an intrinsic size effect [26].

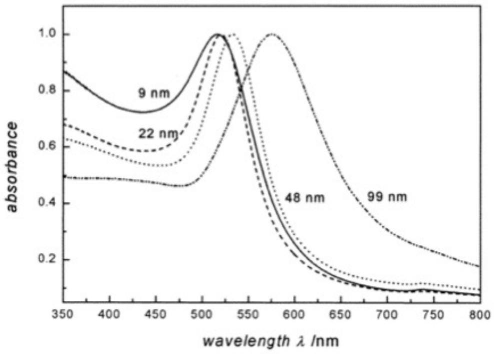

Figure 1.8: UV-Vis absorption spectra of 9, 22, 48 and 99 nm gold nanoparticles in water taken by Link et al [24]. The spectra are normalized at their plasmon absorption maxima, which are 517, 521, 533 and 575 nm respectively.

## 1.5 Light Absorption by Metal Nanorods

For rodlike nanoparticles the direction of the plasmon oscillation depends on the orientation of the particle axis with respect to the oscillating electric field of the incident light. This results in two plasmon absorptions, instead of one single plasmon band for spherical metal colloids, being the transverse resonance and the longitudinal resonance. This is shown schematically in figure 1.9.

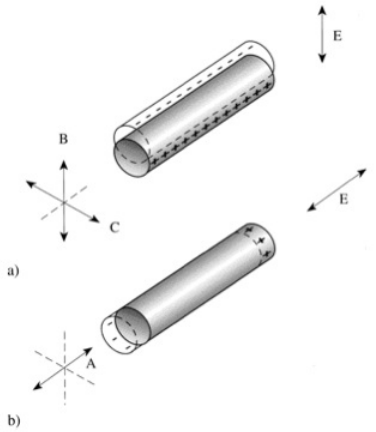

Figure 1.9: Schematic representation illustrating the optical response of rodlike nano particles to an electric field E. Two oscillating modes can be possible: (a) the transverse oscillation along the B or C axis and (b) the longitudinal oscillation along the A axis.

The optical properties of metal nanorods can be theoretically described using the Gans theory, which is an extension of the Mie theory with a geometrical factor [27]. According to this theory, the extinction coefficient $\kappa$ for N particles of volume $V_0$, within the dipole approximation is given by [28] [29]

$$\kappa_{ext} = \frac{2\pi N V_0 \epsilon_m^{3/2}}{3\lambda} \sum_j \frac{(\frac{1}{P_j^2})\epsilon_2}{[\epsilon_1 + (\frac{P_j}{P_j})\epsilon_m]^2} + \epsilon_2 \tag{1.16}$$

whereby the $P_j$ values are the depolarization factors to calculate the absorption of light by the nanorods for the three axes A, B and C as indicated in figure 1.9. The B anc C axes correspond to the particle diameter (d), while the A axis represents the particle length (L). The geometrical factors $P_j$ for nanorods along the A, B and C axes are respectively

$$P_A = \frac{1-e^2}{e^2}[\frac{1}{2e} ln(\frac{1+e}{1-e}) - 1] \tag{1.17}$$

$$P_B = P_C = \frac{1-P_A}{2} \tag{1.18}$$

with

$$e = \sqrt{1 - (\frac{d}{L})^2} = \sqrt{1 - \frac{1}{R^2}} \tag{1.19}$$

with R=L/d the aspect ratio. Link et al. calculated the absorption spectra of gold nanorods using equation 1.16 for various aspect ratios and with the measured dielectric functions of gold. This can be seen in figure 1.10a where the medium dielectric constant was chosen to be 4. The maximum of the longitudinal plasmon band red-shift 150 nm when the aspect ratio increases from 2.6 to 3.6. Moreover, figure 1.10b shows that the increase in the peak position of the longitudinal plasmon ban with increasing nanorod aspect ratio follows a linear trend. The data points shown correspond to the absorption maxima of the longitudinal plasmon band as calculated in figure 1.10a. The dotted line represents a plot of an equation derived by Link et al, in order to predict the maximum of the longitudinal plasmon band $\lambda_{max}$

$$\lambda_{max} = (33.34R - 46.31)\epsilon_m + 472.31 \tag{1.20}$$

It follows from equation 1.20 that the maximum of the longitudinal plasmon resonance also linearly depends on the medium dielectric constant $\epsilon_m$.

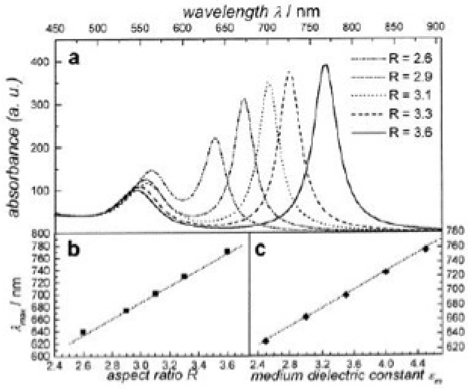

Figure 1.10: Simulation of the surface plasmon absorption for gold nanorods of different aspect ratio by Link and coworkers.

Hence, figure 1.10c shows that with increasing medium dielectric constant, there is also a red-shift of $\lambda_{max}$ for a fixed aspect ratio R = 3.3.

## 1.6 Magnetic Nanoparticles

Magnetic nano-structured materials have attracted much attention due to their unique properties and potential applications. Magnetic induction heating behavior in magnetic particles provides a benefit for biomedical applications, such as targeted drug delivery[30], [31], diagnostics[32], and magnetic separation[33], [34]. The magnetic nano-structured materials are also being explored as contrast agents in MRI[35], [36], thermo responsive, drug carriers[37], and the hyperthermia[38], [8]. Hyperthermia is a promising approach for the thermal activation therapy of tumor. Inevitable technical problems for hyperthermia are the difficulty of heating only the local tumor to the intended temperature without damaging much of the surrounding healthy tissue and precise control of temperature. induction heating of magnetic nanoparticles in an alternating field can solve the above problems with their unique characters of self-heating, self-temperature controlling due to the magnetic loss in AC magnetic field.

Since these are nanoscale devices, the energy deposition in the cancer cells would be extremely localized. This should cause very minimal damage to surrounding tissue, making these systems superior to traditional hyperthermic treatment.
Magnetic particles heat inductively due to magnetic losses associated with the magnetization/demagnetization cycling. Magnetite particles ($Fe_3O_4$) have attracted much interests because they are considered as a material with non-toxicity and biological compatibility due to their main composition of Fe ions. The raising of an organism's body temperature to about 5 or more degrees Celsius above its normal value, is referred to as hyperthermia. A sustained temperature above 42 °C can cause cell apoptosis, and a sustained temperature above 45 °C causes cell necrosis, resulting in irreversible damage to cell function, or heat-induced sensitization of cells to radiation and some cytotoxic drugs.

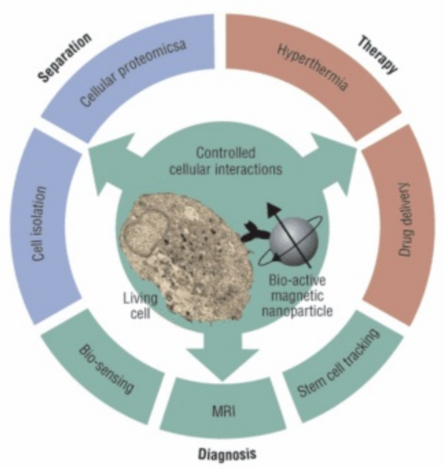

Figure 1.11: Biomedical applications based on the controlled interactions between living cells and biologically activated magnetic nanoparticles.

### 1.6.1 Basic knowledge of magnetic induction heating of ferrite nano-materials

The magnetic induction heating of ferrite materials is originated from their power loss in alternating magnetic field. The total power loss ($P_L$) is composed of three parts, hysteresis loss ($P_h$), eddy current loss ($P_e$) and residual loss ($P_r$). Hysteresis loss is due to the irreversible magnetization process in AC magnetic field. Eddy current loss is the Joule loss due to eddy current induced by alternating magnetic field and hence depende much on the electrical resistivity of the material. The residual loss is originated from various relaxation effects of magnetization in magnetic field. The hysteresis loss refers to the loss due to irreversible magnetization process in AC field. The hysteresis loss for one cycle can be easily estimated from the area of the hysteresis loop, $W_h$ and the power loss is expressed as $P_h = f \cdot W_h$, where f is frequency. For nano-sized magnetic particles, the eddy current loss can be calculated without considering the effect of skin depth by assuming uniform distribution of magnetic field in the particle. The calculated eddy current power loss of the spherical particles is expressed by the following expression:

$$P_e = \frac{\pi}{20} B_m^2 d^2 \sigma f^2 \quad [10^{-10} w/cm^2] \tag{1.21}$$

in CGS unit, where d is the diameter of the particle and $\sigma$ is the conductivity, $P_e$ is generally very small in ferrite materials. The mechanism of residual loss is complicated and the value can only be determined from experiment.

Magnetic anisotropy is the direction dependence of a material's magnetic properties. In the absence of an applied magnetic field, a magnetically isotropic material has no preferential direction for its magnetic moment, while a magnetically anisotropic material will align its moment with one of the easy axes. An easy axes is an energetically favorable direction of spontaneous magnetization. Magnetic anisotropy is a prerequisite for Hysteresis in ferromagnets; without it, a ferromagnet is superparamagnetic. The energy associated with magnetic anisotropy can be expressed as $E = KV$, where K is the anisotropy constant and V is the volume of the magnetic particle. When the particle size is smaller than a single domain critical value the superparamagnetic behavior appears, in which the thermal agitation helps the magnetization reversal to overcome the energy barrier. Then, for magnetic nanoparticles, induction heating can be due to so-called N$\acute{e}$el relaxation process and rotational Brownian motion (see fig. 1.12). The N$\acute{e}$el relaxation process refers to the heat assisted domain rotations in the particles by the AC magnetic field as mentioned above. The Brownian relaxation refers to the rotation of the magnetic particle as a whole because of the torque exerted on the magnetic moment by the external AC magnetic field, and the energy barrier for reorientation of a particle is determined by rotational friction in the surrounding liquid. The total relaxation losses due to both processes could be calculated by the following equation:

$$P = \frac{(mH\omega\tau_{eff})2}{2\tau_{eff}\kappa TV(1+\omega^2\tau_{eff}^2)} \tag{1.22}$$

Here, m is the particle magnetic moment, $\omega$ is the AC field frequency, H is the AC field amplitude, V is the nanoparticle volume and $\tau_{eff}$ is the effecive relaxation. When the AC magnetic field is applied to magnetic nanoparticles, their magnetic moments attempt to rotate following the magnetic field with time lag. The effective relaxation time ($\tau_{eff}$) is given by

$$\tau_{eff} = \frac{\tau_B \tau_N}{\tau_B + \tau_N} \tag{1.23}$$

in which in the Brownian relaxation is

$$\tau_B = \frac{3\eta V_H}{kT} \tag{1.24}$$

where $\eta$ is the viscosity of the carrier fluid, k is the Boltzmann constant, T is the absolute temperature, and $V_H$ is the hydrodynamic volume of the particle. N$\acute{e}$el relaxation is

$$\tau_N = \tau_0 exp\left(\frac{KV}{KT}\right) \tag{1.25}$$

where $\tau_0$ is on the order of $10^{-9}$ s, and K is the anisotropy constant of the magnetic nanoparticle.

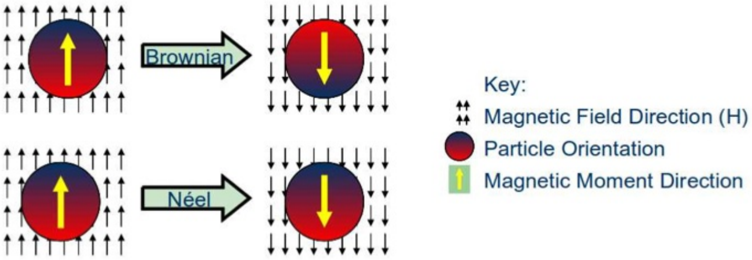

Figure 1.12: Schematic demonstrating the difference between Néel and Brownian relaxation.

The clinical use of magnetic nanoparticles requires that enough volumetric heating power to destroy tumor cells must be produced, while maintaining safe magnetic field strengths and frequencies. The safe and useful range of magnetic field strengths and frequencies for these applications are considered to be $0 < \mathrm{H} < 15\mathrm{kA/m}$ and $0.05 < \mathrm{f} < 1.2$ MHz. Higher field strengths can lead to various problems such as aggregation of magnetic materials, leading to embolisms. Lower frequencies can cause stimulation of the skeletal or peripheral muscles, or even stimulation of the cardiac muscles and arrythmias. Is has also been established that exposure to fields where the product of $H_0 f$ (where $H_0$ is the magnitude of the applied magnetic field) is less than $4.85 \times 10^8\ \mathrm{A\,m^{-1}\,s^{-1}}$ is safe for use in human. Heat generation of magnetic nanoparticle fluids has a square dependence on H leading to greater heating than ferromagnetic or paramagnetic materials at the same magnetic field strength. Heat generation for magnetic fluids is often expressed in terms of the specific absorption rate (SAR), where

$$\text{SAR} \times \text{particle density} = P \tag{1.26}$$

For example, at f = 300 kHz, H = 14 $\mathrm{kA\,m^{-1}}$, SAR = 209 $\mathrm{W\,g^{-1}}$ or 75 $\mathrm{W\,g^{-1}}$ for superparamagnetic ferrofluids or for ferromagnetic magnetite, respectively.

# Bibliography

[1] L. B. Hunt. The true story of Purple of Cassius. Gold Bull., 9(4):134-139, 1976.

[2] F. E. Wagner; S. Haslbeck; L. Stievano; S. Calogero; Q. A. Pankhurt and K. P. Martinek. Before striking gold in gold-ruby glass. Nature, 407:691-692, 2000.

[3] D. J. Barber and I. C. Freestone. Archaeometry, 32:33-45, 1990.

[4] H. M. Leicester. The Historical Background of Chemistry. Dover Publications, Inc., 1971.

[5] G. B. Kauffman. The Role of Gold in Alchemy. Part II. Gold Bull., 18(2):69-78, 1985.

[6] M. Faraday. Experimetal relations of gold (and other metals) to light. Philos. Trans. R. Soc., pages 145-181, 1857.

[7] P. Mulvaney. Surface Plasmon Spectroscopy of Nanosized Metal Particles. Langmuir., 12:788-800, 1996.

[8] R. A. Zsingmondy. Properties of Colloids. Nobel Lecture., 11, 1926.

[9] G. Frens. Controlled Nucleation for the Regulation of the Particle Size in Monodisperse Gold Suspensions. Nature Phys. Sci., 241:19-22, 1973.

[10] M. Brust; M. Walker; D. Bethell; D. J. Schiffrin and R. Whyman. Synthesis of Thiol-derivatised Gold Nanoparticles in a Two-phase Liquid-Liquid System. J. Chem. Soc., pages 801-802, 1994.

[11] N. N. Greenwood; A. Earnshaw. Chemistry of the Elements. Elsevier Science: Oxford, 1997.

[12] J. Zheng; P. R. Nicovich; R. M. Dickson. Annual Review of Physical Chemistry. 58:409-431, 2007.

[13] L. Kvitek; R. Prucek. Journal of Material Science, 2005.

[14] R. L. Johnston. Atomic and Molecular Cluster. Taylor and Francis. London, 2002.

[15] U. Kreibig and M. Vollmer. Optical Properties of Metal Clusters. Springer, Berlin, 1995.

[16] M. C. Daniel and D. Astruc. Chem. Rev., 2004, 104:293-346.

[17] M. G. Warner and J. E. Hutchison. Synthesis, Functionalization and Surface Treatment of Nanoparticles. ed. M.-I. American Scientific Publishers, California. 2003, p. 67.

[18] P. Alivisatos. The use of nanocrystals in biological detections. Nat. Biotechnol., 22:47, 2004.

[19] J. G. Fuijimoto. Optical coherence tomography for ultrahigh resolution in vivo imaging. Nat. Biotechnol., 21:1361, 2003.

[20] J. Chen; F. Saeki; B. J. Wiley; H. Chang; M. J. Cobb; Z. Y. Li; L. Au; H. Zhang; M. B. Kimmey; X. Li and Y. Xia. Gold nanocages: bioconjugation and their potential use as optical imaging contrast agents. Nano Lett., 5:473, 2005.

[21] R. Weissleder. A clearer vision for in vivo imaging. Nat. Biotechnol., 19:316, 2001.

[22] R. Jin; Y. Cao; C. A. Mirkin; K. L. Kelly; G. C. Schatz and J. G. Zheng. Photoinduced conversion of silver nanospheres to nanoprisms. Science., 294:1901, 2001.

[23] K. L. Kelly; E. Coronado; L. L. Zhao; G. C. Schatz. The optical properties of metal nanoparticles: the influence of size, shape and dielectric environment. J. Phys. Chem. B., 107:668-677, 2003.

[24] S. Link and M. A. El-Sayed. Size and Temperature Dependence of the Plasmon Absorption of Colloidal Gold Nanoparticles. J. Phys. Chem. B, 103:4212-4217, 1999.

[25] J. Turkevich, P. C. Stevenson and J. Hillier. A Study of the Nucleation and Growth Processes in the Synthesis of Colloidal Gold. Disc. Farad. Soc., 11:55-75, 1951.

[26] U. Kreibig and M. Vollmer. Optical Properties of Metal Clusters, volume 25. Springer, Berlin, 1995.

[27] S. Link and M. A. El-Sayed. Simulation of the Optical Absorption Spectra of Gold Nanorods as a Function of Their Aspect Ratio and the Effect of the Medium Dielectric Constant. J. Phys. Chem. B, 103:3073-3077, 1999.

[28] S. Link and M. A. El-Sayed. Spectral Properties and Relaxation Dynamics of Surface Plasmon Electronic Oscillations in Gold and Silver Nanodots and Nanorods. J. Phys. Chem. B, 103:84190-8426, 1999.

[29] P. B. Johnson and R. W. Christy. Optical Constants of the Noble Metals. Phys. Rev. B, 6(12):4370-4379, 1972.

[30] Q. Cao, Y. X. Wang, J. F. Yu, J. Y. Xia, C. F. Zhang, D. Z. Yin and U. O. Urs O. H*ddota*feli. J. Magn. Magn. Mater., 277, 165, 2004.

[31] D. K. Kim, Y. Zhang, J. Keher, T. Klason, B. Bjelke and M. Muhammed. J. Magn. Magn. Mater., 225, 256, 2001.

[32] C. H. Dodd, H. C. Hsu, W. J. Chu, P. Yang, H. G. Zhang, Jr J. D. Mountz, K. Zinn, J. Forder, L. Josephoson, R. Weissleder, J. M. Mountz and J. D. Mountz. J. Immunol. Methods, 256, 89, 2001.

[33] Q. A. Pankhurst, J. Connolly, S. K. Jones and J. Dobson. J. Phy. D: Appl. Phys., 36, R167, 2003.

[34] P. Tartai, M. P. Morales, S. Veintemillas-Verdaguer, T. Gonzales-Carreno, and C. J. Serna. J. Phy. D:Appl. Phys., 36, R182, 2003.

[35] P. S. Doyle, J. Bibette, A. Bancaud, and J. L. Viovy, Science, 295, 2237, 2002.

[36] J. M. Nam, S. I. Stoeva and C. A. Mirkin. J. Am. Chem. Soc., 126, 5932, 2004.

[37] U Hafeli, W. Schutt, J. Teller, M. Zborowski. Scientific and Clinical Applications of Magnetic Carriers. New York: Plenum Press, 57, 452, 1997.

[38] W. J. Parak, D. Gerion, T. Pellegrino, D. Zanchet, C. Micheel, S. C. Williams, R. Boudreau, M. A. L. Gros, C. A. Larabell and A. P. Alivisatos. Nanotechnology, 14, R15, 2003.

[39] A. Jordan, R. Scholz, P. Wust, H. Fakhling, R. Felix. J. Magn. Magn. Mater., 201, 413, 1999.

## Chapter 2

# Background Theory

> solo quando la luce splenderá,
> sulla tua bocca lo diró fremente...
>
> G. Adami, Turandot
> G. Puccini

Luminescence is the emission of light from any substance and occurs from electronically excited states [1]. Luminescence is formally divided into two categories, fluorescence and phosphorescence, depending on the nature of the excited state. In excited singlet states, the electron in the excited orbital is paired (of opposite spin) to the second electron in the ground state orbital. Consequently, return to the ground state is spin-allowed and occurs rapidly by emission of a photon. The emission rates of fluorescence are typically $1 \times 10^8\,\mathrm{s}^{-1}$, so that a typical fluorescence lifetime is near 10 ns ($10 \times 10^{-9}\,\mathrm{s}$). As will be described in section 2.1.3, the lifetime ($\tau$) of a fluorophore is the average time between its excitation and its return to the ground state. Because of the short timescale of fluorescence, measurement of the time-resolved emission requires sophisticated optics and electronics.

Phosphorescence is emission of light from triplet excited states, in which the electron in the excited orbital has the same spin orientation as the ground-state electron. Transitions to the ground state are forbidden and the emission rates are slow ($10^3$ - 1 $s^{-1}$), so that phosphorescence lifetimes are typically milliseconds to seconds. Phosphorescence is usually not seen in fluid solutions at room temperature. This is because there exist many deactivation processes which compete with emission, such as nonradiative decay and quenching processes. The first observation of fluorescence from a quinine solution in sunlight was reported by Sir John Frederick William Herschel in 1845 [2].

## 2.1 Principles of Fluorescence

### 2.1.1 Absorption

A molecule, interacting with a photon that carries an energy $h\nu$, equal to the difference between energy levels, can absorb the photon and reach in this way an excited state. This absorption process happens on a very short time scale ($10^{-15}$ s) so that the molecule does not undergo any alteration of its structure. The equation that correlates the fraction of light absorbed by the molecule and its quantity is known as the Beer-Lambert law:

$$A(\lambda) = log\frac{I_0}{I} = C\epsilon\lambda l \tag{2.1}$$

where A is a dimensionless quantity called absorbance or optical density, $I_0$ is the intensity of the incident radiation while $I$ is the intensity of the radiation transmetting through the sample, $C$ is the molar concentration of the absorber and $\epsilon$ its molar extinction coefficient. This parameter is proportional to the one photon absorption cross section of the molecule, $\sigma$, through the following equation:

$$\begin{gathered} \epsilon = \frac{\sigma N_0}{2.303} = \frac{\pi r^2 P N_0}{2.303} \\ [\epsilon] = M^{-1}cm^{-1} = \left(\frac{mol}{l}\right)^{-1} cm^{-1} = \frac{cm^2}{mol} \end{gathered} \tag{2.2}$$

where P is probability for the light to hit the molecule, r the molecular radius and $N_0$ the Avogadro number. One is usually interested in the absorption spectrum of the molecules, that represent the probability for a photon endowed with a particular value of energy to be absorbed by the molecules. There are three main contributions to the overall absorption spectrum:

- *Electronic spectrum*: it corresponds to the electronic gap transition. This absorption process involves energies falling in the UV-visible spectrum (between 200 and 900 nm).

- *Vibrational spectrum*: it corresponds to the transition between vibrational levels inside the same electronic level (these are transitions triggered by IR radiation).

- *Rotational spectrum*: it corresponds to transitions between rotational states within to same vibrational state (the energies involved correspond to the wavelengths of the microwaves).

### 2.1.2 Jablonski Diagram

The process which occur between the absorption and emission of light are usually illustrated by a Jablonski diagram [3]. This is shown in figure 2.1. The singlet ground, first, and second electronic states are depicted by $S_0, S_1$ and $S_2$ respectively. At each of these electronic energy levels the fluorophores can exist in a number of vibrational energy levels, denoted by 0, 1, 2, ect. The transitions between states are depicted as vertical lines to illustrate the instantaneous nature of light absorption. Transitions occur in about $10^{-15}$ s, a time too short for significant displacement of nuclei. This is the Franck-Condon principles. At room temperature, thermal energy is not adequate to significantly populate the excited vibrational states. Absorption typically occurs from molecules with the lowest vibrational energy.

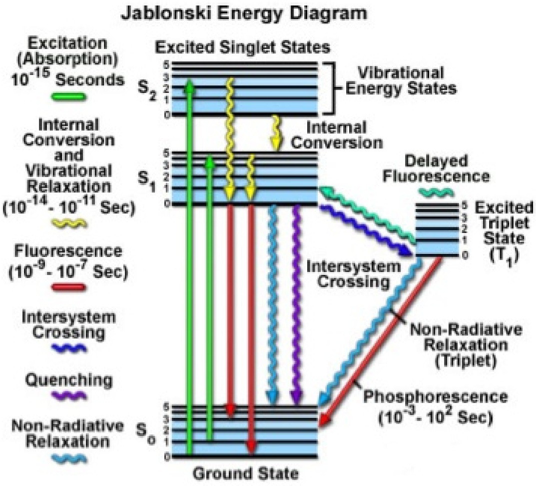

Figure 2.1: One form of a Jablonski diagram

Of course, the larger energy difference between the $S_0$ and $S_1$ excited states is too large for thermal population of $S_1$, and it is for this reason we use light and not heat to induce fluorescence. Following light absorption, several processes usually occur. A fluorophore is usually excited to some higher vibrational level of either $S_1$ or $S_2$. With a few rare exceptions, molecules in condensed phases rapidly relax to the lowest vibrational level of $S_1$. This process is called internal conversion and generally occurs in $10^{-12}$ s or less. Since fluorescence lifetimes are typically near $10^{-8}$ s, internal conversion is generally complete prior to emission. Return to the ground state typically occurs to a higher excited vibrational ground-state level, which then quickly $(10^{-12}s)$ reaches thermal equilibrium (figure 2.1). An interesting consequence of emission to higher vibrational ground states is that the emission spectrum is typically a mirror image of the absorption spectrum of the

$S_0 \rightarrow S_1$ transition. This similarity occurs because electronic excitation does not greatly alter the nuclear geometry. Hence, the spacing of the vibrational energy levels of the excited states is similar to that of the ground state. As a result, the vibrational structures seen in the absorption and the emission spectra are similar. Molecules in the $S_1$ state can also undergo a spin conversion to the first triplet state, $T_1$. Emission from $T_1$ is termed phosphorescence and is generally shifted to longer wavelengths (lower energy) relative to the fluorescence. Conversion of $S_1$ to $T_1$ is called intersystem crossing. Transition from $T_1$ to the singlet ground state is forbidden, and, as a result, rate constants for triplet emission is several orders of magnitude smaller than those for fluorescence. Other two features of fluorescence emission spectra deserve consideration: the *Stokes' Shift* [4] and *Kasha's rule* [5]. Examination of the Jablonski diagram (figure 2.1) reveals that the energy of the emission is typically less than that of absorption. Hence, fluorescence typically occurs at lower energies or longer wavelengths. This phenomenon is called Stokes' shift and was first observed by Sir G. G. Stokes in 1852 in Cambridge. Another general property of fluorescence is that the same fluorescence emission spectrum is generally observed irrespective of the excitation wavelength. This is known as Kasha's rule. This is because after absorption the fluorophores rapidly relax to the lowest vibrational state of $S_1$ from which any transition to $S_0$ starts. The relaxation is probably the result of the overlapping among numerous states of nearly the same energy.

### 2.1.3 Fluorescence lifetime and quantum yields

The fluorescence lifetime and quantum yield are perhaps the most important characteristics of a fluorophore. The quantum yield is the number of emitted photons relative to the number of absorbed photons. The lifetime is also important, as the lifetime determines the time available for the fluorophore to interact with or diffuse in its environment, and hence the information available from its emission.

The meaning of the quantum yield and lifetime is best represented by a simplified Jablonski diagram (figure 2.2). In particular, we are interested in the emissive rate of the fluorophore ($\Gamma$) and its rate of nonradiative decay to $S_0(k_{nr})$. The fluorescence quantum yield is the ratio of the number of photons emitted to the number absorbed. The processes governed by the rate constants $\Gamma$ and $k_{nr}$ both depopulate the excited state. The fraction of fluorophores which decay through emission, and hence the quantum yield, is given by

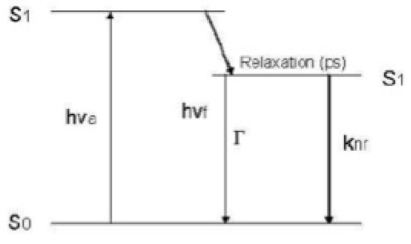

Figure 2.2: A simplified Jablonski diagram

$$Q = \frac{\Gamma}{\Gamma + k_{nr}} \tag{2.3}$$

We note that the energy yield of fluorescence is always less than unity because of Stokes' losses. The lifetime of the excited state is defined by the average time the molecule spends in the excited state prior to return to the ground state. For the fluorophore illustrated in figure 2.2, the lifetime is

$$\tau = \frac{1}{\Gamma + k_{nr}} \tag{2.4}$$

One should remember that fluorescence emission is a random process, and few molecules emit their photons at precisely $t = \tau$. The lifetime is an average value of the time spent in the excited state. For a single exponential decay, 63% of the molecules have decayed prior to $t = \tau$ and 37% decay at $t > \tau$. An opportunity to control the radiative rates arises from the interactions of fluorophores with nearby metallic surfaces or particles. Nearby metal surfaces can respond to the fluorophore oscillating dipole and modify the rate of emission and the spatial distribution of the radiated energy. The electric field felt by a fluorophore is affected by the interactions of the incident light with the nearby metal surface and also by interaction of the fluorophore oscillating dipole with the metal surface (excitation enhancement). Additionally, the fluorophores oscillating dipole induces a field in the metal (emission enhancement). These interactions can increase or decrease, depending on distance, the field incident on the fluorophore, its radiative decay rate and the spatial distribution of the radiated energy.

## 2.2 Metal Enhanced Fluorescence

Metal surface and particles can have dramatic effects on fluorescence, including localized excitation, increased quantum yields, increased photostability and increased distances for resonance energy transfer (RET), and directional emission. Figure 2.3 (top) shows the classical Jablonski diagram for excitation (E) and emission; in this case the quantum yield is the same of eq. 2.3. The unique opportunities of metal to modify fluorescence is due to changes in the rates of excitation and emission. Several effects are possible. One effect is the so called "lightning rod effect". A metal particle can amplify the incident light field by interactions of the light with the freely mobile electrons in the metal. This effect is shown in fig. 2.3 (bottom) by an additional excitation field $E_m$. Another effect of metals is to increase the radiative decay rate. This is an unusual effect which is not encountered for fluorophores in the absence of metallic surfaces, for which the intensities and lifetimes typically increase or decrease in unison. The consequences of increasing the radiative decay rate $\Gamma_m$ can be understood from a modified Jablonski diagram which includes the metal-induced radiative rate $\Gamma_m$. If $\Gamma_m$ increases, weakly fluorescent molecules can become fluorescent while the lifetime decreases, opposite of that found for decreases in $k_{nr}$. For a fluorophore at an appropriate distance from a metal surface the quantum yield ($Q_m$) and lifetime ($\tau_m$) are given by:

$$Q_m = \frac{\Gamma + \Gamma_m}{\Gamma + k_{nr} + \Gamma_m} \tag{2.5}$$

$$\tau_m = \frac{1}{\Gamma + k_{nr} + \Gamma_m} \tag{2.6}$$

As the value of $\Gamma_m$ increases, the quantum yield increases while the lifetime decreases. We may observe then a variety of favorable effects due to metal particles, such as increased fluorescence intensities, increased photostability, and increases distances for FRET. We refer to these favorable effects as metal-enhanced fluorescence (MEF). The most dramatic relative changes are found for fluorophores with the lowest quantum yields.

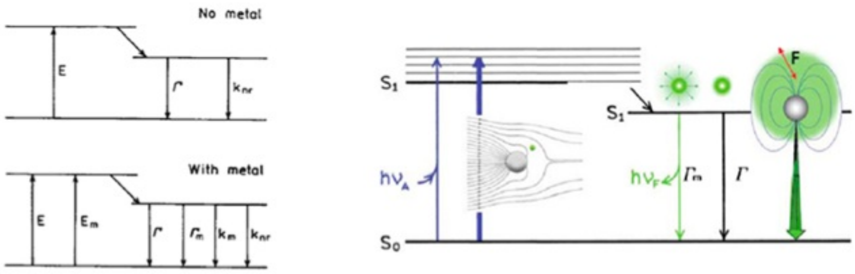

Figure 2.3: Modified Jablonski diagrams which include metal-fluorophore interactions. The thicker arrows represent increased rates of excitation and emission.

## 2.3 Two-Photons Excitation (TPE)

### 2.3.1 Theoretical Basics

From a theoretical stand point, we can talk of TPE processes when one atom or molecule simultaneously absorb two photons (carrying both the same or different energy) in the same quantum event[6]. The keyword simultaneously here means within a temporal windows of $10^{-16}$ sec[1]. It is used to induce emission in fluorescent molecules and in imaging techniques that allows observation of biological specimens in conditions very close to their natural environment. From a quantum point of view, during a TPE process, the electron jumps form an electronic ground state $S_0$ to an excited level $S_1$ passing through

---

[1] This quantum process has been hypothesized for the first time by Maria Goppert-Mayer in 1931.

an intermediate virtual state [7]. The electron with non resonant energy (that means carrying an energy not equal to any energy separation in the target structure) stays on the virtual levels only for some$10^{-16}$s [8] this means that if another photon hits the molecule within this time window the electron will reach the excited level otherwise it will fall back down to the ground state $S_0$. This is the reason why, in order to obtain a TPE absorption, it is necessary to irradiate the sample with a very high photons density ($0.1 - 10 MW/cm^2$).

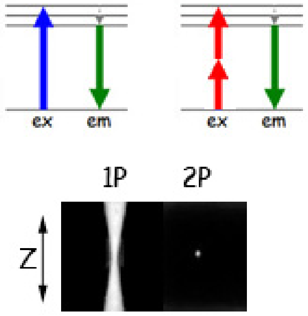

Figure 2.4: OPE vs TPE

In fact, one of the main reason of the wide spreading of the two-photon excitation microscopy has been the development of mode-locked lasers that allow the production of pulsed laser beams with pulse width varying from ps to fs. By employing highly focused pulsed beams, the photon flux is very high and that implies a rise in the TPE probability, that in other conditions would be completely neglegible. In order to have a practical example, a molecule with high absorption cross sections, when exposed to white light, undergoes to about one one-photon excitation every minute, whereas a TPE event may occurs once in $10^7$ years, on the average.
To summarize the two-photon excitation is made possible by the use of a laser source emitting very narrow pulses with a peak power as high as possible and by the focalization of these pulses on the sample with a high aperture number objective. As briefly mentioned above the energy of the two photons have the only requirement to be able to fill up, once summed, the energy gap between the two levels involved in the absorption. This concept expressed in term of wavelength lead to this condition:

$$\lambda_{1-F} \approx \left( \frac{1}{\lambda_A} + \frac{1}{\lambda_B} \right)^{-1} \tag{2.7}$$

where $\lambda_{1-F}$ is the wavelength necessary to perform an OPE absorption process [9]. For the sake of experimental simplicity it is useful to have the two photons with the same energy:

$$\lambda_A = \lambda_B \approx 2\lambda_{1-F} \tag{2.8}$$

so that it is possible to have only one light source. TPE is a non-linear process of the second order and has therefore a quadratic dependence on the instantaneous intensity of the excitation beam. It is then possible to write the fluorescence rate $I_f$ as the product of the second order cross section $\delta_2$ times the square of the excitation intensity: $I_f = \delta_2 I^2$. If we employ a high NA objective the fluorescence rate $I_f$ is then:

$$I_f(t) \approx \delta_2 I(t)^2 \approx \delta_2 P(t)^2 \left(\pi \frac{(NA)^2}{hc\lambda}\right)^2 \tag{2.9}$$

where P(t) is the laser power and NA is the aperture number of the objective used to observe the sample. It can be useful to define the time-averaged two-photon fluorescence intensity defined as:

$$< I_f(t) >= \frac{1}{T}\int_0^T I_f(t)^2 dt \tag{2.10}$$

As mentioned before, if a TPE fluorescence experiment is performed using a pulsed laser beam with pulse width $\tau_P$, repetition rate $f_P$, and average power $P_{AVE} = D \cdot P_{peak}(t)$, where $D = \tau_P f_P$, the P(t) profile, in a simple but effective approximation, can be described as:

$$P(t) = \begin{cases} \frac{P_{ave}}{\tau_P f_P}, & \text{per } 0 < \text{t} < \tau_P \\ 0, & \text{per } \tau_P < t < \frac{1}{f_P} \end{cases}$$

Equation 2.10, when integrated in the time interval in which P(t) is nonzero becomes:

$$< I_{f,P}(t) >= \delta_2 \frac{P_{ave}^2}{\tau_P^2 f_P^2} \left[\frac{\pi (NA)^2}{hc\lambda}\right]^2 \frac{1}{T}\int_0^{\tau_P} dt = \delta_2 \frac{P_{ave}^2}{\tau_P f_P}\left[\frac{\pi (NA)^2}{hc\lambda}\right]^2 \tag{2.11}$$

The conclusion that can be drawn here is that continuous wave (CW) and pulsed lasers operate at the same excitation efficiency if the average power of the CW laser is kept higher by a factor of $(\tau_P f_P)^{-1/2}$[2]. This leads to the commonly used relationship for pulsed beam focused on the sample through an high-numerical aperture objective. In this case the probability $n_a$ for a generic chromophore to absorb simultaneously two photons during the same quantum event is:

$$n_a \propto \frac{\delta_2 P_{ave}^2}{\tau_P f_P^2}\left(\frac{(NA)^2}{2\hbar c\lambda}\right)^2 \tag{2.12}$$

From this last relationship it follows that for optimal fluorescence generation, the desirable repetition rate of pulses should be of the order of a typical excited-state lifetime, which is a few nanoseconds for many of the fluorescent molecules used in fluorescence imaging. In practice, this is what sets the suitable repetition rate at around 100 MHz.

---

[2] This means that 10 W delivered by a CW laser becomes nearly equivalent to 30 mW for a pulsed laser.

The laser source used during this work had a pulses repetition rate of 80MHz. The other condition for the validity of equation 2.12 is that the probability for each fluorophore to be excited during a simple pulse has to be less than unity: that means saturation effects are not taken into account. The reason for this lies in the observation that there is a probability for the excited molecule not to have enough time to relax to the ground state. And this can be considered a prerequisite for absorption of another photon pair. The use of equation 2.12 allows one to choose optical and lasers parameters that maximize excitation efficiency without saturation.

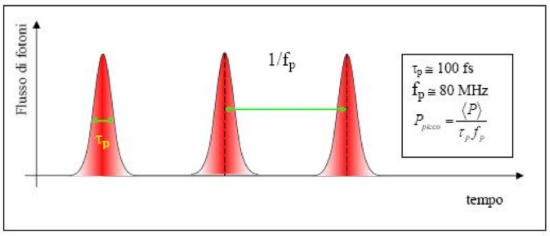

Figure 2.5: Profile of pulsed laser

### 2.3.2 One-photon and two-photon excitation Point Spread Functions

The three dimensional image plane distribution of the light collected from a point source in the focal plane, called *Point Spread Function (PSF)*, is given by[10]:

$$h(u,v) = -i\frac{2\pi n sin^2(\alpha)}{\lambda} exp\left(\frac{iu}{sin^2(\alpha)}\right)\int_0^1 J_0(v\rho)e^{\frac{iu\rho^2}{2}}\rho d\rho \tag{2.13}$$

where $\lambda$ is the light wavelength, n is the refractive index, $N.A. = nsin(\alpha)$ is the numerical aperture of the objective lens, $J_0$ is the $zero^{th}$ order Bessel function and v and u are normalized optical coordinates defined respectively as:

$$\begin{aligned} v &= \frac{2\pi n r sin(\alpha)}{\lambda} \\ u &= \frac{2\pi n z sin^2(\alpha)}{\lambda} \end{aligned} \tag{2.14}$$

where $r = \sqrt{x^2 + y^2}$ is the distance from the z axis taken as the optical axis. Therefore the intensity PSF for one-photon excitation is:

$$PSF_{OPE}(u,v) = |h(u,v)|^2 = h(u,v)h^*(u,v) \tag{2.15}$$

One-photon excitation does not provide optical sectioning capabilities since the total power released per cross-section of the laser beam along the optical axis is constant as can be verified from equation 2.15. On the other hand, TPE is axially confined since its intensity PSF[11] is the square of equation 2.15:

$$PSF_{TPE}(u,v) = |PSF_{OPE}(u,v)|^2 \tag{2.16}$$

Therefore at fixed u, the integral over v assumes a half bell shape[12] (see figure 2.6)

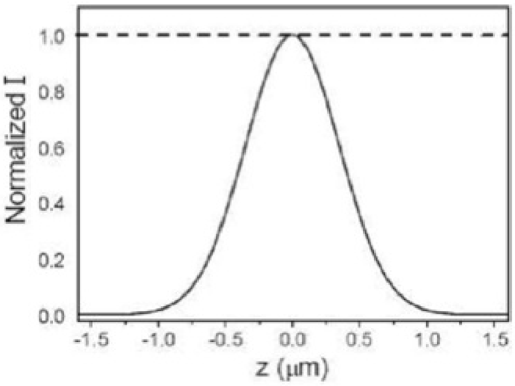

Figure 2.6: Axial confinement of two-photon excitation PSF

More precisely the excitation rate (proportional to $PSF_{TPE}$) falls off as the fourth power of the distance from the focal plane. The TPE excited volume can be calculated by approximating the $PSF_{TPE}$ as a three-dimensional Gaussian volume. This is not a volume with distinct walls but rather one based on averaging the TPE potential over all space. Integrating over all space the three-dimensional Gaussian yields:

$$V_{TPE} = \pi^{3/2}\omega_{xy}^2\omega_z \tag{2.17}$$

where $\omega_{xy}$ and $\omega_z$ are calculated as:

$$\omega_{xy} = \begin{cases} \frac{0.320\lambda}{\sqrt{2}NA}, & \text{if NA} \leq 0.7 \\ \frac{0.325\lambda}{\sqrt{2}NA^{0.91}}, & \text{if NA} > 0.7 \end{cases}$$

$$\omega_z = \frac{0.532\lambda}{\sqrt{2}}\left[\frac{1}{n-\sqrt{n^2-NA^2}}\right] \tag{2.18}$$

For example, the effective two-photon excitation volume for a 1.2 NA lens[13] at $\lambda=$ 900 nm, $V_{exc}$ is $\approx 0.113\ \mu m^3$.

### 2.3.3 OPE versus TPE

For optical sectioning, i.e. for microscopy applications, the most important consequence of two-photon excitation, TPE, or non-linear excitation in general, is the fact that the molecular excitation is limited to a sub-femtoliter region around the focal plane. While in one-photon excitation, OPE, the excitation volume is not confined in the focal plane (see figure 2.7).

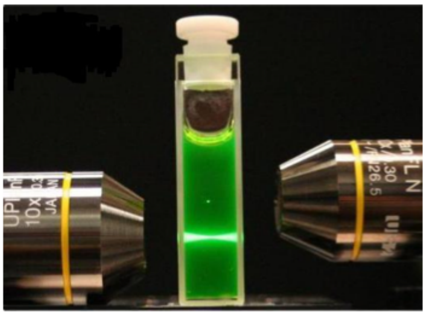

Figure 2.7: Excited volumes by two photon laser source of $\lambda = 760$ nm (upper) and by one photon laser source $\lambda = 380$ nm (lower) in fluorescein solution.

For OPE the optical sectioning is obtained by spatial filtering the emission in front of the detector in the so called confocal detection scheme. The rejection of out of focus plane is achieved by placing a screen with a pinhole in front of the detector. The focal point of the objective lens forms an image onto the pinhole screen: the specimen plane and the pinhole screen are conjugate planes (and hence the name confocal). The ability of a confocal microscope to create sharp optical sections makes it possible to build 3D renditions of the specimen. One drawback, using a lamp source, with imaging a point onto the specimen is that there are fewer emitted photons to collect at any given instant. Thus, to avoid building a noisy image each point must be illuminated for a long time to collect enough light to make an accurate measurement. In turn, this increases the length of time needed to create a point-by-point image. The solution is to use a light source of very high intensity. The modern choice is a laser light source, which has the additional benefit of being available in a wide range of wavelengths[14]. Unfortunately, fluorescence emission has not an infinite duration: molecules can undergo photobleaching. The phenomenon of photobleaching occurs when a fluorophore permanently loses the ability to fluoresce due to photon-induced chemical damage and covalent modification. Upon transition from an excited singlet state to the excited triplet state, fluorophores may interact with another molecule or with light to produce irreversible covalent modifications. The triplet state is relatively long-lived with respect to the singlet state, thus allowing excited molecules more time to undergo chemical reactions with reactive components in the environment. The average number of excitation and emission cycles that occur for a particular fluorophore before photobleaching is dependent upon the molecular structure and the local environment. The excitation power released per plane is independent of the focusing plane position along the optical axis. Thus, the main drawback of OPE confocal microscopy is the photobleaching of molecules in out of focus planes: when the focal plane moves to their plane they are no longer fluorescent. Since TPE requires the molecule to interact simultaneously with two photons (within $10^{-16}$ s), a high flux of photons ($10^{24}$ photons $cm^{-2}s^{-1}$) is needed at the focal plane. Only in the Ô90s, the development of mode-locked laser sources, that provide high peak power femtosecond pulses with a repetition rate of $\approx$ 100MHz and the introduction of high efficiency detectors (cooled photo-multiplier tubes, or single photon avalanche diodes), allowed laser scanning microscopy to take full advantage of TPE. Non-linear excitation, in fact, offers a series of unique features that make TPE very suitable for many applications. First, the two-photon absorption bands of the dyes commonly used in biological studies are wider than their one-photon analogous allowing the simultaneous excitation of multiple fluorophores with a single excitation wavelength. Second, the excitation light beam has a high penetration depth because IR radiation allows to penetrate deeper inside the tissues than in the conventional OPE excitation, in fact the longer wavelength employed in TPE are less affected by scattering. The scattering is the deflection of the light rays away from their original direction. Its angular distribution depends on the refractive index inhomogeneities, objects size and beam wavelength. For small objects in homogeneous media the scattering angular distribution is described by Rayleigh's law: it is isotropic and strongly ?-dependent $\propto \lambda^{-4}$ (for dipoles) $\approx \lambda^{-2}$ (for larger scatterer). Third, excitation takes place only at the plane of focus, due to the scaling of the probability of simultaneous photon absorption with the square of the light intensity. As a consequence TPE avoids the simultaneous absorption of photons outside the specimen drastically reducing both photo-toxicity and fluorophore bleaching. Moreover the fact that excitation, and therefore emission, take place only in a tiny well defined volume, makes unnecessary to place a pin-hole aperture in front of the detectors for the purpose of rejecting the signal arising from out of focus region. This latter fact simplifes the optical set-up and reflects also in a reduction of the background noise.

## 2.4 Optical pathway

In Figure 2.8 is reported an overview of the two-photon excitation setup used to perform FCS, time-domain lifetime measurements and spectra using nano-molar concentration. It is based on a mode-locked Ti:Sapphire laser (Tsunami 3960, Spectra Physics, CA) pumped by a solid state laser at 532 nm (Millennia V, Spectra Physics) coupled to a Nikon (Japan) TE300 inverted microscope. The laser provides 280 fs pulses on the sample plane at a repetition frequency of 80 MHz in the range of 700 - 1000 nm. Mirrors and beam steering are used to direct light to the back door of the microscope. Here, the fluorescence signal is collected by the objective (Plan Apochromat 60 X water, NA = 1.2, Nikon, Japan), is separated from the excitation beam by the dichroic mirror to be detected by a CCD camera (spectra measurements) or APDs. Except for spectra measurements, light is further selected by emission filters and split by a non-polarizing 50 % cube splitter to perform cross correlation functions. The minima values of the radial and axial FHWM of the microscope point spread function (PSF) are 240 ± 40 nm and 780 ± 50 nm, respectively, at a wavelength of 800 nm. With the introduction of a beam expander on the optical pathway, it is possible to change the excitation volume reducing the laser beam diameter at the entrance pupil of the objective lens. Typical excitation volume employed in this work ranges 0.5 to 0.8 $\mu m^3$. Fluorescence signals and autocorrelation functions are acquired by an ALV5000E (ALV, Langen, D) board and then analyzed by means of the non least-squares routine of the Origin 7.0 software (OriginLab Inc., Northampton, MA).

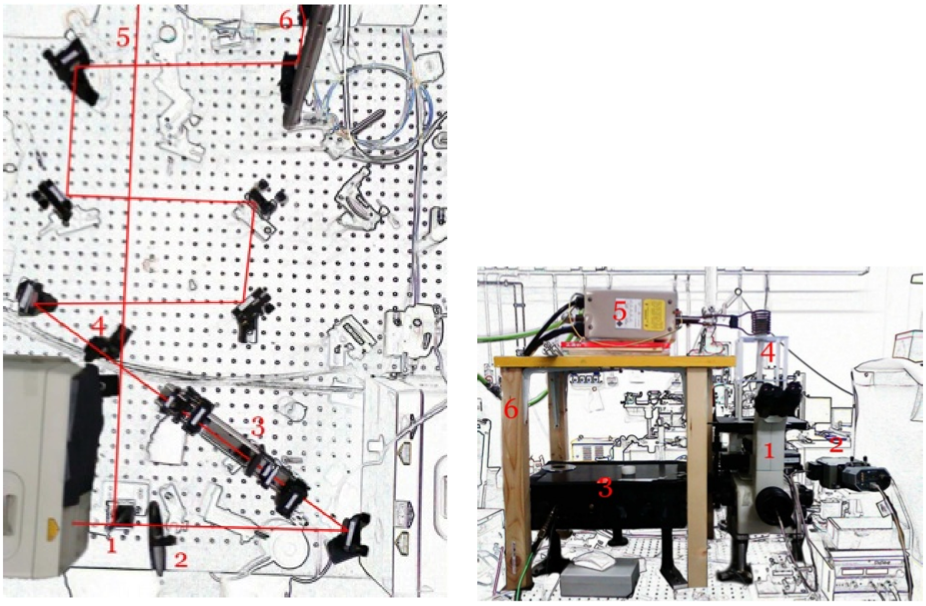

(a) *1) Tsunami, 2) Gray filter, 3) Beam Expander, 4) Pin-hole, 5) Photodiode, 6) Beam stearing.*

(b) *1) Microscope, 2) Spectral camera, 3) SPAD, 4) Grin Lens, 5) RF source.*

Figure 2.8: Schematic representation of the experimental setup.

The RF source and Grin Lens (figure 2.8) required for the measurements with magnetic nanoparticles will be described later (Chapter 5).

# Bibliography

[1] Lakowicz J.R. In principles of fuorescence spectroscopy. Kluwer Academic Plenum Press, New York., 1999.

[2] Herschel Sir J.F.W. Uber den mechanisms des photolumineszenz von farbstoffphosphoren. Phil. Trans. R. Soc. London, 135:143Ð145, 1845.

[3] Jablonski A. On a case of superficial colour presented by an homogeneous liquid internally colourless. Z. Phys., 94:38Ð46, 1935.

[4] Stokes G.G. On the change of refrangibility of light. Phil. Trans.R. Soc. London, 142:463Ð562, 1852.

[5] Kasha M. Characterization of electronic transitions in complex molecules. Disc. Faraday Soc., 9:14Ð19, 1950.

[6] Goppert-Mayer M. Uber elementarakte mit zwei quantensprunngen. Ann. Phys. (Leipzig), 9:273-295, 1931.

[7] C. Xu and W. W. Webb. Journal of the Optical Society of America B, 13(03): 481, 1996.

[8] Louisell W. H. Quantum statistical properties of radiation. Wiley New York, 1973.

[9] Diaspro A. Methods in cellular imaging. Oxford University Press, New York, 2001.

[10] Born M. and Wolf E. Principles of optics. Cambridge University Press, Cambridge, 1999.

[11] Nakamura O. Fundamental of two-photon microscopy. Micr. Res. Tec., 47(3):165-171, 1993.

[12] Cannell M. B. and Soeller C. High resolution imaging using confocal and two-photon molecular excitation microscopy. Pro. R. Microsc. Soc., 32:3-8, 1997.

[13] Williams et al. Nature Biotechnology, 21(11):1369-1377, 2003.

[14] Sheppard and Shotton. Springer-Verlag New York Inc., New York, 1997.

Chapter 3

# Hybrid FITC-Gold Nanosensor for protein detection

questa sera spirerá...sotto i pini
del boschetto

L. Da Ponte, Le Nozze di Figaro
W. A. Mozart

IMMUNOLOGICAL methods have a large impact on tumor treatment. For example the detection, through the use of specific antibodies, of protein (receptors) over-expressed on malignant cells is a good candidate to recognize very small tumors. Recent statistical data that indicate that micro-metastasis detected and treated at early stages correspond to a better patient prognosis[1], have motivated a large interest in the detection of cancers based on traces of tumor markers. Immuno-targeting is possible due to a number of receptors that are slightly more specifically expressed by some cancer cells. For example, epithelial precancers express EGFR receptor[2] and LNCaP prostate cancer cells over-express the Her-2/neu receptor[3] while B16 melanoma cells have some definite over-expression of the TRP1 receptor[4].Immune recognition has been coupled to a variety of optical detection methods: changes in the optical response of thin gold layers[5] or in the fluorescence signal from antibody functionalized surface by total internal reflection methods[6], or colorimetric assays based on immuno-driven aggregation of gold colloids[7]. The sensitivity reached by these methods is of the order of 1 pM[8] and the in vitro selectivity depends on the availability of monoclonal antibodies for the specific protein or protein mutant. The selectivity for the malignant cell line, instead, depends on the relative abundance of the receptor on the malignant cells with respect to the healthy ones. This difference is unfortunately not very large and its estimate is not straight forward[9].

Biotechnology is pushing the minimum amount of detectable material toward lower and lower values. The limiting values of detection depend on the experimental method, and they are of the order of 1-10 pM that, for a 60 000 Da molecular weight protein, correspond to about 6-60 ng/L. One of the best known detection methods is the so-called surface plasmon resonance (SPR) assay. This method is based on the change of the position of the plasmonic band induced by the binding of a biomolecule to a complementary molecule attached to the surface of a thin gold layer. The shift is measured by detecting the angular dependence of the reflectivity of the thin gold layer. The sensitivity in the concentration measurement is related to the amplitude of the shift of the reflectivity minimum. It has been also shown that gold NPs coverage of the SPR chip enhances the detection sensitivity. Recently it has been suggested that biorecognition on the surface of gold and silver NPs can provide large sensitivity, also depending on the NPs form anisotropy. Gold or silver nanoparticles, 5 - 20 nm in size, are endowed with a characteristic extinction spectrum that lies in the visible near infrared region of the electromagnetic spectrum. We have studied the interaction of gold nanoparticles a few nanometers in size with fluorophores and exploit the changes of the dye excited-state lifetime and brightness induced by our interaction in solution under physiological conditions. We have investigated the system based on 5 and 10 nm gold NPs coupled (via a biotin-streptavidin linker) to a fluorophore (FITC) and to a specific protein antibody. The binding of protein to the gold NPs through antigen-antibody recognition modifies the dye excited-state lifetime, which change can then be used to measure the protein concentration. In particular, we have tested the nanodevice measuring the change of the fluorophore excited-state lifetime after the binding of the model protein bovine serum albumine (BSA) and p53 protein, a marker for early cancer diagnosis and prognosis (both in standard solution and in total cell extracts).

## 3.1 p53: the guardian of the genoma

The history of cancer brings us back some thousands years B.C. to Egypt where the first descriptions of what we today call cancer, were recorded on papyri. About 2000 years later the name of carcinoma from karkinos (the Greek name for crab) was implemented by Hippocrates, (460 - 370 B.C.) after his observations where he noticed that blood vessels around a malignant tumor looked like the claws of a crab. Today, cancer is a general term whose definition can be shortened to the pathology related to abnormal and uncontrolled cell growth. The disease is divided in four major groups, carcinomas, sarcomas, lymphomas and leukemias which are themselves subdivided into subgroups leading to a total of over 200 types of cancers. Even if they all share the same definition, there is a wide range of variations between them in their origins and causes, their symptoms and their treatments. Cancer has become one of the leading causes of death in the world after cardio-vascular related diseases. In the year 2002, there were 10.9 million new cases, 6.7 million deaths and 24.8 million persons living with cancer. Although epidemiological evidence has shown a causative link between genetic predisposition, tobacco consumption, diet, sexual habits, environmental exposure or viral infection, cancer can affect all human beings independently of social rank, ethnic background, education level or geographic location as illustrated in figure 3.1.

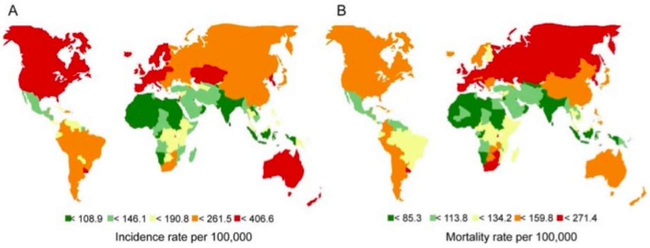

Figure 3.1: World map of the age standardized (A) incidence and (B) mortality rate per 100,000 males of all cancer sites but non-melanoma skin, the GLOBOCAN database 2002, WHO, IARC (http://www-dep.iarc.fr/)

The development of cancer, carcinogenesis, is a long and complex accumulation of genetic and epigenetic alterations. It can take years to decades from the first hit to the development of a tumor. There are six major cellular functions governing cell proliferation and homeostasis that need to be acquired by the cells in order to become malignant. These acquired capabilities are insensitivity to growth-inhibitory signals, autosufficiency with growth signals, evasion from apoptosis, limitless replication, sustained angiogenesis and tissue invasion. Alterations leading to these phenotypes are genetic, including point mutation, deletion, chromosomal translocation and gene amplification, as well as epigenetic including DNA hypermethylation and histone modification. They generally lead to the activation of proto-oncogenes to oncogenes (K-ras, src, c-myc) and/or to the inactivation of tumor suppressor genes (p53, Rb, APC). As genetic alterations of these genes occurs, they confer to the cells a growth or survival advantage. They can then expand as they proliferate more than their normal neighbors. According to both theories, cancer appears as a multistep process of accumulation of alterations on specific genes leading to clonal expansions and tumor formation.

### 3.1.1 The History

During the 1960s and 70s when studies on tumor viruses and oncogenes was the focus of many cancer researchers, several groups reported about the existence of a cellular protein that was overexpressed in many tumors. This protein, with an approximate molecular weight of 53 kDa was termed p53 (protein p53). In one of the first studies, p53 was identified in complex with the simian virus 40 (SV40) large-T oncoprotein in SV40-transformed cells. Subsequently, p53 was shown to bind several other oncoproteins produced by different tumor viruses, including the human papillomavirus (HPV) E6 protein and the adenovirus E1B 55K protein. The ability of p53 in cooperation with ras, a well known oncogene to transform rat embryo fibroblasts further confirmed the "oncogenic" property of p53. Together these findings led to the conclusion that p53 may be a novel cellular oncogene whose overexpression associated with cellular transformation when coexpressed with viral oncoproteins and mutant Ras.

Overexpressed p53 in tumors was later shown to be a result of accumulation of mutant p53 and missense mutations in the p53 gene indeed conferred strong transforming potential. Also the originally cloned p53 cDNAs used in the early studies contained dominant negative missense mutations within a region important for the biological activity of wild type (wt) p53 protein. The idea of p53 as an oncogene was in transition and the wt p53 was instead considered a key tumor suppressor. Furthermore, binding of p53 to the viral oncoproteins was shown to cause inactivation or degradation of p53. These oncoproteins through complex formation with p53 abrogated p53 transactivation function, an activity that was later found to be essential for its role in tumor suppression. Other observation that further strengthened this new view of p53 was that certain cellular stresses such as DNA-damage caused by UV-irradiation or chemicals increased the cellular level of wt p53 in non-transformed mouse cells. Such genotoxic agents are known to act in a cytostatic manner, forcing cells to either arrest their progression through cell cycle or trigger activation of cell suicide program.

### 3.1.2 p53 the Gatekeeper

The most important due on p53 function as a tumor suppressor emerged from the findings that p53 deficient mice are susceptible to spontaneous tumorigenesis. p53 null mice, although develop normally, show high incidence of sarcomas and lymphomas at an early age. Another crucial piece of evidence came from the observation that patients with the cancer-prone Li-Fraumeni syndrome, an inherited susceptibility disorder, carry a gremlin mutation in the p53 allele. These patients have an increased risk of developing a variety of cancers including soft tissue sarcoma, tumors of breast, bone, brain and bladder. Subsequently, mutations in the p53 locus have been identified in nearly half of all human tumors. It is well established that the tumor suppressor p53 is a loyal cellular watchman in charge of ensuring the maintenance of the cellular household in order. The level of p53 in normal cells is tightly controlled by its major inhibitor MDM2 that binds and targets p53 for cytoplasmic shuttling and degradation. When the genomic integrity of a cell is threatened by metabolic or genetic disorder such as oncogene activation, DNA-damage, nutrient deprivation and hypoxia, latent p53 is stabilized and transformed into an active form. Upon activation it triggers a wide range of cellular responses depending on the type of cell and stress. These processes include cell cycle arrest, DNA-repair, programmed cell death (apoptosis), differentiation, senescence, inhibition of angiogenesis and metastasis and possibly other unknown cellular responses (figure 3.2). Cell cycle arrest and apoptosis are the two most studied p53-mediated cellular responses that reflect the choice of p53 leading to a cell's ultimate fate, life or death.

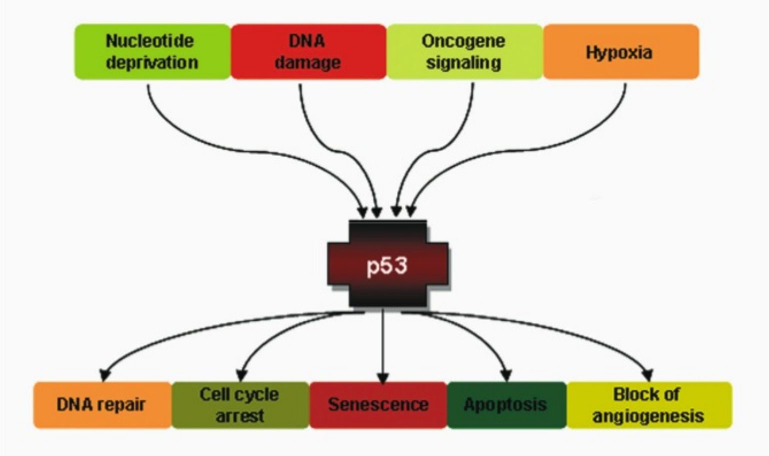

Figure 3.2: p53 activating signals and its downstream cellular responses

How does p53 function? The molecular functions of p53 have been a subject of intensive research over the past 25 years. The first activity to be depicted was p53 ability to bind DNA in a sequence specific manner through its central core domain. When fused to a DNA-binding polypeptide GAL4, p53 mediates transcriptional activation function. These groundbreaking findings laid the foundation for the future characterization of the major p53 function, the transcriptional regulation of target genes. Numerous targets of p53 that participate in various cellular processes have been identified and actions of these targets ultimately decide the final destiny of a cell in stress. Recent data suggest that p53 can induce apoptosis directly at the mitochondria and indeed, the tumor suppressive function of p53 also comprises transcriptional independent mechanism which is a growing field of research today.

### 3.1.3 The protein structure

The p53 gene is located on the short arm of the chromosome 17 at the locus 17p13. The genomic sequence is transcripted into a mRNA transcript composed of 11 exons but whose first exon is non-coding. mRNA is then processed and translated into a 393 amino acid nuclear protein conserved throughout evolution. Based on structural and functional analysis, p53 is subdivided in 5 domains, the transactivation domain at the N-terminus, the proline rich domain, the DNA binding domain, also called core domain, the oligomerization domain followed by the nuclear localization signals at the C-terminus (figure 3.3). Each domain has a specific function.

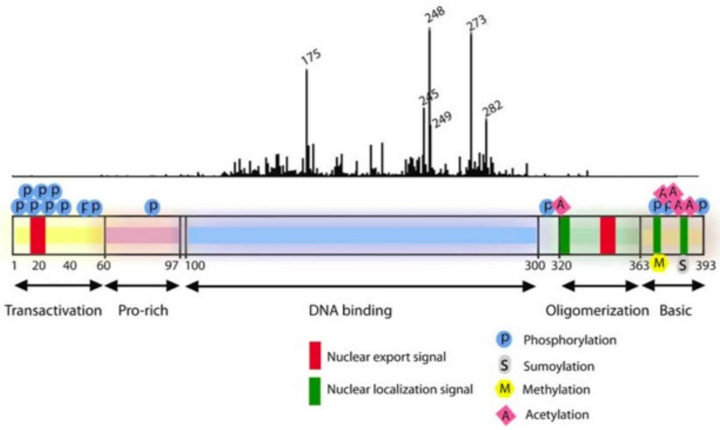

Figure 3.3: Schematic representation of the p53 protein. The protein is made of 5 domains, both C- and N-termini are prone to post translational modifications as indicated. The majority of p53 mutations are clustered in the DNA binding domain. The so called hot spot mutants are illustrated with bar indicating the frequency of reported mutations.

The transactivation domain, located between amino acids 20-60, is split into two smaller sub- domains both required for full p53 transactivation activity. p53 negative regulator, MDM2 or viral proteins such as E1B 55K can bind this domain repressing p53 transcription activity. Next the proline-rich domain made of the five repeats $PXXP$ has been shown to be implicated in the p53-dependent apoptosis. In the central part of the protein, the DNA binding domain stretched between amino acids 100-300. This domain binds to the p53 consensus DNA sequences which consist of two PuPuPuC(A/T)(A/T)GPyPyPy palindromes separated by a 0 to 21 base pair spacers, where Pu is a purine and Py is a pyrimidine. Through its binding p53 can transactivate or transrepress specific genes containing a consensus p53 response element. The structure of the core domain is made of 3 loops. The first loop binds the major groove of the DNA strand and the second loop binds its minor groove. The third loop stabilizes the second loop. This structure is maintained by a zinc ion which binds to the core cysteine residues Cys176, Cys 238 and Cys242, and the histidine His179. A total of 10 cysteines residues are localized in the DNA binding domain. Interestingly the majority of p53 mutations tend to be clustered within the DNA binding domain and tend to result in a loss of p53

DNA binding and transactivation potential. The oligomerization domain is located at the C-terminus, between amino acids 320-360. It is involved in the formation of dimers and tetramers which are dimers of dimers. Upon stabilization p53 monomers form tetramers leading consequently to a higher p53 affinity to bind DNA and thus transactivation of downstream target genes.

The last 30 amino acids, also called the basic domain, contain two nuclear localization signals. This last part of the C-terminus is a negative regulator of DNA binding. Post translational modifications of this terminus increase p53 stability and transactivation activity. Interestingly in response to DNA damage, Ser315 and Ser392 are phosphorylated, Lys320, 373 and 382 are acetylated, and Lys386 is sumoylated. Overall following stress, both termini are highly post-translationnaly modified as reviewed by Appella & Anderson. While the N-terminus is more prone to phosphorylation, the C-terminus is subject to more diverse modifications.

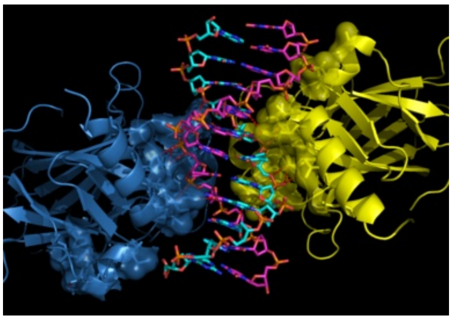
Figure 3.4: Dimeric form of p53 interacting with DNA.

### 3.1.4 p53 Regulation

When activated p53 has the ability to determine between life and death of a cell by inducing cell cycle arrest or apoptosis. Therefore, in normal undamaged cells it is extremely important to keep it under strict control to avoid unnecessary killing by unleashed p53. The protein half time is about 30 minutes. Regulation of p53 occurs at both mRNA and protein levels, although most published data deals with protein regulation. Upon cellular stresses p53 due to oncogenic stress, hypoxia or UV irradiation, p53 is stabilized mainly via post-translational modifications, such as phosphorylation, acetylation, ubiquitination and glycosylation. One of the major players protein in p53 regulation is MDM2, however other proteins can also, directly or indirectly, affect p53 stability and thus activity. It includes MDMX, JNK1, ARF, and the more recently identified Pirh2 and COP1.

#### Stabilisation

MDM2, in humans also referred to as HDM2, plays the most central role in p53 regulation. Originally identified as overexpressed in a large proportion of sarcomas, MDM2 was demonstrated to co-purify and interact with p53 *in vitro*. Subsequent analysis showed that MDM2 binds to the N-terminal (aa residues 17-27) part a region containing several phosphorylation sites of p53 and inhibits p53-dependent transcription. MDM2 functions

as an E3 ligase, the final component of the enzyme cascade that leads to the conjugation of ubiquitin to their substrate proteins and the following degradation by the proteosome. It binds and ubiquitinates p53 already in the nucleus and shuttles it to the cytoplasm where proteosome-mediated degradation takes place. MDM2 also contributes to its own degradation as it can auto ubiquitinate itself. The promoter of MDM2 gene carries a p53-binding motif and is transcribed in a p53-dependent manner. Thus, high levels of MDM2 by increased p53 activity generate an autoregulatory loop that leads to rapid turnover of the p53 protein, allowing induced p53 to act during a short time window before it is withdrawn to its normal cellular levels. The critical role of MDM2 for p53 regulation is further supported by the rescue of the embryonic lethal phenotype of MDM2 null mice through elimination of p53. Furthermore, two other ubiquitin ligases, COP1 and Pirh-1 independently of each other form autoregulatory loop by promoting p53 degradation. Clearly, inhibition of MDM2 is a prerequisite for p53 stabilization which is accomplished by various independent pathways. Upon DNA damage one of the key p53 stabilization process involve phosphorylation of p53 by its upstream DNA-damage-induced kinases. The checkpoint kinases Chk1 and Chk2 phosphorylate p53 at several DNA-damage-inducible sites. More specifically phosphorylation of p53 on Ser20 by Chk2 counteracts MDM2-p53 binding to stabilize p53 after DNA damage. It was later shown that Ckh2 is dispensable for p53-dependent G1 arrest but is required for p53-mediated apoptosis. ATM, a further upstream kinase and a sensor of double-stranded DNA breaks causes phosphorylation of p53 on Ser15 after IR-induced DNA-damage and this phosphorylation although not essential contributes to efficient p53 stabilization and activation.
Interruption of MDM2-p53 interaction is also achieved by phosphorylation of MDM2. The non receptor tyrosine kinase, c-Abl positively regulates p53 by targeting MDM2. It phosphorylates MDM2 on Tyr394 *in vivo* and inhibits MDM2-mediated degradation of p53 and thereby promotes p53 accumulation and p53-induced cell death upon DNA damage.

### Activation

Several forms of stress can lead to DNA damage and consequently p53 activation such as genotoxic chemicals such as cisplatin, UV radiation, shortening of telomeres, ROS (reactive oxygen species), ionizing radiation. p53 can also be activated by non genotoxic stress such as oncogenic stress caused by over activity of a proto-oncogene as for example the amplification of the proto-oncogene c-myc which leads to DNA damage by inducing ROS. Following stress p53 is stabilized and protein accumulates due to a longer halt life and to an increase rate of translation while mRNA level does not change. The activation of p53 is also modulated by phosphorylation events mediated by effector protein kinases.

DNA-PK belongs to PI3-kinase family and is activated following DNA strand breaks as the ones induced by ionizing radiation. Moreover DNA-PK phosphorylate Ser15 in the N-terminus of p53. As expected exposing cells to ionizing radiation leads not only to an increase of p53 level but also to Ser15 phosphorylation. The stabilization of p53 can be explained by the phosphorylation which disrupts p53-MDM2 interaction, as the amount of MDM2 protein coimmunoprecipitated with p53 protein strongly decreased upon phosphorylation by DNA-PK . However DNA-PK is not required for p53 response following DNA damage as shown in DNA-PK deficient MEF cells which upon ionizing radiation still had p53 accumulation, Ser15 phosphorylation and p53 DNA binding. Another member of the PI3-kinase family, ATM can also phosphorylate Ser15 following ionizing radiation. However phosphorylation of this residue following UV radiation was not induced by ATM, but by ATR 66. Moreover ATM activates downstream Chk2 kinase, and ATR activates downstream Chk1 kinase, in both cases resulting in Ser20 phosphorylation and p53 stabilization. However when mutating the murine Ser23 to Ala23 (equivalent to human Ser20), it did not prevent p53 accumulation nor p21 and MDM2 upregulation, suggesting that Ser20 is not required for p53 stabilization. Phosphorylation of Thr18 is also induced by DNA damage, and is known to be responsible for the disruption of the MDM2-p53 interaction. However the responsible kinase is not known, but casein kinase I has been suggested as a candidate by in vitro study using recombinant proteins. However inhibing phosphorylation of Ser15 prevent phosphorylation of Thr18 by casein kinase I. Stabilization of p53 may be achieved via modifications of other proteins as well. Phosphorylation of MDM2 at Ser395 by ATM inhibits the binding of MDM2 to p53. Beside phosphorylation, dephosphorylation can happen also in a ATM-dependent manner. Indeed Ser376 is dephosphorylated after ionizing radiation, creating a binding site for 14-3-3 which has been shown to activate p53 DNA binding activity. As discussed later, activity of p53 can also be regulated by its interaction with other proteins such as the ASPP1 and 2, p300, and the two other members of the p53 family p63 and p73.

### Cellular Localization

Nuclear import and export of p53 is a tightly controlled process. Nuclear localization is required for p53-mediated transcriptional regulation. p53 contains three nuclear localization signals (NLS) that upon stimuli enable its nuclear import whereas nuclear export of p53 is mediated by two nuclear export signals (NES). However, efficient nuclear export of p53 to the cytoplasm requires the ubiquitin ligase function of MDM2. Mutations of the lysine residues in the C-terminus, where MDM2-mediated ubiquitination of p53 occurs, abrogate MDM2-directed nuclear export. This is possibly due to the exposure or activation of the nuclear export sequence of p53 caused by MDM2-mediated ubiquitination which affects p53 oligomerization state. Nuclear export of p53 is necessary for efficient p53 degradation. Loss of p53 function in some tumor types such as in neuroblastomas carriyng wt p53 is coupled with its failure to accumulate in the nucleus. The observed nuclear exclusion may be an effect of hyperactive MDM2 or the activity of glucocorticoid receptors (GR). The latter involves complex formation between p53 and GR, resulting in cytoplasmic sequestration of both p53 and GR. Dissociation of this complex by GR antagonists, results in accumulation of p53 in the nucleus, activation of p53-responsive genes, growth arrest and apoptosis. Other proteins that directly or indirectly effect p53 nuclear import/export are importin-$\alpha$, PI3/Akt, p14ARF, Pacr, actin, vimentin and mot2.

### 3.1.5 p53 in cancer - loss and consequences

The p53 function is disrupted by mutations, in about 50 % of all sporadic human tumors and in the other half the p53 protein is inactivated by various cellular and viral antagonists, including MDM2. in fact, p53 mutation is the most frequent genetic event found in a broad range of human tumors to date including cancers of the ovary (48%), stomach (45%), colon (43%), esophagus (43%), lung (38%), and breast (25%)

Unlike other tumor suppressor genes that are inactivated by truncation or deletion of their gene more than 80% of p53 alterations are caused by missense point mutations that result in full length stable p53 levels. Therefore, high expression of mutant p53 is often detected in human tumors. In tumors, p53 mutations are distributed in all coding exons, however with a strong predominance in exons 5-8, encoding the DNA-binding domain. Mutation of p53 typically occurs in one allele whereas the other one is often lost by loss of heterozygosity (LOH). Some mutants exhibit dominant-negative activity that disrupts the p53 function produced by the wt allele through hetero-oligomerization of mutant p53 with the wt p53. Mutant p53 is capable of activating alternate subset of promoters such as of c-myc oncogene and MDR1 induction of these genes facilitates cell proliferation and multiple drug resistance respectively. Mutant p53

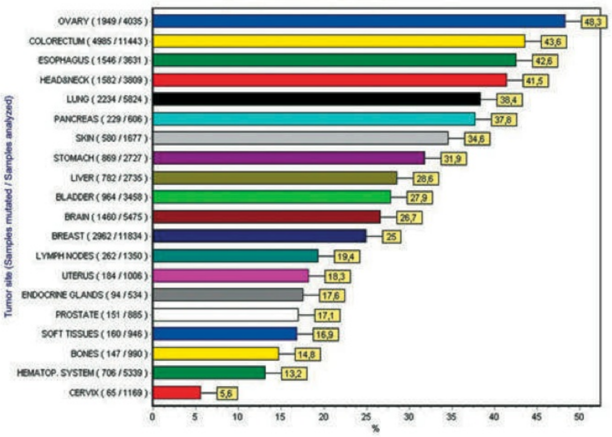

Figure 3.5: Frequency of mutant p53 allelels in human tumor cell genomes as recorded in the IARC database, 2006. (http://www-p53.iarc.fr/P53main.html).

also interacts with transcriptional co-activators including p300 and CBP to promote deregulated gene expression. Thus, human tumors favor selection for accumulation of p53 mutations bestowing growth advantage properties by mutant p53 to endorse tumor progression.

Most of the point mutations (90%) occur in the hot spot region (as residues 110 - 290), targeting the sequence-specific DNA-binding core domain and thereby rendering p53 transcriptionally inactive. The p53 mutations can be divided into two groups. Group I mutations e.g. codon R248, the most frequently occurring mutation in tumors, affect DNA-binding of p53 but generate a protein with wt conformation. The second group of mutations e.g. codon R175 produces a protein with altered conformation conferring more severe phenotype in vitro. As mentioned earlier in half of the tumors p53 inactivation occurs via non-mutational mechanism (i.e. in the p53 gene). Instead, the p53 pathway is disrupted either through inactivation of p53 protein by its antagonizers or via disruption of its upstream regulators. Overexpression of the p53 negative regulator MDM2, through gene amplification is a common strategy that appears in a variety of tumors. Deregulated expression of MDM2 leads to continuous degradation of p53 rendering the cell with p53 null condition. Disruption of the p53-MDM2 complex is the critical step for activation of p53 during stress. The upstream kinase such as the DNA-damage-induced protein kinase, ATM in the human disease ataxia-telangiectasia (AT), renders p53 unphosphorylated at Ser15, Ser20 and MDM2 at Ser395 and thus abrogating IR-induced p53 activation. The AT-patients show multiple abnormalities including increased risk for lymphomas, Chk2, another DNA-damage-checkpoint kinase and a major effector of ATM also phosphorylates p53 at Ser20 upon $\gamma$-irradiation and enhances apoptotic response.

### 3.1.6 Choice of Response - Life or Death

When a cell faces cancer threats p53 gets activated to elicit a response that either repairs the damage and keeps the cell halted but alive or eliminates the damaged cell from the system. An obvious question is how p53 makes the decision between life and death. This choice is primarily dependent on the balance between the availability of cellular factors as well as the extracellular signaling events. Firstly, the type of stress versus the extent of damage that triggers p53 is an important factor since the damage caused by it dictates whether or not it is worth repairing the injury. If the damage is too extensive apoptotic response might be the preferred choice. In addition, the survival signals such as high levels of secreted growth factors, cell-matrix interactions conferring anti-apoptotic features render cells resistant to apoptosis. In these cells p53 activation may facilitate transient or irreversible termination of cell cycle. Secondly, the intracellular molecular events, that in various ways affect p53 and thus also determine the outcome of its effects. This includes the availability and activity of p53 regulators, positive and negative. The genetic alterations, characteristics of a cancer cells are potential modulators of p53-mediated responses. Hence, the specific genotype of a cancer cell governs the biological consequence of p53 activation.

p53 is primarily a sequence-specific transcription factor and the proteins encoded by its target genes contribute to the biological outcome of p53 induction. However, transcription independent function of p53 also has substantial impact on its effects. The choice between life and death will ultimately depend on its ability to preferentially switch on or off particular subsets of genes, i.e. cell cycle inhibitory genes or pro-apoptotic genes. The first studies separating the two functions of p53 i.e. activation of cell cycle arrest genes and pro-apoptotic genes came from the analysis of tumor-derived p53 mutants capable of activation of p21 promoter and G1 arrest but not of BAX or IGF-BP3. These apoptosis deficient mutants with slight conformational changes can interact with high affinity binding sites but are unable to bind lower affinity motifs present in pro-apoptosis genes. This model has been supported by others confirming the presence of high or low affinity binding sites in different p53 target gene promoters. Furthermore, earlier work demonstrated differential binding affinity of p53 by the observation that low levels of p53 induces cell cycle arrest but higher levels or DNA-damage-induced p53 triggers apoptosis. Many other molecular mechanisms participate in p53 target gene selectivity. Post-translational modification of p53 has been shown to affect promoter selectivity by p53. The selective DNA binding caused by covalent modifications is possibly a result of changes in p53 conformation altering its DNA binding specificity. Recent data suggests that the E2F1 transcription factor, in the absence of mouse p19ARF, can induce phosphorylations of p53 at multiple sites with striking similarity as observed upon DNA damage. These p53 modifications were shown to be crucial for E2F1-mediated apoptosis. An example of a modifier that favors p53-mediated apoptosis without inducing covalent modifications of p53 is the p300 coactivator JMY, which during stress interacts with p300 and is recruited to activated p53 to conduct transactivation of BAX and induction of apoptosis.

Although most work has identified pro-apoptotic modulators of p53, factors that direct p53 selectivity to growth inhibitory, DNA repair or anti-apoptotic genes also have been identified. The WT-1 tumor suppressor has been shown to stabilize and lead p53 towards cell cycle arrest but inhibit p53-mediated apoptosis. Likewise, the BRCA1 tumor suppressor can shift p53-mediated transcriptional response en route for cell cycle arrest and DNA repair. In contrast upon DNA-damage p53 can switch to apoptotic response by downregulating BRCA1. The corepressor mSin3a and histone deacetylases play an important role in repression of several p53-downregulated targets and p53-mSin3a-mediated transrepression has been shown to trigger apoptosis. Presence of mSin3a in cells overexpressing p53-repressed proteins can facilitate the apoptotic response by assisting p53 to downregulate these targets. The RB tumor suppressor can enter the MDM2-p53 complex and prevent p53 degradation. Formation of this trimeric complex contributes to regained repression function by p53 and increased apoptosis but no effect on its transcriptional activation function (figure 3.6).

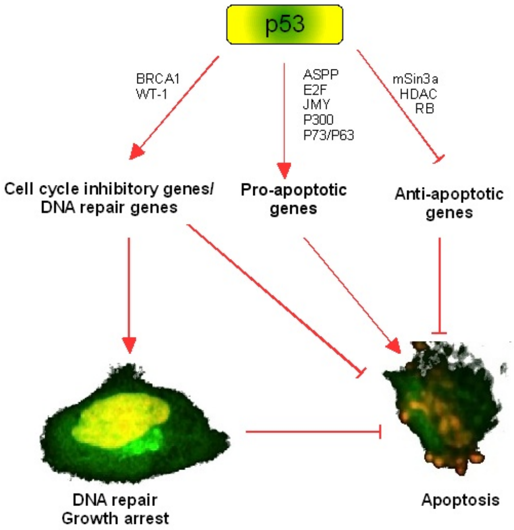

Figure 3.6: Decision making by p53. The coactivator and corepressor proteins as well as posttranslational modifications of p53 dictate the choice between life and death decision by p53.

Evidence suggests that ER (endoplasmic reticulum) stress caused by protein misfolding can induce p53-mediated cell cycle arrest involving MDM2. ER stress enhances interaction between MDM2 and ribosomal proteins inhibiting MDM2-mediated ubiquitination and degradation of p53. The role of p21 seems to be important for p53-induced cell cycle arrest by ER. The p53 family members, p63 and p73 are also contributors to the choice of apoptotic response. p53 needs at least one of its relatives for activation of apoptotic genes upon DNA damage. In the p63/p73 double knockouts, p53 fails to bind the promoters of specific apoptotic genes. The significance of this finding is currently unknown as wt p53 does not interact with p63 or p73 suggesting an indirect mechanism of this cooperative action.

### 3.1.7 p53 functions

p53 exerts its various cellular functions by transcriptional-dependent and independent pathways. The transactivating function was established by the discovery that p53 interacts with specific double stranded DNA sequences. Subsequent analysis revealed the consensus sequence and its presence in many p53 activated gene promoters. Function of multiple p53 targets has been analyzed and linked to diverse cellular processes including cell cycle arrest, apoptosis, DNA repair, senescence, angiogenesis and metastasis. Information on cell cycle arrest and in particular, apoptosis by p53 nonetheless beat the other events by many publications which is not surprising since p53-induced apoptosis is crucial for tumor suppression. However, knowing the complexity of cellular mechanisms it is logical to assume that some of the other events may ultimately diverge by one or the other way into the apoptotic response.

### Cell Cycle Arrest

Cell cycle is a complex process and is tightly regulated by multiple actors with cyclins and their corresponding cyclin dependent kinases (CDKs) and the CDK inhibitors being the core components of this process. Successful completion of cell cycle is monitored and controlled by cell cycle checkpoints that block progression when flaw in terms of damage DNA is detected. p53 transactivates components of both G1/S and G2/M checkpoints upon physiological stress.

In the first phase (G1) the cell grows. When it has reached a certain size it enters the phase of DNA-synthesis (S) where the chromosomes are duplicated. During the next phase (G2) the cell prepares itself for division. During mitosis (M) the chromosomes are separated and segregated to the daughter cells, which thereby get exactly the same chromosome set up. The cells are then back in G1 and the cell cycle is completed (figure 3.7).

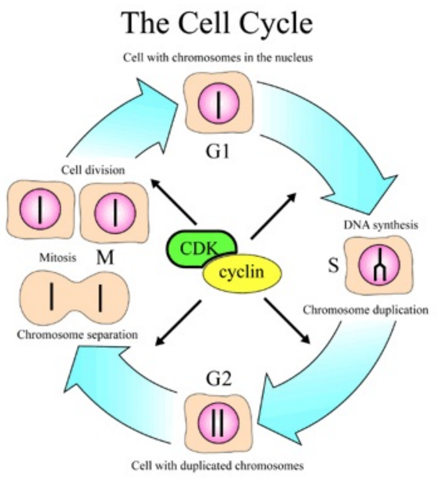

Figure 3.7: The different phases of cell cycle.

p21 is the most famous p53-induced cell cycle inhibitory gene that can induce both G1 and G2 arrest by inhibiting cyclinE/CDK2 and cyclinB/Cdc2 respectively. Cdc2 (also known as CDK1) required for entrance to mitosis is downregulated at RNA and protein level in a p53-dependent manner after IR and involves p21 for this negative regulation. Furthermore, p21 is also involved in activation of the RB tumor suppressor pathway. RB is inactivated through hyperphosphorylation mediated by cyclin/CDKs during active cell cycle process. Upon induction, p21 inhibits cyclinE/CDK2 causing hypophosphorylation of RB that binds E2F to inhibit E2F-mediated transcription of cell cycle genes. Hence, p21 integrates the two tumor suppressor pathways following cellular stress. Others have demonstrated that activation of p21 protects cells from Fas-mediated apoptosis by direct binding and inhibition of pro-caspase-3 (one of the downstream effectors of apoptosis signaling). Protein kinaseA-mediated phosphorylation of p21 is essential for this complex formation that takes place at the mitochondria. This could be an additional strategy for cells to avoid cell death. Another p53-induced target 14-3-3$\sigma$ (sigma) belongs to a family of proteins that regulate cellular activity by binding and sequestrering phosphorylated proteins. Induced 14-3-3$\sigma$ inactivates Cdc25 and Cdc2 by sequestering them to the cytoplasm to trigger pre-mitotic G2/M block upon DNA damage. Furthermore, 14-3-3$\sigma$ has been shown to promote translocation of pro-apoptotic Bax out of the cytoplasm and thereby delay apoptotic signal and enforce cells into G2 arrest.

### Apoptosis

The first proof of p53 function is apoptosis comes from studies of temperature sensitive mutant p53 that acquires the conformation of wt p53 when the cells are grown at a permissive temperature of 32 °C. The first proof of p53 function in apoptosis comes from studies of temperature sensitive mutant p53 that acquires the conformation of wt p53 when the cells are grown at a permissive temperature of 32 °C. The observed rapid cell death upon temperature shift to 32 °C implicated a role of p53 in cell death. p53-mediated tumor suppression is primarily dependent on its apoptotic function. This notion is based on several mouse model studies. in one such model where p53-dependet growth arrest is defective due to expression of SV40 large T-antigen whereas the apoptotic pathway is intact, the mice develop slow growing tumors. In contrast crossbreeding of these mice on p53 null background generates mice with aggressive tumor growth. Another study showed that in myc-driven lymphoma, block of p53-mediated apoptosis does not confer any selection for inactivating p53 mutations unlike their apoptosis proficient counteparts and that no cell cycle defects could be detected in the apoptosis defective cells. Hence, the function of p53 as an inducer of apoptotic cell death is the most significant one. According to some analyses, p53 DNA binding is crucial for tumor suppression, whereas other studies have shown that transactivation mutant p53 can still or even more potently induce apoptosis and therefore p53-mediated transactivation is dispensable for this function. Many transcriptional dependent and independent p53 targets have been implicated in p53-mediated apoptosis. However, only a few seem to be essential for induction cell death. Members of both the extrinsic and intrinsic apoptotic club have been identified. Although initiated by different actors both lead to caspase-mediated apoptosis.

### Senescence

Cellular senescence is a program that is triggered by normal cells in response to different types of stress such as telomere shortening, oxidative stress and DNA damage. Upon entering senescence, cells cease to divide and undergo a number of morphological and metabolic changes. Although detailed description of its in vivo manifestation is lacking, cellular senescence is considered to have a key role in tumor suppression and organismal aging. Both p53 and RB pathways are active during senescence and inactivation of p53 in MEFs is sufficient to prevent senescence. p53-induced p21 seems to be important for activation of the RB pathway and for triggering cellular senescence in response to DNA damage and telomere uncapping. Telomere shortening can be prevented by activation or everexpression of the human telomerase catalytic subunit, hTERT that facilitates tumorigenesis overexpression of the human telomerase catalytic subunit, hTERT that facilitates tumorigenesis.Interestingly, hTERT is downregulated by p53 and overexpressed hTERT exhibits anti-apoptotic activity. This suggests that the two anti-tumor events senescence and apoptosis are linked via p53 and p53-regulated proteins. Moreover, recent evidence suggest that restoration of p53 function in sarcomas leads to tumor regression via cell cycle arrest with features of cellular senescence.

### DNA repair

Damage to DNA triggers signaling that involves activation of multiple factors that act in parallel to repair the damage. Involvement of p53 in both base excision repair (BER) and nucleotide excision repair (NER) has been demonstrated. p53 enhances NER mainly by induction of target genes such as GADD45, a gene induced by IR in cells with wt p53 cells. Regulation of the BER by p53 is on the other hand, correlated with its ability to directly associate with AP endonuclease (APE) and DNA polymerase $\beta$ (DNA pol$\beta$). The interaction between DNA pol$\beta$ and the abasic DNA sites is further stabilized by p53. Moreover, following $\gamma$-irradiation p53 induction is accompanied by increased activity of the 3-methyladenine DNA glycosylase (3-MeAde), the first enzyme acting in the BER pathway.

### Mechanisms of repression

In contrast to p53-activated genes that almost exclusively require p53 binding to their consensus sequence, negative regulation by p53 can be mediated by different mechanisms. Moreover, binding of p53 to novel DNA sequences in some repressed promoter has been shown. Downregulation by p53 probably occurs by any of the three mechanisms that transcriptional repressors are thought to function through.

The first comprises interference with other activators at the target promoter. In this model, transcriptional repression by p53 falls into two categories. In the first category, downregulation takes place through p53 binding to the consensus DNA elements. For instance, repression of the alpha-fetoprotein gene (AFP) mediated by p53 results in inhibition of the activating transcription factor HNF-3. Competitive binding to the AFP promoter containing overlapping binding sites for p53 and HNF-3 results in displacement of HNF-3 and net repression by p53. However, repression via noncompetitive binding, where p53 interferes with the function of an activator, but not its DNA binding has been shown for repression of Bcl-2. In the second category, repression occurs in the absence of apparent p53 binding to the consensus sites. Downregulation of hTERT occurs in this manner by physical interaction of p53 with in this case with the coactivator Sp1and consequent inhibition of Sp1 without p53 DNA binding, resulting in hTERT downregulation. Recent analysis using ChiP on ChiP assay revealed direct binding of p53 to the DNA-binding NF-Y complex for repression of target genes.

### 3.1.8 p53 and cancer therapy

The requirement of p53 inactivation for tumor cell survival makes it an attractive target for cancer therapy. Recent studies suggest that restoration of p53 function alone causes regression of various established tumors in vivo confirming that it indeed represents an effective therapeutic strategy to treat cancer. Many scientists are devoted to develop strategies for reinstalling the p53 tumor suppressor function. These include wild type p53 gene therapy, reactivation of mutant p53 and relief of wt p53 from overexpressed MDM2.

#### Gene Therapy

The p53 gene is mutated in almost 50 % of all human tumors. Several approaches have been taken to reintroduce wt p53 into tumor cells using gene transfer. In most cases an adenoviral vector (Adp53) has been used to insert an intact cDNA copy of the p53 gene. Although the outcome of these trials has not been that promising, stabilized tumor growth and even tumor regression has been observed in some treated patients. Treatment of head and neck cancer with Adp53 gene therapy has shown clinical effect in half of the patients and has advanced into phase III trials in USA. Several tumor promoting genes including VEGF, MMP and MDR1 have been shown to be repressed upon Adp53 gene delivery. Another approach utilizes a mutant adenovirus lacking the E1B 55K gene, ONYX-015 that replicates and lyses tumor cells lacking wt p53. Upon systemic administration ONYX-015 inhibits tumor growth in animals in vivo, and its anti-tumor effect is enhanced by combination treatment with chemotherapeutic drugs.

#### Reactivation of mutant p53

The missense p53 mutations primarily affect p53 interaction with DNA as these mutations most commonly occur in the DNA-binding core domain leading to defective activation/repression of target genes. Several small molecular compounds able to restore the wild type function of mutant p53 have been identified by screening of chemical libraries of low molecular weight compounds. An example of such compound is PRIMA-1. Treatment of tumor cells carrying mutant p53 e.g. the R175H with PRIMA-1 efficiently induces apoptosis in a mutant p53-dependent manner. The conformation of mutant p53 is altered by PRIMA-1 treatment that promotes p53-mediated transcriptional activation of target promoters such as PUMA, MDM2 and p21, possibly by facilitating mutant p53 DNA binding.

## 3.2 Experimental details

Our aim is to exploit changes of the dye excited-state lifetime and brightness induced by its interaction with the gold surface plasmons for detection of tiny amounts of protein in solution under physiological conditions. The system we investigated is based on 10 and 5 nm diameter gold NPs coupled (via a biotin-streptavidin linker) to the FITC dye to a specific antibody ($Ab_{BSA}$, $Ab_{p53}$). The interaction of the fluorophore with the gold surface plasmon resonances, mainly occurring through quenching, a effects the excited state lifetime that is measured by fluorescence burst analysis in standard solutions. The binding of protein to the gold NPs through antigen-antibody recognition further modifies the dye excited-state lifetime. This change (as explained below) can therefore be used to measure the protein concentration.

### 3.2.1 Materials and Methods

#### Chemicals, Proteins and Nanoparticles

Gold colloids 10 and 5 nm in size, functionalized by streptavidin, were purchased from Ted Pella Inc. (Redding,CA, code 15840 and 15841) and purified by two steps of 13000 rpm centrifugation. As reported on the product data sheets, the 10 nm and 5 nm gold NPs have an average number of 20 and 5 streptavidins and a concentration of 28 and 280 nM, respectively (stock solutions). The p53 protein, its monoclonal antibody and the monoclonal antibody of BSA protein were obtained from Abcam (Cambridge, UK, P53, ab43615-50, mAb to p53 (biotinylated) ab27696-100, RbpAB to BSA (BIOTIN) ab7636-1) and the biotinylated fluorescein isothiocyanate (FITC) dye from Pierce (Rockford, IL, code 22030). Bovine serum albumin (BSA), beta-lactoglobulin (BLG) and lysozyme proteins were purchased from Sigma-Aldrich (codes A-0281, L-8005, L-6876) and used without further purification. After the NP-fluorophores binding reaction, all the solutions of gold colloids were dialized (15000 D molecular weight cut-off) against phosphate buffer in order to separate the unlabeled fraction of the fluorescent molecules. The solutions were then centrifuged twice at 13000 rpm before use. For the fluorescence experiments, the stock solutions were diluted 1:1000 in phosphate buffer at pH 7.5.

### Cell Lines, Culture Conditions and Treatments

Human HCT116 colon cancer cells (wild type p53, wt p53) and H1299 lung cancer cells (homozygous partial deletion of the TP53 gene[1][10]) were maintained as monolayers in DMEM supplemented with 10 % heat-inactivated fetal calf serum, 2 mM L-Glutamine, Penicillin-Streptomycin (EuroClone) at 37 °C in a 5 % $CO_2$ atmosphere. The HCT116 line expresses the wild-type p53 (wt p53) protein. The H1299 cells have a homozygous partial deletion of the TP53 gene and as a result do not express the tumor suppressor p53 protein, which in part accounts for their proliferative propensity[10]. For DNA damage induction, sub-confluent cells were UV irradiated with $20\,\mathrm{J\,cm^{-2}}$ for 30 seconds and harvested 18 h later. Cell pellets were stored at 80 °C until lysed for further analysis. TCEs were obtained by incubating the cells for 30 min with lysis buffer [50 mM Tris HCl (pH 7.5), 5 mM EDTA, 250 mM NaCl, 1 % NP-40, 0.5 % sodium deoxycholate, 0.1 % SDS] supplemented with a protease inhibitor mix.

### Nanoparticle-Dye Complexes

In order to understand the changes in the fluorescence emission of the dye when coupled to the gold NPs we devised a series of constructs all based on the strong streptavidin-biotin interaction. The basic sensor construct (NP-FITC-Ab) is obtained by binding biotin-FITC and the protein biotinilated antibody (Ab) to the gold NP functionalized with streptavidin (Sav), as shown in Figure 3.8. As reported on the product data sheets, the 10 and 5 nm gold NPs have an average number of 20 and 5 Sav, respectively. The binding of the two components, FITC and Ab, to the Sav-NP was performed in a single step in order to avoid saturation of the binding sites on the NP with either the Ab or the FITC. All binding reactions were performed overnight in the dark under mild stirring conditions in phosphate buffer. The ratio, $R_{FITC} = [\mathrm{Ab}] : [\mathrm{FITC}]$, of the sites on the gold

---

[1] special thanks to Silvia Soddu, Experimental Oncology Department, Molecular Oncogenesis Laboratory, Regina Elena Cancer Institute, Rome.

NPs occupied by the antibodies to those occupied by FITC was tuned by changing the stoichiometric ratio of the two components during labeling. We performed preliminary tests on various $R_{FITC}$ ratios and found that the best sensitivity in terms of the relative change in the FITC excited state lifetime and limited reduction of the FITC fluorescence signal when bound to the gold NP corresponds to a ratio [Ab]:[FITC] = 3:1 (construct A in Figure 3.8). The ratio R = [Ab]:[protein] was varied in the experiments as detailed in successive section.

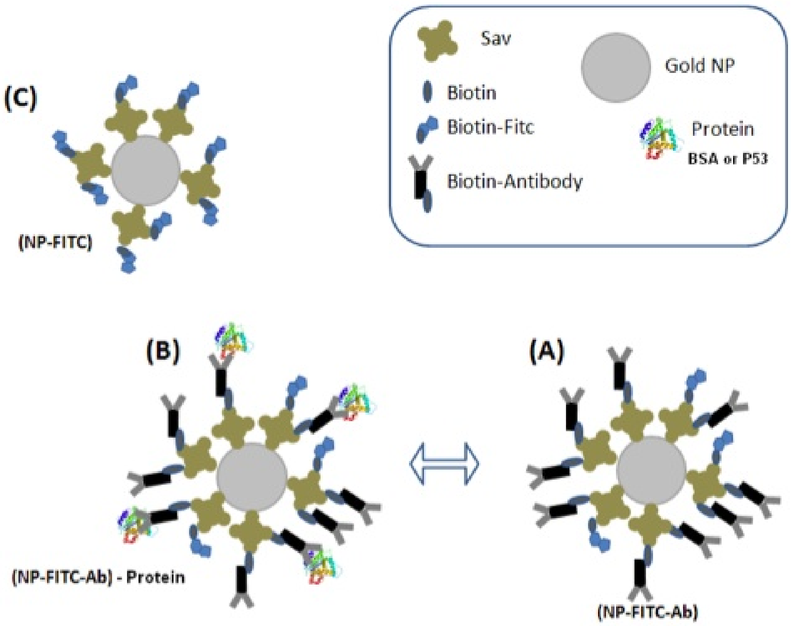

Figure 3.8: (A-C) Basic constructs used to investigate the possibility of fluorescence detection of proteins at picomolar concentrations. The symbols refer to Streptavidin (Sav), gold nanoparticles (NP), fluorescein isothiocyanate (FITC). Relative sizes not drawn to scale. The constructs are (C) the gold NP conjugated to the biotinilated FITC through the Sav-biotin binding (NP-FITC); (A) gold NP coupled to the biotin-FITC and the protein antibody at a ratio [Ab]:[FITC]=3:1 (NP-FITC-Ab); (B) construct A after reaction with the protein BSA or p53 (NP-FITC-Ab-protein).

### Absorption Spectroscopy and Dynamic Light Scattering

The spectrophotometric measurements were performed on a Jasco V750 spectrophotometer (Jasco, Japan). For Dynamic Light Scattering (DLS) a home-made setup[15] for variable angle measurement of the scattered light autocorrelation function has been used with a He-Ne 30 mW polarized laser source. The correlator board was an ISS (Urbana Champaign, IL) single photon counting acquisition board and the data were analyzed as described below. The normalized intensity ACFs were fit to a multiexponential decay

$$G(\tau) = \frac{< I(t+\tau)I(t) >_t}{< I >^2} = 1 + f_{coh}\left(\sum_k A_k exp[-D_k q^2 t]\right)^2 \qquad Q = \frac{4\pi n}{\lambda} sin\left(\frac{\theta}{2}\right) \tag{3.1}$$

where $D_k$ is the translational diffusion coefficient of the k-th species of the NPs or NP aggregates, q is the wave vector, n is the solution (water) index of refraction, and $\lambda$ is the laser light wavelength (633 nm). The parameter $f_{coh}$ is an indication of the ratio of the detector to the coherence area and was left as a free fitting parameter, typically in the range 0.35 - 0.15. The pre-exponential factors, $A_k$, which are proportional to the product of the square of the molecular mass $M_k$ times the number concentration $n_k$ can be used as an estimate of the relative concentration of the particles according to

$$A_k \approx n_k M_k^2 \approx n_k V_k^2 \tag{3.2}$$

where $V_k$ is the hydrated volume of the k-th species. The cumulant analysis of the data was performed by fitting the ACFs (maximum lag time = 600 - 800 $\mu s$) to a third-order cumulant function

$$G(\tau) = \frac{< I(t+\tau)I(t) >_t}{< I >^2} = Aexp\left[-2\left(D_{cum}q^2 - \frac{t^2}{2}(D_{cum}q^2)^2\sigma + \frac{t^3}{6}(D_{cum}q^2)^3\mu_3\right)\right] \tag{3.3}$$

The polydispersity of the samples, $\sigma$, depends on the NP construct as discussed later. The analysis of p53 protein based constructs was performed both with cumulant analysis and, in a more exhaustive way, with the Maximum Entropy Method, through the procedure described in the following.

The second order autocorrelation functions (ACFs) of scattering light ($G_E(\tau)$) were first converted into the first order ACFs, G(t), and the first order ACFs were analyzed by means of the Maximum Entropy Method obtaining the distribution of relaxation times according to the relation:

$$G(t) = A\int_{-\infty}^{\infty} dlog(\tau)P_\tau(log(\tau))exp[-t/\tau] \tag{3.4}$$

The relaxation time $\tau$ is inversely proportional to the particles diffusion coefficient, D, and the exchanged wave vector, Q, by the relation $\tau = 1/(DQ^2)$. The Q vector is computed from the solution refraction index, $n \approx 1.33$, the laser light wavelength, $\lambda =$ 633 nm, and the scattering angle $\theta$, as:

$$Q^2 = (4\pi n/\lambda)^2 sin^2(\theta/2) \tag{3.5}$$

The diffusion coefficient is related to the particle average hydrodynamic radius, $R_h$, as, $D = K_B T/(6\pi\eta R_h)$. We assume here an average globular shape of the bare and the protein coated nanoparticles. Therefore the linear relation between the relaxation time and the hydrodynamic radius,

$$\tau = \frac{R_h(6\pi\eta)}{(K_B T Q^2)} = \frac{R_h}{\rho} \tag{3.6}$$

can be used to compute the number distribution of particles with radius $R_h$ by fitting the $P_\tau$ distributions to a sum of log-normal functions of the type:

$$P_R(log(R_h))|_{R_h=\rho\tau} = A\sum_j \alpha_j < R >_j^6 exp\left[-\frac{(log(R_h) - log(< R >_j))^2}{2\sigma_j^2}\right] \tag{3.7}$$

where $< R >_j$ and $\sigma_j$ are the average values of the hydrodynamic radius and the width of the distribution component and $\alpha_j$ is the number fraction of the j-th component ($\sum_j \alpha_j = 1$) in the distribution. The number distribution of size shown is given by the computation of the function:

$$P_{n,R}(log(R_h))|_{R_h=\rho\tau} = A\sum_j \alpha_j exp\left[-\frac{(log(R_h) - log(< R >_j))^2}{2\sigma_j^2}\right] \tag{3.8}$$

with the parameters obtained by the best fit of the experimental distribution of the relaxation times.

### Fluorescence Spectroscopy

The fluorescence spectroscopy and lifetime measurements were performed on a custom-made micro-spectrometer. We have exploited the two-photon excitation of the fluorophore at 800 nm in order to achieve a small excitation volume. The average laser power was 40 mW for 10 nm and 80 mW for 5 nm NP samples. The fluorescence emission was acquired by a Single Photon Avalanche Diode (SPCM-AQR15 Perkin-Elmer, USA) whose signal was fed to a digital TimeHarp 200 (Picoquant, Berlin, D) board. The analysis was performed either with a dedicated software written in CVI (National Instruments, USA) or with the SymPhoTime program by Picoquant in order to compute the rate trace at the desired sampling time and the lifetime histograms. For the lifetime histogram analysis the setup impulse response function (IRF), close to 350 ps, was measured by collecting the signal scattered from the pure solvent. The IRF and the decays were then deconvoluted by means of the SymPhoTime program.

In the fluorescence traces, distinct photon bursts approximately 10 - 200 ms wide were detected and ascribed to the passage of the NP constructs through the excitation beam waist. The diffusion coefficient of the constructs can be evaluated as $D \approx \omega_0^2/8\tau_D$, where the diffusion time, $\tau_D$, is taken here as the FWHM of the burst. The lifetime histograms were computed on the selected bursts and, for comparison, on the background. The lifetime histograms have been fitted to a multiexponential decay according to

$$I(t) = \sum_i \alpha_i exp(-t/\tau) \tag{3.9}$$

where $\alpha_i$ are the pre-exponential factors of the i-th component with lifetime $\tau_i$. The pre-exponential factors are related to the fractional intensities $f_i$ by

$$f_i = \frac{\alpha_i \tau_i}{\sum_i \alpha_i \tau_i} \tag{3.10}$$

For a double-exponential decay the average lifetime can be defined as

$$< \tau >= f_1\tau_1 + f_2\tau_2 \quad \text{since} \quad f_2 = 1 - f_1 \tag{3.11}$$

The fitting of the FCS autocorrelation function, $G(t)$, was performed according to a 3D diffusion model with a Gaussian-Lorentzian beam profile described by the function

$$G(t) = \frac{0.076}{< N >} \left(1 + \frac{t}{\tau_D}\right)^{-1} \left(1 + \left(\frac{\lambda}{\sqrt{2}\pi\omega_0}\right)^2 \frac{t}{\tau_D}\right)^{-0.5} \tag{3.12}$$

where <N> is the average number of molecules in the excitation volume, $\tau_D$ is the diffusion time, and $\omega_0$ is the beam waist, typically 0.67 $\mu m$. The typical excitation volume, at an excitation wavelength $\lambda = 800$ nm, was $V_{exc} = \pi\omega_0^4/\lambda = 0.8 \pm 0.1\ \mu m^3$.

**Photon Counting Statistics** In order to estimate the particle brightness we have computed the first two moments of the photon counting distribution according to the Photon Counting Histogram (PCH) method[12] and its subsequent modification to Photon Counting Moment Analysis (PCMA)[13, 14]. The photon counting was computed over 50 $\mu s$ sampling time, much shorter than the diffusion time both of the free FITC dye and the gold NPs, and the average number of particles per observation volume, N, and the average brightness, $\epsilon$, where computed according to the relations:

$$\begin{cases} < k >=< N > \epsilon \\ \frac{<k^2>-<k>}{<k>} - 1 = 0.076 \cdot \epsilon \end{cases}$$

Dead-time and afterpulsing corrections were applied as is[14].

## 3.3 Results and Discussion

### 3.3.1 Characterization of the Gold NPs

The effective radii of these constructs can be estimated by taking into account the size of the streptavidin ($4.5 \times 4.5 \times 5.0$ nm )[16], of the BSA specific antibody ($R_H = 5.5$ nm)[17], and of the BSA itself ($R_H = 3.4$ nm)[18]. Since the Sav completely covers the gold nanoparticle surface we can estimate the NP-Sav radius as $R_{mon} \approx (5{+}4.5{+}4.5)/2 \approx 7$ and $(10+4.5+4.5)/2 \approx 9.5$ nm for the 5 and 10 nm diameter NPs, respectively. Upon antibody addition the maximum radius that can be obtained at the highest degree of saturation is $R_{mon} \approx 12.5$ and 15 for the 5 and 10 nm diameter NPs, respectively. When BSA is also added these values become $R_{mon} \approx 15.9$ and 18.4 nm, at most, for the 5 and 10 nm diameter NPs, respectively. The monomer NP with its Sav and antibody layer cannot be easily obtained from DLS analysis due to polydispersity of the solutions. The absorption spectrum of both the 10 and 5 nm size colloids is well superimposed on the dye absorption and emission spectra (fig. 3.9), and therefore, we expect a substantial interaction of the plasmon resonance with the dye transitions in both cases.

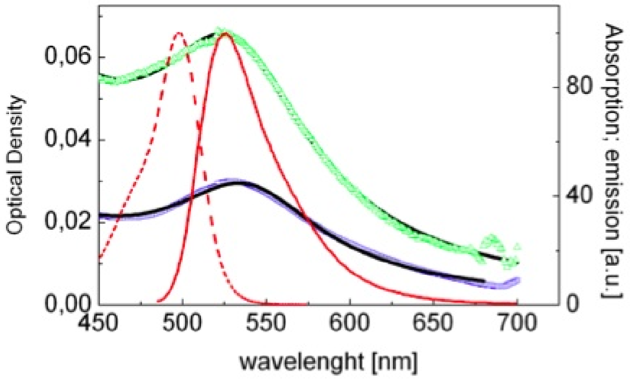

Figure 3.9: Absorption spectra of the solutions of Sav-NP. Blue squares and green triangles refer to the 10 and 5 nm diameter gold NPs, respectively. The solid lines superimposed on the data are the best fit functions to eq. 3.13. The thick dashed and solid red lines refer to the biotin-FITC absorption and emission spectrum.

The absorption spectra of the 5 and 10 nm gold NPs can be fit to a single Lorentzian peak superimposed on a smooth $1/\lambda^4$ scattering law according to

$$y = b + \frac{2A_1}{\pi} \frac{\Gamma_1}{(4(\lambda - \lambda_1^2) + \Gamma_1^2)} \frac{B_{scatt}}{\lambda^4} \tag{3.13}$$

as shown in fig. 3.9 and table 3.1. The plasmon peak occurs at slightly different wavelengths, 530 and 536 nm (table 3.1) for the two size of NPs, due to the dependence

Table 3.1: Analysis of the Sav-NP Absorption Spectra

| | $A_1$ | $\Gamma_1$ | $\lambda_1$ (nm) | $B_{scatt}$ $(nm^{-4})$ | b |
|---|---|---|---|---|---|
| 10 nm NPs | $8.3 \pm 0.5$ | $116 \pm 1$ | $530 \pm 0.2$ | $1.7 \times 10^9$ | 0.001 |
| 5 nm NPs | $4.0 \pm 0.1$ | $112 \pm 2$ | $536 \pm 0.2$ | $5.7 \times 10^8$ | 0.001 |

of the resonance on the particle sizes [22] and the effect of the surface dielectric constant (here affected by the presence of Sav) on the plasmon peak wavelength[18, 24].

For AFM (Atomic Force Microscope) experiments NPs were deposited on Si wafers covered with a thermal silicon dioxide layer, 100 nm thick. Prior to deposition substrates were cleaned by piranha solution, washed thoroughly with twice-distilled water, and silanized. AFM analyses were performed using a commercial system (TopoMetrix, Accurex II). Measurements were acquired in noncontact mode using silicon probes. Although the image resolution is 300 × 300 dots per lines, use of a large tripod scanner (100 $\mu m$ maximum scan area), which was necessary to locate the particles on the surface, resulted in a reduced resolution for small area measurements. EFM (Electric Force Microscopy) measurements were performed using an in-house developed extension. An AC signal with amplitude ranging from 0.5 to 2 V and frequency ranging from 20 to 40 kHz was applied to the conductive AFM probe while operating in noncontact mode. The resulting oscillating electrostatic force arising between the probe and the sample was analyzed at each point by a lock-in amplifier at either the first or the second harmonic and registered simultaneously to the morphology image. The signal at the first harmonic is proportional to the surface potential distribution, whereas the signal at the second harmonic accounts for the local probe-sample capacitance variations. The images reported (fig. 3.10) are obtained by analyzing the second-harmonic component of the electric signal. Direct characterization of the aggregation number and shape of the aggregates, spread on solid substrates, was performed by means of AFM imaging, as shown in figure 3.10. In order to better distinguish the gold NPs, EFM measurements were also performed. Figures 3.10 A and 3.10 C show the morphology and corresponding electrostatic force contrast image of a sample surface. The detected particles show a significant dark contrast in the EFM image, thus revealing their conductive nature against the dielectric surface. The size of the single NPs could be recovered with sufficient accuracy only for the 10 nm NPs due to the x-y resolution of the AFM microscope, which is close to the size of the smallest NPs investigated here. Concerning the single particles or unresolved aggregates (see fig. 3.10 A) of gold NPs we measure a diameter distribution peaked at $20 \pm 6$ nm with an average size of $27 \pm 4$ nm (fig. 3.10 D). These values must be compared to the estimated diameter of the functionalized NPs that is $\approx$ 19 nm. The measured increased lateral size is due to the convolution of the particle with the AFM probe, which has a nominal curvature radius of few nanometers. We can estimate the average aggregation number from the average size by assuming a fractal shape for the NP aggregates as indicated by the AFM images (fig. 3.10 B) and substantiated by the diffusion-limited aggregation theory[25, 26]. The aggregation number $N_{agg}$ scales according to the metal colloids fractal dimension[27, 28], $d_f \approx 1.9$, and is related to the aggregate and monomer size by

$$N_{agg} = \left(\frac{R_{ave}}{R_{mon}}\right)^{d_f} \tag{3.14}$$

Our experimental estimate of the average aggregate size made on the distribution reported in fig. 3.10 D leads to an average aggregation number $\approx$ 2.5.

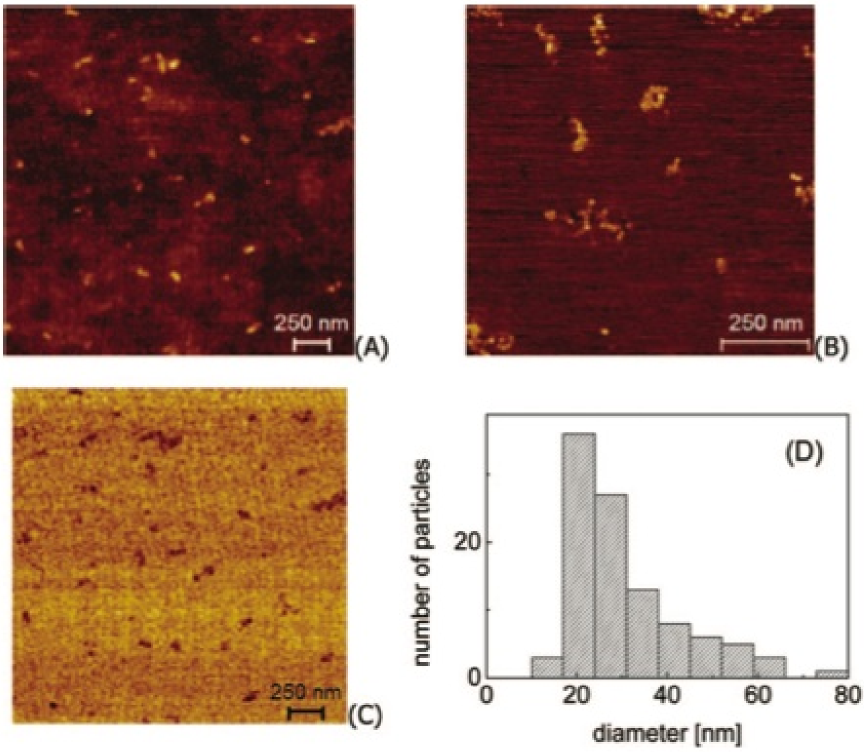

Figure 3.10: AFM and EFM analysis of the NPs size and aggregation: 10 nm NP-ab. (A and B) Wide field AFM images of gold colloids on Si/silicon dioxide surfaces. Several single gold NPs are visible together with small aggregates. (C) EFM image (second-harmonic component) of sample A. (D) Distribution of the diameter of the particles detected in AFM images.

We notice that this low value of the aggregation number depends on the fact that the size distribution reported in fig. 3.10 D was obtained from single particles or unresolved aggregates. A direct visual estimate on the larger aggregates visible, for example, in fig. 3.10 B provides aggregation numbers $N_{agg} \approx 10 - 15$.

### 3.3.2 Characterization of FITC and bound to the Gold NPs

We characterized the fluorescence response of biotinilated FITC (pH $\approx$ 7) in terms of its fluorescence brightness and excited-state lifetime. Since we want to reach low limit of detection values we investigated highly diluted (nanomolar to picomolar) solutions by performing single-particle detection. The excitation mode used here, based on two-photon absorption, allows reducing the contribution of the Rayleigh and Raman scattering to the dye fluorescence emission. Negligible direct absorption of the gold NPs in the near-infrared is expected for isotropic gold NPs[12], though the nonlinear cross-section of fluorophores bound to the gold surface[30] may be enhanced by the plasmon-fluorophore interaction. The fluorescence traces of 10 nM solutions of FITC coupled to biotin at pH $=$ 7 are relatively uniform, and the excited-state lifetime histogram can be fit to a single-exponential decay finding $\tau_{FITC} = 3.50 \pm 0.05$ ns (computed over 10 measurements of $10^5$ photons each) as shown in fig. 3.11 A. This value, smaller than that measured in solution at basic pH values, $\tau^0_{FITC} \approx 3.9 \pm 0.04$ ns, or on the polystyrene microspheres surface, agrees with the lifetime value measured for FITC coupled to antibodies.

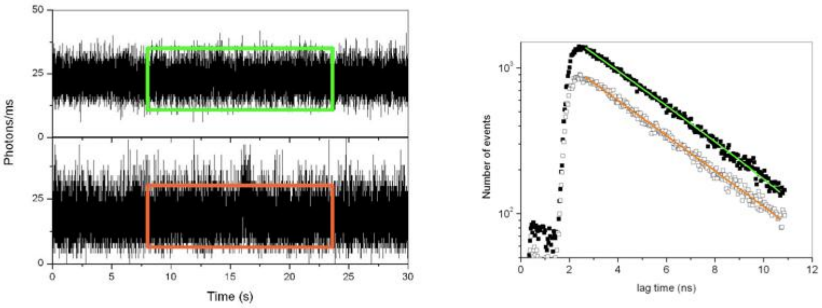

Figure 3.11: Left: Fluorescence traces of the biotin-FITC (upper trace) and NP-FITC-Ab for the 5 nm NP (lower trace). Right: Excited-state lifetime decays of the biotin-FITC (upper curve) and NP-FITC-Ab for the 5 nm NP (lower curve). Solid lines represent fits obtained with eq. 3.15 and the fitting parameters are reported in table 3.2

The brightness (fluorescence rate per molecule) can be obtained from the average fluorescence rate divided by the number of molecules in the excitation volume, $\epsilon = \langle F(t) \rangle / \langle N \rangle$. The diffusion time and average number of molecules per excitation volume are derived from the fitting of the fluorescence ACFs to eq. 3.12. This procedure provides

Table 3.2: Excited-State Lifetime Values for the FITC and NP-FITC-Ab constructs

| Construct | $\tau_1$ (ns) | $f_2$ | $\tau_2$ (ns) | $\langle\tau\rangle$ (ns) |
|---|---|---|---|---|
| Biotin-FITC | $3.50 \pm 0.05$ | | | |
| NP-FITC-Ab (10 nm) | $3.3 \pm 0.1$ | $0.06 \pm 0.04$ | $0.8 \pm 0.1$ | $3.2 \pm 0.3$ |
| NP-FITC-Ab (5 nm) | $3.2 \pm 0.1$ | $0.04 \pm 0.02$ | $0.6 \pm 0.1$ | $3.1 \pm 0.3$ |

the value $\tau_D \approx 85 \pm 15$ $\mu s$ that corresponds to a translational diffusion coefficient $D \approx 300 \pm 30$ $\mu m^2/s$, in agreement with literature results.

### Absence of BSA

When the biotin-FITC is bound to the gold NP (NP-FITC-Ab) the fluorescence fluctuations correlate over relaxation times systematically longer than that of free FITC diffusion that correspond to the best fit values $D = 9 \pm 4$ (5 nm gold NP constructs) and $11 \pm 4$ $\mu m^2/s$ (10 nm gold NP constructs). In the case of monomeric NP constructs the diffusion coefficients should be $D_{5nm} \approx 13.3$ $\mu m^2/s$ and $D_{10nm} \approx 11.5$ $\mu m^2/s$. If we additionally take into account some aggregation ($N_{agg} \approx 10$) as suggested by AFM measurements, according to the relation

$$D \approx \left(\frac{k_B T}{6\pi\eta R_{ave}}\right) = \left(\frac{k_B T}{6\pi\eta R_{mon}}\right) (N_{agg})^{-1/d_f} \tag{3.15}$$

we obtain $\langle D_{5nm}\rangle_{agg} \approx 4.2$ $\mu m^2/s$ and $\langle D_{10nm}\rangle_{agg} \approx 3.7$ $\mu m^2/s$. The ACFs fitting is then compatible with a distribution of sizes ranging from the monomer to small aggregates with $N_{agg} \approx 10 - 15$. The histograms of the excited-state lifetime of NP-FITC-Ab constructs can be fit by two exponential decays (table 3.2) where the weight of the shortest component (0.6 - 0.8 ns) is $f_2 = 4 - 6\%$. The corresponding average lifetime values are $\langle\tau\rangle \approx 3.1 \pm 0.3$ and $3.2 \pm 0.3$ ns for FITC complexed to the 5 and 10 nm gold NPs, respectively.

### Presence of BSA

We investigated the effect of the binding of BSA to the gold NPs through its specific antibody (Ab) on the FITC lifetime and brightness as a function of the ratio R =[Ab]:[BSA] in the range 5:1 to 1:1 with an average constant concentration of antibodies ≈ 1500 and 180 pM for the 10 and 5 nm gold NP, respectively. The concentration of protein was varied in the range 60 - 1500 pM, and the $R_{FITC}$ between the antibodies and the biotinilated FITC dyes on the gold NPs was kept at 3:1 in all experiments reported

Table 3.3: Analysis and fitting parameters of the DLS ACFs. The scattering angle was 90, and the laser wavelength was $\lambda = 633$ nm.

| NPs | $A_1$ | $D_1$ ($\mu$m$^2$ s$^{-1}$) | $R_{h1}$ (nm) | $A_2$ | $D_2$ ($\mu$m$^2$ s$^{-1}$) | $R_{h2}$ (nm) | $N_{agg}$ | $R_{cum}$ (nm) |
|---|---|---|---|---|---|---|---|---|
| 5 nm | $0.22 \pm 0.02$ | $52 \pm 5$ | $82 \pm 8$ | $0.76 \pm 0.02$ | $9.3 \pm 0.3$ | $0.45 \pm 0.02$ | $10 \pm 3$ | $55 \pm 5$ |
| 10 nm | $0.30 \pm 0.05$ | $19.5 \pm 0.7$ | $215 \pm 15$ | $0.59 \pm 0.07$ | $1.4 \pm 0.1$ | $3 \pm 0.2$ | $25 \pm 5$ | $100 \pm 10$ |

hereafter unless otherwise explicitly stated. In order to detect any change in the FITC brightness upon BSA addition it is important to know the degree of aggregation of the constructs.

For this purpose, dynamic light scattering studies have been performed on these same compounds. The high scattering cross-section of the gold NPs allowed us to perform experiments on the same diluted solutions ($n_{10nm} \approx 100$ pM; $n_{5nm} \approx 50$ pM) used in the fluorescence experiments. Typical ACFs of the scattered light collected from 5 to 10 nm NP-FITC-Ab-BSA at R = 1:1 are reported in fig. 3.12. The cumulant analysis of the ACFs according to eq. 3.3 yields a polydispersity $\sigma \approx 0.6$ for the 5 nm NPs and $\sigma \approx 1.6$ for the 10 nm NPs. For the smaller constructs a continuous mass distribution is present, whereas for the 10 nm NPs the contribution of larger aggregates gives rise to a separate component in the ACF decay. The average hydrodynamic radius obtained by the cumulant analysis is $R_{cum} = D_{cum}/(k_B T) = 55 \pm 5$ and $100 \pm 10$ nm for the 5 and 10 nm gold NPs solutions, respectively, yielding through eq. 3.14 $N_{agg}^{(DLS)} \approx 10 \pm 3$ and $25 \pm 5$ for 5 and 10 size gold NPs respectively (table 3.3).

A fit of whole ACFs decay can be performed by a double-exponential analysis according to eq. 3.1, and it provides the average diffusion coefficients for each component together with their amplitudes, summarized in table 3.3. The faster component corresponds to an average hydrodynamic radius of $\langle R_{h1} \rangle \approx 82$ nm for the 5 nm NPs and $\langle R_{h2} \rangle \approx 215$ nm for the 10 nm NPs, while the slower component corresponds to a size $\langle R_{h2} \rangle \approx 0.45\ \mu m$ for the 5 nm NPs and $\langle R_{h2} \rangle \approx 3\ \mu m$ for the 10 nm NPs.

As derived from eq. 3.3 the molar concentration of each species is proportional to $n_i = (A_i)/(\langle R_{hi} \rangle^{2d_f})$. Therefore, the concentration ratio of the two populations can be estimated as $n_1/n_2 \approx 200$ for the 5 nm gold NPs and $\approx 10^4$ for the 10 nm gold NPs. This finding indicates the presence of less than 1% in number of very large aggregates. Since $n_1 \approx 100$ pM, the corresponding number concentration of these large aggregates should be $n_2 \approx 0.5 - 0.01$ pM. It must be noted that the size derived from DLS is related to the mass average through the relation

$$\frac{1}{\langle R \rangle} = \frac{\sum_i \frac{1}{R_i} n_i M_i^2}{\sum_i (n_i M_i^2)} \tag{3.16}$$

Therefore, more massive aggregates give a larger contribution to the ACFs, thus explaining the more marked presence of the larger aggregate component for 10 nm NPs ACFs in spite of their lower number concentration compared to the 5 nm constructs.

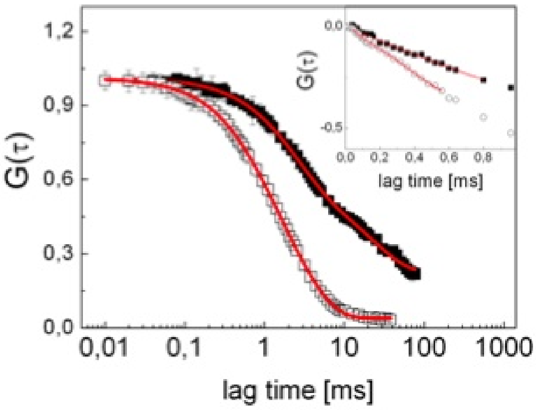

Figure 3.12: ACFs of the light scattered by the 5 (open squares) and 10 nm (full squares) NP-FITC-Ab-BSA constructs at [Ab]:[BSA] = 1:1. Lines represent best fit to a two-component decay as discussed in the text. The inset shows the cumulant analysis expressed by a log-lin plot of the field correlation function $\approx \sqrt{G(\tau)}$ together with a third-order polynomial fit (solid lines). The symbols are as in the main panel. The best fit polynomials are as follows: $-025 - 135t + 11243t^2 - 570842t^3$ (5 nm NPs) and $-0.61 - 47.4t + 3801t^2 - 129334t^3$ (10 nm NPs). DLS parameters are reported in table 3.3

### 3.3.3 Dynamic Light Scattering of p53 construct

The estimate of the average size of the antibody and the streptavidin is not straight forward. From the pdb data bank (www.pdb.org) we evaluate radii of about 4 and 8 nm for the streptavidin (entry 2IZJ, http://www.rcsb.org/) and the antibody (entry 1 IGT, http://www.rcsb.org/), respectively. We then estimate an average radius $R^{(5)}_{mon} \cong 2.5 + 8 + 16 \cong 26.5$ nm for a 5 nm diameter gold colloid and $R^{(5)}_{mon} \cong 29$ nm for the 10 nm size gold colloid. This implies that the diffusion time of the construct through the laser beam waist falls in the tens of millisecond range allowing us to collect several thousands of photons per burst, enough to estimate the lifetime of the fluorophore with a few percent of uncertainty on a single burst.

This is actually found in the fluorescence traces acquired on the NP-FITC-$Ab_{p53}$ constructs. The bursts that occur as multiple peaks were analyzed by multi-component Gaussian fit and the most likely value of their FWHM, assumed here as the diffusion time, was $\tau_D \cong 45$ ms, for both the NP size, with an average value $\langle \tau_D \rangle = 60 \pm 10$ ms.

These values correspond to an average hydrodynamic radius $\langle R_h \rangle = 230 \pm 50$ nm and to a most likely value $R_h \cong 170$ nm, substantially larger than the estimated monomer radius, indicating that some degree of aggregation must be present at least when the protein is interacting with the gold constructs. The Maximum Entropy analysis of the first order scattered light ACFs (fig. 3.13) indicates the presence of at least two populations with widely different number concentrations and sizes (table 3.4). For the NP-FITC-$Ab_{p53}$ construct in the absence of p53, the major population in terms of number concentration, has an average radius $\cong 45 \pm 20$ nm, independently of the size of the NP used for the construct (table 3.4). This is consistent with the observation that most of the size of the NP-FITC-$Ab_{p53}$ construct is due to the streptavidins and to the antibodies.

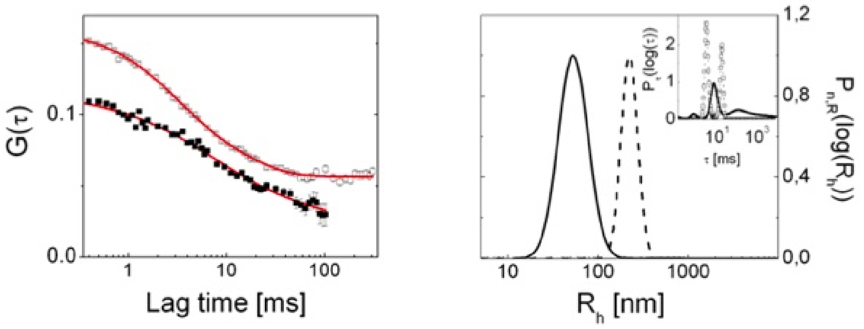

Figure 3.13: Left: the ACFs of the light scattered by the 5 nm NP-FITC-$Ab_{p53}$ constructs without (filled symbols, R = ∞) and with (open symbols, R = 5:1) p53, together with their MEM best fit functions (red solid lines). Right: the number distributions of the $R_H$ computed from the best fit parameters of the relaxation time distribution functions (MEM analysis). The solid and dashed lines refer to the R = ∞ and R = 5:1 cases (NP size 5 nm), respectively. The relaxation time distribution functions are reported in the inset with the same symbols as in panel on the left.

The MEM analysis indicates also the presence of tiny amounts ($< 0.1\%$ in number concentration) of larger aggregates in the sample, that correspond to sizes $\cong 500 - 600$ nm. If we assume that the NP-FITC-$Ab_{p53}$ constructs have a fractal shape and that the aggregation number scales as $N_{agg} = (R_{ave}/R_{mon})^{d_f}$, where $d_f \approx 1.9$ is the fractal dimension of the aggregates, we can estimate, from the average size of 45 nm, aggregation numbers of the order of $2.8 \pm 0.8$ and $2.3 \pm 0.8$ for the 5 and 10 nm NP constructs in the presence of p53. For the case of the NP-FITC-$Ab_{p53}$ constructs interacting with the p53 we measure, through the MEM analysis, that the major component of the size distribution has an average hydrodynamic radius, $\langle R_{5nm} \rangle = 200 \pm 60$ nm and $\langle R_{10nm} \rangle = 170 \pm 70$ nm, for a 1:1 stochiometric ratio between the protein and the NP-FITC-$Ab_{p53}$ construct. In the computation of the aggregation number we can also take into account

Table 3.4: The hydrodynamic radii, $< R_{h1} >$ and $< R_{h2} >$, and the number fractions, $\alpha_2$, were obtained by fitting the MEM distributions of the relaxation times to eq. 3.7 as described in the text. $R = [Ab_p53] : [p53] = \infty$ indicates that no p53 was added to the sample.

| Construct | 10 nm | | 5 nm | |
|---|---|---|---|---|
| | $R = \infty$ | R = 5:1 | $R = \infty$ | R = 5:1 |
| $< R_{h1} >$ [nm] | $130 \pm 30$ | $166 \pm 70$ | $45 \pm 24$ | $210 \pm 60$ |
| $< R_{h2} >$ [nm] | $1100 \pm 400$ | $1400 \pm 600$ | $700 \pm 400$ | $1200 \pm 450$ |
| $\alpha_2(\%)$ | $\cong 0.003$ | $0.01 \pm 0.005$ | $\cong 0.001$ | $0.5 \pm 0.3$ |

the small increase of the monomer size due to the p53 binding, $\cong$ 2 nm (entry 2J0Z, http://www.rcsb.org), and evaluate $N_{agg} = 5 \pm 0.8$ and $7 \pm 0.6$ for the 5 and 10 nm NP constructs. It should however be noted that for such low aggregation numbers the fractal aggregation assumption may fail.

### 3.3.4 Burst Analysis

**BSA protein** The time fluorescence traces of (NP-FITC-Ab-BSA) are shown in fig. 3.14 for the 5 and 10 nm NPs at the maximum [AB]:[BSA] ratio R = 1:1. Several fluorescence bursts are evident. The average width of the fluorescence bursts during the BSA titration experiments can give information on the average aggregate size, and from each burst, the number of photons emitted and the lifetime histogram can be computed.

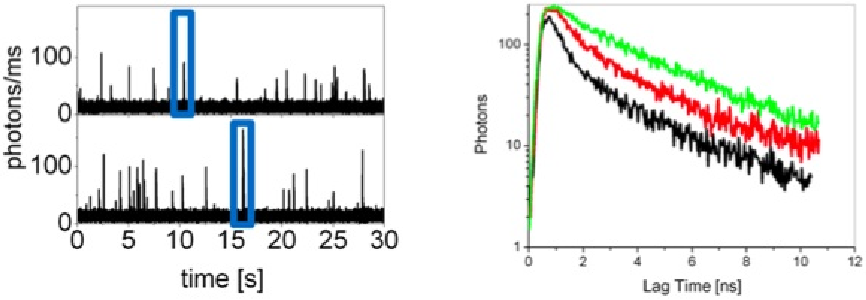

Figure 3.14: Left: Fluorescence traces of the NP-FITC-Ab-BSA constructs at a molar ratio R=[Ab]:[BSA]=1:1 for the 10 (upper trace, 40 mW excitation power) and 5 nm (lower trace, 100 mW excitation power) NPs. Right: Excited-state lifetime decays calculated on the bursts of NP-FITC-Ab-BSA 5 nm NPs at R=1:1, bottom curve, and 5:1, middle curve, and calculated on the background (top curve).

For the maximum ratio R = 1:1 typical burst width values are ~ 150 and 90 - 100 ms for the 10 (under 40 mW excitation power) and 5 nm (under 100 mW excitation power) gold NPs, respectively. The diffusion coefficients for NPs in the presence of BSA are $D_{5nm} \cong 13.3\ \mu m^2/s$ and $D_{10nm} \cong 11.5\ \mu m^2/s$. These values imply average diffusion times of the NPs through the excitation volume, $V_{exc} \cong 0.8\ \mu m^3$, of approximately $\tau_{D,5nm} = 4.2$ ms and $\tau_{D,10nm} = 4.9$ ms, much smaller than the observed value of the burst width ≅ 100 - 60 ms. If we additionally take into account the aggregation number (table 3.3) we compute values of the diffusion coefficients $\langle D_{5nm} \rangle_{agg} \cong 4.0\ \mu m^2/s$ and $\langle D_{10nm} \rangle_{agg} \cong 2.3\ \mu m^2/s$, yielding diffusion times $\tau_{D,5nm} = 13.4 \pm 3$ ms and $\tau_{D,10nm} = 25 \pm 4$ ms, still smaller than the experimental data. However, the burst width depends on the excitation power, as shown in fig. 3.15, suggesting the occurrence of optical trapping for the gold NPs.

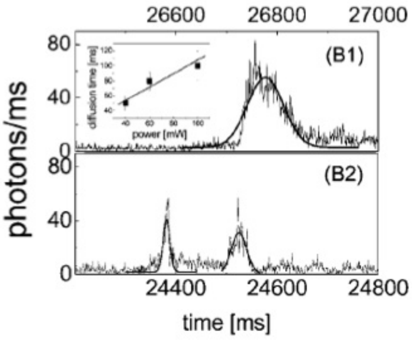

Figure 3.15: Zoom of fluorescence bursts in a time trace for the NP-FITC-Ab-BSA constructs at R=1:1, excitation power P=100 (B1) and 40 mW (B2). Inset: power dependence of the peak FWHM width for the same constructs.

In fact, by performing experiments at decreasing laser excitation power on the 5 nm gold NPs constructs we found that the average burst width decreases linearly with the excitation power (insert of fig. 3.15) and reaches, in the limit of vanishing excitation power, a value of the width ≅ 18 ± 3 ms, in good agreement with the theoretical estimate made above for an average aggregate size of approximately 10 NPs.

A further indication in this sense comes from measurements of the recurrence frequency of the fluorescence bursts, $\gamma_R \cong 0.1 \pm 0.06$ Hz (fig. 3.14). A similar value can be recovered by employing the expression

$$\gamma_R = 4\pi\omega_0 \left(\frac{n}{N_{agg}}\right) \left(\frac{k_B T}{6\pi\eta R_{mon}}\right) (N_{agg})^{-1/d_f} \tag{3.17}$$

with a number concentration $n \cong 70 - 100$ pM, a laser beam waist $\omega_0 \cong 0.67\ \mu m$, and an aggregation number $N_{agg} \cong 10 - 20$. Therefore, DLS and burst width analysis indicate that, in the presence of BSA, the aggregation is similar to that found for the NP-FITC-Ab constructs, as probed also by AFM and FCS. Besides the burst width we can also consider the average value of the total number of photons collected per burst, $\langle N_{BP} \rangle$. In the case of 5 nm NP constructs, we obtain an increase of the average value of $N_{BP}$ when raising the BSA concentration. The value $\langle N_{BP} \rangle \cong 3000 \pm 300$ photons/burst found for the ratio R = [Ab]:[BSA] = 5:1 increases to $\langle N_{BP} \rangle \cong 7200 \pm 900$ photons/burst for the ratio R = [Ab]:[BSA] = 1:1 (100 mW of laser power.) The value of $\langle N_{BP} \rangle$ for the 10 nm gold NPs, on the contrary, is almost independent of the stoichiometric ratio

R giving $\langle N_{BP} \rangle \cong 6350 \pm 500$ photons/burst at a power of 40 mW. The excited-state fluorescence decay appears to be affected by the protein binding to the NP-FITC-Ab constructs, as seen by comparing fig. 3.11 and fig. 3.14. It is noted that the excited-state lifetime does not change appreciably with the excitation power (fig. 3.15, inset). Upon BSA addition the fractional intensity of the faster component of the lifetime values derived from the histograms calculated on the bursts increases to $f_2 \cong 30\%$ depending on the [Ab]:[BSA] ratio. On the other hand, the lifetime values computed on the histograms obtained from the fluorescence background signal detected in between the bursts are close to those obtained without BSA.

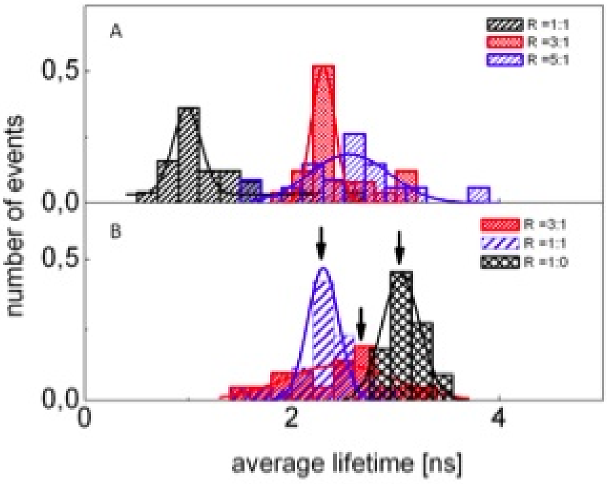

Figure 3.16: Distribution of FITC average excited-state lifetimes for the NP-FITC-Ab-BSA based on the 5 (A) and 10 nm (B) gold NPs (at the ratio [Ab]:[FITC] = 3:1). The solid lines correspond to the Gaussian best fit of the histograms. The stoichiometric ratio R = [Ab]:[BSA] is indicated in the figures.

The lifetime decay has been systematically investigated for the NP-FITC-Ab constructs based on the 5 and 10 nm gold NPs as a function of the BSA concentration in standard solutions, and the obtained average time distributions are shown in fig. 3.16. For comparison, the distribution in the absence of protein has been reported also. The distribution center shifts toward shorter average lifetimes at increasing BSA concentration for both construct sizes due to the increase in the fractional intensity of the shorter component. The result of the data analysis reported in table 3.5 indicates that the 5 nm gold NP construct displays larger sensitivity to the protein-antibody binding than the 10 nm constructs.

The change of the protein concentration from ~ 40 to ~ 180 pM induces a decrease in the mean excited-state lifetime for the 5 nm gold NP constructs from $2.7 \pm 0.1$ to $0.9 \pm 0.2$

Table 3.5: Excited-State Lifetime values for the NP-FITC-Ab-BSA constructs. Effect of the binding of BSA to NP-FITC-Ab on the excited-state lifetime of FITC: the data reported refer to the constructs with [FITC]:[Ab] = 1:3. The binding of BSA is performed at different stoichiometric ratios R = [Ab]:[BSA]. The reported excited-state lifetimes of FITC are the mean of the average lifetime distributions.

| NPs | $\langle\bar{\tau}\rangle$ (ns) | $\langle N_{BP}\rangle$ | R = [Ab]:[BSA] | [BSA] (pM) |
|---|---|---|---|---|
| 10 nm diameter | $2.3 \pm 0.1$ | $6700 \pm 400$ | 1:1 | 1500 |
| | $2.3 \pm 0.2$ | $8400 \pm 1200$ | 2:1 | 1000 |
| | $2.5 \pm 0.2$ | $6050 \pm 350$ | 3:1 | 500 |
| 5 nm diameter | $0.9 \pm 0.2$ | $7200 \pm 900$ | 1:1 | 180 |
| | $2.3 \pm 0.1$ | $7200 \pm 1000$ | 3:1 | 60 |
| | $2.7 \pm 0.1$ | $3000 \pm 300$ | 5:1 | 36 |

ns, mostly due to metal induced quenching of FITC dyes. These are in fact bound to an estimated distance from the gold surface of the order of 3-4 nm and therefore lie in a region where the quenching mechanism due to nonradiative energy transfer is dominant though metal-enhanced fluorescence (MEF) may begin to play a role as indicated by the slight anticorrelation between $\langle N_{PB}\rangle$ and $\langle\bar{\tau}\rangle$ (fig. 3.18), which can be considered as a MEF fingerprint. For the 10 nm sized NPs, contrary to the 5 nm constructs, the average number of photons emitted does not show appreciable changes, in agreement with the constant value found for the mean lifetime that reaches a "saturation" value of $\langle\bar{\tau}\rangle = 2.3 \pm 0.2$ ns, already at the lowest protein to antibody ratio explored (table 3.5). It should be noticed that a change in the lifetime is indeed occurring also for the 10 nm constructs upon BSA binding for [BSA] $<$ 100-150 pM though with a reduced sensitivity since the maximum change in the lifetime is ca. -30% compared to the ca. -70% decrease found for the 5 nm constructs. We checked that the presence of the bursts should not be ascribed to photons coming from scattering bleeding through the green band-pass filter since control experiments performed on unlabeled gold NPs observed through the same emission filter (band-pass 535/20 nm) has not shown any fluorescence burst. Therefore, the parameter that appears to be the most robust and sensitive to the protein concentration is the average lifetime of FITC on the 5 nm constructs that is linearly dependent on the BSA concentration in solutions (fig. 3.17).

The solid line is a linear fit to the data leading to $\langle\tau\rangle = 3.2(\pm 0.1) - 0.026(\pm 0.002)$ $\mathrm{ns\,pM^{-1}}$*[BSA]. This behavior can be exploited as a calibration for detection of unknown BSA concentration in solution. The experimental uncertainty of 0.1 ns on the mean lifetime limits the sensitivity of the technique to a protein concentration of $\sim$ 5 pM, thereby allowing detection of traces of protein in solution. A possible rationale for the

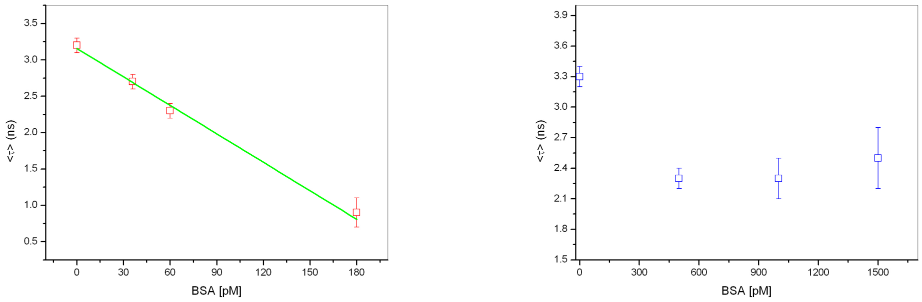

(a) *5 nm NP. The solid line is a linear fit of the data.*

(b) *10 nm NPs.*

Figure 3.17: Mean lifetime of FITC in NP-FITC-Ab-BSA constructs versus the concentration of protein in solution.

observed phenomenon, i.e., the marked sensitivity of the FITC lifetime on the BSA bound to the 5 nm constructs (larger than that found for the 10 nm constructs), can be drawn starting from a few considerations of the metal-dipole interaction theory[33, 34] and the experimental observations reported in the literature[17, 35].

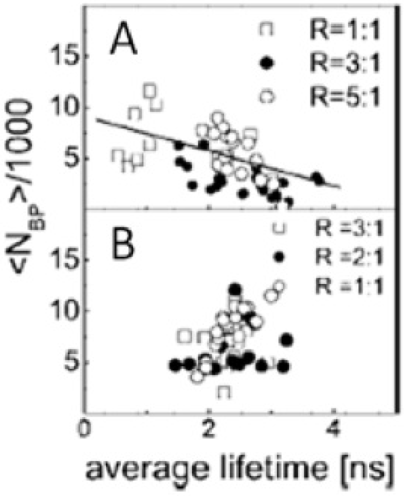

Figure 3.18: Average number of fluorescence photons per burst versus the average excited-state lifetime of NP-FITC-Ab-BSA constructs for the 5 (A) and 10 nm (B) NPs. The solid line is a linear fit to the data. The stoichiometric ratio R = [Ab]:[BSA] is indicated in the figures.

The interaction between a metal surface and a molecular dipole is a complex interplay of different phenomena. First, we can recognize an enhancement of the absorption and emission due to the increase in the local field, related to the field reflection on the gold surface[37], and to the surface roughness[38]. In this case we expect a substantial increase in the emission rate with a limited change in the excited-state lifetimes. Actually a slight increase of the lifetime with the amplitude of the surface electric field has been reported[35]. Second, metal-dye interactions also include quenching of the molecular emission due to dipole energy transfer to the surface plasmons and electron-hole couples within the metal (nonlocal effects) which results in a decrease of the dye lifetime and brightness. Third, the dye emission may be enhanced due to the radiation in the far field of a fraction of the energy transferred to the surface plasmons, basically that corresponding to high spatial frequencies in the near field emission of the molecule. In this case we expect to observe an anticorrelation of the excited-state lifetime and the number of emitted photons. In those cases when the chromophores and gold NPs are separated by bulky spacers, such as antibodies that correspond approximately to a distance $> 7$ nm, the fluorescence is actually less quenched. Quenching is dominating for distances up to a few nanometers[17, 37], and it is largely determined by the shape of the metal structure, by the dipole orientation with respect to the surface, by the size of the metal particle, and by the difference between the dielectric permittivities of the metal and the surface layer[40]. Since in our case the distance between the metal and FITC is only ca. 3-4 nm, we believe that the main result reported here, namely, the change in the FITC lifetime upon BSA-NP binding, is mostly due to a change of quenching efficiency rather than to an effective emission enhancement. To partially support this hypothesis, we can bring the observation of the initial decrease in the lifetime of FITC upon binding to the gold surface (table 3.2) and of the additional larger decrease induced by the BSA binding (table 3.5). The tiny increase of the emitted photons per burst, $< N_{BP} >$, at rising BSA concentrations (fig. 3.18), on the other hand, can be taken as an indication of the presence of high (and heterogeneous) local electric fields on the surface of the nanoclusters that produces a concomitant increase in the molecular brightness.

The gold-induced quenching of FITC is directly related to the Fresnel coefficients at the metal-surface boundary. Their change upon binding of proteins to the surface is determined then by the change in the surface layer dielectric permittivity related to the protein relative concentration on the surface layer. For this reason, we tried to keep the relative concentration of BSA on the surface high while keeping the FITC signal per gold NP cluster at measurable levels. This reasoning has also driven our choice of the ratio [Ab]:[FITC] = 3:1 reported above. As anticipated, the choice of the ratio [Ab]:[FITC]

= 3:1 has provided us with the better sensitivity. FITC bound to constructs prepared at the lower value of [Ab]:[FITC] = 1:1 displays a reduced average excited-state lifetime already at [BSA]:[Ab] = 0 with respect to the case [Ab]:[FITC] = 3:1. For example, we found $\langle\tau\rangle = 2.1 \pm 0.3$ ns for the 10 nm constructs prepared at [Ab]:[FITC] = 1:1, more than 30% lower than the [Ab]:[FITC] = 3:1 case. Moreover, upon BSA addition the FITC average lifetime increases in the [Ab]:[FITC] = 1:1 constructs upon to 30% but with very large uncertainty. This behavior, which makes the construct prepared at [Ab]:[FITC] = 1:1 less adequate than the case [Ab]:[FITC] = 3:1 for protein assay applications, is due to the interplay of the different mechanisms that have been discussed above. In particular, we find that the increase in the FITC lifetime measured in the [Ab]:[FITC] = 1:1 case is due to a marked increase of the long lifetime component which is also affected by a large variability (data not shown). This behavior is probably related to the increase in the local surface field and its inhomogeneity on the surface of the larger gold NP nanoclusters[41] present in the 10 nm gold-dye constructs. These issues may be also at the basis of the observed reduced sensitivity of the 10 nm gold NPs constructs with respect to the 5 nm constructs. In fact, small colloids are expected to quench fluorescence more efficiently than larger ones since the absorption component of the extinction coefficient is dominant over the scattering one, which is responsible for the plasmon-induced fluorescence enhancement[33, 42], and this would result in a reduced lifetime. On the other hand, the local field enhancement is expected to be larger and more inhomogeneous on larger, possibly aggregated, structures, such as those expected for the 10 nm NPs constructs, and this would result in an increase of the FITC lifetime for these larger constructs. The fine balancing of these two opposite behaviors would then determine the reduced sensitivity of the 10 nm particles constructs compared to those based on the 5 nm gold NPs described here.

**p53 protein** The FITC fluorescence emission can be characterized on the fluorescence bursts in terms of the particle brightness and the fluorophore lifetime. As described above, the ratio $R_{FITC}$ between the Abs and the FITC dyes on the gold NPs was kept constant at 3:1 in all experiments, with an average constant concentration of $Ab \approx 1000$ and 510 pM for 5 and 10 nm NP, respectively. The fluorescence brightness can be computed by means of PCH methods and the average lifetime is evaluated through the analysis in terms of one or two of exponential components of the FITC fluorescence decay. The size of the constructs was further characterized by the average burst width, $\Delta t$, analyzed as a Gaussian function (fig. 3.19).

It is important to notice that when no protein is added to the NP-FITC-$Ab_{p53}$ constructs solutions, rare if any fluorescence bursts were detected and the lifetime of FITC

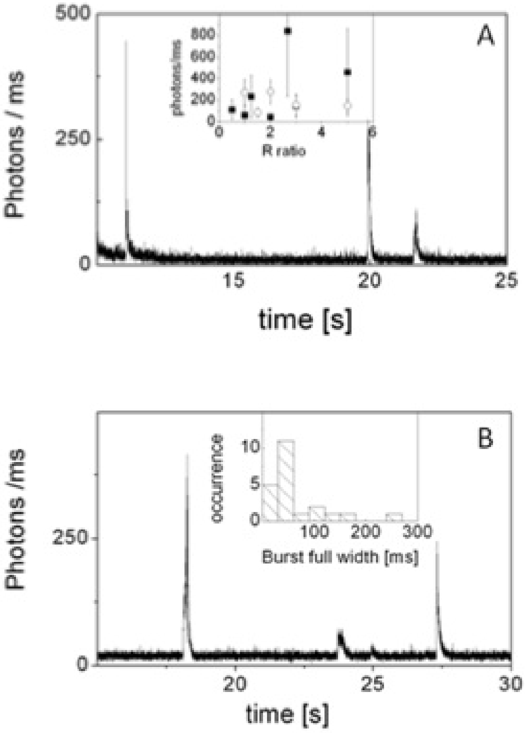

Figure 3.19: Fluorescence traces collected from R = 1:1 solutions of p53 and 5 nm (panel A) or 10 nm (panel B) NP-FITC-$Ab_{p53}$ constructs. Inset of panel A reports the average particle brightness measured on the bursts for the 5 (open squares) and the 10 nm (filled squares) NP-FITC-$Ab_{p53}$ constructs. Inset of panel B reports the distribution of the bursts full width measured through a multi-component Gaussian fit to the bursts.

was determined on the background that we ascribed to the NP-FITC-$Ab_{p53}$ constructs. The average fluorescence brightness is in this case $4.4 \pm 1.7$ photons/ms. The average brightness NP-FITC-$Ab_{p53}$ constructs in the presence of p53, computed by PCH method on the fluorescence bursts, increases to $\cong 50$ photons/ms (fig. 3.19 A, inset), that would correspond to approximately an aggregate of 8 to 10 NPs. This result is in qualitative agreement with the light scattering analysis of the size of the NP constructs reported above. The uncertainty in the size measurement does not allow to draw quantitative conclusions on any possible change in the FITC molecular brightness upon protein binding to the NP surface. We have then analyzed the effect of the protein-antibody recognition on the value of the average FITC lifetime measured on the fluorescence bursts. In the control case in which no protein is added to the solutions the fluorescence decay is well described by a single exponential component (fig. 3.20 A) and we measure $\bar{\tau} = 3.4 \pm 0.2$ and $3.5 \pm 0.2$ ns for the 5 and 10 nm NP-FITC-$Ab_{p53}$ constructs, respectively.

This value is close to that found in solution at basic pH ($\cong 9$), for the biotynilated form

Table 3.6: Excited-state lifetime values for the FITC and NP-FITC-$Ab_{p53}$ constructs

| Construct | $\bar{\tau}$ (ns) |
|---|---|
| Biotin-FITC (uncomplexed) | $3.50 \pm 0.05$ |
| NP-FITC-$Ab_{p53}$ (10 nm) | $3.50 \pm 0.2$ |
| NP-FITC-$Ab_{p53}$ (5 nm) | $3.40 \pm 0.2$ |

of FITC, $\bar{\tau} = 3.5 \pm 0.05$ ns (table 3.6). When p53 is added to the solutions of NP-FITC-$Ab_{p53}$ constructs, the FITC lifetime decreases substantially. Actually, when fitting the histogram decay, a faster component in addition to the $\cong 3.5$ ns one is required (fig. 3.20 B). Since the fitting procedure involves the deconvolution of the decay with the system IRF and is therefore affected by some uncertainty, we describe the overall fluorescence decay by average lifetime $\langle \tau \rangle$. The average of $\langle \tau \rangle$ over a sample of fluorescence bursts will be indicated as $\langle \bar{\tau} \rangle$.

### 3.3.5 Dependence of the FITC Lifetime on the p53 Concentration

The effect of p53 concentration on the FITC lifetime has been investigated by changing the ratio R = [$Ab_{p53}$]:[p53] in the range 5:1 to 1:2. The protein concentration for these experiments was varied in the range 180 - 1000 pM for 5 nm NPs and 90 - 510 pM for 10 nm NPs.

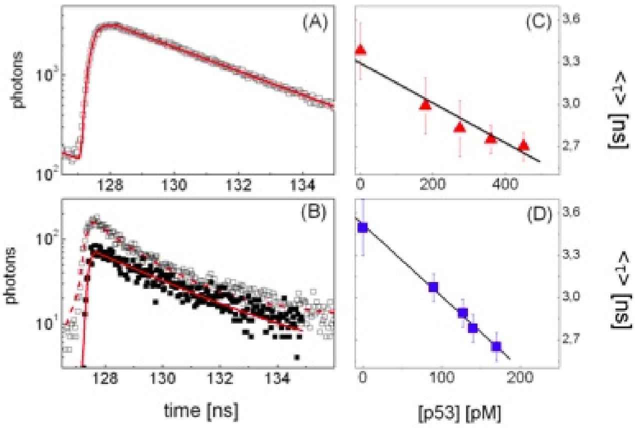

Figure 3.20: Panel (A): lifetime decays of the NP-FITC-$Ab_{p53}$ construct for the 5 nm NPs in the absence of p53. The solid line corresponds to the best fit of the data to a single exponential decay. Panel (B): lifetime decays of the NP-FITC-$Ab_{p53}$ construct for the 5 nm NPs in the presence of p53 at a stochiometric ratio R = 1:1 (upper curve, open symbols) and R = 5:1 (lower curve, filled symbols). Panel (C) and (D) report the trend of the average lifetime as a function of the p53 concentration and refer to the 5 nm and 10 nm constructs, respectively. The solid lines are the linear best fit of the data.

The result of the data analysis reported in fig. 3.20 C e D indicates that both constructs display large sensitivity to protein-antibody binding and that a range of protein concentrations, up to 200 - 250 pM, can be selected in which the FITC lifetime varies linearly with the protein concentration. The sensitivity of the p53 detection is related to the slope of the linear dependence of $\langle\bar{\tau}\rangle$ upon the p53 concentration, that is

$$-\frac{\partial<\bar{\tau}>}{[p53]} = 0.0014 \pm 10^{-4} \quad \frac{[ns]}{[pM]} \quad \text{for 5 nm NP} \tag{3.18}$$

$$-\frac{\partial<\bar{\tau}>}{[p53]} = 0.005 \pm 0.001 \quad \frac{[ns]}{[pM]} \quad \text{10 nm NP} \tag{3.19}$$

The 10 nm NP constructs appears therefore to be at least five times more sensitive to the p53 detection.

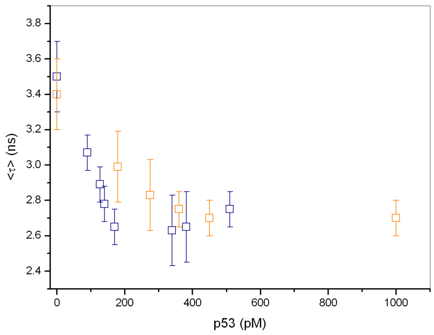

Figure 3.21: The figure reports the trend of the average lifetime as a function of the p53 concentration and refer to the 5 nm (blue symbols) and 10 nm (orange symbols) constructs, respectively.

### 3.3.6 In vitro selectivity of the assay

In order to verify the possible use of the proposed p53 assay for in-vivo screening, we must check for possible false positive results induced by recognition of other proteins and perform titration of cell extracts. Regarding the issue of the protein selectivity, we have tested the 5 nm NP-FITC-$Ab_{p53}$ constructs for recognition of small globular proteins that may compete with p53 by specific or aspecific binding to the NPs. p53 is a mainly protein that can be also found in the cytoplasm 25. Therefore the possible competitiveness of serum proteins with p53 should not hinder the application of this NP based p53 assay to in vivo tests. We have then tested the competitive binding of BLG and lysozyme, used as here as reference globular proteins, for the p53 antibody on the NPs. As a reference

Table 3.7: Average lifetime as a function of the p53 concentration refer to the 5 nm and 10 nm constructs.

| 5 nm NP | | | 10 nm NP | | |
|---|---|---|---|---|---|
| $[Ab_{p53}]/[\text{p53}]$ | [p53] pM | $<\tau>$ (ns) | $[Ab_{p53}]/[\text{p53}]$ | [p53] pM | $<\tau>$ (ns) |
| - | 0 | $3.40 \pm 0.2$ | - | 0 | $3.50 \pm 0.2$ |
| 5:1 | 180 | $2.99 \pm 0.2$ | 5:1 | 90 | $3.07 \pm 0.1$ |
| 3:1 | 275 | $2.83 \pm 0.2$ | 3:1 | 127 | $2.89 \pm 0.1$ |
| 2:1 | 360 | $2.75 \pm 0.1$ | 4:1.5 | 140 | $2.78 \pm 0.1$ |
| 3:2 | 450 | $2.70 \pm 0.1$ | 2:1 | 170 | $2.65 \pm 0.1$ |
| 1:1 | 1000 | $2.70 \pm 0.1$ | 1:2 | 340 | $2.63 \pm 0.2$ |
| - | - | - | 1:3 | 382 | $2.65 \pm 0.2$ |
| - | - | - | 1:1 | 510 | $2.75 \pm 0.1$ |

for the serum proteins we have taken BSA. Indeed when we add BSA to the NP-FITC-$Ab_{p53}$ constructs we observe large and wide ($\cong$ 3 s) bursts on which sharper bursts are superimposed (fig. 3.22 A).

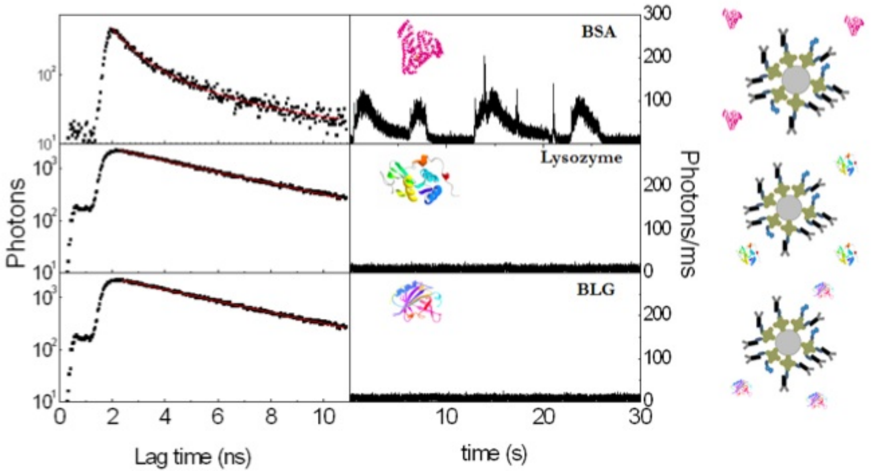

Figure 3.22: Fluorescence time decay of FITC bound to the NP-FITC-$Ab_{p53}$ constructs (5 nm in size) in the presence of BSA, lysozyme and BLG. All proteins were added to the solution in order to obtain R=1:1. The laser excitation power was 40 mW. The panels on the right report exemplary fluorescence traces for the three proteins.

This behavior can be taken as an indication of a massive aggregation of the constructs. However, the average FITC lifetime computed on these bursts is definitely smaller ($\langle\bar{\tau}\rangle \cong 2.7 \pm 0.2$ ns) than the reference value of $\tau \cong 3.5$ ns (fig. 3.22 A). BSA can therefore interfere with p53 detection by the NP-FITC-$Ab_{p53}$ construct. On the contrary, we were not able to observe fluorescence bursts in the case of lysozyme and BLG over repeated

30 s long traces (fig. 3.22 B, C), indicating that there is little or no recognition of these proteins by the NP-FITC-$Ab_{p53}$ construct. Moreover, from the single exponential analysis of the fluorescence decays (fig. 3.22 B, C), we obtained an average FITC lifetime $\bar{\tau} = 3.4 \pm 0.2$ ns for the case of both BLG and lysozyme. These observations indicate that, apart from probably aspecific binding of BSA, the NP-FITC-$Ab_{p53}$ constructs are highly specific for the p53 in vitro.

### 3.3.7 In vivo test of the assay

The ability of the NP-FITC-$Ab_{p53}$ constructs to recognize p53 in vivo has been tested on extracts from HC116 (p53 positive) and H1299 (p53-null) cell lines. We have first checked the pure TCEs for fluorescence emission at 515 nm finding an average emission of $7.5 \pm 3$ photons/ms and a single exponential decay of the fluorescence with average time $\bar{\tau} = 2.6 \pm 0.1$ ns (fig. 3.23 A).

We also detected no evident burst over 120 s of measurement (fig. 3.23 A, inset). This signal is probably due to auto-fluorescence of the protein bound coenzyme NADH present in the TCEs. 26,27. When we mixed the p53-null TCEs ($p53^{-/-}$) with the 5 nm NP-FITC-$Ab_{p53}$ constructs in a 1:1 volume stochiometry, we found rare bursts with width $\Delta t = 200$ ms or larger (fig. 3.23 B, inset). The fluorescence decay is always well described by a single exponential function (data not shown) both on the background and on the wide fluorescence peaks, and the lifetime distribution indicates the presence of two populations with $\langle\tau\rangle \cong 3.2 \pm 0.2$ ns and $\langle\tau\rangle \cong 2.3 \pm 0.15$ ns (fig. 3.23 B). We ascribe these two lifetime populations to the emission of FITC bound to the NP-FITC-$Ab_{p53}$ constructs that have not recognized p53 proteins (region III in fig. 3.23 B), as found in the in-vitro experiments, and to the cell proteins auto-fluorescence (region II in fig. 3.23 B). When adding to this mixture a p53 solution with a stochiometric ratio R=[$Ab_{p53}$]:[p53] = 1:1, we observed new sharp and intense fluorescence peaks (fig. 3.23 A, inset) with an average frequency $\cong 170$ mHz and width $\Delta t = 27 \pm 5$ ms. The fluorescence decay computed on these peaks is described by a double exponential model (fig. 3.23 A) whose average lifetime has a wide distribution around $\langle\bar{\tau}\rangle = 1.45 \pm 0.3$ ns, a value definitely smaller ($\cong 50\%$) than that found both for FITC emission and for NADH enzyme autofluorescence.

The data collected on these bursts fall in a separated new region of the correlation plot shown in fig. 3.23 B (region I). It is noteworthy that when we added to the TCEs of the p53 positive cells the NP-FITC-$Ab_{p53}$ constructs in a 1:1 volume stochiometry, we found again sharp and intense bursts on the fluorescence traces (fig. 3.23 A, inset). The average frequency of these sharp bursts ($\Delta t = 17 \pm 5$ ms) was $\cong 90 \pm 30$ mHz and decreased to $40 \pm 15$ mHz for a [NP-FITC-$Ab_{p53}$]:[p53 positive TCEs] = 1:2 volume stochiometry. these values are comparable to that found for the R = 1:1 in vitro solutions that corresponds to [p53] $\cong$ 400 pM, indicating that the range of p53 concentration that can be explored with this assay is appropriate for in-vivo screening. Also in this case, the description of the fluorescence decay requires two components (fig. 3.23 A) with average values $\langle\tau\rangle$ falling in all the three regions reported in fig. 3.23 B, as found for the p53 titration experiments of the p53 null TCEs.

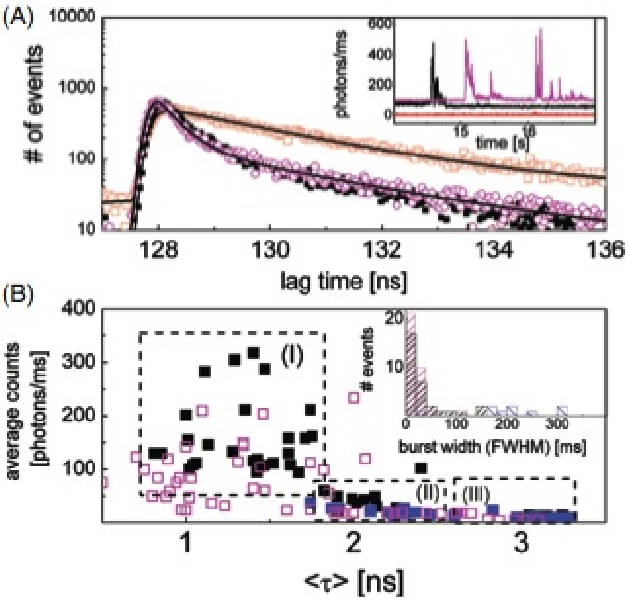

Figure 3.23: Experiments on TCEs. Panel (A): fluorescence decay measured from pure TCEs (open squares, red), p53 positive TCEs in the presence of 5 nm NP-FITC-$Ab_{p53}$ constructs (filled squares, black), p53-null TCEs in the presence of 5nm NP-FITC-$Ab_{p53}$ constructs and with the addition of p53, R=1:1 (open circles, magenta). The solid lines and the best fit decays convoluted with the IRF and they correspond to a single exponential decay and to double exponential decays for the p53 positive and the p53-null plus p53 cases, respectively. Inset: fluorescence traces for the three cases reported in the main panel: pure TCEs (red), p53 positive TCEs (black) and p53-null TCEs with the addition of p53 protein (magenta). For sake of clarity two traces have been displaced by 50 and 100 units (photons/ms), respectively. Panel (B): correlation plot of the average number of photons collected over each burst with the average value of the lifetime for solutions of 5 nm NP-FITC-$Ab_p$53 constructs and p53 positive TCEs (filled squares, black), p53-null TCEs without the addition of p53 (filled squares, blue) or p53-null TCEs with the addition of p53 (open squares, magenta). The boxes indicate the p53-(NP-FITC- $Ab_p$53) complexes (I), the cell proteins auto-fluorescence (II) and the uncomplexed NP-FITC-$Ab_p$53 constructs (III). Inset: distribution of the average bursts width for the three cases reported in the main panel (colors as in the main panel).

In particular, the average value of the lifetime decay computed over the sharp and large fluorescence bursts, corresponding to $\langle\bar{\tau}\rangle = 1.3 \pm 0.3$ ns (region I in fig. 3.23 B) for the two [NP-FITC-$Ab_{p53}$]:[p53 positive TCEs] stochiometry ratios investigated, is again markedly shorter than the control measurements on the background of the fluorescence traces (regions II and III). In general the correlation plot between the average number of photons per burst and the average lifetime measured on the bursts (fig. 3.23 B), reveals then the existence of three distinct classes of fluorescent behavior of our samples:

1. high fluorescence with very low lifetimes ($\approx 1.3$ ns), that we attribute to the NP-FITC-$Ab_{p53}$-p53 constructs
2. intermediate fluorescence with an average lifetime $\approx 2$ ns, related to cell proteins auto-fluorescence
3. very low emission and longer lifetime ($\approx 3$ ns), due to the un-complexed NP-FITC-$Ab_{p53}$ constructs.

The appearance of the region I in the correlation plot, both for the p53 null TCEs with addition of p53 (data not shown) and for the p53 positive TCEs (fig. 3.23 B), is an indication of a clear effect of the binding of p53 to the NP-FITC-$Ab_{p53}$ on the FITC fluorescence lifetime. The correlation plot reported in fig. 3.23 B is then a valuable tool to clearly discern the presence of p53 in the TCEs. However, since the lifetime value found in the TCEs is much smaller than the values found in vitro, in order to apply the presented assay to the quantification of p53 concentration in the TCEs, a calibration of the dependence of the FITC average lifetime on the protein concentration directly in the TCEs is recommended.

# Bibliography

[1] K. J. Rowan. Natl. Cancer Inst., 101, 1374-1376, 2009.

[2] T. Maruo, M. Yamasaki, C. Ladinesllave and M. Mochizuki. Cancer, 69, 1182-1187, 1992.

[3] D. B. Agus, H. I. Scher, B. Higgins, W. D. Fox, G. Heller, M. Fazzari, C. Cordon-Cardo and D. W. Golde. Cancer Res., 59, 4761-4764, 1999.

[4] H. Y. Jin, T. Yamashita, Y. Minamitsuji, F. Omori and K. Jimbow. J. Dermat. Sci., 33, 169-176, 2003.

[5] J. R. Lakowicz. Plasmonics, 1, 5-33, 2006.

[6] N. S. Lai, C. C. Wang, H. L. Chiang and L. K. Chau. Anal. Bioanal. Chem., 388, 901-907, 2007.

[7] Y. Liu, Y. Liu, R. L. Mernaugh and X. Zeng. Biosens. Bioelectr., 24, 2853-2857, 2009.

[8] N. Rosi and C. A. Mirkin. Chem. Rev., 105, 1547-1562, 2005.

[9] X. Huang, I. H. El-Sayed, W. Qian and M. A. El-Sayed. J. Am. Chem. Soc., 128(6), 2115-2120, 2006.

[10] D. L. Lin and C. CHang. J. Biol. Chem., 271, 14649-14652, 1996.

[11] S. Freddi, L. DAlfonso, M. Collini, M. Caccia, L. Sironi, G. Tallarida, S. Caprioli and G. Chirico. J. Phys. Chem. C, 113, 2722-2730, 2009.

[12] Y. Chen, J. D. Mueller, P. T. C. So and E. Gratton. Biophys. J., 77, 553, 1999.

[13] J. D. Mueller. Biophys. J., 86, 3891, 2004.

[14] M. Caccia, E. Camozzi, M. Collini, M. Zaccolo and G. Chirico. Appl. Spec., 59, 227, 2005.

[15] G. Chirico. Phys. Rev. E., 60, 2148-2153, 1999.

[16] A. Arakaki, S. Hideshima, T. Nakagawa, D. Niwa, T. Takana, T. Matsunaga and T. Osaka. Biotechnol. Bioeng., 88, 543-546, 2004.

[17] D. Prosperi, C. Morasso, P. Tortora, D. Monti and T. Bellini. Vhem. Bio. Chem., 8, 1021-1028, 2007.

[18] F. Flecha and V. Levi. Biochem. Mo. Biol. Educ., 31, 319-322, 2003.

[19] F. Gao, L. tang, L. Dai and L. Wang. Spectrochim. Acta, Part A, 67, 517-521, 2007.

[20] M. Martin and L. J. Lindqvist. Luminesc., 10, 381-390, 1975.

[21] A. Kurian, S. D. George, C. V. Bindhu, V. P. N. Nampoori and C. P. G. Vallabhan. Spectrochim. Acta, Part A. 67, 678-682, 2007.

[22] P. N. Njoki, I.-I. S. Lim, M. Derrick, H.-Y. Park, B. Khan, S. Mishra, R. Sujakumar, J. Luo and C.-J. J. Zhong. J. Phys. Chem. C, 111, 14664-14669, 2007.

[23] S. Link and M. A. El-Sayed. Int. Rev. Phys. Chem., 19, 409-453, 2000.

[24] T. Ung, L. Liz-Marzan and P. Mulvaney. J. Phys. Chem., 105, 3441-3452, 2001.

[25] S. Z. Ren, E. Tombacz and J. Rice. Phys. Rev. E, 53, 2980-2983, 1996.

[26] G. Wang and C. M. Sorensen. Appl. Opt., 41, 4645-4651, 2002.

[27] O. Malcai, D. A. Lidar, O. Biham and D. Avnir. Phys. Rev. E, 56, 2817-2828, 1990.

[28] J. Liu, W. Y. Shih, M. Sarikaya and I. A. Aksay. Phys Rev. A, 41, 3206-3213, 1990.

[29] N. J. Durr, T. Larson, D. K. Smith, B. A. Korgel, K. Sokolov and A. Ben-Yakar. Nano Lett., 7, 941-945, 2007.

[30] J. R. Lakowicz, I. Gryczynski, J. Malicka, Z. Gryczynski and C. D. J. Geddes. J. Phys. Chem. B, 106, 299-302, 2002.

[31] J. A. Steinkamp and J. F. Keij. Rev. Sci. Instrum., 70, 4682-4688, 1999.

[32] C. Deka, B.-E. Lehnert, N. M. Lehnert, G. M. Jones, L. A. Sklar and J. A. Stelnkamp. Cytometry, 25, 271-279, 1996.

[33] J. Gersten and A. Nitzan. J. Chem. Phys., 75, 1139-1152, 1981.

[34] P. Das and H. Metiu. J. Phys. Chem., 89, 4680-4687, 1985.

[35] R. Pibrik, K. Aslan, Y. Zhang and C. D. Geddes. J. Phys. Chem., 112, 17969-17973, 2008.

[36] E. Dulkeith, M. Ringler, A. Klar, J. Feldmann and W. J. Parak. Nano Lett., 5, 585-589, 2005.

[37] R. Amos and W. L. Barnes. J. Phys. Rev. B, 55, 7249-7254, 1997.

[38] P. Liao and A. Wokaun. J. Chem. Phys., 76, 751-752, 1982.

[39] R. D. Powell, C. M. R. Halsey and J. F. Hainfeld. Microsc. Res. Technol., 42, 2-12, 1998.

[40] A. Hohenau, A. Leitner and F. R. Aussenegg. In Surface Plasmon Nanophotonics.

[41] V. A. Podolskiy and V. M. Shalaev. Laser Phys., 11, 26-30, 2001.

[42] K. Aslan, Z. Leonenko, J. R. Lakowicz and C. D. J. Geddes. J. Fluoresc., 15, 643-654, 2005.

# Chapter 4

# Metal spherically and non-spherically symmetric NPs: Au and oxides

All'idea di quel metallo
portentoso, onnipossente, un
vulcano la mia mente incomincia
a diventar

C. Sterbini, Il barbiere di Siviglia
G. Rossini

Since its introduction about 20 years ago[1], two-photon microscopy has become a fundamental tool in high-resolution imaging, especially of biological tissues, because of the quadratic dependence of absorption on the excitation intensity, which confines fluorescence and photobleaching to the proximal region of the focal volume. Two-photon luminescence (TPL) from molecules is a nonlinear process described by a third-order susceptibility tensor $\chi^{(3)}$ and the rate of absorption of energy is quadratically dependent on the laser intensity[2]. Gold nanostructures often display strong multiphoton absorption[3, 5], which derives from the large electric fields that can be locally induced at their surface due to lightning-rod effects or collective electron oscillations[10]. Indeed, in recent years, the use of noble-metal nanoparticles has emerged as a valid and nontoxic alternative to fluorophore-based labeling for in vitro and in vivo imaging[11]. One of the most relevant application in this field is high-resolution analysis of tumor tissues with targeting gold nanoparticles[12–14], which holds promise for superior contrast and increased biocompatibility. The appeal of such an approach lies also in the possibility to exploit the same nanoparticles for localized and enhanced photothermal therapies[15, 16]. The strong nonlinear optical response can also be employed as an effective tool to map spatially localized field-amplitude enhancements in nanostructured systems.

In this chapter we report the characterization, with several techniques (absorption spectra, TEM images, FCS (Fluorescence Correlation Spectroscopy) and DLS (Dinamic Light Scattering) experiments), of nanorods and asymmetric branched gold nanoparticles, synthesized with LSB and CTAB, respectively. Laurylsulphobetaine (LSB) is a zwitterionic surfactant used for the first time in the seed growth method. In the second part of the spectroscopic characterization we study the luminescence of these nanoparticles for cell imaging; additional we measure cytotoxicity in order to verify their potential application for in-vivo cell treatment.

In the last part we evaluated the teragenic potential of commercially available copper oxide (CuO), titanium dioxide ($TiO_2$) and zinc oxide (ZnO) nanoparticles (NPs) using the standardized FETAX test. In particular, we have characterized suspensions of NP by TEM and DLS; histopathological screening and advanced confocal and energy-filtered electron microscopy techniques were used to characterize the induced lesions and to track NPs in tissues.

## 4.1 Two-photon luminescence (TPL)

TPL has been proposed to generate from the recombination of an electron in the *sp* band with a hole in the *3d* band, created by a two-step process consisting in two sequential one-photon absorption transitions[18]. As sketched in fig. 4.1, the first photon excites an electron to the *sp* conduction band above the Fermi energy ($E_F$) via an intraband transition, leaving a hole in the *sp* conduction band located below $E_F$.

Note that intraband transitions, which are dipole-forbidden in bulk materials, are characterized by large cross sections in nanostructures because of the presence of intense evanescent fields, whose associated field gradients give rise to higher-order multipolar transitions [5]. Once the *sp* hole has been created by the first photon, the second photon excites an electron from the *d* band to recombine with the *sp* hole in the conduction band. In gold crystals, this optical transition preferentially occurs near the X and L symmetry points of the Brillouin zone, since there the $3d$-projected electronic density of states is larger. Before they recombine, both the *sp* and *d* holes may undergo scattering events. The excited *d* hole resulting from the two sequential one-photon absorption steps can, eventually, decay radiatively, directly contributing to generate TPL, but can also recombine nonradiatively with *sp* electrons by generating SPPs (surface-plasmon-polariton) that subsequently radiate, further contributing to the total luminescence yield[17].

F(t) is the instantaneous photon flux and $\sigma_{sp\rightarrow sp}(\sigma_{d\rightarrow sp})$ stands for the cross section

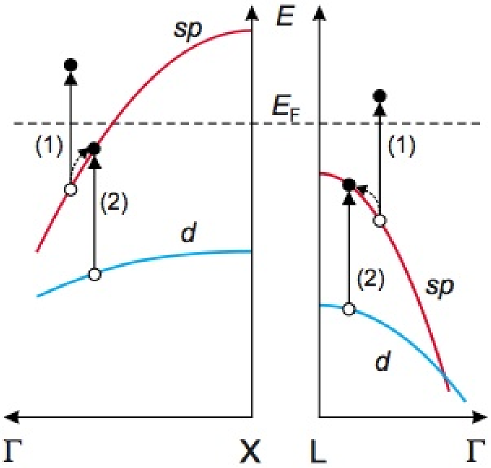

Figure 4.1: Two-photon-induced excitation of a $3d$ hole in gold. The first photon (1) induces an indirect $sp \rightarrow sp$ intraband transition. Then, absorption of the second photon (2) creates a hole in the $d$ band by exciting an electron to recombine with the previously created $sp$ hole.

of the first (second) absorption event illustrated in fig. 4.1. Radiative relaxation energies are therefore strongly connected to the interband separation, and for bulk material these energies are ~ 1.5 - 2.4 eV and occurs around the X and L points of the Brillouin zone. Much of the interest is generated by the potential biomedical applications of nanoparticles. TPL can be spectrally separated from tissue autofluorescence and the power densities required for TPL imaging are orders of magnitude below the damage threshold of biological tissue. We have studied the nanorods' TPL properties, which will be illustrated below.

## 4.2 Nanoparticles synthesis

Non spherical gold nano-objects have localized surface plasmon resonance (LSPR) that in many cases falls in the near-infrared region (750 - 1300 nm)[19], where tissue, blood and water display high transmission of electromagnetic radiation. This has prompted to propose nanorods (NR) for therapeutic and diagnostic biomedical application[36]. Beside nanorods, other low symmetry nano-objects, like nanostars [21] and more generally branched nanoparticles, have been reported to display such optical features. The syntheses of nanostars and branched NPs rely on the seed/growth concept originally elaborated for NR. In the wet synthesis of the latter, spherical gold nano-seeds are added to a growth solution of an Au(III) complex in the presence of a mild reductant and in most cases a surfactant[24] cetyltrimethylammonium bromide (CTAB). The CTAB role has been hypothesized to be the preferential coating of the {100} face of the crystalline gold seed[23], thus protecting it and allowing the anisotropic growth of the nano-object by Au(0) deposition on the {111} face. In the syntheses using CTAB, an essential role is also played by $Ag^+$ that must be present at low concentrations to obtain high aspect ratios (AR = ratio of the long to short axis of a NR)[24]. Minor variations in the concentration of seed, surfactant, $Ag^+$ and gold salt in the growth solution may lead to nanorods of different aspect ratio or to anisotropic nano-objects with different shapes. Beside few other shorter chain surfactants with the same quaternary ammonium head[25] as CTAB, and similar cetyl surfactants with tributyl or tripropyl quaternary ammonium heads ($Br^-$ as counter anion)[26], no other amphiphile has been reported to promote the growth of anisotropic gold nano-objects. In collaboration with the group of Prof. P.Pallavicini of the University of Pavia (General Chemistry Department, Pavia), we have discovered a new seed-growth synthesis by replacing CTAB with laurylsulfobetaine (LSB, N-dodecyl-$N^{'}$, $N^{''}$-dimethyl-3-ammonio-1-propanesulfonate), leading to branched Au NP whose LSPR position is controlled by LSB concentration. LSB is a zwitterionic surfactant with 2 mM critical micelle concentration. In a typical preparation a gold NP seed solution is prepared by mixing 5 mL of $5 \times 10^{-4}$ M $HAuCl_4 \cdot 2H_2O$ with 5 mL 0.20 M LSB in water, and by adding 600 $\mu L$ of $NaBH_4$ 0.010 M, obtaining the typical brownish colour of a few-nm sized Au NP dispersion. Transmission electron microscopy (TEM) reveals the formation of spherical NPs with d $<$ 4 nm. Growth solutions were prepared with 5 mL of LSB of varying concentration (0.2 - 0.6 M), 180 - 550 $\mu L$ 0.004 M $AgNO_3$, 5 mL 0.001 M $HAuCl_4 \cdot 2H_2O$ and 70 $\mu L$ ascorbic acid. After the addition of ascorbic acid, the solution became colorless. Addition of 12 $\mu L$ of seed solution made the growth solution to become first grey, then to develop a deep blue-violet color. It is important to stress that we have used concentrations and volumes identical to those that with 0.2 M CTAB (instead of LSB) were reported to produce NR (AR $<$ 4.5, LSPR $<$ 850 nm).

## 4.3 Result

### 4.3.1 UV-Vis Spectra

The extinction spectra of the NPs are shown in figure 4.2 : five sample were synthesized according to the method described in section with LBS concentration variable in the range 0.2 - 0.6 M, and one with 0.2 M CTAB, as shown in the panel.

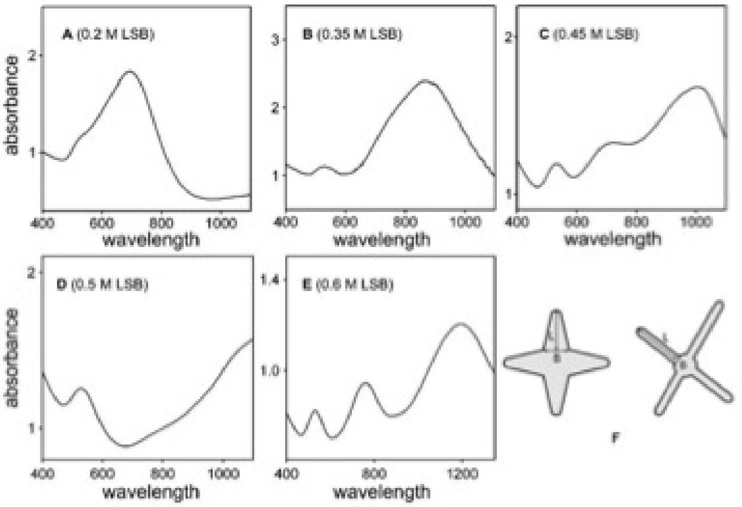

Figure 4.2: A-E: UV-Vis spectra of the nano-objects dispersions from growth solutions made with 0.2 - 0.6 M LSB. The relevant LSB concentrations are shown in the panels. All spectra except E are in the 300 - 1100 nm range. Spectrum D has a negligible intermediate band. F represents the ideal shape features of the nano-objects (L = branch length, B = branch base width).

Observation of UV-Vis spectra revealed presence of three bands:

1. the growth of a major band at $\lambda_{max}$ 700 - 1000 nm ("long" band, L), whose exact position depends on LSB concentration,
2. a less intense band at 520 - 530 nm ("short" band, S)
3. a third band with $\lambda_{max}$ positioned in the 650 - 750 nm range, depending on LSB concentration ("intermediate" band, I).

The latter appears as a single peak or a shoulder, depending on the position of the band L. Moreover, its a absorbance varied randomly from negligible to comparable to that of the band L. Identification of the origin of three bands was obtained by TEM (see par. 4.3.2). Regarding the LSB growth method we observe that the position of the L LSPR band scales linearly with the LSB concentration (fig. 4.3) and its origin can be assigned by investigating the NR spectrum.

In figure 4.4 f the extinction spectrum of the sample obtained with 0.2 M CTAB sedd growth is reported; in this case the solution is homogeneous and presents a single kind of NPs, named nanorods (fig. 4.4) and the spectrum presents only the L and S bands. Therefore we can ascribe the "long" and "short" band to the SPR parallel and perpendicular (which is close to the nanosphere spectrum SPR) to the rod axis.

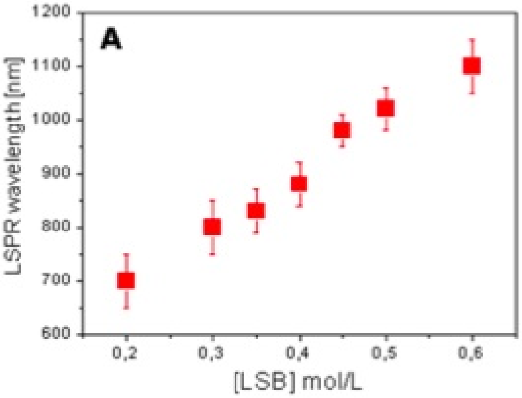

Figure 4.3: Variation of LSPR position as a function of the LSB molarity added to the growth solution.

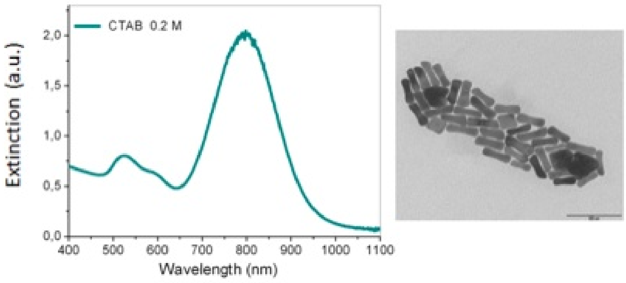

Figure 4.4: Left: UV-Vis spectra of samples synthesized with 0.2 M CTAB surfactant. Right: TEM image.

Further considerations can be done based on TEM.

### 4.3.2 Transmission Electron Microscopy (TEM) characterization

Figure 4.5 shows the comparison between the TEM images acquired for nanoparticles synthesized with CTAB and variable concentration of LSB surfactant. As seen also in fig. 4.4, the CTAB growth method provides nanorods with well defined aspect ratio; instead, the constructs obtained with LSB exhibit a prevalent star-like structure with thin fingers.

Three typologies of objects are present: (A) nanospheres ($<$ 20 nm diameter), to which the 520-530 nm LSPR band is obviously attributed (although a contribution to this band may also be due to the transverse LSPR of the larger nano-objects); (B) nanostars, with large trapezoidal branches (intermediate band); (C) branched asymmetric NPs, with narrow, long branches (long band) of high AR (fig. 4.6iii-v) display isolated and magnified images of the three typologies).

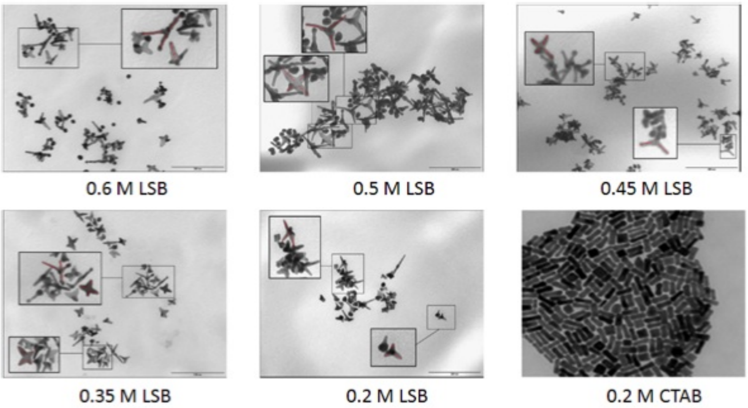
0.6 M LSB 0.5 M LSB 0.45 M LSB

0.35 M LSB 0.2 M LSB 0.2 M CTAB

Figure 4.5: The panels show the comparison between NPs synthesized with LSB or CTAB surfactants.

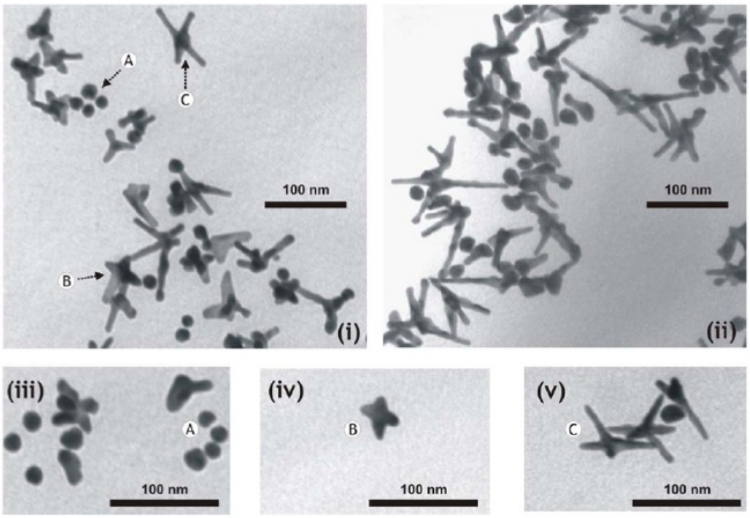

Figure 4.6: TEM images. (i) obtained from a growth solution prepared with 0.6 M LSB, with a three band absorption spectrum. (ii) obtained from a growth solution 0.5 M LSB with a negligible intermediate band. (iii) detail of nanospheres (from a 0.6 M LSB growth solution), 30% magnified. (iv) detail of nanostar, (v) detail of branched asymmetric nano-objects 30% magnified (both from a 0.2 M LSB growth solution).

Image 4.6 ii has been taken on a dispersion obtained with a 0.5 M growth solution displaying a negligible intermediate band in the UV-Vis spectrum: in this case objects of typology B (green) are absent and type A 28% (blue), type C 70% (red). For anisotropic branched NPs, the LSPR position has been reported to be proportional to the length/base ratio of branches (L/B) or, similarly, to the length/aperture angle ratio of the branches, while it is independent on the number of branches grown on the core. This agrees with the assignment of the intermediate band to the B typology objects (nanostars) and of the long band to the C typology objects. The population distribution is typically ~10% type A, 30 - 50% type B, 40 - 60% type C. The yield, calculated as total Au found in the nano-objects mixture with respect to total starting Au, is typically 29 - 55%.

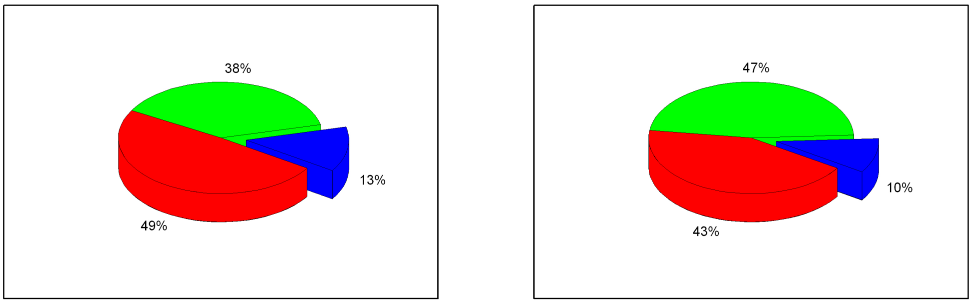

(a) *0.2 M LSB.* (b) *0.35 M LSB.*

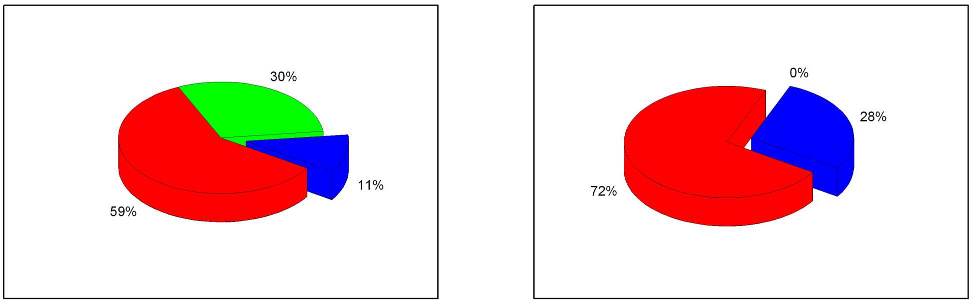

(c) *0.45 M LSB.* (d) *0.5 M LSB.*

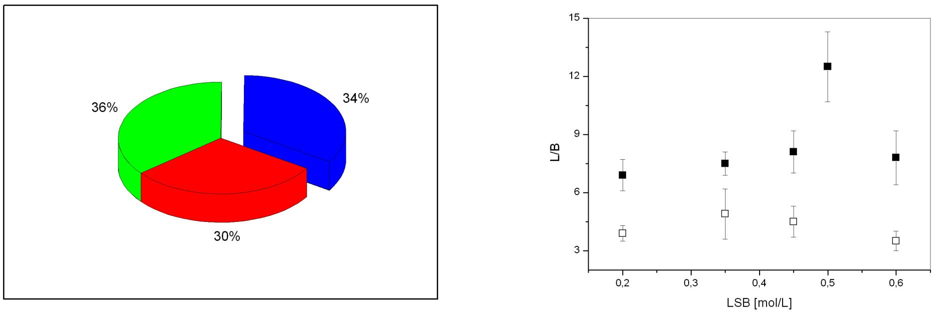

(e) *0.6 M LSB.* (f) *Aspect ratio.*

Figure 4.7: Population distribution with different growth solution.

The L/B ratio for type B objects has been calculated only on images from 0.2 to 0.45 M solutions, as with higher LSB concentrations the tendency of the nano-objects to crop

Table 4.1: Values of the parameters for samples synthesized with LSB

| [LSB] [M] | C object | | | | B object | | | |
|---|---|---|---|---|---|---|---|---|
| | $L_1$ | $B_1$ | $AR_1$ | $F_1(\%)$ | $L_2$ | $B_2$ | $AR_2$ | $F_2(\%)$ |
| 0.2 | $54.5 \pm 3$ | $8.0 \pm 0.8$ | $6.9 \pm 0.8$ | 49 | $35.8 \pm 1.9$ | $9.1 \pm 1.3$ | $3.9 \pm 0.4$ | 38 |
| 0.35 | $65.4 \pm 5.3$ | $8.7 \pm 0.3$ | $7.5 \pm 0.6$ | 43 | $41.0 \pm 10.9$ | $8.5 \pm 1.5$ | $4.9 \pm 1.3$ | 47 |
| 0.45 | $60.9 \pm 1.9$ | $7.5 \pm 1.1$ | $8.1 \pm 1.1$ | 59 | $38.7 \pm 5$ | $8.7 \pm 0.7$ | $4.5 \pm 0.8$ | 30 |
| 0.5 | $98.9 \pm 5.1$ | $7.9 \pm 1.2$ | $12.5 \pm 1.8$ | 72 | - | - | - | - |
| 0.6 | $64.3 \pm 11.1$ | $8.2 \pm 3.7$ | $7.8 \pm 1.4$ | 30 | $39.9 \pm 4.7$ | $11.4 \pm 1.9$ | $3.5 \pm 0.5$ | 36 |

Table 4.2: Values of the parameters for two samples synthesized with CTAB

| CTAB [M] | L (nm) | D (nm) | AR |
|---|---|---|---|
| 0.2 | $47.9 \pm 4.5$ | $17.2 \pm 2.1$ | $2.8 \pm 0.3$ |
| 0.2 $PEG_{2000}$ | $41.8 \pm 3.1$ | $11.2 \pm 2.9$ | $3.7 \pm 0.9$ |

in dense assemblies on the TEM grids prevented graphical evaluations on the star nano-objects. In each synthesis a $\sim$ 3 units lower L/B ratio is found for the B population with respect to type C objects, with a slight tendency to increase with LSB concentration.

Also the samples synthesized with the more conventional surfactant CTAB were characterized through transmission electron microscopy. In these cases only one typology of nanoparticles is observed; the values of the length L and the width B are reported in table 4.2.

### 4.3.3 High Resolution TEM

The structural details, the crystal structure growth directions and the crystallinity of type B and C objects have been further investigated by High Resolution TEM by group of Prof. P. Pallavicini (University of Pavia, Department of Chemistry). The products are crystalline with fcc structure. All the examined type B objects are monocrystalline with 4 or 5 branches (in many examined object a sixth branch may be hidden behind the structure). Branches are grown along the [220] and [002] directions, as shown in fig. 4.8 a. Type C objects, see fig. 4.8 b are always twinned crystals with {111} contact planes, with branches grown along the [220] or [002] directions. Reasoning with the widely accepted model developed for the anisotropic growth of nanorods[23], both for the type B and C objects the {111} faces must be selectively protected by LSB adsorption, while branches growth takes place by Au deposition on the free {220} and {002} faces.

LSB has been reported to adsorb and form stable aggregates on the {111} face of bulk gold electrodes. Moreover, it should be remembered that the formation of an anionic layer on the surface of any Au nano-object is necessary for its stabilization[27]. In syntheses

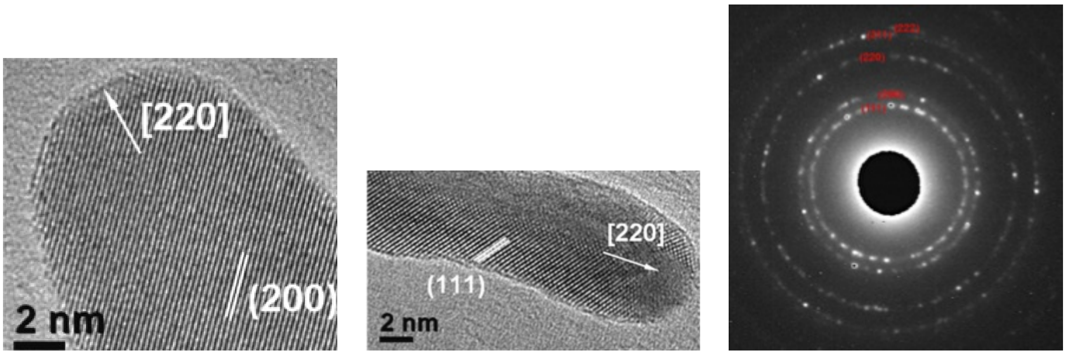

(a) *A detail of a monoscrystalline nanostar (typology B).* (b) *A detail of a twinned asymmetric branched NP (typology C).* (c) *The different diffraction rings of NP synthesized with 0.4 M LSB.*

Figure 4.8: HR TEM and Electron diffraction pattern images from group of Prof. P. Pallavicini (University of Pavia, Department of Chemistry). The images was performed by using a Jeol JEM 2200FS TEM/STEM working at 200 kV.

identical to ours, that use CTAB instead of LSB, $Br^-$ is $\sim$ 0.2 M and nanorods are obtained. In our synthetic conditions there are no anions in such huge concentration.

### 4.3.4 $\zeta$-potential characterization

The nanoparticles solutions are characterized by a $\zeta$-potential value of -27.2 ± 6.1 mV and of -13.4 ± 4.55 mV for 0.3 M and 0.45 LSB, respectively. This numerical value indicate that the nanoparticle have a prevalent negative surface charge; the first solution is moderatly stable and the second one is in an incipient instability condition. The nanoparticles synthesized with 0.2 M CTAB surfactant have a $\zeta$-potential of -14.0 ± 10.5 mV; the charge distribution is wide and the solution is in an incipient instability form.

### 4.3.5 Dynamic Light Scattering

#### Solution of LSB (LSB micelles)

Solutions of Laurylsulphobetaine (LSB, $N-dodecyl-N,N-dimethyl-3-ammonio-1-propane-sulphonate$) were prepared in water at increasing concentrations from 0.2 to 0.6 M. The scattering experiments have been performed on a home made setup that uses a He-Ne laser (Nec, 50 mW, $\lambda = 633$ nm, vertical polarization) and a digital acquisition and correlator board by ISS (ISS, inc, Urbana, IL). The sample is lodged in a cylindrical cell kept at T = 24 °C. The AutoCorrelation Function (ACF) of the intensity of the light scattered at the angle $\theta = 90°$ can be fit to a single exponential decay according to the relation:

$$G(t) = \langle I \rangle^2 \left(1 + f^2 exp[-2DQ^2 t]\right) = \langle I \rangle^2 \left(1 + f^2 |g^{(1)}(t)|^2\right) \tag{4.1}$$

where Q is the scattering vector and f is the signal/noise ratio (typically $\cong 0.03$). The translational diffusion coefficient D is then translated into the hydrodynamic radius, $R_h$, by means of the Stokes-Einstein relation:

$$D = \frac{k_B T}{6\pi\eta R_h} \tag{4.2}$$

In the above equation $\eta$ and $n$ are the viscosity and the refraction index of the solution, T = 297.15 K, is the solution temperature. The ACFs reported in fig. 4.9 indicates clearly that the relaxation time increases with the LSB concentration. Indeed the average hydrodynamic radius changes from $R_h \cong 1.6$ nm at LSB = 0.2 M, to $R_h \cong 3$ nm for LSB = 0.6 M, with linear trend.

Table 4.3: Average hydrodynamic radii of micelles in solutions.

| LSB [M] | $R_h$ (nm) |
|---|---|
| 0.2 | $1.6 \pm 0.12$ |
| 0.3 | $2.1 \pm 0.2$ |
| 0.4 | $2.3 \pm 0.2$ |
| 0.5 | $2.6 \pm 0.2$ |
| 0.6 | $3.0 \pm 0.2$ |

### NPs solutions

The scattering of the solutions of the NPs has been measured through a vertical polarizer, i.e. parallel to the direction of the polarization of the laser light. In this case two exponential decays are needed to fit the data with relaxation times of the order 10 and 200 $\mu s$ approximately (fig. 4.10). The presence of the faster component is taken as an evidence of the polarizability anisotropy of the NPs. In the view of the TEM analysis, the anisotropy of the polarizability is probably entirely due to the shape anisotropy of the NPs. The two relaxation components are then ascribed to the rotational and the translational diffusion of the NPs. According to the TEM image analysis the shape of the NPs may vary from spherical to branched and no clear cylindrical symmetry can be pointed out. The polarizability of the particle is in general a rank two tensor and can be diagonalized to give three eigenvalues that have the meaning of the polarizability along three orthogonal axes in the particle frame of reference. For sake of simplicity, we assume here that we can define in the NP a direction along which the polarizability ($\alpha_{\parallel}$) of the electrons is much larger than in the other two orthogonal directions ($\alpha_{\perp} \ll \alpha_{\parallel}$).

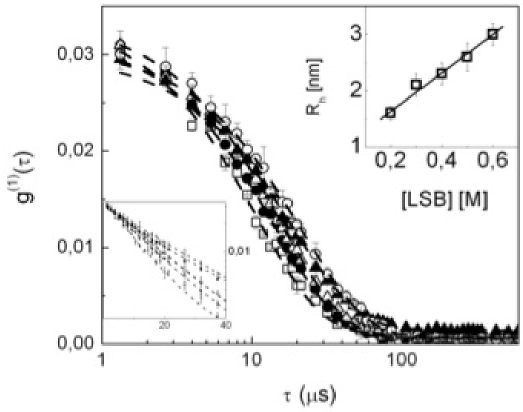

Figure 4.9: ACFs of the light scattering by the LSB micelle solutions. The symbols refer to [LSB] = 0.2 M (open squares); [LSB] = 0.3 M (filled circles); [LSB] = 0.4 M (open triangles); [LSB] = 0.5 M (filled triangles); [LSB] = 0.6 M (open circles). The dashed lines are the best fit of eq. 4.1 to the data. A small baseline has been added to the data fitting and is probably due to residual dust contribution to the scattering intensity. The top inset shows the linear trend of the $R_h$ as a function of the LSB concentration. The bottom inset shows the ACFs in log-linear scale.

Within this assumption, the intensity autocorrelation function may be written in the form (Berne&Pecora 1976):

$$G(t) = \langle I \rangle^2 \left(1 + f^2 exp[-2DQ^2 t] \left(\langle \alpha \rangle^2 + \frac{4}{45}(\alpha_{\parallel} - \alpha_{\perp})^2 exp[-6\Theta t]\right)\right) \tag{4.3}$$

In the above expression, $\alpha$ indicates the average excess polarizability of the NP, $\alpha_{\parallel}$ is the polarizability along the long axis and $\alpha_{\perp}$ indicate the polarizabilities along the shorter axes (whose mutual difference with respect to $\alpha_{\parallel}$ can be neglected). The translational, D, and the tumbling rotational, $\Theta$, diffusion coefficients can be used to derive the average hydrodynamic radius of the NP. The amplitudes of the two exponential components are instead used to estimate the degree of shape anisotropy as detailed hereafter. The experimental ACFs are fit then to a trial equation of the type:

$$G(t) = \langle I \rangle^2 \left(1 + Ae^{-\Gamma_T t} \left(1 + Re^{-\Gamma_R t}\right)\right) \tag{4.4}$$

We assume that the anisotropy along a particle axis is proportional to the length of the axis and therefore:

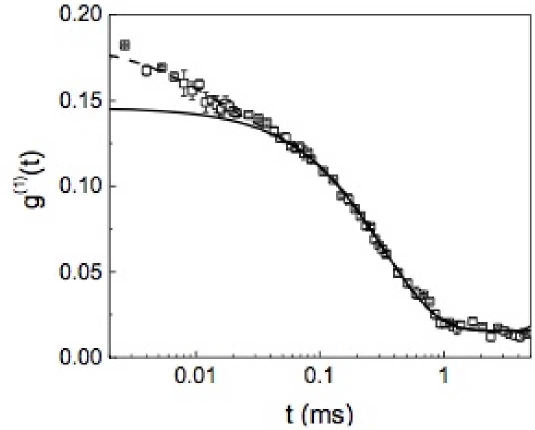

Figure 4.10: ACFs of the light scattering by a solution of NPs prepared at [LSB] = 0.2 M observed through a polarizer whose axis is parallel to the polarization direction of the excitation beam (vertical). The dashed line is the best fit to the best fit to the eq. 4.4. The solid line represent the translational component of the ACFs. A small baseline accounts for the presence of larger aggregates as also indicated by the TEM analysis.

$$\alpha_{\parallel} \div L \tag{4.5}$$

$$\alpha_{\perp} \div D \tag{4.6}$$

$$\alpha \div \frac{1}{3}(L + 2D) \tag{4.7}$$

The ratio of the amplitudes of the translational to the rotational exponential components obtained from the best fit, $R_{fit}$ is then given by:

$$A_{fit} = \frac{4}{45}\frac{(\alpha_{\parallel} - \alpha_{\perp})^2}{\alpha^2} = \frac{4}{45}\frac{\delta_{\alpha}^2}{\langle\alpha\rangle^2} \tag{4.8}$$

From eq. 4.8 it is straightforward to derive the (effective) axial ratio, D/L, as:

$$\frac{L}{D} = 3\left(\frac{2\delta_{\alpha}}{3\langle\alpha\rangle} - 1\right)\left(1 - \frac{\delta_{\alpha}}{3\langle\alpha\rangle}\right)^{-1} \tag{4.9}$$

The best fit values of the ratio (eq. 4.8) are shown in fig. 4.11 of the main text and reported here in table 4.4 together with the estimates of the axial ratios, L/D. The comparison to the L/B (length/base) values measured on the branches of asymmetric NP (type C objects, $TEM_C$ in table 4.4) and on the branches of nanostars (type B objects, $TEM_B$ in table 4.4) from TEM images indicates that the analysis reported here underestimate the shape anisotropy. This fact is expected since the axial ratio values

Table 4.4: DDLS amplitude analysis: $A_{fit}$ from eq. 4.8, $R_{h,T}$ and $R_{h,R}$ are the hydrodynamic radii, L/D is from eq. 4.9 and $(L/D)_{TEM}$ from TEM measurement.

| LSB [M] | $R_{fit}$ | $R_{h,T}$ (nm) | $R_{h,R}$ (nm) | $(L/D)_{A6}$ | $(L/B)_{TEM_C}$ | $(L/B)_{TEM_B}$ |
|---|---|---|---|---|---|---|
| 0.20 | $1.8 \pm 0.2$ | $24 \pm 2$ | $21 \pm 3$ | $5.5 \pm 0.9$ | $6.9 \pm 0.8$ | $3.9 \pm 0.6$ |
| 0.35 | $1.9 \pm 0.2$ | $29 \pm 2$ | $28 \pm 4$ | $6.2 \pm 0.9$ | $7.5 \pm 0.8$ | $4.8 \pm 1.5$ |
| 0.45 | $2,2 \pm 0.3$ | $21 \pm 3$ | $27 \pm 3$ | $8.9 \pm 3.0$ | $8.1 \pm 1.2$ | $4.4 \pm 0.7$ |
| 0.50 | $2,4 \pm 0.2$ | $19 \pm 3$ | $27 \pm 3$ | $13.2 \pm 5.0$ | $12.4 \pm 2.0$ | - |
| 0.60 | $2,4 \pm 0.2$ | $21 \pm 3$ | $25 \pm 3$ | $13.6 \pm 5.0$ | $7.8 \pm 3.7$ | $3.5 \pm 0.5$ |

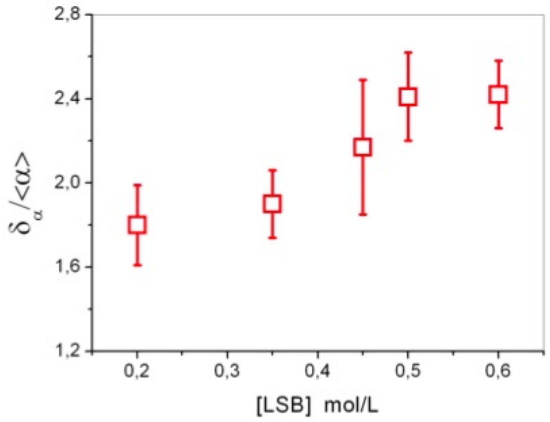

Figure 4.11: Values of the ratio $\delta_\alpha/\alpha$ as a function of LSB concentration.

are measured on the single branches on the TEM images, while eq. 4.9 makes use of an overall polarizability anisotropy.

From the translational relaxation component ($\Gamma_T$ in the fitting function) we can derive the average hydrodynamic radius of the NPs according to eq. 4.2. Finally, regarding the information that can be obtained from the rotational relaxation rate $\Gamma_R = 6\Theta$, we observe that to the first approximation we can estimate an average hydrodynamic radius from the relation:

$$\Theta = \frac{k_B T}{8\pi\eta R_{h,R}^3} \tag{4.10}$$

From eq 4.10 a very rough estimate of the overall encumbrance can be done, reported in table 4.4, that, however, appears to be consistent with the estimate obtained from the analysis of the translational relaxation rate. The average values of the hydrodynamic radii obtained from the analysis of the translational and rotational components of the ACFs are in fact: $\langle R_{h,T} \rangle = 22.8 \pm 4$ nm and $\langle R_{h,R} \rangle = 26 \pm 3$ nm. An more refined analysis of the rotational relaxation component can be done according to a number of

Table 4.5: Evaluation of the long and short effective axes of the NPs. L/D is taken from $A_{fit}$ and eq. 4.8 and 4.9

| LSB [M] | DDLS | | | | | TEM | |
|---|---|---|---|---|---|---|---|
| | (L/D) | $\Theta$ (kHz) | $\sigma$ | $L_R$ (nm) | $D_R$ (nm) | $L_{TEM}$ (nm) | $B_{TEM}$ |
| 0.2 | $5.5 \pm 0.9$ | $16.6 \pm 3$ | -0.497 | $65 \pm 4$ | $12 \pm 2$ | $55 \pm 3$ | $8.0 \pm 0.8$ |
| 0.35 | $6.2 \pm 0.9$ | $6.9 \pm 0.4$ | -0.515 | $89 \pm 2$ | $14 \pm 2$ | $65 \pm 5$ | $8.8 \pm 0.6$ |
| 0.45 | $8.9 \pm 3.0$ | $8.1 \pm 0.4$ | -0.559 | $91 \pm 1$ | $10 \pm 4$ | $61 \pm 2$ | $7.5 \pm 1.1$ |
| 0.5 | $13.2 \pm 5.0$ | $8.2 \pm 0.5$ | -0.593 | $97 \pm 2$ | $7.3 \pm 3$ | $99 \pm 5$ | $8.0 \pm 1.2$ |
| 0.6 | $13.6 \pm 5.0$ | $10.0 \pm 1$ | -0.595 | $92 \pm 3$ | $6.7 \pm 2$ | $64 \pm 9$ | $8.2 \pm 3.7$ |

relations. We assume here the formulation given by Tirado and Garcia de la Torre for the rotational diffusion coefficient of a rod:

$$\begin{aligned} \Theta &= \frac{3k_BT}{\pi\eta L^3}\left[ln\left(\frac{L}{D}\right)+\sigma\right] \\ \sigma &= -0.662+0.917\frac{D}{L}-0.05\left(\frac{D}{L}\right)^2 \end{aligned} \tag{4.11}$$

From the measurement of the rotational diffusion coefficient, $\Theta = \Gamma_R/6$, and of the axial ratio, obtained above from the amplitudes of the two components of the ACFs, we can gain an additional estimate of the long and short axes of the effective ellipsoid with which we have approximated the NPs.

When trying to compare the values of length of the long and short axes of the NPs obtained from DDLS and from TEM, one should consider that in the analysis of the TEM images, the lengths are taken on the single branches while in the assumptions made for the analysis of the DDLS ACFs we have described the whole NP as revolution ellipsoid. In this sense the overestimation of the length of the long axis observed in table 4.5, can be understood and the DDLS data can be considered consistent with the TEM data.

### 4.3.6 FCS autocorrelation analysis

Fluorescence correlation spectroscopy (FCS) is a correlation analysis of fluctuation of the fluorescence intensity. It is a versatile, noninvasive technique that has been used to monitor translational diffusion, blinking dynamics, biochemical reactions, interactions in live cells, and many more biochemical and photophysical phenomena. Besides giving information about translational diffusion, FCS was found to be useful for monitoring rotational diffusion. Fluorescence methods can measure rotational diffusion by utilizing the dependence of a fluorophores's absorption and emission of light on its dipole orientation. The absorption depends, according to the dipole-electric field approximation, on $|\vec{\mu} \cdot \vec{E}|^2 \propto cos^2\theta$, where $\vec{\mu}$ is the transition dipole, $\vec{E}$ is the electric field, and $\theta$ is the angle between $\vec{\mu}$ and $\vec{E}$. If a fluorophore is irradiated with light polarized parallel to its absorption transition dipole, it will be excited and emit light according to its emission transition dipole within its fluorescence lifetime. In most fluorophores, absorption and emission dipoles have nearly the same orientation. If the dipole orientation changes within this lifetime (due to rotation), the emitted light will have a polarization different than the excitation polarization. Polarization optics in the detection path will convert polarization differences due to rotation into intensity fluctuations. If the excitation light is polarized perpendicular to the absorption transition dipole, light will have a low probability to be absordeb, decreasing also the probability for emission. Since FCS measures the self-similarity of photon intensities, fluctuations in intensities due to rotating absorption and emission dipoles can be analyzed for diffusing molecules in solution. Unfortunately, rotational diffusion FCS studies of dye molecules are complicated by overlapping time scales for rotational diffusion, triplet blinking, fluorescence lifetime and antibunching. Like dyes, gold nanoparticles have a single-dipole polarized emission but are of large enough size to exhibit well-separated time scales for rotational and translational diffusion and fluorescence lifetime. According to Kask et al. [31] and Widengren et al. [32], the autocorrelation function can be expressed as

$$G(\tau) = \left(1 + \frac{A}{1-A} e^{-\tau/\tau_R}\right) \frac{G_T(0)}{\left(1 + \frac{8D_T}{\omega_0^2}\right) \sqrt{1 + \frac{8D_t}{\omega_0^2} \left(\frac{\lambda}{\sqrt{2}\pi\omega_0}\right)^2}} \tag{4.12}$$

This analytical expression of the correlation function has been derived assuming spherical diffusors (having isotropic polarizability) and fluorescence lifetimes much shorter than the rotational correlation times. The effective hydrodynamic radius $R_h$ was derived by extracting $\tau_D$ and $\tau_R$ from the correlation function, determining the diffusion constant D and the rotational diffusion constant $\Theta$, and using the Stokes-Einstein:

$$\begin{aligned} D &= \frac{k_B T}{6\pi\eta R_h} \propto \frac{1}{L} \\ \Theta &= \frac{k_B T}{8\pi\eta R_h^3} \propto \frac{1}{L^3} \end{aligned} \tag{4.13}$$

where $k_B$ is the Boltzmann constant, T is the temperature, $\eta$ is the solvent viscosity, $R_h$ is the particle radius and L is the length of nanoparticle's branches. FCS ACFs were acquired for the samples synthesized with both LSB and CTAB surfactant, diluted from 1:10 to 1:250 respect to the stock concentration. The fitting of FCS curves acquired with both circular and linear polarized excitation polarization provides the translational and rotational diffusion coefficients D and $\Theta$. From these and eqs. 4.13 we obtain the hydrodynamic radius, which is an indipendent first estimate of the nanoparticle's branch lenght. Figures 4.12 4.13 and 4.14 show the FCS curves and the distribution of hydrodynamic radii obtained for the samples synthesized with 0.2, 0.45 and 0.6 LSB surfactant.

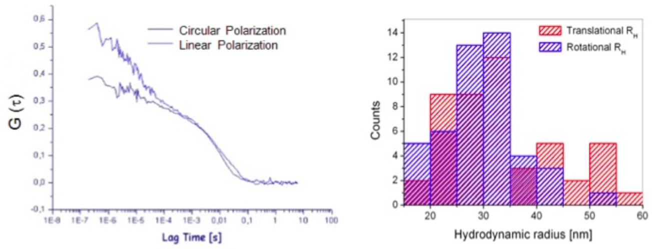

Figure 4.12: Left: FCS curves obtained with linear and circular polarization. Right: Distribution of the hydrodynamic radii determined through relations 4.13 for sample obtained with 0.2 M LSB.

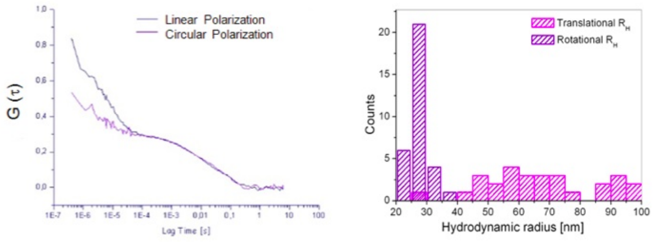

Figure 4.13: Left: FCS curves obtained with linear and circular polarization. Right: Distribution of the hydrodynamic radii determined through relations 4.13 for sample obtained with 0.45 M LSB.

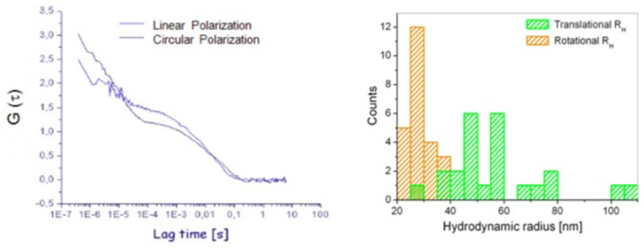

Figure 4.14: Left: FCS curves obtained with linear and circular polarization. Right: Distribution of the hydrodynamic radii determined through relations 4.13 for sample obtained with 0.6 M LSB.

In table 4.6 are reported the mean translational and rotational diffusion times $\tau_D$ and $\tau_R$, the diffusion coefficients D and $\Theta$ and the mean hydrodynamic radii $R_{h,T}$ and $R_{h,R}$, for each sample.

Table 4.6: Translational and rotation parameters for anisotropic NPs obtained with variable LSB concentration from FCS ACFs analysis.

| Sample | Rotation | | | Diffusion | | |
|---|---|---|---|---|---|---|
| | $\tau_R$ ($\mu s$) | $\Theta$ ($\mu s^{-1}$) | $R_{h,R}$ (nm) | D ($\mu m^2/s$) | $\tau_D$ (ms) | $R_{h,T}$ (nm) |
| 0.2 M | $33.1 \pm 4.2$ | $0.008 \pm 0.001$ | $30 \pm 1$ | $7.0 \pm 0.3$ | $7.8 \pm 0.3$ | $34 \pm 2$ |
| 0.45 M | $22.0 \pm 4.2$ | $0.009 \pm 0.001$ | $27 \pm 1$ | $3.5 \pm 0.2$ | $15.6 \pm 0.8$ | $67 \pm 4$ |
| 0.6 M | $25.2 \pm 2.1$ | $0.008 \pm 0.001$ | $29 \pm 1$ | $4.2 \pm 0.3$ | $13.2 \pm 0.9$ | $57 \pm 4$ |

For the sample synthesized with 0.2 M LSB, the hydrodynamic radii obtained from the translational and rotational diffusion coefficient are in good reciprocal agreement with the DLS measurements (see table 4.4); in this case $R_{h,T} \cong R_{h,R}$ demonstrating that spherical approximation is valid. On the contrary, the radii obtained from D and $\Theta$ are different from DLS measurements for samples synthesized with 0.45 and 0.6 M LSB. This reflects the inhomogeneity of NPs populations; in fact, the samples consist of spherical, star-like and NPs with high aspect ratio branches. Because $\Theta \propto L^{-3}$, $\Theta$ is largely affected by high aspect ratio branched NPs.

We pass now to the control NPs synthesized with CTAB. The FCS autocorrelation functions for the sample synthesized with 0.2 M CTAB (nanorods) are shown in fig. 4.15 and the rotational diffusion coefficients are reported in table 4.7.

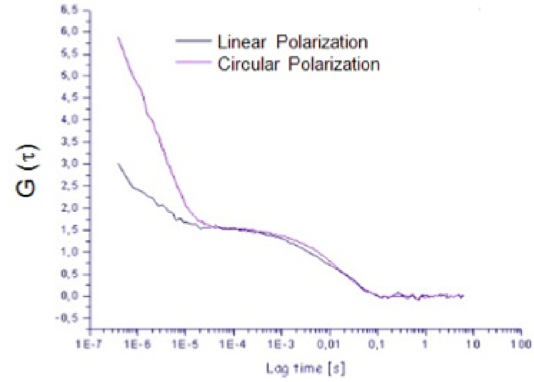

Figure 4.15: Left: FCS curves obtained with linear and circular polarization. Right: Distribution of the hydrodynamic radii determined through relations 4.13 for sample obtained with 0.2 M CTAB.

The spherical approximation for this kind of NPs is not valid and it was not possible to estimate an average size. However, due to TEM results (see table 4.2), we can assume for this sample the formulation given by Tirado and Garcia de la Torre for the rotational diffusional coefficient of a rod (eq. 4.11). By replacing L and D with the values found

Table 4.7: Rotational diffusion coefficients obtained from FCS data and evaluated from Tirado-Garcia de la Torre relations (eq. 4.11 and table 4.2).

| Sample | $\Theta_{FCS}$ ($\mu s^{-1}$) | $\Theta_{TG}$ ($\mu s^{-1}$) |
|---|---|---|
| 0.2 M CTAB | $0.021 \pm 0.002$ | $0.024 \pm 0.001$ |
| 0.2 M CTAB + PEG2000 | $0.040 \pm 0.004$ | $0.047 \pm 0.002$ |

Table 4.8: Concentration of the samples synthesized with LSB and CTAB surfactant.

| Sample | C [nM] | C [mg/ml] |
|---|---|---|
| 0.2 M CTAB-PEG2000 | $8.1 \pm 1.7$ | $2.1 \pm 0.4$ |
| 0.3 M LSB | $8.6 \pm 0.6$ | $1.7 \pm 0.2$ |
| 0.35 M LSB | $10 \pm 2$ | $1.5 \pm 0.3$ |
| 0.45 M LSB | $6.2 \pm 0.4$ | $1.03 \pm 0.06$ |
| 0.5 M LSB | $1.05 \pm 0.07$ | $0.32 \pm 0.02$ |

in TEM measurement in eq. 4.11, we computed $\Theta$, reported in table 4.7: the values $\Theta_{TG}$ and $\Theta_{FCS}$ are in good agreement. The translational diffusion were $8.5 \pm 0.8$ $\mu m^2/s$ (for NP obtained with 0.2 M CTAB) and $4.3 \pm 0.2$ $\mu m^2/s$ (for NP obtained with 0.2 M CTAB and functionalized with PEG2000). These values are lower than there estimated from Tirado-Garcia de la Torre formulation ($13.8 \pm 0.1$ and $18.2 \pm 0.1$ for NP synthesized with 0.2 M CTAB and 0.2 M CTAB-PEG2000 respectively) probably due to a residual spherical component.

By fitting the theoretical expression for G($\tau$) to the experimental data, it is possible to evaluate the nanoparticles concentration from the zero lag time auto-correlation function:

$$G(0) \approx \frac{\gamma}{\langle N \rangle} \approx \frac{0.076}{\langle N \rangle} \tag{4.14}$$

Because $\rho_{Au} = 19.3 g/cm^3$ and the excitation volume and the dilution respect to the stock solution are known ($\omega^2 \sim 0.5$ $\mu m^2$), the number of particles/L and also the molar concentration of the stock solution can be derived, as reported in table 4.8:

### 4.3.7 TPL dependence on the excitation power

An important feature of two-photon excitation is the dependence of the luminescence intensity $I_{TPL}$ as a function of excitation power $P_{exc}$. We were evaluated two different samples:

1. gold NPs synthesized with 0.2 M CTAB
2. gold NPs synthesized with 0.4 M LSB

The measure was performed on a drop of gold nanoparticles solution dried on top of a coverslip; the signal is obtained averaging 3 images through a 535/50 pass band filter. The excitation wavelength $\lambda_{exc}$ was set equal to the wavelength of surface plasmon resonance $\lambda_{SPR}$, which is 780 nm for the first sample (0.2 M CTAB) and 900 nm for the second one (0.4 M LSB). The evaluation of the signal level on the images was accomplished by computing an average on at least 5 different regions of interest (ROIs) taken from bright regions of the image. Signal intensities were collected for increasing incident power from 0 to 2 mW.

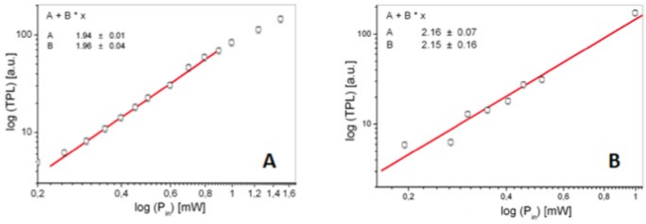

Figure 4.16: Quadratic dependence of the signal intensity $I_{TPL}$ on the input power for samples obtained with 0.45 M LSB (A) and 0.2 M CTAB (B).

Figure 4.16 show the log-log plot of the emitted TPL intensity for the samples analyzed; a quadratic dependence of the signal intensity $I_{TPL}$ on the input power was observed, with slope values of $2.15 \pm 0.16$ in the range 0.1 - 0.8 mW and $1.95 \pm 0.04$ in the range 0.1 - 1 mW for the gold nanoparticles synthesized with CTAB and LSB, respectively.

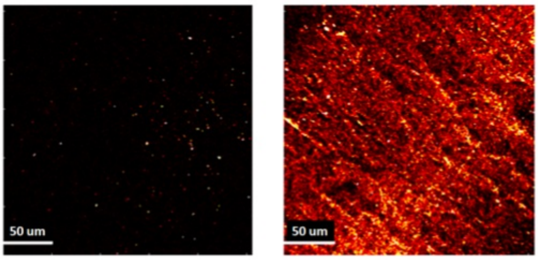

Figure 4.17: Irradiation of nanorods in CW laser mode (left) and 80 MHz-pulse laser configuration (right).

To confirm qualitatively that the emission signal is due to a two-photon excitation process, the laser was switched also in the continuos wave (CW) operation mode. In this case, no signal was emitted by sample (fig. 4.17): irradiation of the nanorods in a wide range of power levels reduced the signal to background noise level, confirming the two-photon nature of the luminescence [44].

### 4.3.8 TPL emission spectra

TPL spectra were obtained by using a solution of gold nanorods at different excitation wavelengths (see fig. 4.18), variable in the range 730 - 920 nm with $P_{exc} \approx 2$ mW, measured on the focal plane. The emission spectra of the different sample synthesized with CTAB (fig. 4.18 A) and LSB surfactant (fig. 4.18 B,C) are reported. The emission spectra is a broad band [44] in the visible region (400 - 640 nm); the cut-off at 670 nm is due to the presence of a dichroic filter in the optical path which avoid the incident radiation reaching the CCD. The peak positions in the TPL spectra are independent on the excitation energy and on LSB concentration (and the NP aspect ratio as consequence).

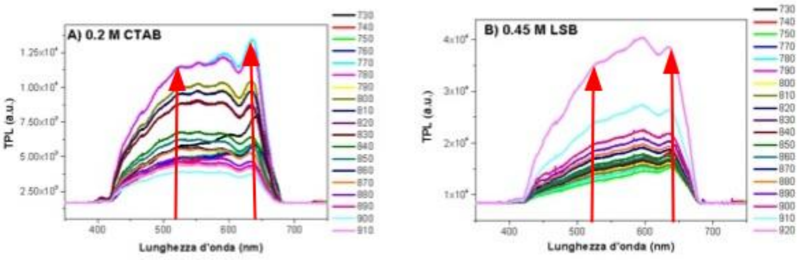

(a) *0.2 M CTAB with different excitation wavelength.* (b) *0.45 M LSB with different excitation wavelength.*

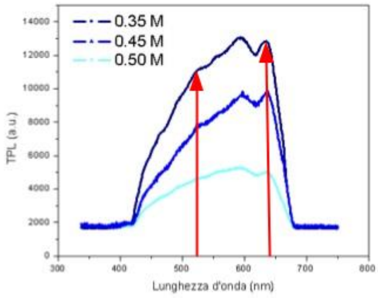

(c) *0.35, 0.45, 0.5 M LSB with same excitation wavelength.*

Figure 4.18: Emission spectra of NPs synthesized with CTAB or LSB. The red arrows indicate the transitions (electron-hole recombination) L at 518 nm and X at 654 nm.

### 4.3.9 TPL excitation spectra

To ascertain if the observed TPL was related to the longitudinal plasmon mode of the gold nanorods, we checked the dependence of TPL intensity on the excitation wavelength $\lambda_{exc}$ against the extinction spectrum, also measured from solution. We found that the excitation spectrum overlaps well (fig. 4.19) with the longitudinal plasmon band, indicating that the TPL intensity is governed by the local field enhancement from the plasmon resonance. In order to reconstruct the excitation spectra and to determine the relation between the TPL and the surface plasmon resonance (SPR), the area below under the emission TPL spectra was calculated for each excitation wavelength $\lambda_{exc}$ and the values were reported as a function of $\lambda_{exc}$ in fig. 4.19.

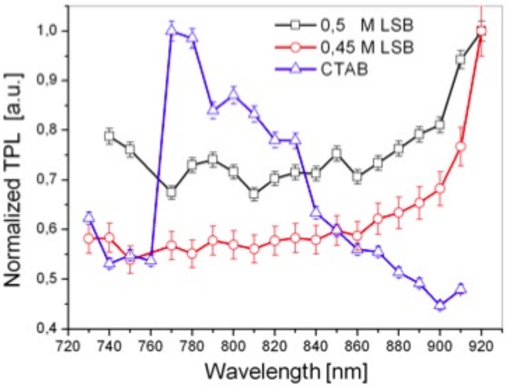

Figure 4.19: Two-photon excitation spectra for the samples synthesized with 0.45 M (red) and 0.5 M LSB (black) and 0.2 M CTAB (blue). The excitation power was corrected for the setup transmission.

### 4.3.10 Dependence of Excitation Polarization

The TPL intensity of the nanorods was examined as a function of polarization angle of the incident beam ($\theta$). A drop of sample (NPs synthesized with 0.3, 0.4 M LSB and 0.2 M CTAB) was dispersed and immobilized onto glass cover slips such that isolated particles could be irradiated by fs-pulsed excitation at their longitudinal plasmon resonance wavelength with an average excitation power of 1 mW on the sample. An half-wave plate was inserted in the optical path of the experiment, in order to rotate the polarization of the incident radiation on the whole 360° range. The TPL image was obtained by averaging 3 images collected through a 535/50 nm pass band filter and no analyzer was used. The evaluation of the TPL signal of the NPs was accomplished by computing the average signal on different regions of interest (ROIs) on the images, taken around single bright spots ascribed to isolated particles, as judged from the emission level of the single spot respect to the distribution of levels computed on a full frame. The signal corresponding to each particle was then plotted as a function of $\theta$.

We assume that TPL is maximized when the incident field, tuned at the plasmon resonance, has its polarization parallel to the long axis of nanorod or the principal axis of a branched nanostar [10]. Two typical results are shown in fig. 4.20 and 4.21 ; in both cases, the data can be fitted to a $cos^4$ function. In fact

$$(Ecos\theta)^2 = I \quad \longrightarrow \quad I^2 \propto cos^4\theta \tag{4.15}$$

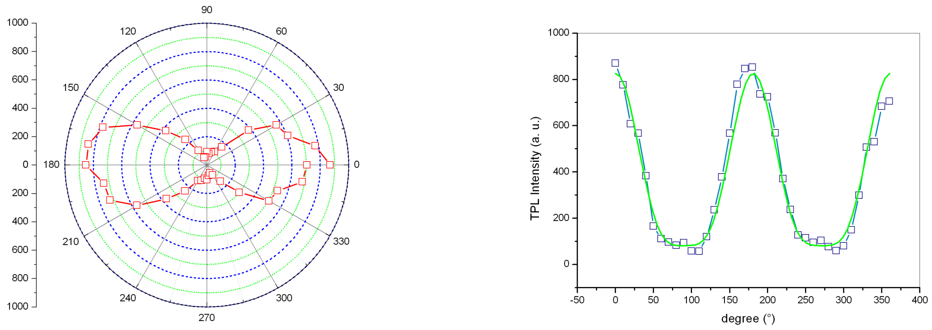

Figure 4.20: Dependence of TPL emission on incident polarization for NPs synthesized with 0.40 M LSB.

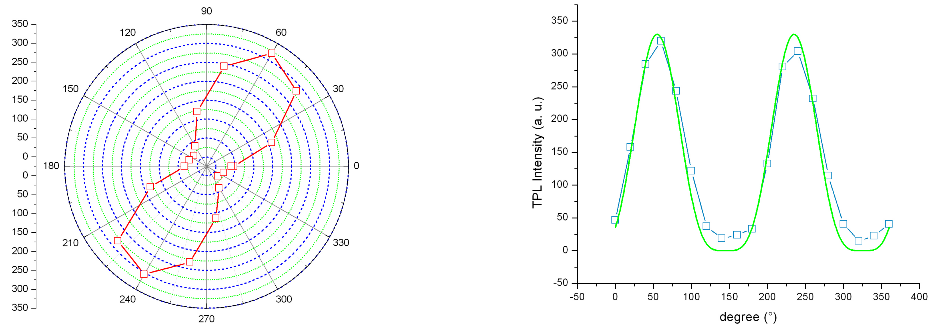

Figure 4.21: Dependence of TPL emission on incident polarization for NPs synthesized with 0.20 M CTAB.

The fluorescence polarization $\nu$ defined as:

$$\nu = \frac{I_{max} - I_{min}}{I_{max} + I_{min}} \tag{4.16}$$

is a good measure of the sensitivity to the polarization vector where $I_{max}$ and $I_{min}$ are the TPL intensity for the polarization excitation oriented along the longitudinal and transverse axis, respectively.
For every spot of each separated sample the $\nu$ parameters were calculated and their frequency count histograms are shown in fig. 4.22. From a gaussian fit of the histograms it was possible to obtain the results reported hereafter:

- $\nu = 0.70 \pm 0.15$ for sample obtained with an LSB concentration of 0.3 M

- $\nu = 0.9 \pm 0.1$ for 0.4 M LSB
- $\nu = 0.9 \pm 0.1$ for 0.2 M CTAB

The anisotropy parameter increases with the increasing of the LSB concentration and therefore with the aspect ratio (and the shape anisotropy) of the nanoparticles synthesized. The fluorescence polarization can then be used as simple method to obtain a rough evaluation of nanoparticles shape anisotropy. Having characterized the NPs from structural an spectroscopic point of views, we now pass to analyze their application in the biomedical research.

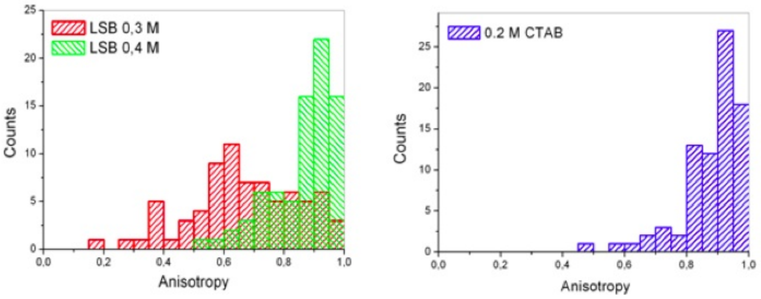

Figure 4.22: Histograms of the anisotropy distribution for NPs obtained with 0.3 and 0.4 M LSB (left) and 0.2 M CTAB (right). The anisotropy increases with the increasing of LSB concentration.

## 4.4 Nanoparticles Cellular Toxicity

Human skin, lungs and the gastro-intestinal tract are in constant contact with the environment.

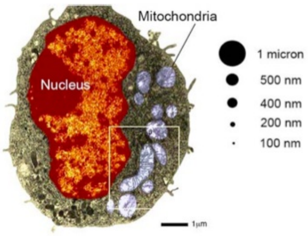

Figure 4.23: Comparison of rat machophage cells size to nanoparticles size (at scale).

While the skin is generally an effective barrier to foreign substances, the lungs and gastro-intestinal tract are more vulnerable. These three ways are the most likely points of entry for natural or anthropogenic nanoparticles. Injections and implants are other possible routes of exposure, primarily limited to engineered materials. Due to their small size, nanoparticles can translocate from these entry portals into the circulatory and lymphatic systems, and ultimately to body tissues and organs. Some nanoparticles, depending on their composition, charge and size, can produce irreversible damage to cells by oxidative stress or/and membranes or organelle injury. Figure 4.4 illustrates the size of an example cell and its organelles compared to nanoparticles of various sizes, making it easy to understand why nanoparticles are able to enter cells and interact with various cell components (nucleus, mitochondria, etc.). In fig. 4.24 we summarize the possible adverse health effects associated with inhalation, ingestion and contact with nanoparticles.

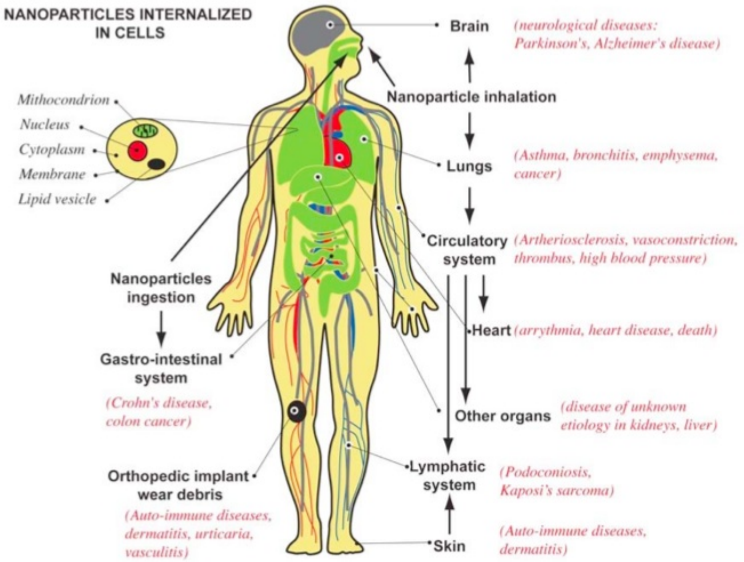

Figure 4.24: Schematics of human body with pathways of exposure to nanoparticles, affected organs, and associated diseases from epidemiological, in vivo and in vitro studies.

We emphasize that not all nanoparticles produce these adverse health effects.
The toxicity of nanoparticles depends on various factors, including: size, aggregation, composition, crystallinity, surface functionalization, charge etc. Diseases associated with inhaled nanoparticles are asthma, bronchitis, emphysema, lung cancer, and neurodegenerative diseases, such as Parkinson's and Alzheimer's diseases. Nanoparticles in the gastro-intestinal tract have been linked to Crohn's disease and colon cancer. Nanoparticles that enter the circulatory system are related to occurrence of arteriosclerosis and blood clots, arhythmia, heart diseases. Translocation to other organs, such as liver, spleen, etc., may lead to diseases of these organs as well.

### 4.4.1 Cytotoxicity of gold NR

The humans have always been exposed to nanoparticles and dust from natural sources and human activities, the recent development of industry and combustion-based engine transportation profoundly increasing anthropogenic nanoparticulate pollution. The key to understanding the toxicity of nanoparticles is that their minute size, smaller than cells and cellular organelles, allows them to penetrate these basic biological structures. The toxicity [33–36] was tested for gold NPs with different concentrations and surfactants. The cells viability was tested after the treatment for 24h with an increasing concentration of the NPs, as shown in fig. 4.25 for NPs obtained with 0.2 M CTAB-PEG 2000, 0.35 M LSB and 0.5 M LSB, respectively. To determine cell viability the colorimetric MTT metabolic activity assay was used. MTT (3-(4,5-dimetiltiazol-2-yl)-2,5-difenil tetrazolium bromide) is a salt of yellow, across the plasma membrane and is converted, in metabolically active cells, by the mitochondrial enzyme succinate dehydrogenase, in purple formazan. These reductions take place only when reductase enzymes are active, and therefore conversion is often used as a measure of viable cells. A solubilization solution, usually DMSO (dimethyl sulfoxide), is added to dissolve the insoluble purple formazan product into a colored solution. The absorbance of this colored solution can be quantified by measuring at 570 nm by a spectrophotometer. The concentration measurements of formazan is an indication of metabolic efficiency and then of the cell viability.

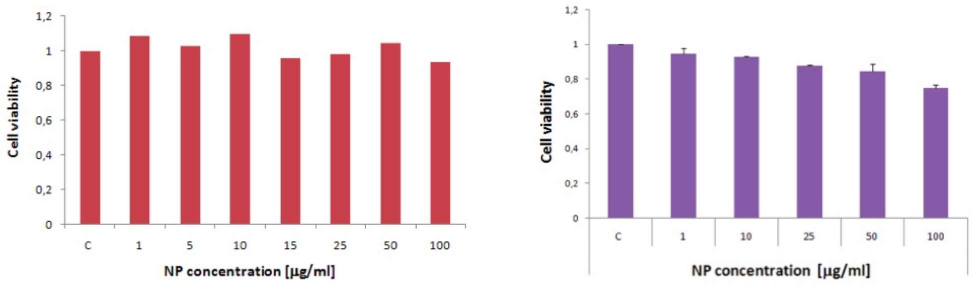

(a) *0.2 M CTAB functionalized with PEG2000.* (b) *0.35 M LSB.*

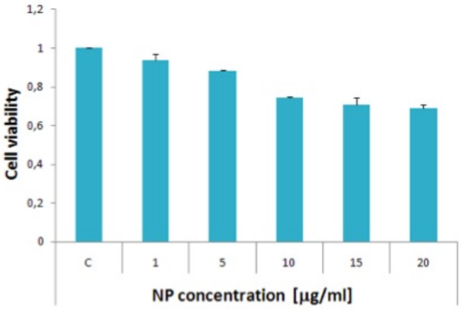

(c) *0.5 M LSB.*

Figure 4.25: Cell viability as a function of increasing differentes NPs concentration; C is the control case in which no NPs were added to cells.

The concentration of the NP suspension used for toxicity measurements was obtained by FCS; as described in par. 4.3.6 (table 4.8). Samples were rinsed three times with MilliQ (no aggregation effect was present). From the data reported in fig. 4.25 we can infer that the nanoparticles synthesized with 0.2 M CTAB and functionalized with PEG polymer are not toxic for the cells also at high concentration [37, 38]. Otherwise the number of dead cells increase rising the concentration of the NPs obtained with the LSB surfactant; in particular at concentration used in the experiments reported above the 80% of the cells are in viability conditions for NPs obtained with 0.35 M LSB (fig. 4.25b), and this percentage lower to $\cong$ 70% for NPs synthesized with 0.5 M LSB (fig. 4.25c). The toxicity is probably due to the LSB surfactant: in fact also after 3 centrifugation and resuspension in Milli-Q water cycles, a tiny amount is present in the solution which may be the origin of the cells death. In order to reduce the toxicity, it is necessary to shield the surfactant with PEG or polyelectrolyte layers (Viability $\sim$ 95%, fig. 4.25a). The toxic concentration can be evaluated from fig. 4.25. By viability $>$ 80 % we find $\sim$ 80 $\mu g$/ml for 0.35 M LSB, $\sim$ 5 $\mu g$/ml for 0.5 M LSB and $>$ 100 $\mu g$/ml for 0.2 M CTAB with PEG.

## 4.5 Cellular Uptake of NPs

Due to strong enhancement of the electric fields at the surface at the gold NP, the absorption and scattering of electromagnetic radiation by these nanoparticles are strongly enhanced. These unique properties provide the potential of designing novel optically active reagents for simultaneous molecular imaging and photothermal cancer therapy. We have therefore investigated the ability of the NPs to permeate cell membranes, by measuring the cellular uptake from HEK-239 cells, macrophages and A549 cells, at the conditions of minimum toxicity that can be obtained from fig. 4.25.

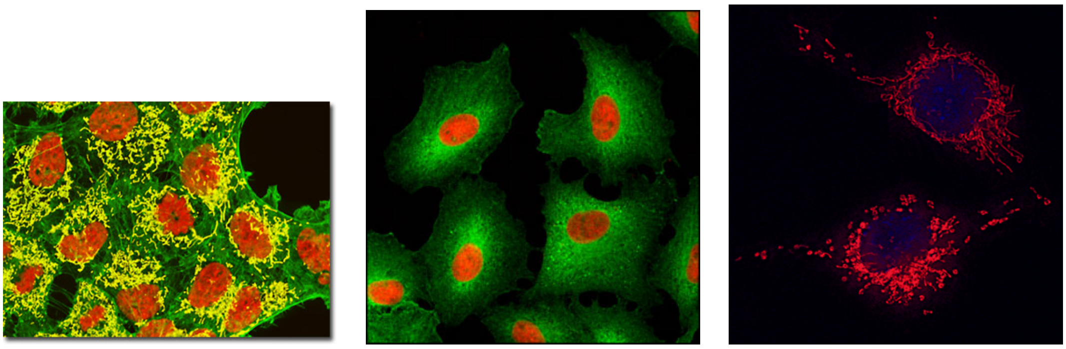
(a) *HEK cells.* (b) *A549 cells.* (c) *Macrophages.*

Figure 4.26: Images obtained with a confocal microscope

Phagocytes engulf and break down pathogenic microorganisms, damaged or apoptotic cells, and inert particles. In addition to the "professional cleaners" (neutrophils and monocyte/macrophages), most cells also have some phagocytic ability. The main difference between the phagocytic ability of professional and non-professional phagocytes is related to the presence of dedicated receptors able to recognize molecules pertaining to pathogens. Phagocytosis take up to several hours and involves several steps:

1. specific receptors on the phagocyte membrane bind with specific molecules (ligands) localized on the surface of particle.

2. after the binding of the phagocyte receptor with a ligand, the cytoskeleton (a network of protein filaments) of the phagocyte rearranges, resulting in pseudopod formation, and ultimately leading to internalization of the particle with the formation of a phagocytic vesicle (phagosome).

3. the phagosome fuses with a lysosome (an organelle containing digesting enzymes), forming a phagolysosome. The fusion process can take from 30 minutes up to several hours, depending on the chemical interaction between the surface of the particle and the phagosome membrane. Lysosoms release protease (which break down proteins) and NADPH oxidase.

4. If the particle is digested by lysosome enzymes, the residues are removed by exocytosis (release of chemical substances into the environment).

Phagocytosis is a specific form of endocytosis involving the vesicular internalization of solid and occurs in different areas of the body, phagocytes present in lungs, spleen, liver, etc..
We have investigated the ability of the NPs to permeate cell membranes, by measuring the cellular uptake from HEK-239 cells, A549 and mice macrophages in tissue plated cells. In particular the uptake of four different samples was analyzed, as shown in the table:

- NPs 0.5 M LSB
- NPs 0.35 M LSB
- NPs 0.2 M CTAB
- NPs 0.2 M CTAB + PEG-2000

Images have been recorded 30 min after the addition of the NPs (10 $\mu g$/ml for 0.5 M LSB, 40 $\mu g$/ml for 0.35 M LSB and 100 $\mu g$/ml for 0.2 M CTAB functionalized with PEG-2000.) by exploiting two photon excitation at 800 nm. The TPL emission was detected in a wide spectral range, through 485/30, 535/50 and 600/40 nm band pass filters. Images shown in the following panels are the result of 5 kalman average scans with 10 $\mu s$ of residence time per pixel. The absence of relevant bleeding through of autofluorescence has been verified on non stained cells by measuring the fluorescence emission with and without the band pass filter used to select the TPL emission of the NPs.

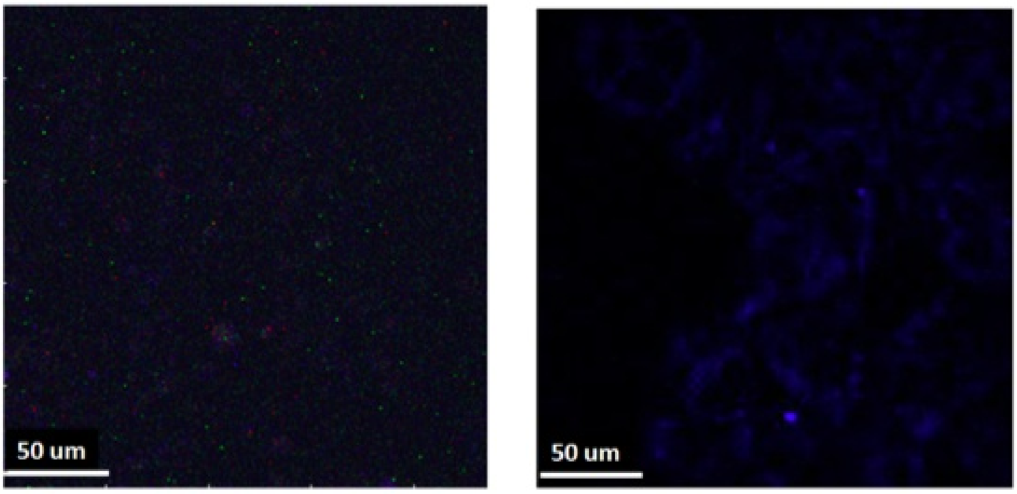

(a) *Macrophages cells .* (b) *HEK cells.*

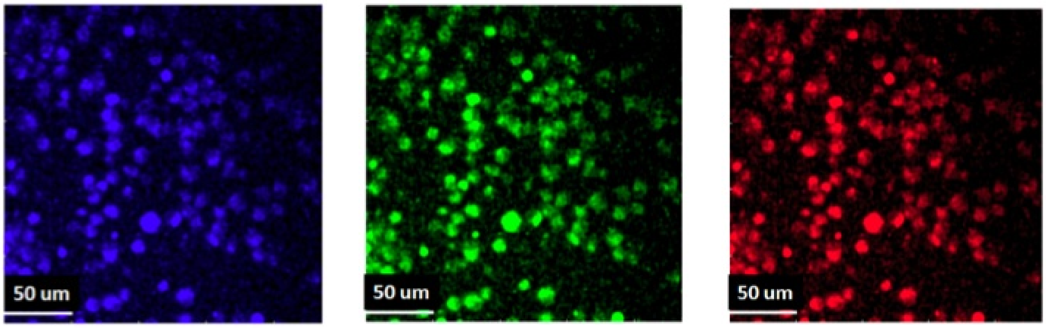

(c) *485/30 nm.* (d) *535/50 nm.* (e) *600/40 nm.*

Figure 4.27: Top: Autofluorescence with $\lambda = 800$ nm and $P_{exc} = 50$ mW. No emission filter was present. Bottom: Autofluorescence signal of macrophages cells selected through different band pass filters, with $P_{exc} = 150$ mW.

Measurements performed under the same laser power in the absence of NPs showed that cells autofluorescence was negligible both for HEK and macrophages cells. Figures (4.27 a, b) shows that autofluorescence of macrophages and HEK cells with an excitation power $P_{exc} = 50$ mW is negligible; otherwise with $P_{exc} = 150$ mW a strong autofluorescence signal is measured through the different band pass filters (see figure 4.27 c, d, e).

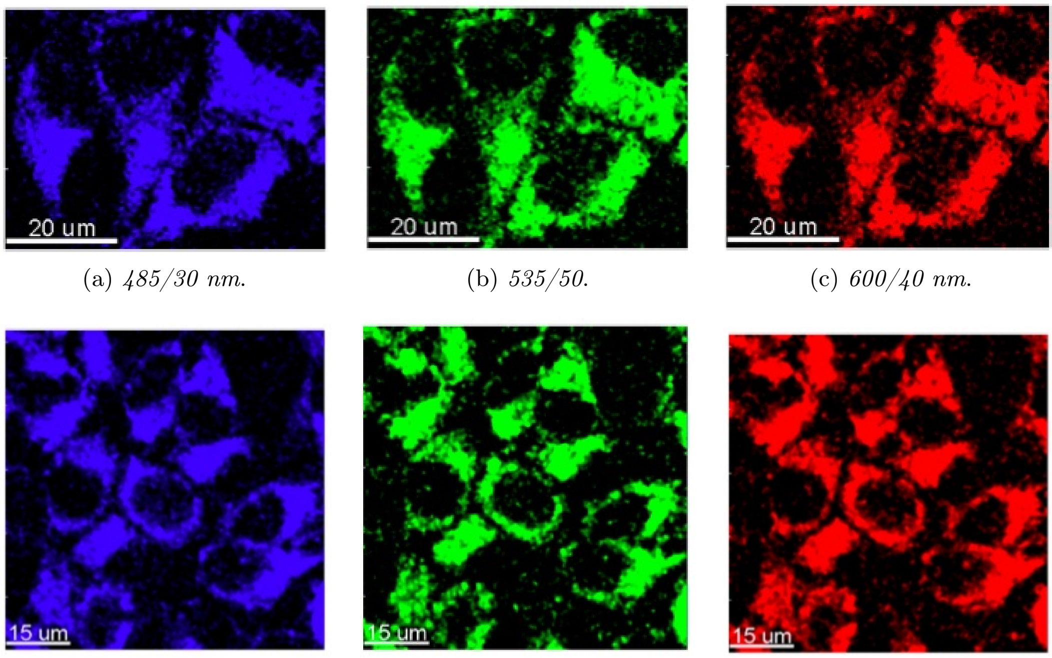

(a) *485/30 nm.* (b) *535/50.* (c) *600/40 nm.*

(d) *485/30 nm.* (e) *535/50 nm.* (f) *600/40 nm.*

Figure 4.28: The six images refer to the NPs emission selected through different band pass filters internalized in HEK cells. Only cytoplasm seems to be stained by the NPs. Top: NPs obtained with 0.5 M LSB with C $= 10\ \mu g/$ml with $P_{exc} = 40$ mW. Bottom: NPs obtained with 0.35 M LSB with C $= 40\ \mu g/$ml with $P_{exc} = 20$ mW.

The figures 4.28 and 4.29 refer to the NPs emission through different band pass filters; intense luminescence was observed, indicating that NPs penetrates the cell membrane of HEK cell staining the cytoplasm but not the nucleus, with a $P_{exc} < 50$ mW, a value which is lower than that needed to excite autofluorescence emission. In general, gold nanoparticles, including rods, enter cells by a non-specific process of endocytosis and concentrate in endosomes. In collaboration with M. Gualtieri and Department of Environmental Science, we have also performed measures of immunofluorescence on HEK and A549 cells, using dyes with different emission band: TRITC (Tetramethylrhodamine-5-(and 6)-isothiocyanate, red) for cell membrane, FITC (Fluorescein isothiocyanate, green) for cytoskeleton and DAPI (4',6-diamidino-2-phenylindole, blue) for nucleus.

Figure 4.30 shows the activity of endocytosis of HEK when interact with nanoparticles; in particular the green spots indicate active endosomes. HEK show high endocytosis already in control sample and no substantial differences between simple nanoparticles or nanoparticles coated with PEG-2000. This confirms the result obtained by the images of TPL. A different situation is found in the case of interaction between NPs and A549 cells. Unfortunately, we were unable to obtain images of TPL, but we obtained information on

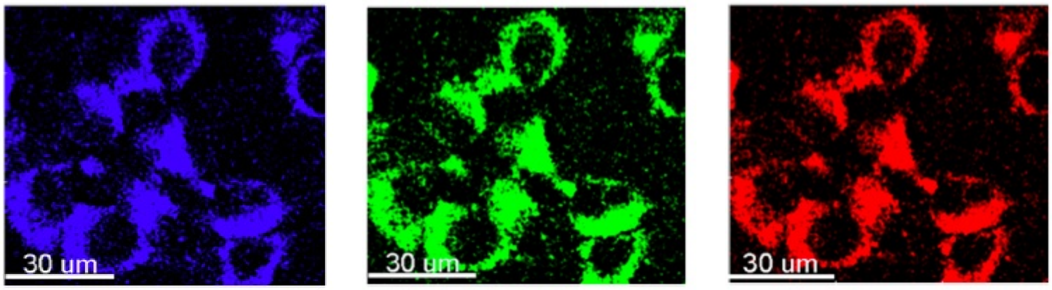

(a) *485/30 nm.* (b) *535/50.* (c) *600/40 nm.*

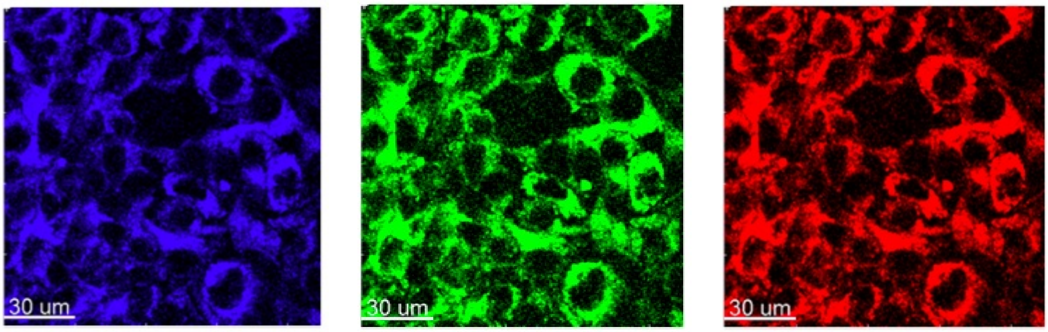

(d) *485/30 nm.* (e) *535/50 nm.* (f) *600/40 nm.*

Figure 4.29: The six images refer to the NPs emission selected through different band pass filters internalized in HEK cells. Only cytoplasm seems to be stained by the NPs. Top: NPs obtained with 0.2 M CTAB with C = 100 $\mu g$/ml with $P_{exc}$ = 15 mW. Bottom: NPs obtained with 0.2 M CTAB and functionalized with PEG-2000 with C = 100 $\mu g$/ml with $P_{exc}$ = 15 mW.

the internalization by measures of immunofluorescence.

Figures 4.31 show endocytosis of A549 cells with NR and NR functionalized with PEG-2000; the endosomes are more active in the case of NR. This means that the NP functionalized with PEG-2000 are not internalized into cells. In fact coating the particle with thiolated polyethylene glycol (PEG) renders it invisible to endocytic system [39, 41, 42].

An early study of the interaction of NPs and cells of the immune system, such as macrophages, was then accomplished. Not only do macrophage-based misfunctions play a central role in auto-immune diseases such as artherosclerosis, diabetes or rheumatoid arthritis, but these cells are also frequently the host for parasitic organisms such as Toxoplasma gondii, Mycobacterium tuberculosis and Listeria monocytogenes. Therefore the concept of designing nanoparticle vehicles that will attach to and/or be selectively ingested by macrophages appears to hold considerable potential.

Figures 4.32 and 4.33 show that macrophages internalize NPs obtained with 0.2 M

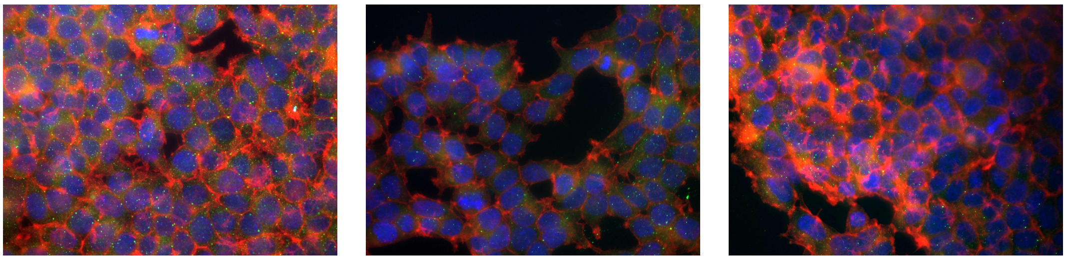

(a) *HEK control cells.* (b) *HEK and NR 100 $\mu g/ml$ .* (c) *HEK and NR with PEG-2000 100 $\mu g/ml$ .*

Figure 4.30: The three images refer to the emission of three different fluorophores. Blue is DAPI, red is TRITC and green is FITC that emphasized nucleus, cytoskeleton and endosomes in HEK cells, respectively.

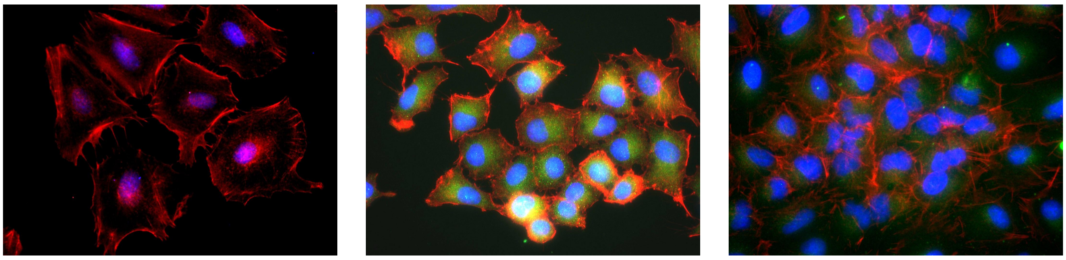

(a) *HEK control cells.* (b) *HEK and NR 100 $\mu g/ml$ .* (c) *HEK and NR with PEG-2000 100 $\mu g/ml$ .*

Figure 4.31: The three images refer to the emission of three different fluorophores. Blue is DAPI, red is TRITC and green is FITC that emphasized nucleus, cytoskeleton and endosomes in A549 cells, respectively.

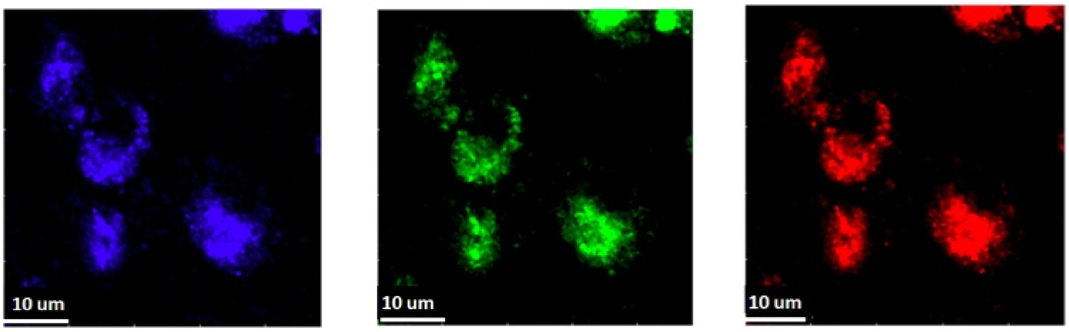

Figure 4.32: NPs obtained with 0.2 M CTAB with C $=$ 100 $\mu g$/ml internalized in macrophages cells. The three images refer to the NPs emission selected through 485/30, 535/50 and 600/40 nm band pass filters with $P_{exc}$ $=$ 15 mW; NPs are internalized in cytoplasmatic vesicles.

CTAB (C $=$ 100 $\mu g$/ml) and 0.35 M LSB (C $=$ 40 $\mu g$/ml) respectively; the NPs are distributed in cytoplasmatic vesicles but not in the nuclei and are visible with the excitation power as low as $P_{exc} \cong 15$ mW. In order to demonstrate this fact, the nuclei were stained with the DAPI dye: in figure 4.33 the nuclei are shown in blue (DAPI emission was selected through the band pass filter 485/30 nm) and the emission of NPs in red (band pass filter 600/40 nm).

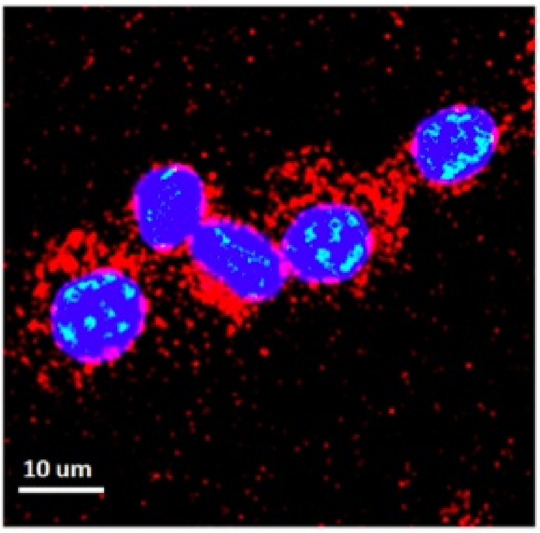

Figure 4.33: NPs obtained with 0.35 M LSB with C = 40 $\mu g$/ml internalized in macrophages cells. The nuclei, stained with the DAPI dye and are shown in blue and the emission of NPs in red. $P_{exc} = 15$ mW.

## 4.6 Copper, titanium and zinc nanoparticles

Nanotechnology is field of increasing economic and scientific interest that continues to exhibit rapid development. New nanomaterials (NMs) are being manufactured and promptly used in a variety of applications, including cosmetics and personal care products, electronics, drug delivery systems, manufacturing, technologies and paints. The lack of toxicological data available for NMs makes it difficult to predict the real risk associated with exposure to these substances and compels the scientific community to undertake research to guarantee the sustainable development of this recently developed technology. The growing use of NPs in a number of applications in different fields in becoming increasingly worthy of attention from institutional organizations related to their possible effects on public health and ecosystems. During their life cycle, NPs will enter the environment, and experimental evidence has already shown that exposure to NMs may be associated with an increased risk of certain diseases, not only for aquatic organisms but also for humans. The behavior of NPs in the environment, as well as their fate remain unclear, and it is well known that their state of aggregation and their consequent settlement to sediments depend on the hydrodynamic properties of freshwater systems, making prediction of these phenomena almost unreliable. Despite this significant gap in our understanding, it is well known that aquatic environments are certainly at risk of exposure to these pollutants, as they represent a sink for most environmental contaminants. Thus, considering NPs as a new class of hazardous material, in collaboration with P. Mantecca (University of Milano-Bicocca, Department of Environmental Science ) we have aimed to study the effects of metal oxide-based NPs on the amphibian *Xenopus laevis* using the Frog Embryo Teratogenesis Assay-Xenopus (FETAX) test. We have investigated the degree of aggregation of three different nano-sized metal-oxides (nCuO, $nTiO_2$ and nZnO) in FETAX solution at 10, 100 and 500 mg/L.

### 4.6.1 Materials and Methods

#### Chemical and NPs used

All analytical grade reagents, human chorionic gonadotropin (HCG), 3-amino-benzoic acid ethyl ester (MS222), salts for FETAX solutions, $CuSO_4 \cdot H_2O$, $ZnSO_4$ and metal oxide NPs were purchased from Sigma-Aldrich S.r.l., Italy. The advertised sizes of these particles were $< 50$ nm for nCuO (#544868) and $< 100$ nm for $nTiO_2$ and nZnO (#677469 and #544906, respectively). All suspensions and stock solutions were prepared in FETAX solution with a composition (in mg/L) of 625 NaCl, 96 $NaHCO_3$, 30 KCl, 15 $CaCl_2$, 60 $CaSO_4 \cdot 2H_2O$ and 70 $MgSO4$ at pH 7.6-8.0. Test suspensions (10, 100 and 500 mg/L) were sonicated for 10 min in a Branson2510 sonifier and stored in the dark at 4 °C. Solutions of $CuSO_4 \cdot 5H_2O$ and $ZnSO_4$ were used as controls for size-dependent and solubility effects at a nominal concentration of the metal ions of 0.5 mg/L, which is very close to the maximum concentrations measured by atomic absorption spectroscopy (AAS) in NP suspensions. These solutions were prepared without sonication.

### 4.6.2 Results

TEM analysis, performed in collaboration with Dott. P. Mantecca (University of Milano-Bicocca, Department of Environmental Science), allowed the visualization of single metal oxide NPs, as well as their aggregates. Figure 4.34 A - C shows the morphology of the nCuO, $nTiO_2$, and nZnO particles and their tendency to aggregate once suspended in aqueous medium. Based on measuring hundreds of single NPs by TEM, the calculated mean diameters of nCuO, $nTiO_2$, and nZnO were $34.38 \pm 0.76$, $46.97 \pm 0.89$ and $66.91 \pm 0.86$ nm, respectively. As shown by the size distributions (fig. 4.34 D), nCuO mainly clustered in the range of 20-50 nm, with only a few larger particles. $nZnO$ was mainly distributed in the interval between 70 and 100 nm, whereas the $nTiO_2$ population was almost normally distributed around its mean in the interval 20-80 nm. Despite these measures, single NPs were only rarely detected by TEM, and almost all particles aggregated in small clusters ranging from a few NPs to large aggregates. This behavior was shared by all three types of metal oxide NPs, although $nTiO_2$ and nZnO appeared to produce larger aggregates that were much more regular in shape compared to those of nCuO.

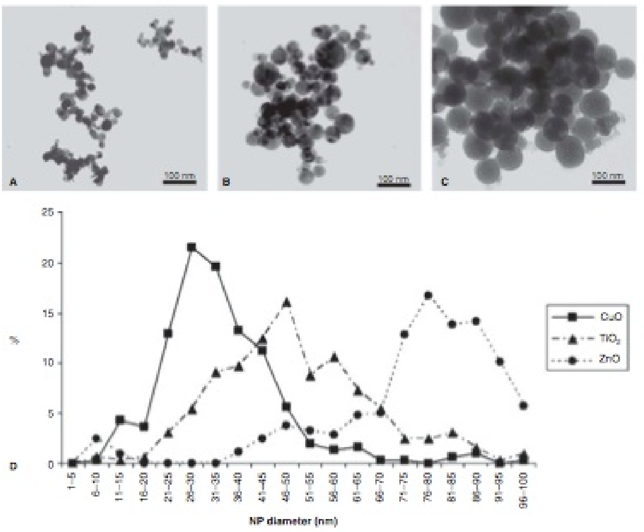

Figure 4.34: Tem images of metal oxide NPs from 100 mg/L. A = nCuO; B = nZnO; C = $nTiO_2$.

To characterize the degree of aggregation and the effective average size of the particulates used in the experiments, we performed a Dynamic Light Scattering analysis of the NP suspensions in FETAX solution at 10, 100 and 500 mg/L.

Based on the analysis of the light scattering autocorrelation functions performed as described in the section 4.6.1, we obtained the distribution of sizes reported in fig. 4.35. A first qualitative inspection of these distributions indicated the presence of two or three major components, all of which were larger than 250 nm in their hydrodynamic radius and, therefore, larger than the single NPs. This is not unexpected because the light scattered increases with the square of molecular weight, and thus, small components of large aggregates contribute to the correlation function similarly to much larger components of single NPs. Therefore, rare aggregates that could not be analyzed by TEM are easily detected. Some degree of aggregation was observed, even at a concentration of 10 mg/L, and it increased with the NP concentration.

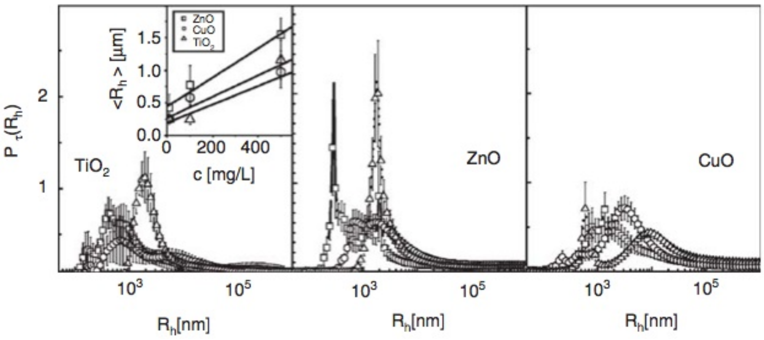

Figure 4.35: Results of the Maximum Entropy analysis of the DLS autocorrelation functions collected from FETAX suspensions of $nTiO_2$ (left panel), nZnO (middle panel) and nCuO (right panel). In each panel, three distributions are reported, referring to concentrations of 10 (squares), 100 (circles) and 500 mg/L (triangles). The inset reports the average values of the hydrodynamic radii of the NPs as a function of the concentration. The data refer to titanium (triangles), zinc (squares) and copper (circles).

To provide a measure of the average encumbrance of the NP aggregates as a function of the NP concentration in the medium, we computed an average radius for each NP suspension and compared the behavior of the different NPs, as shown in fig. 4.35 (inset).

# Bibliography

[1] W. Denk, J. H. Strickler and W. W. Webb, Science 248, 73, 1990.

[2] J. D. Bhawalkar, G. S. He and P. N. Prasad, Rep. Prog, Phys. 59, 1041, 1996.

[3] M. R. Beversluis, A. Bouhelier and L. Novotny, Phys. Rev. B 68, 115433, 2003.

[4] P. M*ü*hlschlegel, H. J. Eisler, O. J. F. Martin, B. Hecht and D. W. Pohl, Science 308, 1607, 2005.

[5] R. A. Farrer, F. L. Butterfield, V. W. Chen and J. T. Fourkas, Nano Lett, 5, 1139, 2005.

[6] Q. Q. Wang, J. B. Han, D. L. Guo, S. Xiao, Y. B. Han, H. M. Gong and X. W. Zou, Nano Lett. 7, 723, 2007.

[7] W. Dickson, P. R. Evans, G. A. Wurtz, W. Hendren, R. Atkinson, R. J. Pollard and A. V. Zayats, J. Microsc. 229, 415, 2008.

[8] K. Imura, T. Nagahara and H. Okamoto, J. Phys. Chem. B 109, 13214, 2005.

[9] C. Ropers, D. R. Solli, C. P. Schulz, C. Lienau and T. Elsaesser, Phys. Rev. Lett. 98, 043907, 2007.

[10] L. Novotny and B. Hecht, Principles of Nano-Optic Cambridge University Press, Cambridge, 2006.

[11] D. Nagesha, G. S. Laevsky, P. Lampton, R. Banyal, C. Warner, C. Dimarzio and S. Sridhar, Int. J. Nanomedicine 2, 813, 2007.

[12] N. J. Durr, T. Larson, D. K. Smith, B. A. Korgel, K. Sokolov and A. Ben-Yakar, Nano Lett. 7, 941, 2007.

[13] H. Wang, T. B. Huff, D. A. Zweifel, W. He, P. S. Low, A. Wei and J. X. Cheng, Proc. Natl. Acad. Sci. U.S.A. 102, 15752, 2005.

[14] L. Bickford, J. Sun, K. Fu, N. Lewinski, V. Nammalvar, J. Chang and R. Drezek, Nanotechnology 19, 315012, 2008.

[15] D. P. O'Neal, L. R. Hirsch, N. J. Halas, J. D. Payne and J. L. West, Cancer Lett. 209, 171, 2004.

[16] I. H. El-Sayed, X. Huang and M. A. El-Sayed, Cancer Lett. 239, 129, 2006.

[17] E. Dulkeith, T. Niedereicholz, T. A. Klar, J. Feldmann, G. von Plessen, D. I. Gittins, K. S. Mayya and F. Caruso, Phys. Rev. B 70, 205424, 2004.

[18] S. Link, M. A. El-Sayed, Int. Reviews in Physical Chemistry, 19 (3), 409-453, 2000.

[19] C. Burda, X. Chen, R. Narayanan and M. A. El-Sayed, Chem. Comm., 105, 1025, 2005.

[20] C. J. Murphy, A. Cole, J. W. Stone, P. N. Sisco, A. M. Alkilany, E. C. Goldsmith and S. C. Baxter, Acc. Chem. Res., 41, 1721-1730, 2008.

[21] (a) M. Yamamoto, Y. Kashiwagi, T. Sakata, H. Mori and M. Nakamoto, Chem. Mater., 17, 5391-5393, 2005; (b) G. C. Khoury and T. Vo-Dinh, J. Phys. Chem. C, 112, 18849-18859, 2008; (c) P. S. Kumar, I. Pastoriza-Santos, B. Rodriguez-Gonzales, F. J. Garcia de Abajo and L. M. Liz-Marzan, Nanotechnology, 19, 015606, 2008.

[22] N. R. Jana, L. Gearheart and C. J. Murphy, J. Phys. Chem. B, 105, 4065-4067, 2001.

[23] C. J. Johnson, E. Dujardin, S. A. Davis, C. J. Murphy and S. J. Mann, J. Mater Chem. 12, 1765-1770, 1962.

[24] N. R. Jana, L. Gearheart and C. J. Murphy, Adv. Mater., 13, 1389-1393, 2001.

[25] J. Gao, C. M. Bender and C. J. Murphy, Langmuir, 19, 9065-9070, 2003.

[26] X. Kou, S. Zhang, C.- K. Tsung, Z. Yang, M. H. Yeung, G. D. Stucky, L. Sun, J. Wqng and C. Jan, Chem. Eur., 13, 2929-2936, 2007.

[27] S. Ozkar and R. G. Finke, J. Am. Chem. Soc., 124, 5796-5810, 2002.

[28] D. Magde, E. L. Elson and W. W. Webb. Biopolymers, 13(1), 29-61, 1974.

[29] M. Ehrenberg and R. Rigler. Chemical Physics, 4(3), 390-401, 1974.

[30] S. R. Aragon and R. Pecora. Biopolymers, 14(1), 119-137, 1975.

[31] P. Kask, P. Piksarv, M. Pooga, U. Mets and E. Lippmaa. Biophysical Journal, 55(2), 213-220, 1989.

[32] J. Widengren, U. Mets and R. Rigler. Chemical Physics, 250(2), 171-186, 1999.

[33] A. M. Alkilany, P. K. Nagaria, C. R. Hexel, T. J. Shaw, C. J. Murphy and M. D. Wyatt. Small, 5(6), 701-708, 2009.

[34] Y. S. Chen, Y. C. Hung, I. Liau and G. S. Huang. Nanoscale research letters, 4(8), 858-864, 2009.

[35] H. C. Fischer and W. C. W. Chan. Current opinion in biotechnology, 18(6), 565-571, 2007.

[36] C. J. Murphy, A. M. Gole, J. W. Stone, P. N. Sisco, A. M. Alkilany, E. C. Goldsmith and S. C. Baxter. Accounts of chemical research, 41(12), 1721-1730, 2008.

[37] N. Lewinski, V. Colvin and R. Drezek. Small, 4(1), 26-49, 2008.

[38] F. Alexis, E. Pridgen, L. K. Molnar and O. C. Farokhzad. Molecular pharmaceutics, 5(4), 505-515, 2008.

[39] D. Pissuwan, S. M. Valenzuela, M. C. Killingsworth, X. Xu and M. B. Cortie. Journal of Nanoparticle Research, 9(6), 1109-1124, 2007.

[40] S. M. Moghimi, A. C. Hunter and J. C. Murray. tHE faseb JOURNAL, 19(3), 311, 2005.

[41] M. R. Hamblin, J. L. Miller, I. Rizvi, H. G. Loew and T. Hasan. British journal of cancer, 89(5), 937-943, 2003.

[42] A. M. Arnida and H. Ghandehari. Journal of Applied Toxicology, 30(3), 212-217, 2010.

[43] H. Takahashi, T. Niidome, A. Nariai, Y. Niidome and S. Yamada. Chemistry Letters, 35(5), 500-501, 2006.

[44] D. S. Wang, F. Y. Hsu and C. W. Lin. Optics Express, 17(4), 11350-11359, 2009.

[45] C. K. Riener, G. Kada and H. J. Gruber. Anal. Bioanal. Chem. 373, 266-276, 2002.

# Chapter 5

# Hyperthermic effects of Metal Nanoparticles

> Di quella pira l'orrendo
> foco.Tutte le fibre m'arse
> avvampó...
>
> S. Cammarano, Trovatore
> G. Verdi

Hyperthermia is currently under consideration as a noninvasive approach to cancer therapy, in which biological tissues are exposed to higher than physiological temperatures to promote the selective destruction of abnormal cells [1]. Systematic hyperthermia has long been considered as an adjuvant therapy for treating various disease states [2, 3], and its clinical potential in cancer treatment is an active area of investigation [4]. Hyperthermia is known to have diverse therapeutic effects at both the systemic and cellular level. In the latter case, a marked increase in local temperature ($\Delta T > 5\,^{\circ}\mathrm{C}$) can induce the denaturation of proteins or the disruption of organized biomolecular assemblies in the nucleus and cytoskeleton. Moderate increases in temperature can also sensitize cancer cells to cytotoxic agents by increasing membrane permeability and lowering hydrostatic pressure. In addition, mild hyperthermia can induce the production of heat shock proteins and other immunostimulants, trigger disfunctional cellular metabolism, and promote the onset of acidosis or apoptosis. The first is an increased acidity in the blood and other body tissue (i.e., an increased hydrogen ion concentration), the second is the process of programmed cell death (PCD) that may occur in multicellular organisms

Localized hyperthermia has particular relevance in the treatment of primary tumors and early-stage cancers, although its long-term impact on cancer patient survival remains to be established. Tumor cells are considered to be more susceptible to hyperthermic effects than healthy cells because of their higher metabolic rates, and numerous clinical studies have demonstrated a marked reduction in tumor size after treatment by localized hyperthermia[5]. Several methods have been developed for the external delivery of thermal energy in a nontopical manner, such as microwave irradiation, radiofrequency pulses, and acoustic waves (ultrasound). These are capable of deep tissue penetration but may require a high fluence because of their diffuse nature, possibly producing undesirable hyperthermic effects in surrounding tissues.

In this chapter, we have compared the increase in temperature of gold nanorods and magnetic nanoparticles solutions. The first ones, have additional capacibility to absorb photons and to convert into heat by nonradiative processes, the second ones heat by induction due to magnetic losses. We have studied the increase in temperature of bulk samples using a direct visualization by means of a sensitive thermocamera. Since the applications involve the highly localized thermal release, we have developed a nano-sensor to measure the local temperature on the surface of the nanoparticles under excitation. The rationale is to bind an organic chromophore whose excited state lifetime (ESLT) is particularly sensitive to the temperature, and to refer to its lifetime which is an intensive parameter. Rhodamine B is such a fluorophore, with a temperature dependence of the excited state lifetime $\approx 0.029 \pm 0.001$ ns/°C, as we also measure here. Moreover this nanoconstruct can target tissues or single cells and used for imaging before the therapy. Fluorescence lifetime measurements in the time domain are commonly performed by means of Time-Correlated Single Photon Counting (TCSPC) and using TimeHarp and Symphotime softwares (see Appendix A).

Part of these experimental results have been successfully coupled to numerical simulations of light induced heating of gold nanorods, using the Two Temperature Model (TTM) in order to calculate the raising in temperature due to laser irradiation.

## 5.1 Heating of Magnetic Nanoparticles

We can classify biomedical applications of magnetic nanoparticles according to their application inside (in vivo) or outside (in vitro) the body. In vivo applications could be further separated in therapeutic (hyperthermia and drug-targeting) and diagnostic applications (nuclear magnetic resonance (NMR) imaging), while for in vitro applications the main use is in diagnostic.Hyperthermia is a therapeutic procedure used to raise the temperature of a region of the body affected by malignancy or other anomalous growth. The rationale is based on a direct cell-killing effect at temperatures above 40 - 41 °C [6, 8]. Modern clinical hyperthermia trials focus mainly on the optimization of the thermal homogeneity at moderate temperatures (42 - 43 °C) in the target volume. The temperature increase required for hyperthermia can be achieved, among other methods, by using ultra fine iron oxide magnetic particles [13]. The physical principle of the basis of heat production by a magnetic material under the action of an external alternating magnetic field is the loss process that occurs during the reorientation of the magnetization of magnetic materials.[10, 11]. The advantage of magnetic hyperthermia is that allows the heating to be restricted to the tumour area. Moreover, the use of subdomain magnetic particles (nanometre-sized) is preferred instead multidomain (micron-sized) particles because nanoparticles absorb much more power at tolerable AC magnetic fields [12, 14]. Finally, it should be mentioned that the heating potential is strongly dependent on the particle size and shape, and thus well-defined synthetic routes to produce uniform particles are essential for a rigorous control of the induced temperature.

### 5.1.1 Physical and chemical properties

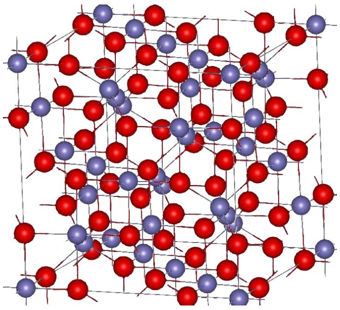

Figure 5.1: Crystal structure of magnetite.

We have studied magnetic nanoparticles composed of $Fe_3O_4$ and a outer layer of $C_3H_5(COO_3)^{3-}$ (citrate). The NPs are produced by dott. Baldi and dott. Mazzantini at the research center Colorobbia. Magnetite can be prepared using Schikorr reaction. Under anaerobic conditions, the ferrous hydroxide ($Fe(OH)_2$) can be oxidized by the protons of water to form magnetite and molecular hydrogen. The reaction is:
$3\,Fe(OH)_2 \longrightarrow Fe_3O_4 + H_2 + 2\,H_2O$
A measure of zeta potential ($\zeta$-potential) has showed that the colloids have a superficial charge of -40 mV: the nanoparticles suspensions have a good stability. Figure 5.2 shows the absorption spectrum of magnetic nanoparticles; the spectrum shows low absorption in the visible and near infrared. From measures of DLS and FCS (see also chapter 4) we have obtained the hydrodynamic radius ($r_h$) and concentration (C) of the magnetic nanoparticles:

$$r_h = 62 \pm 3 \quad \text{nm}$$
$$C = 43.2 \pm 13.8 \quad \text{mM}$$

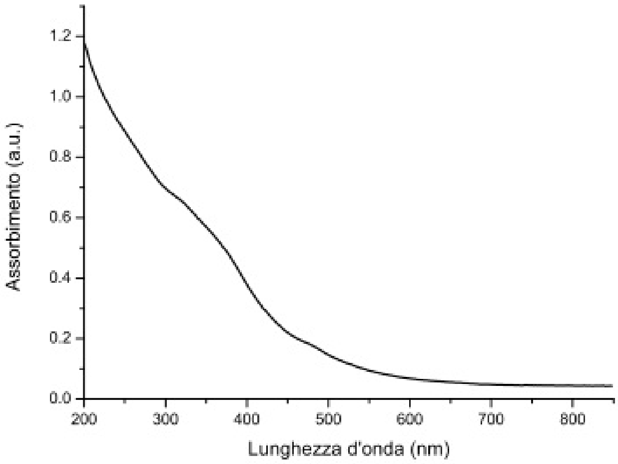

Figure 5.2: Absorption spectra of magnetic nanoparticles. The spectrum shows low absorption in the visible and near infrared.

### 5.1.2 Experimental Setup

#### Microbolometer Thermo Camera

A microbolometer is a specific type of bolometer used as a detector in a thermal camera. Infrared radiation with wavelengths between 7.5 - 14 $\mu m$ strikes the detector material, heating it, and thus changing its electrical resistance. This resistance change is measured and processed into temperatures which can be used to create an image.

A microbolometer consists of an array of pixels, each pixel being made up of several layers. The cross-section diagram shown in fig. 5.3 provides a generalized view of the pixel. Each company that manufactures microbolometer has their own unique procedure for producing them and they even use a variety of different absorbing materials. In this example the bottom layer consists of a silicon substrate and a readout integrated circuit (ROIC). Electrical contacts are deposited and then selectively etched away.

A reflector, for example, a titanium mirror, is created beneath the IR absorbing material. Since some light is able to pass through the absorbing layer, the reflector redirects this light back up to ensure the greatest possible absorption, hence allowing a stronger signal to be produced. Next, a "sacrificial" layer is deposited so that later in the process a gap can be created to thermally isolate the IR absorbing material from the ROIC. A layer of absorbing material is then deposited and selectively etched so that the final contacts can be created. To create the final bridge like structure shown in fig. 5.3, the sacrificial layer is removed so that the absorbing material is suspended approximately 2 $\mu m$ above the readout circuit. Because microbolometers do not undergo any cooling, the absorbing material must be thermally isolated from the bottom ROIC and the bridge like

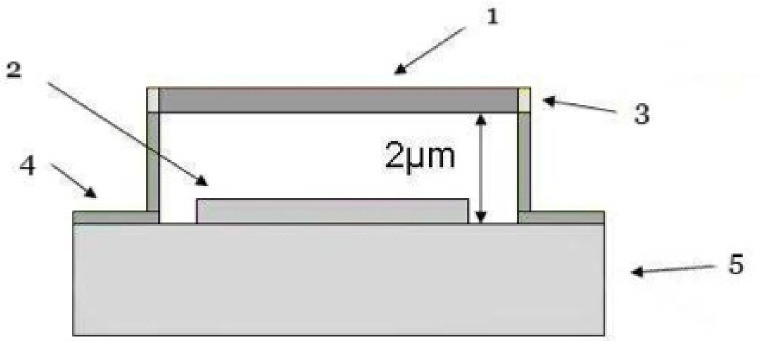

Figure 5.3: Cross-section view of a microbolometer. 1) IR absorbing material, 2) reflector, 3) gold contact, 4) electrode, 5) readout circuit/silicon substate.

structure allows for this to occur. After the array of pixels is created the microbolometer is encapsulated under a vacuum to increase the longevity of the device. In some cases the entire fabrication process is done without breaking vacuum.

Since infrared radiation is emitted by all objects above absolute zero according to the black body radiation law, thermography makes it possible to see one's environment with or without visible illumination. Our thermo camera (ThermaCAM SC 3000, FLIR Systems) is an array of 320 × 240 microbolometers. The optical system consists of a zinc sulfide lens (ZnS), with coating for the spectral range of acquisition. The outer lens is interchangeable: the one in use has an acceptance angle of 24° × 18°, which corresponds to a numerical aperture of 0.46 × 0.34. The thermo camera has a focal length of 0.5 m and a system of manual focus. The detector allows to acquire with a frequency of 9 Hz. The sensitivity of system is 0.1 °C and accuracy of ± 2 °C in the range of acquisition.

For a correct analysis of scanned images it is necessary to take into account the emissivity $\epsilon$ of the sample, defined as the ratio between the radiative power of the sample $W_\lambda c$ and that of a blackbody at the same wavelength and temperature $W_\lambda b$

$$\epsilon = \frac{W_\lambda c}{W_\lambda b} \tag{5.1}$$

To set a value of $\epsilon$, we have measured the temperature of the sample with a thermocouple and compared this measure with the average value recorded by the camera. We have estimated a emissivity of the sample $\epsilon = 0.96$ ($\epsilon_{water} = 0.98$). The radiofrequency inductor requires the use of a cooling system to compensate the ohmic dissipation of the solenoid. This cooling system is very efficient, so in addition to maintaining the optimal temperature of the solenoid, it cooled the air inside. This results in a systematic error in the measurement of temperature of the sample. We can estimate the minimum heat absorbed by the chiller considering the difference in temperature between the air inside the solenoid and the surroundig air. The mass of air contained in the solenoid is $V_A \cdot \rho_A = 0.19$ g where $V_A$ is the volume of the solenoid and $\rho_A$ is air density. We have measured a difference in temperature between air inside and outside of solenoid of $\Delta T_A$=2.20 °C (at 19 °C), from which we have obtained the heat absorbed by the chiller $Q = mc_P\Delta T_A = 0.418$ J. If the sample is composed primarily of water and weighs about 0.2 g, the difference between the temperature of the sample in the presence or absence of chillers is estimated to the 0.5 °C.

### Radio frequency Inductor

To excite magnetic nanoparticles we have used a radio frequency magnetic field generator (Novastar5, Ameritherm, Scottsville, NY). The instrument is composed of a generator and an inductor, both water-cooled.

Figure 5.4: Novastar 3 & 5 kW RF Power Supplies.

The generator converts a line input 380 V rms, 50 Hz alternating current (15 A) in a continuous signal using a rectifier. The resulting signal then passes to a voltage multiplier, that returns a maximum potential of 740 V rms. This potential is adjusted by changing the hardware configuration and through a multifunction control. The configuration used provides 558 V rms. The continuous signal is then converted in radio frequency and transferred to a portable inductor connected to the generator through RF cables. The latter part of the circuit is equivalent to a RLC circuit in series. The portable inductor was positioned above the microscope by means of a wooden support.

**Simulation of magnetic field** The magnetic field distribution was a simulated using the finite element routines in the MagNet software (Infolytica, Montreal, CA).

Initially we have defined the three-dimensional structure of the object (characteristics are shown in table 5.1); the solenoid was enclosed in a air box size of 60 × 60 × 60 cm and the faces of the box were simulated by means of boundary conditions that reproduces an infinite space. This type of condition is called Asymptotic Boundary Conditions (for

Table 5.1: Characteristics of solenoid.

| | |
|---|---|
| Height | 75 mm |
| Number of coils | 9 |
| ⌀ solenoid | 52 mm |
| ⌀ tube | 2 mm |

a detailed discussion of the mathematical problem see [16]). The boundary condition set at the edge of the solenoid is a Neumann condition. To study the numerical solution of this problem, we have considered mathematical equivalent class of problems in two dimensions. For more details, see [15].

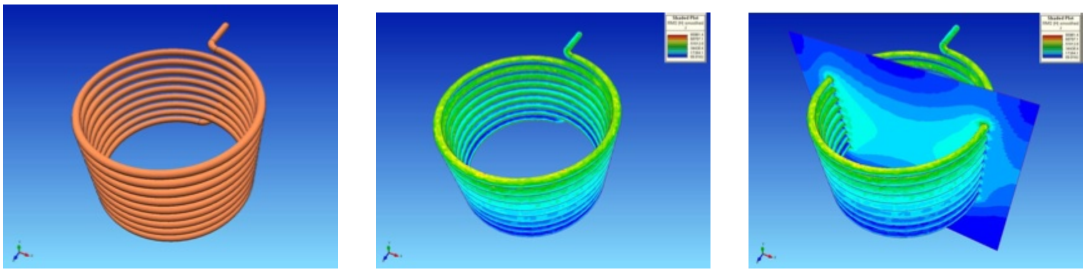

Figure 5.5: Left: 3D Model. Center: electromagnetic field of solenoid. Right: electromagnetic field on solenoid and sagittal plane.

To determine the magnetic field is necessary to calculate the current flowing in the solenoid and set it to extremes of simulated solenoid. The generator produces a signal with frequency $\nu =$ 0.168 MHz. In our case the potential was 93 % of the maximum potential Vrms = 600V. For RLC series circuit with C = 0.66 $\mu F$, the potential mean square and peak are

$$V_{rms} = V_i = 600 \cdot 0.93 = 558.00 \quad \text{V} \tag{5.2}$$

$$V_{peak} = \sqrt{2} V_{rms} = 789.12 \quad \text{V} \tag{5.3}$$

The average and peak inductive current at the extremes of inductor is

$$I_{rms} = V_{rms} C\omega = 558.00 \cdot 0.66 \cdot 10^{-6} \cdot 2\pi \cdot 0.168 \cdot 10^{6} = 377.17 \quad \text{A} \tag{5.4}$$

$$I_{peak} = V_{peak} C\omega = 789.12 \cdot 0.66 \cdot 10^{-6} \cdot 2\pi \cdot 0.168 \cdot 10^{6} = 533.39 \quad \text{A} \tag{5.5}$$

Figure 5.7 shows the evolution of H as a function of distance from the sagittal and radial center of the coil. The simulation shows a magnetic field maximum of $H_{max} =$

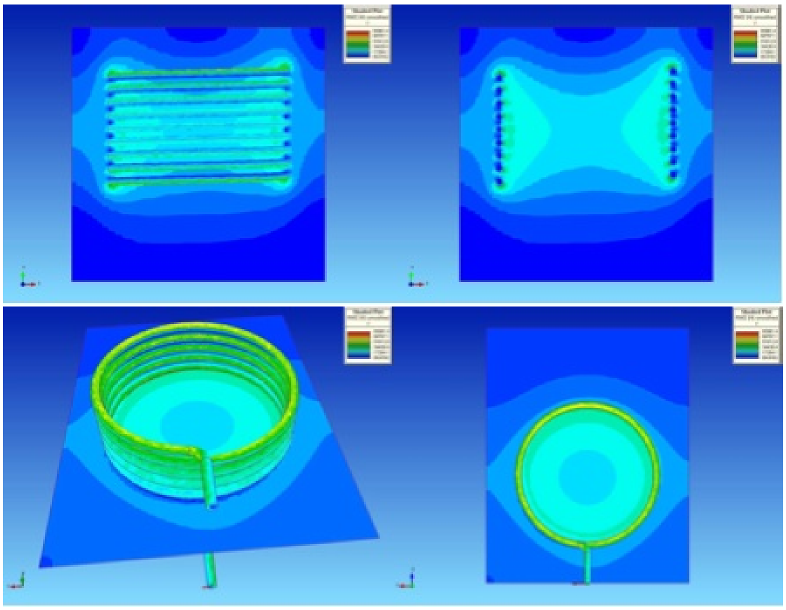

Figure 5.6: Up: Evolution of H along the longitudinal plane. Down: Evolution of H along the sagittal plane

24500 A/m, corresponding to $B_{max} = 0.032$ T. From simulations we can also see that the magnetic field becomes negligible for a distance along the axes of about 20 cm.

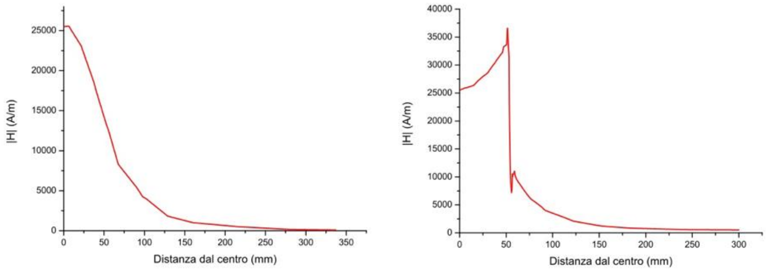

Figure 5.7: Left: Evolution of H along the sagittal plane; discontinuity is due to the presence of the solenoid. Right: Evolution of H along the sagittal plane; discontinuity is due to the presence of the solenoid.

### Gradient index lens

The problem of optical measurement combined with a field generator is to avoid the interaction between the field and the metal of which consists most of the optical system. The solution adopted is to use an endoscope to gradient index (GRINTEC, Jena, DE) to bring the focal plane of the microscope 30 cm higher so that the effect of the magnetic field is negligible.

The gradient index lenses (GRIN lenses) are optical systems in which the refractive index $n(x, y, z)$ varies depending on the position. The most common configurations are those in which the refractive index $n(z)$ varies along the optical axis z, or radially $n(r = x^2 + y^2)$, or is a function a single direction $n(x)$ or, finally, can vary with spherical symmetry $n(r = x^2 + y^2 + z^2)$. The lens used has a refractive index $n(r) = n_0 sech(g(r))$, where g(r) is a characteristic parameter of the lens, which varies radially in the plane perpendicular to the direction of propagation, with a central maximum $n_0$. As in the case of optical fibers, the numerical aperture is a function of the refractive index of the fiber core $n_0$ and the refractive index of cladding $n_f$:

$$NA = \sqrt{n_0^2 - n_f^2} = n_0\sqrt{1 - sech^2\frac{g(r)d}{2}} \tag{5.6}$$

where d is the diameter. The focal length and working distance are related to the parameters from the relationships:

$$f = \frac{1}{n_0 gsin(g\zeta)} \tag{5.7}$$

$$WD = \frac{1}{n_0 gtan(g\zeta)} \tag{5.8}$$

where $\zeta$ is the axial length of the lens. GRIN lens is made by several techniques: neutron irradiation, chemical vapour deposition and ion exchange. The main doping materials are $Na^+$, $Li^+$, $K^+$, $Ag^+$, $Cs^+$. The endoscope is a composite system of three lenses, with different gradient index length and numerical aperture. The first lens has numerical aperture of 0.4 and pitch 0.25; this lens focuses a point source to infinity. The parallel rays enter into a relay lens with lower numerical aperture (0.1) and pitch 6. The last lens has the same characteristics as the first and it is used to collimate the rays parallel output from the relay lens to a focal point at finite distance. The total pitch is 6.5, then the image is reflected and unmagnified. The sample was placed on a common slide of the thickness of about 170 $\mu m$ in contact with a surface of the endoscope. In this case, the working

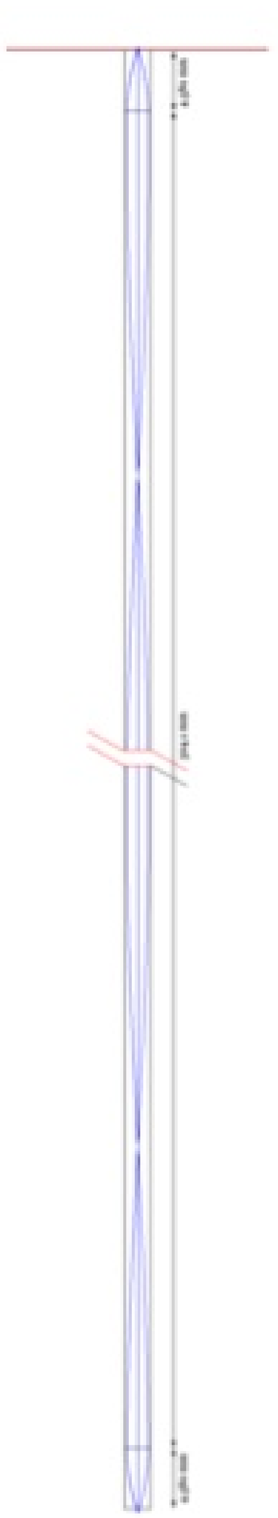

Figure 5.8: Diagram of the GRIN lens used.

distance is modified by the presence of the slide.
We have performed numerical simulations of the optical transfer function. These simulations show that the total working length is by means of the software ZEMAK 97 $\mu m$ within the sample. The gradient index lens is coated with a layer of wax to strength it resistant to impact. It was also fixed to a support with coarse regulation (1 mm) of the height (fig. 5.9).

Figure 5.9: The gradient index lens, with wax coating and support adjustable in height.

To align endoscope we have positioned a glass slide with a solution of Rhodamine B and we have compared its spectrum, acquired with the spectral camera in real time with a reference spectrum (fig. 5.10). We have changed the position of the endoscope in the xyz until the spectrum acquired with the spectral camera is similar that of reference, it means that the endoscope is aligned properly.

### 5.1.3 Rhodamine-B thermal characterization

The dependence of the Rhodamine-B emission spectra in solution was first measured while increasing the temperature from 10 to 60 °C. Rhodamine-B emission spectra were measured with a spectrofluorimeter *Varian Eclipse* (Varian, UK); as shown in figure 5.11 and in table 5.2, the peak emission intensity decreases when increasing the temperature.

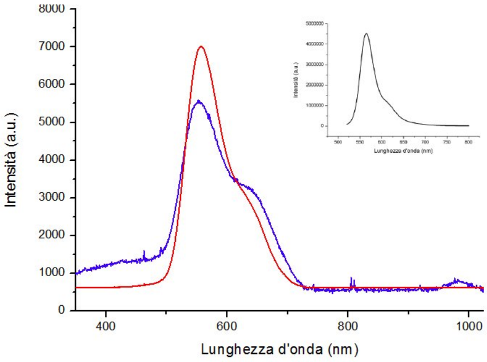

Figure 5.10: Spectrum of Rhodamine B at different alignments; in red we have the correct spectrum, which is similar to reference spectrum of Rhodamine B (above).

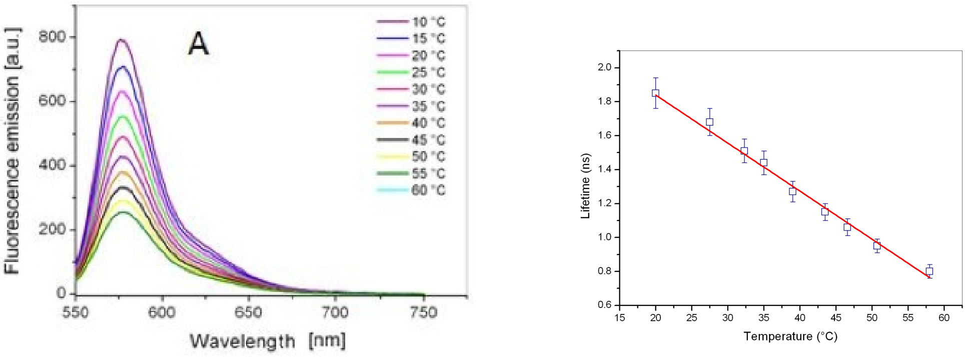

Figure 5.11: Rhodamine B emission spectra of increasing the temperature (left). Lifetime of Rhodamine B versus temperature; the linear fit is described by the relation 5.11

The quantum yield is defined as:

$$\phi = \frac{k_R}{k_R + k_{NR}} \tag{5.9}$$

where $k_R$ and $k_{NR}$ are the rate of radiative and non-radiative decay of Rhodamine-B, respectively. Since $k_R$, the decrease in the Rhodamine-B fluorescence emission (and as consequence of $\phi$) of fluorophore is due to the increasing of the number of non-radiative de-excitation ($k_{NR}$).

Also the excited state lifetime $\tau$ of Rhodamine-B decreases when increasing the temperature. Since $\tau$ is:

$$\tau = \frac{1}{k_R + k_{NR}} \tag{5.10}$$

in agreement with the emission, we can infer from the data that $k_{NR}$ increases with T, leading to the excited state lifetime decrease. The results are reported in table 5.2

Table 5.2: Dependence of Rhodamine-B emission intensity and lifetime on temperature.

| Temperature (°C) | Emission Intensity (a.u.) | Temperature (°C) | Lifetime $\tau$ (ns) |
|---|---|---|---|
| 10 | $882 \pm 8$ | 20 | $1.85 \pm 0.09$ |
| 15 | $794 \pm 8$ | 27.5 | $1.68 \pm 0.08$ |
| 20 | $704 \pm 7$ | 32.3 | $1.51 \pm 0.07$ |
| 25 | $631 \pm 6$ | 35 | $1.44 \pm 0.07$ |
| 30 | $552 \pm 7$ | 39 | $1.27 \pm 0.06$ |
| 35 | $487 \pm 8$ | 43.5 | $1.15 \pm 0.05$ |
| 40 | $429 \pm 7$ | 46.6 | $1.06 \pm 0.05$ |
| 45 | $379 \pm 7$ | 50.7 | $0.95 \pm 0.04$ |
| 50 | $331 \pm 6$ | 58 | $0.80 \pm 0.04$ |

and in figure 5.12.

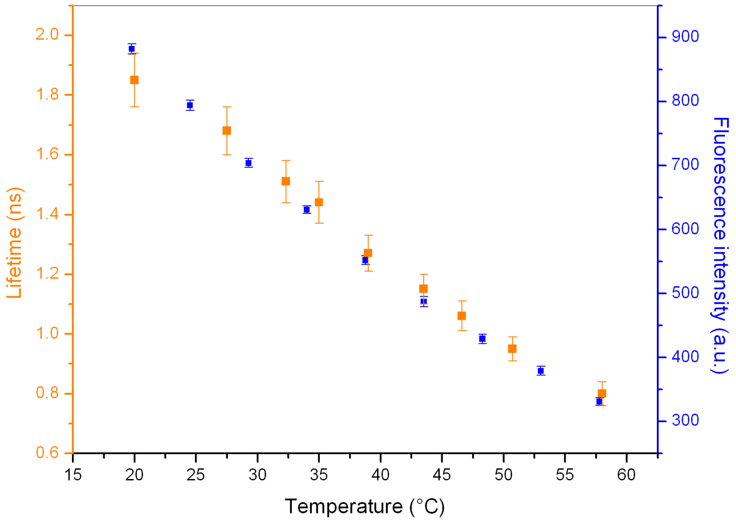

Figure 5.12: Emission intensity (blue) and excited-state lifetime (orange) of Rhodamine B dye decrease as a function of the temperature.

The fluorescence intensity and the lifetime of Rhodamine-B as a function of T show a very similar trends (figure 5.12), confirming our hypothesis that $k_R$ stays $\cong$ constant with T. As shown in figure 5.11, data are well approximated by a linear fit described by the following relation:

$$\tau = [(2.4 \pm 0.3) - (0.029 \pm 0.005) \times T(^\circ\mathrm{C})] \quad \mathrm{ns} \tag{5.11}$$

which enables to evaluate the temperature increase T from the dye excited state lifetime $\tau$. These results show that Rhodamine-B is a good temperature sensor in the range 10 - 60 °C. We can then conjugate it with gold NPs in order to create a novel assay for the online monitoring of the local temperature on nanorods and magnetic nanoparticles to be used for hyperthermic therapy.

### 5.1.4 Global and Local Temperatures

The thermo camera allows a direct measurement of the heating and cooling for a solution of nanoparticles. The sample of magnetic nanoparticles (MNPs) is placed on a cover slip at the center of the solenoid and the thermo camera is positioned on a support at distance of 0.5 m. Figure 5.13 summarizes the behavior of the solenoid and the sample. In fig. 5.13 a we report the acquisition of the camera when the magnetic field is still off, but the chiller is on. The chiller (as discussed above) causes cooling in the air inside the solenoid and this causes an underestimation of the real temperature rise of the sample. In fig. 5.13 b-d we show the behavior of the sample respectively after 30, 60 and 90 s after power of the magnetic field. At time t = 311 s the magnetic field is turned off (fig. 5.13 e). Figure 5.13 f shows the sample at time t = 391 s, during the cooling, under B = 0.

The average temperature of the sample after 5 minutes of exposure to the magnetic field is 303.9 ± 0.2 K (fig. 5.14); the average temperature before turning on the field is 291.1 ± 0.2 K. Then, considering the underestimation of the real temperature rise causes of the chiller, we obtain an increase in temperature of 13.3 ± 0.4 K.

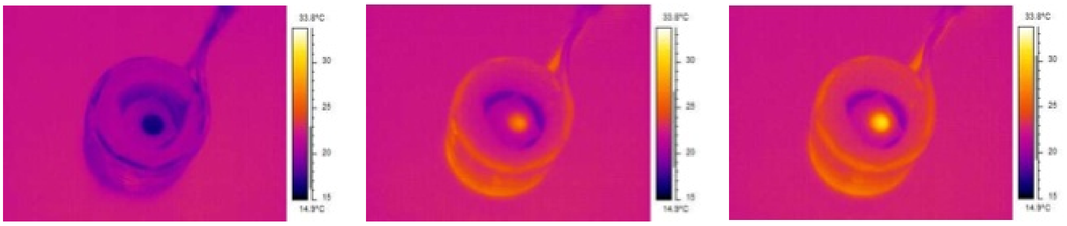

(a) *no B field, t = 0.* (b) *B field, t = 30 s.* (c) *B field, t = 60 s.*

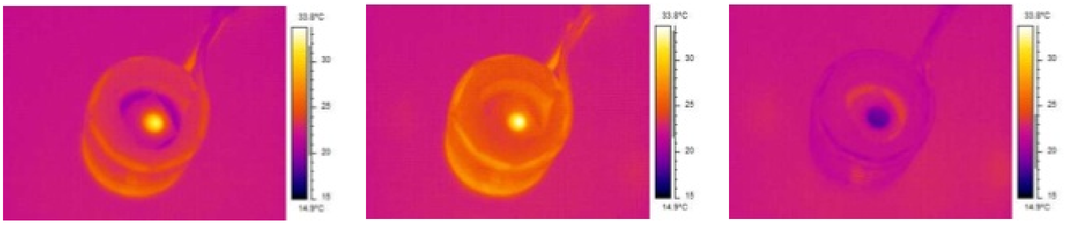

(d) *B field, t = 90 s.* (e) *no B field, t = 311 s.* (f) *no B field, t = 391 s.*

Figure 5.13: Images captured with thermocamera.

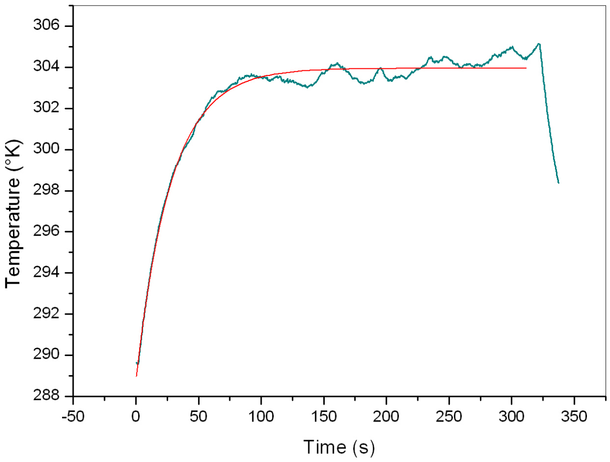

Figure 5.14: Temperature profiles at different times after exposure to magnetic field, interpolated with an exponential function.

With the same sample, we have tried to measure the temperature rise on the surface of magnetic nanoparticles by means of lifetime measurements. The negatively charge of particles and their good stability allowed to bind Rhodamine B electrostatically. We have used a concentration of Rhodamine B lower than the magnetic nanoparticles (RhB : MNP = 1:2 ); we can therefore assume that the dye is enough linked to magnetic nanoparticles. The first issue was to verify that these nanoparticles did not show the typical plasmonic effects of gold nanoparticles. We have irradiated the sample with a pulsed laser at 800 nm (P = 50 mW) and have measured the average lifetime of the excited state of Rhodamine B. The value of lifetime obtained is the same of Rhodamine B in solution at room temperature. In order to measure the lifetime of Rhodamine B bind to MNP under the magnetic field, we have aligned the endoscope and placed a slide with sample into contact with the endoscope at the center of the solenoid. Figure 5.15 shows a plot histograms of fluorescence counts of Rhodamine B. The histograms are acquired with a delay of 10 s after turning on the magnetic field.

A increase of slope indicates decrease of lifetime, therefore due to a decrease in temperature. The lowering of the total numbers of counts indicates fluorescence quenching due to temperature. Curves are obtained by interpolating the measurements of the lifetimes summarized in table 5.3. The temperature corresponding to these lifetimes is obtained by fitting with the eq. 5.11 .

The longest increase in local temperature observed is of 11± 5 K, comparable to that observed with the thermocamera measurements.

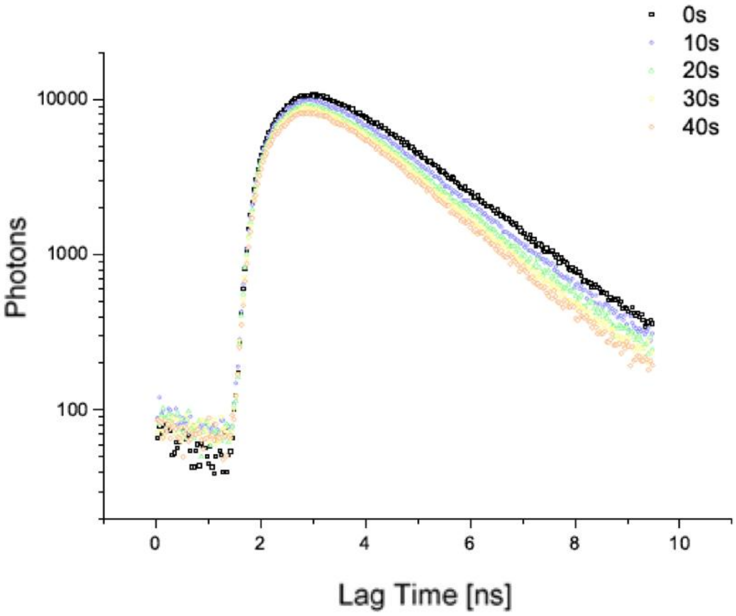

Figure 5.15: Histograms of fluorescence counts of MNP-Rhodamine B construct acquired with a delay of 10 s after turning on the magnetic field.

Table 5.3: Average lifetime of Rhodamine B with magnetic nanoparticles at different times of acquisition.

| Time (s) | $\langle\tau\rangle$ (ns) | Temperature (°C) |
|---|---|---|
| 0 | $1.90 \pm 0.01$ | $19.1 \pm 2.4$ |
| 10 | $1.80 \pm 0.01$ | $22.5 \pm 2.5$ |
| 20 | $1.76 \pm 0.01$ | $23.9 \pm 2.5$ |
| 30 | $1.71 \pm 0.01$ | $25.7 \pm 2.6$ |
| 40 | $1.70 \pm 0.01$ | $30.0 \pm 2.6$ |

We have also performed a first test of cellular uptake in HEK (Human Embyonic Kidney) cells, with a solution of MNP-Rhodamine B complex ($\sim 10\ \mu M$). Images have been recorded 30 minutes after the addition of the solution by exploiting two photon excitation at 800 nm. The fluorescence emission of Rhodamine B was detected through 560/40 band pass filter at different times.

Analyzing the intensity of fluorescence within the cells as a function of acquisition time, an increase in intensity versus time is observed (fig 5.17). The fluorescence intensity starts to increase after about 10 minutes. The free rhodamine, has shorter time internalization; this it means that also MNP-Rhodamine B complex was internalized into cells and the Rhodamine B remained free is very few. Obviously this is a preliminary result,

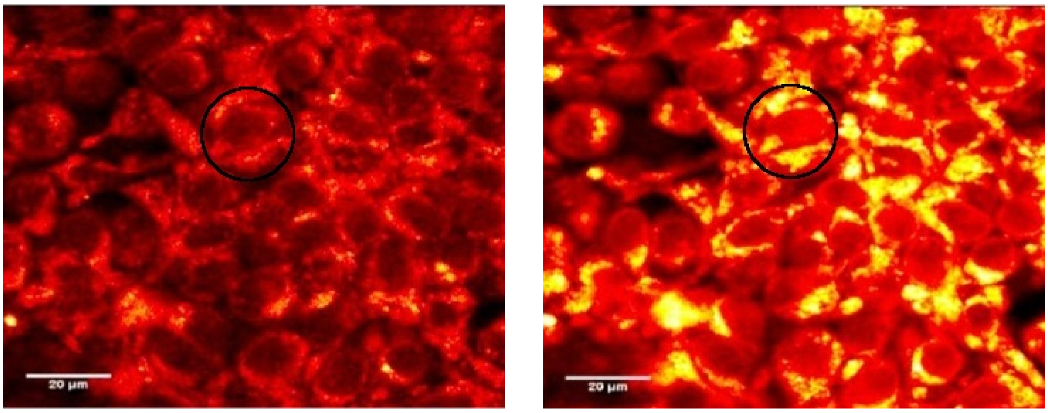

Figure 5.16: The images refer to fluorescence emission of Rhodamine B after incubation at t = 0 (on the left) and t = 30 min with RhB-MNP in HEK, respectively.

which provides only qualitative information, but it bodes well for future developments.

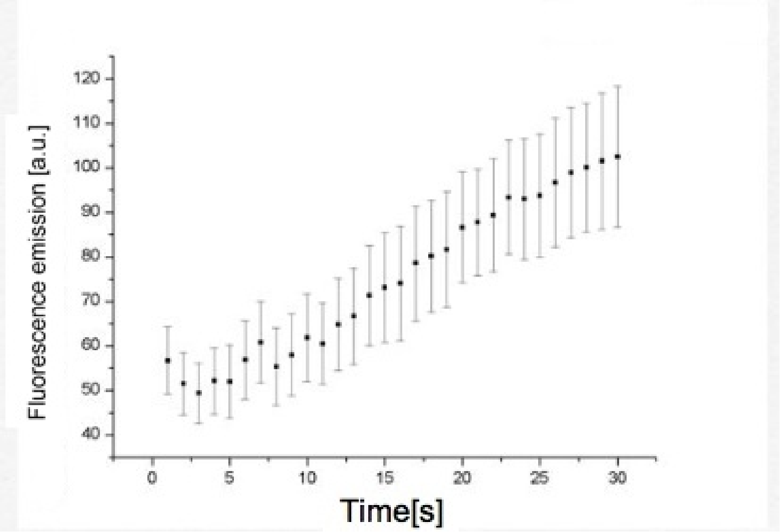

Figure 5.17: Fluorescence intensity of Rhodamine B versus acquisition time quantified on ROI (black circle in fig. 5.16).

## 5.2 Photothermal effect of gold Nanorods

Application of heat to inhibit or destroy specific cells is a well-known concept for the treatment of cancer. Generally, a non-invasive method to destroy tumor cells by heat is referred to as thermotherapy or hyperthermia. The increase in the target zone may be generated with a variety of heating sources, including infrared lamps, ultrasound, radio frequency sources and lasers. The processes mentioned, however, have the problem of not limiting the heat generated to a defined and specific area of target tissue. In photodynamic therapy greater specificity is obtained by ensuring that the target tissue, for example a tumour, is infiltrated with a photoabsorbing dye, and then laser irradiation is used [17]. As mentioned earlier, gold nanorods have properties which make them very attractive candidates for photothermal therapy. Although spherical gold nanoparticles do exhibit plasmon resonance, they have several limitations: not only is the efficiency of heating comparatively low but the wavelength at which the resonance mode occurs is in the mid-visible and therefore outside of the "tissue window". These limitations can be overcome by the use of gold nanorods since there are more efficient converters of light to thermal energy and of course the wavelength at which the plasmonic heating is a maximum can be tuned to the tissue window. In combination, these properties should decrease the damage to healthy cells during photothermal therapy. These principles have recently been test by in vitro studies in which the nanorods have been functionalized with specific targeting molecules, found on the membrane of target cells, and then irradiated. For example, Huff and co-workers conjugated folate ligands with oligoethyleneglycol onto gold nanorods. The folate conjugated gold nanorods were selectively bound to KB cancer cells (a tumor cell line derived from oral epithelium) which led to photothermal damage on cell membranes following laser irradiation.

### 5.2.1 Global and Local Temperatures

To measure the temperature rise of a solution of gold NR, irradiated with a IR laser at 800 nm, we have again used a thermo camera (manca modello), that measures the intensity of a radiation in the far infrared (7.5 $\mu m$ - 13 $\mu m$) (ThermaCAM SC 3000, FLIR Systems). The solution of gold NRs (C $\sim$ 5 nM) is placed in a plastic well and irradiated with IR laser pulse; the thermo camera is positioned on a support at distance of 0.5 m. Figure 5.18 shows heating (10 min) and cooling of gold NR in solution at different power levels; figure 5.19 shows the solution of nanorods at different irradiation times.

By interpolation we have obtained a limit temperature of 305.8 $\pm$ 0.2 K .

We have also measured heating of gold nanoparticles (NP, r = 30 nm), milliQ water ($H_2O$), magnetic nanoparticles (MNP, $Fe_3O_4$) and gold nanobranched (NB, see Chapter 4).

The table 5.4 shows the results; in particular, to use gold NRs excited with IR excitation (pulsed or CW mode) provides a rise in temperature sufficient to lead a cell to apoptosis, minimizing the irradiation of biological tissue surrounding the treatment area.

As with the magnetic nanoparticles, we have tried to measure the local temperature on the surface of gold nanorods. Gold nanorod-dye complex is based on electrostatic

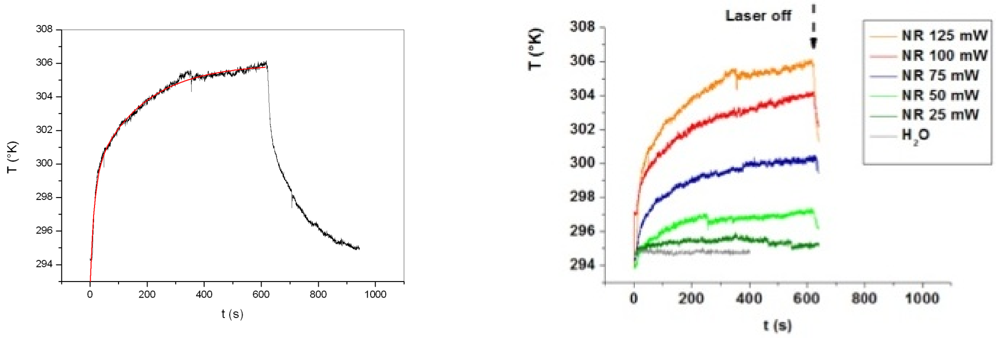

Figure 5.18: Up: heating of NR in solutions with P = 125 mW interpolated with an exponential function. Down: heating of NR with different power.

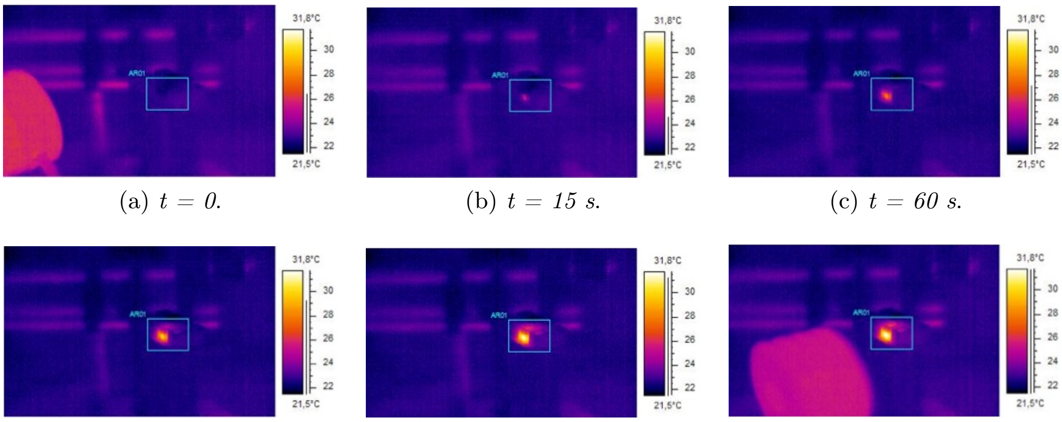

(a) $t = 0.$ (b) $t = 15\ s.$ (c) $t = 60\ s.$

(d) $t = 120\ s.$ (e) $t = 180\ s.$ (f) $t = 600\ s.$

Figure 5.19: Gold nanorods in solution heated with IR laser with P = 125 mW captured with thermocamera at different times.

bound between negative and positive charged polyelectrolyte, and the NPs.

Since gold nanorods stabilized with CTAB show strong cytotoxicity, polyelectrolyte coating was used in order to enable in-vivo application of the sensor. Moreover multiple polyelectrolyte layers avoid a "direct" interaction between gold nanoparticles and fluorophores, which could result in fluorophore damage or quenching of the dye fluorescence emission by resonant energy transfer. The functionalization was performed as reported in the following; about 10 mL of as prepared NRs was centrifuged twice at 5000 rpm for 10 min, the super-

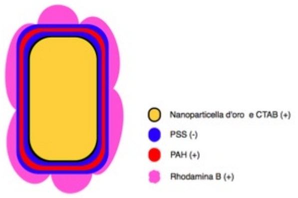

Figure 5.20: NR - layers - Rhodamine B construct.

Table 5.4: Temperature increase at equilibrium

| Power | NR | | | MNP | NP | NB | $H_2O$ |
|---|---|---|---|---|---|---|---|
| | Pulse | CW | Argon | | | | |
| 25 | 1 | - | - | - | 0.3 | - | - |
| 50 | 3 | 5.8 | - | - | - | - | - |
| 75 | 6 | 6.8 | 3.1 | - | - | - | - |
| 100 | 7 | - | - | - | - | 8.5 | - |
| 117 | | 9.8 | - | - | - | - | - |
| 125 | 12 | - | - | 5.8 | 1.2 | - | 0.2 |

Table 5.5: $\zeta$-potential as a function of the number of PSS-PAH layers adsorbed to the GNRs.

| Layer | $\zeta$-potential (mV) |
|---|---|
| PSS | - 36 ± 4 |
| PAH | + 12 ± 7 |
| PSS | - 26 ± 2 |
| Rhodamine B | + 49.7 ± 0.5 |

natant was discarded, and the precipitate was redispersed in 5 mL milliQ. Subsequently, it was added dropwise to 5 mL of the negative charged polyelectrolite PSS (2 g/L) aqueous solution. After 1 h adsorption time, it was centrifuged twice at 5000 rpm to remove excess polyelectrolyte and dispersed in 5 mL deionized water. Finally, the PSS-coated GNRs were added dropwise to 5 mL of the positive charged polyelectrolyte PAH (2 g/L) aqueous solution. After 1 h, it was centrifuged twice at 5000 rpm to remove excess polyelectrolyte and dispersed in 5 mL of deionized water. The procedure was iterated and a second layer of PSS was added. In order to obtain the NP-dye complex, the NPs ($\sim$ 500 pM) were added dropwise to 5 mL Rhodamine-B solution (5 nM). Finally, the solution was centrifuged at 5000 rpm to remove excess unbound dye molecules. Zeta potentials ($\zeta$) were measured to follow of the NPs charge of bioconjugates. The $\zeta$-potential after the adsorption of each layer is reported in table 5.5.

In order to follow the change in lifetime of Rhodamine B bound to the nanoparticles as a function of local temperature solution of nanorods-Rhodamine B complex heated. Initially, we have analyzed only Rhodamine B and the nanorod-Rhodamine B construct. The sample was irradiated with IR pulse laser at 800 nm (power 50 mW) and we have captured a series of fluorescence traces (30 s each) (see fig. 5.21).

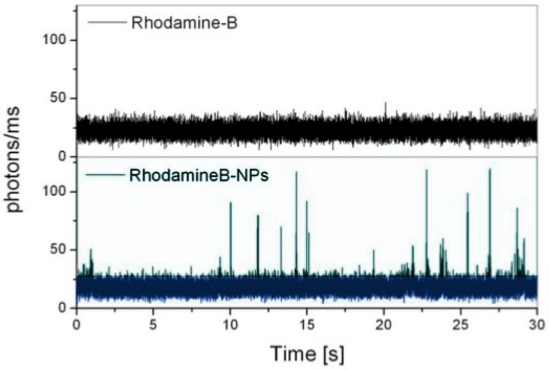

Figure 5.21: Fluorescence traces of Rhodamine B and gold nanorod-Rhodamine B complex.

When the tracks were analyzed by taking into account only the background (fig. 5.21 side blu) the lifetime was obtained of Rhodamine B free, on the other hand when the bursts (fig. 5.21 side green) were considered the average lifetime of nanorod-Rhodamine B construct was measured. In this case we do not expect any change in temperature of the sample and in the lifetime of the fluorophore. From the analysis of traces of fluorescence we have obtained the following average lifetime for the background ($\tau_B$) and bursts ($\tau_b$):

Table 5.6: Average lifetime of nanorods-fluorophore complex at room temperature.

| $\tau_B$ (ns) | $\tau_b$ (ns) |
|---|---|
| $1.93 \pm 0.06$ | $1.27 \pm 0.05$ |

On the bursts the lifetime is shorter than the lifetime of free Rhodamine B because we have the contribution of both the nanorod that of Rhodamine B. In particular, this lifetime was fitted to double exponential functions with fractional intensities, $f_1$ and $f_2 = 1 - f_1$, and relaxation times, $\tau_1$ and $\tau_2$. From this analysis the average lifetime was also computed as:

$$\langle \tau \rangle = f_1 \tau_1 + f_2 \tau_2 \tag{5.12}$$

where $\tau_1 \approx 400$ ps was ascribed to the NRs lifetime, while $\tau_2 \approx 1$ - 3 ns is due to the Rhodamine B dye lifetime. Then, we have heated the sample on a hotplate until 50 °C; when turned off the hotplate we have acquired decays of fluorescence every 30 seconds. Since $\tau_1$ does not change with temperature we can analyze only lifetime of Rhodamine B $\tau_2$ (table 5.7).

The lifetime of the background and the bursts provides us informations about global

Table 5.7: Average lifetime of Rhodamine B at different times. The temperature were obtained by eq. 5.11

| time (s) | Background | | Burst | |
|---|---|---|---|---|
| | $\tau$ (ns) | Temperature (°C) | $\tau_2$ (ns) | Temperature (°C) |
| 0 | $1.45 \pm 0.07$ | $34.1 \pm 2.5$ | $1.26 \pm 0.03$ | $40.5 \pm 2.1$ |
| 30 | $1.52 \pm 0.08$ | $31.7 \pm 2.5$ | $1.56 \pm 0.04$ | $30.2 \pm 2.4$ |
| 60 | $1.61 \pm 0.08$ | $28.8 \pm 2.7$ | $1.51 \pm 0.04$ | $32.0 \pm 2.7$ |
| 90 | $1.77 \pm 0.09$ | $23.1 \pm 2.8$ | $1.56 \pm 0.1$ | $30.5 \pm 2.6$ |
| 120 | $1.90 \pm 0.09$ | $18.7 \pm 2.9$ | $1.89 \pm 0.05$ | $18.8 \pm 2.7$ |

Table 5.8: Number of burst and increase in temperature of gold NR in solutions.

| $\lambda_{exc}$ | Numbers of burst | $\Delta T$ |
|---|---|---|
| 760 | $11 \pm 3$ | $4.6 \pm 0.2$ |
| 780 | $58 \pm 15$ | $5.6 \pm 0.2$ |
| 800 | $112 \pm 23$ | $7.8 \pm 0.2$ |
| 820 | $60 \pm 8$ | $5.4 \pm 0.2$ |
| 840 | $8 \pm 2$ | $4.6 \pm 0.2$ |

or local temperature of sample. In both cases the trend of the lifetimes is consistent with what expect; indeed the solution cools and thus increases the lifetime of Rhodamine B. This means that the Rhodamine bound, even when to the nanoparticle surface respond properly to the temperature change. In the next future, we will use two laser beams: the first (CW) to induce heating of the nanoparticles, the second (pulsed) to excite the Rhodamine in the complex and then measure the lifetime (and then the temperature).
To this point we have verified the dependence of the thermal release by excitation wavelength of the nanorod-Rhodamine B construct. The sample was irradiated with 50 mW at wavelengths between 760 nm and 840 nm at intervals of 20 nm. For each wavelength we collected ten fluorescence traces for 30 s. The fluorescence emission of gold nanorods is maximum when they are excited in their plasmonic absorption peak, an effect that results in a larger number of bursts in the fluorescence traces. When exciting the sample at 800 nm we observed several bursts of fluorescence (rate $\approx$ 300 kHz), while moving away from this wavelength the excitation peaks become rare (rate $\approx$ 50 kHz) (see table 5.8 and fig. 5.22). For comparison, we measured the increase in temperature of nanorods in solution at the power (100 mW) but at different wavelengths of excitation (with the thermo camera). Again, we observed a larger heat release when gold NR were excited at 800 nm (see table 5.8).

Localized heating is generally considered the primary mechanism of photoactivated

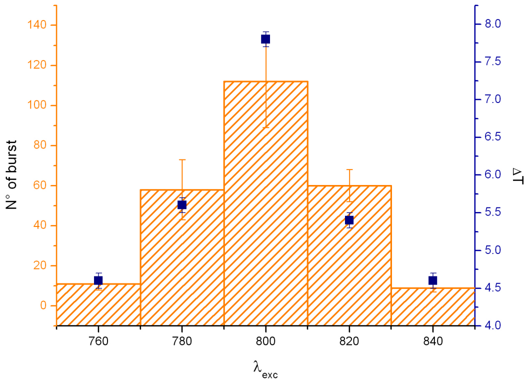

Figure 5.22: The histogram and blue points represents the number of bursts and the increases in temperature as a function of excitation wavelength of the nanorod-Rhodamine B constructs, respectively.

injury inflicted by gold NRs. We have made experiments in murine macrophages that have internalized GNR ($\sim 100\ \mu g$/ml) exposed to IR laser.

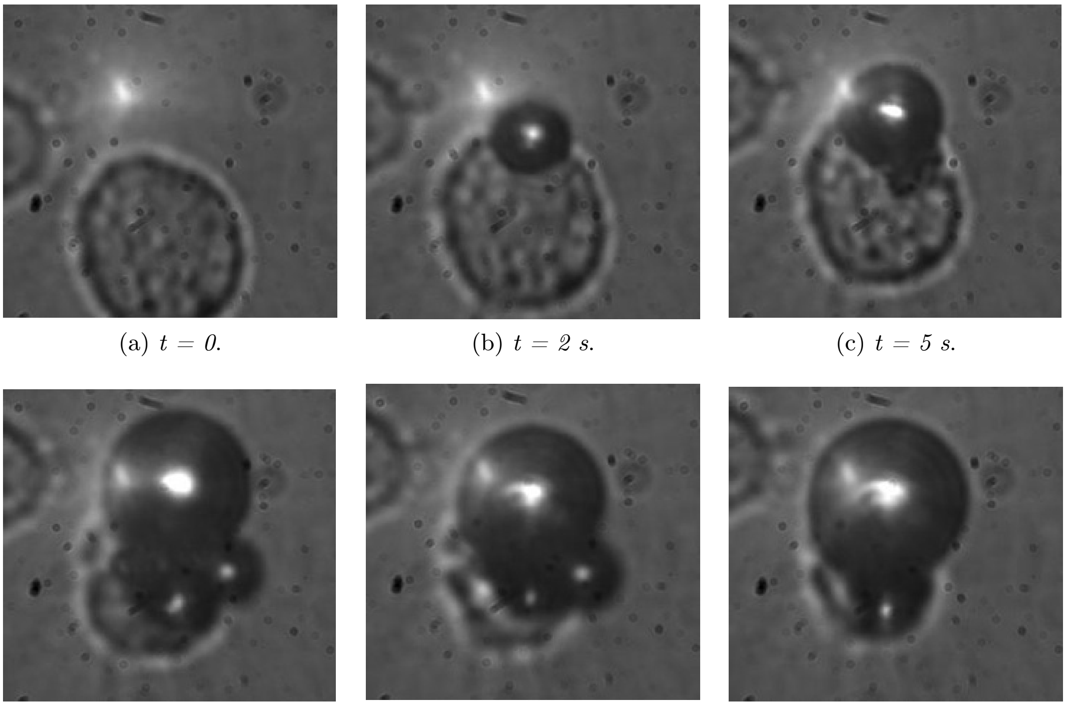
(a) $t$ = *0.* (b) $t$ = *2 s.* (c) $t$ = *5 s.*

(d) $t$ = *10 s.* (e) $t$ = *15 s.* (f) $t$ = *20 s.*

Figure 5.23: Images of macrophages and NR exposed to IR laser (50 mW), captured with CCD camera.

The experiments were performed with the help of a CCD camera, which visualizes the image of the sample in transmission. We have performed a series of experiments in which macrophages were irradiated with a pulsed laser in a wide range of laser power (30 mW - 1 W). Irradiating the NR treated macrophage (with NRs) at the power of 10 mW, cell death (detected from the disruption of the membrane) occurs within a few minutes, while non-treated macrophages require irradiation times that exceed tens of minutes at the power of 1 W.

Figure 5.23 shows some frames of the sequence realized with P = 50 mW; as it can be see, it was enough to irradiate the macrophage few seconds before the membrane start destroying. This means that NRs internalized in macrophage, release heat destroying the cell upon laser irradiation. The cell apoptosis could be well induced at even laser irradiation powers.

### 5.2.2 Computational model for heating processes

With the increasing interest in the use of NPs, several levels of heat transfer modeling have been developed in support of experimental studies. These models have helped to gain a better understanding of the thermal processes involved in laser heating of NPs. Figure 5.24 summarizes various processes associated to ultrafast laser heating of metal nanoparticles.

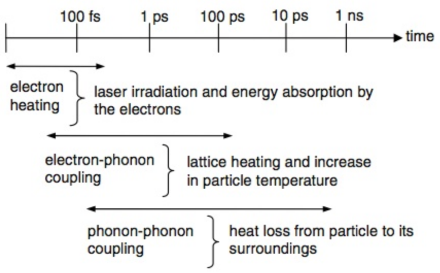

Figure 5.24: Time scales of the fundamental processes in ultrafast laser heating of metal nanoparticles before the onset of particle melting or bubble formation in the surrounding aqueous solution.

When the particle is exposed to an ultrafast laser pulse, free electrons absorb the energy of photons, increases by their kinetic energy. These energetic electrons, having initially a nonequilibrium distribution of energy, are relaxed through electron - electron scattering on the order of 10 - 50 fs. Practically, there is no energy exchange occurring between electrons and phonons within these time scales and electrons stay in high energy levels. Once the electron cloud raises its temperature, there is an imbalance in the energy level of the electrons and the crystal lattice. The energy transfer to the lattice excites vibrations of the lattice about their mean position. This leads to thermal expansion of the nanoparticle. As the lattice starts to vibrate, there is an energy imbalance between the phonons in the nanoparticle lattice and the surrounding fluid. This energy imbalance relaxes through phonon-phonon interactions. Because the energy dissipation is the order of hundreds of picoseconds, conduction dominates other potential modes of heat transfer. At pulse fluences of 5 $Jm^2$ (for example), using the linear absorption coefficient of water at 760 nm di $\mu_a = 2.5\ m^{-1}$, the energy absorbed is 12.5 $\mu Jcm^{-3}$ per pulse. This estimate indicates that the temperature increase is less than $10^{-6}$ °C at the focal point; heating contributions due to direct linear and nonlinear absorption of photons by water can be neglected. Furthermore, our peak irradiance is $\sim$ 2 GW $cm^{-2}$, which is approximately two orders of magnitude below the threshold of 260 GW $cm^{-2}$ necessary to create a single free electron during the pulse duration. However, enhancement of electromagnetic fields in the near-field of the nanorods, could lead to:

- modification of nanorod geometry through near-field ablation
- free electron generation in water leading to its additional heating and thus creation of bubbles.

The equations describing the transient temperature response of the gold nanorod in a water medium under the influence of laser radiation are given by equations 5.13 and 5.14. Since the conduction electrons in the gold nanorod absorb the laser pulse energy, a two-temperature model (TTM) is used to describe the laser absorption and the subsequent electron-phonon equilibration in the particle:

$$C_e \frac{dT_e}{dt} = g(T_l - T_e) + \frac{E_{abs}}{V_p \cdot \tau_{pulse}} \tag{5.13}$$

$$C_l \frac{dT_l}{dt} = g(T_e - T_l) - \frac{\dot{Q}_W}{V_p} \quad T_l < T_m \tag{5.14}$$

Here $V_p$ is the volume of the particle, $\tau_{pulse}$ is the laser pulse width, $T_e$ and $T_l$ are the electron and lattice temperatures of the particle, $E_{abs}$ is the laser pulse energy absorbed by the particle, g is the coupling factor to calculate the heat transfer rate from electrons to the lattice, $\dot{Q}_W$ is the rate of heat loss from the particle to its surroundings, $C_e$ and $C_l$ are the heat capacities for electrons and the lattice of bulk gold respectively. Table 5.9 summarizes the specific values of the thermophysical properties.

We have modeled the heating of a single gold nanorods (100 nm × 50 nm) in water medium irradiated by 250 fs laser pulses at the peak plasmonic frequency centered at 800 nm. The laser energy absorbed by the particle depends on the laser fluence, $F_{pulse}$, and the absorption cross-section of nanorod, $\sigma_{abs}$, according to:

$$E_{abs} = \sigma_{abs} \cdot F_{pulse} = \sigma_{abs} \frac{P_p \cdot d_c \cdot \tau_{pulse}}{\pi \omega_0^2} \tag{5.15}$$

Table 5.9: Thermophysical properties of gold and water.

| | Gold (bulk) properties | |
|---|---|---|
| Properties | | values |
| Electron heat capacity | $C_e$ $(\mathrm{J\,m^{-3}\,K^{-1}})$ | $70.0 \cdot T_e$ |
| Specific heat of lattice | $C_l$ $(\mathrm{J\,m^{-3}\,K^{-1}})$ | $\rho_{gold}[109.579 + 0.128T-$<br>$-3.4 \cdot 10^{-4}T^2 + 5.24 \cdot 10^{-7}T^4-$<br>$-3.93 \cdot 10^{-10}T^4 + 1.17 \cdot 10{-}13T^5]$ |
| Thermal conductivity | $k_{Au}$ $(\mathrm{W\,m^{-1}\,K^{-1}})$ | 320 |
| Electron-lattice coupling factor | g $(\mathrm{W\,m^{-3}\,K^{-1}})$ | $20 \cdot 10^{16}$ |
| Density | $\rho_{Au}$ $(\mathrm{Kg\,m^{-3}})$ | 19300 |
| Melting temperature | $T_m(K)$ | 1337 |
| | Water properties at standard conditions | |
| Density | $\rho_w$ $(\mathrm{Kg\,m^{-3}})$ | 1000 |
| Specific heat | $c_{p,w}$ $(\mathrm{kJ\,Kg^{-1}\,K^{-1}})$ | 4.184 |
| Thermal conductivity | k $(\mathrm{W\,m^{-1}\,K^{-1}})$ | 0.61 |
| Critical temperature | $T_{c,\mathrm{H_2O}}$ (K) | 647 |
| | At the gold/water interface | |
| Thermal conductance | $G_{int}$ $(\mathrm{W\,m^{-2}\,K^{-1}})$ | $105 \cdot 10^6$ |

where $P_p$ is average power of laser, $d_c = 1/(f_R \cdot \tau_{pulse})$ is the duty cycle and $\omega_0$ is the beam waist. When noble metal NPs are exposed to light at their plasmonic frequency, the effective absorption cross-section will be much larger than the geometrical one. The absorption cross-section area was calculated using the ADDA code package according to the discrete dipole approximation method which has been extensively reviewed in the literature. A NR with $d_{max} = 100$ nm and $d_{min} = 50$ nm, was modelled as a spherically capped cylinder (figure 5.25).

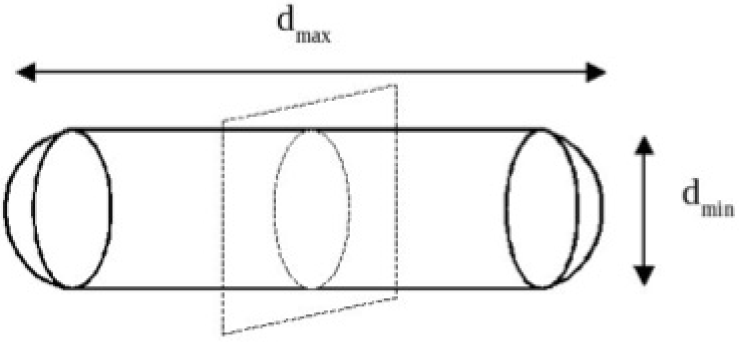

Figure 5.25: Approximation of the geometry used in simulations

When excited with a pulsed laser at $\lambda_{exc} = 800$ nm, with $\omega_0 = 0.58\ \mu m$, using a number of dipoles N = 2336, we obtain the following values:

Table 5.10: Parameters obtained from ADDA code package.

| | |
|---|---|
| $\sigma_{ext} = 197546.625\ nm^2$ | extinction cross section |
| $Q_{ext} = 3.803$ | extinction efficiency |
| $\sigma_{abs} = 37672.994\ nm^2$ | absorption cross section |
| $Q_{abs} = 0.725$ | extinction efficiency |
| $\sigma_{sca} = \sigma_{ext} - \sigma_{abs} = 159873.631\ nm^2$ | scattering cross section |
| $\eta_{abs} = Q_{abs}/Q_{ext} = 0.19$ | efficiency ratio |

The rate of heat loss from the particle to its surroundings in equation 5.14 is calculated by taking into account the interface conductance given by:

$$\dot{Q}_w = A_{surf} G_{int} (T_l - T_{w,s}) \tag{5.16}$$

where $T_{w,s}$ is the water temperature at the particle surface, $G_{int}$ is the thermal conductance at the particle/fluid interface and $A_{surf}$ is the surface area of the particle. The thermal conductance $G_{int}$ relates the temperature drop at an interface to the heat flux crossing the interface and constitutes the coupling parameter between a particle and surrounding medium energy equations. The particle geometry, a cylindrical nanorod, allows us to use a model to describe the energy transfer within the surrounding medium. Therefore, the energy conservation equation for water can be written in cylindrical coordinates as

$$\rho_w c_{p,w} \frac{\partial T_w}{\partial t} = \frac{\partial}{\partial z}\left(k \frac{\partial T_w}{\partial z}\right) + \frac{1}{r}\frac{\partial}{\partial r}\left(kr \frac{\partial T_w}{\partial r}\right) \tag{5.17}$$

For a differential equation of the type:

$$\frac{dy(x)}{dx} = f(x, y) \tag{5.18}$$

numerical integration is performed resulting in a recursive algorithm, which allows to approximate the value $y_n$ (to n-th step), from the value $y_{n-1}$. Equations 5.13 and 5.14 were integrated using Runge-Kutta Method, that belongs to the class of algorithms for resolution of ordinary differential equations (ODE). For a system of two linear differential equations similar to TTM:

$$\begin{aligned} \frac{d}{dt}x &= f(x, y, t) \quad \text{con} \quad x(t_0) \equiv x_0 \\ \frac{d}{dt}y &= g(x, y, t) \quad \text{con} \quad y(t_0) \equiv y_0 \end{aligned} \tag{5.19}$$

the integration algorithm provides approximations

$$x_{i+1} \cong x_i + \frac{1}{6}(k_1 + 2k_2 + 2k_3 + k_4) \quad \text{with} \begin{cases} k_1 = hf(x_i, y_i, t_i) \\ k_2 = hf\left(x_i + \frac{k_1}{2}, y_i + \frac{l_1}{2}, t_i + \frac{h}{2}\right) \\ k_3 = hf\left(x_i + \frac{k_2}{2}, y_i + \frac{l_2}{2}, t_i + \frac{h}{2}\right) \\ k_4 = hf\left(x_i + \frac{k_1}{2}, y_i + \frac{l_1}{2}, t_i + \frac{h}{2}\right) \end{cases}$$

$$y_{i+1} \cong y_i + \frac{1}{6}(l_1 + 2l_2 + 2l_3 + l_4) \quad \text{with} \begin{cases} l_1 = hg(x_i, y_i, t_i) \\ l_2 = hg\left(x_i + \frac{k_1}{2}, y_i + \frac{l_1}{2}, t_i + \frac{h}{2}\right) \\ l_3 = hg\left(x_i + \frac{k_2}{2}, y_i + \frac{l_2}{2}, t_i + \frac{h}{2}\right) \\ l_4 = hg\left(x_i + \frac{k_1}{2}, y_i + \frac{l_1}{2}, t_i + \frac{h}{2}\right) \end{cases}$$

As can be seen from the equation 5.17, uniform temperatures are assumed across the particle (Uniform Temperature Approximation, UTA). This assumption is quite appropriate considering the characteristic length scales of the problem. The calculated Biot number, $B_i = G_{int} \cdot L_c/k_{Au}$, is about $10^{-3}$. The characteristic length, $L_c$, is defined as the volume of the particle divided by the surface area of the particle and $k_{Au}$ is the thermal conductivity of bulk gold. Typically the lumped capacitance model of transient heat transfer introduces less than 5 % error for Biot numbers smaller than 0.1. In our case, a nanorod of 100 nm × 50 nm has $V_p$ = 163624.62 $nm^3$, $A_{surf}$ = 4463.49 $nm^2$, $R_{eq}$ = 33.73 $nm$; then $B_i$ = 1.718 $\cdot 10^{-2}$ and we can use UTA.
To integrate the equations of temperature $T_e$ and $T_l$ the water temperature $T_w$ is needed as determined by the heat flow to the surrounding medium. We have made a spatial map of the temperature as a function of the distance from the axis of symmetry of the NR, using a cartesian grid for the cylindrical part and polar grid for spherical one (figure 5.26 a). The temperature in the water was determined by a balance of heat flux input $Q_{int}$ and output $Q_{out}$, through internal and external surfaces (with area $A_{pi}$ and $A_{pe}$) of each cell (figure 5.26 b), at each time step dt; if we denote $f_i$ the temperature of water in the cells i-th:

$$Q_{in} = \frac{A_{pi}k}{pix} \frac{(f_{i-1} - f_i)dt}{\rho_w c_{p,w} V_{pix}} \tag{5.20}$$

$$Q_{out} = \frac{A_{pe}k}{pix} \frac{(f_i - f_{i+1})dt}{\rho_w c_{p,w} V_{pix}} \tag{5.21}$$

where pix indicates the unit of length to the map.

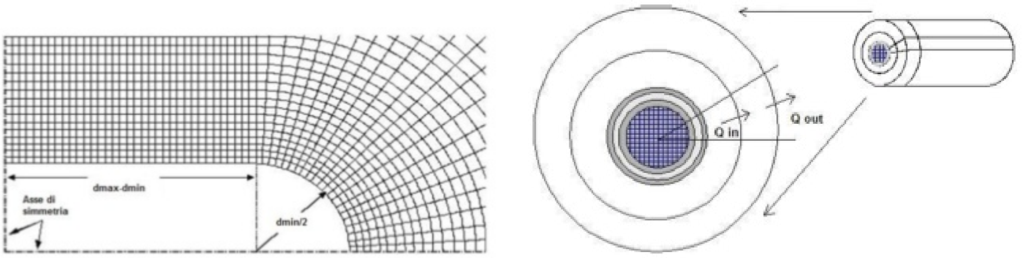

(a) *Grid simulation.* (b) *Transversal section.*

Figure 5.26: Computational domain and nanorod dimensions

The cylindrical symmetry of the propagation of heat is included in the volume of the voxel, which varies depending on the distance from the axis. We have chosen the values of pix = 0.25 - 5 nm and dt = 2.5 for time the step. The coating of polyelectrolytes around the NR, has been modelled by three thin layers ($\sim$ 1 nm) with low thermal conductivity and specific heat. For the thermodynamic parameters of the layers have used the values summarized in table 5.11

Table 5.11: Thermodynamic parameters of the polyelectrolites

| | PSS | PAH |
|---|---|---|
| $c_p$ ($\mathrm{J\,m^{-3}\,K^{-1}}$) | 1200 | 1200 |
| k ($\mathrm{W\,m^{-1}\,K^{-1}}$) | 0.5 | 0.3 |
| $\rho$ ($\mathrm{Kg\,m^{-3}}$) | 1500 | 1500 |

**Simulations single beam** We have simulated the heating of a NR (100 nm × 50 nm) in water medium irradiated by $\tau_p = 250$ fs, a beam waist $\omega_0 = 0.58$ $\mu m$ and $P_p = 25$ mW (figure 5.27 a). The maximum temperature reached by the lattice is $T_{l,Max} = 607$ K, 21 ps after the first laser pulse (figure 5.27 b), while the water reaches $T_{w,Max} = 495$ K at t = 136 ps (figure 5.27 c). These temperatures are lower than the melting temperature of gold nanorod ($T_{m,\mathrm{Au}} = 1337$ K) and the critical temperature of water ($T_{c,\mathrm{H_2O}} = 647$ K); then we can exclude rod-to-sphere shape change and formation of vapor bubbles, respectively.

The total heat obtained after a subsequent pulse delayed of $\tau_R = 12.5$ ns from the first; then the total heat obtained in an experiment with a pulsed laser, for times very large compared to time step ($\sim$ 10 ns), is the result of thermodynamic equilibrium between the heat provided and the dissipated. For $P_p = 25$ mW, with a box of 40 nm (distance

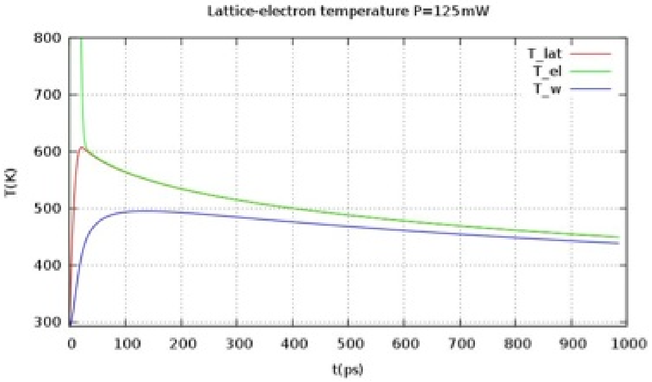

(a) *Temporal evolution after first pulse .*

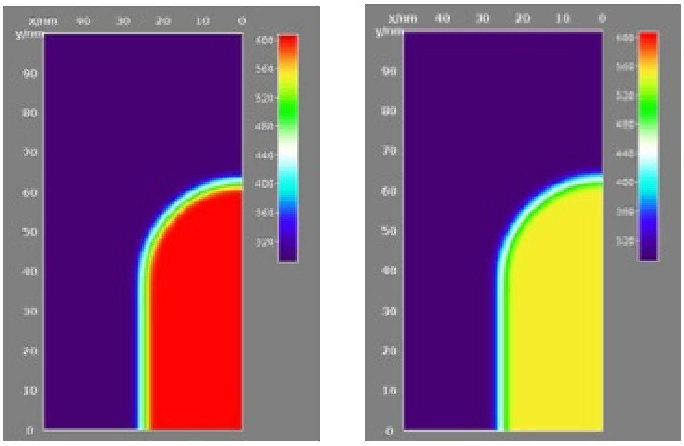

(b) *Thermal map at t = 21 ps.* (c) *Thermal map at t = 136 ps.*

Figure 5.27: Temperatures $T_e$, $T_l$ and $T_w$ for NR 100 nm × 50 nm after pulse with P = 25 mW and box size 40 nm.

between the cylinder axis and surround, figure 5.25), just few tens of ns are needed to reach the maximum temperature of the lattice, despite of the arrival of successive pulses (figure 5.28 a). We have simulated heating experiments with different excitation powers, reported in table 5.12, determining the temperature of the RhB at a distance of three layers from surface metal species and then what calculated the expected average lifetime of fluorescent probe.

We have considered the envelope of the minimum temperature of the RhB at different power, obtaining the temperatures shown in figure 5.28 b. As mentioned above, PTT (PhotoThermal Therapy) is based on the induction of localized hyperthermia to cause cellular necrosis. We can then use the TTM (Two-Temperature Model) to determine the efficacy of a possible therapy with GNR considered in the simulations. We have

Table 5.12: Simulated temperatures of NR-RhB complex at different power

| P (mW) | T (K) | $\tau_{RhB}$ (ns) |
|---|---|---|
| 4 | 297.3 | 1.7 |
| 8 | 301.6 | 1.6 |
| 15 | 309.2 | 1.4 |
| 20 | 314.7 | 1.2 |
| 25 | 320.2 | 1.0 |

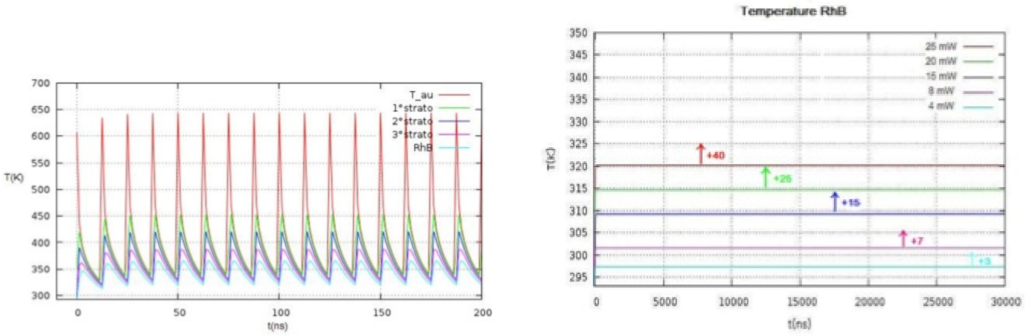

(a) *Temporal evolution of temperatures* $T_l$*,* $T_w$ *and* $T_{layers}$*.*

(b) *Minimum temperatures of RhB with different power.*

Figure 5.28: Results obtained from simulations for NR 100 nm × 50 nm with P = 25 mW and box size 40 nm.

studied heating induced by an exogenous object, with high absorption cross section for infrared radiation, in a volume of variable size of tissue equivalent material. Essentially, we consider cases in which a single GNR radiates heat in a box of only water and in the presence of adipose tissue. To determine the effectiveness of inducing hyperthermic death of an exogenous object within a cell, two modes of excitation with pulsed and continuous laser are considered.The continuous excitation, induces a gradual heating in time, which leads to changes in the shapes of the gold NP (reshaping), due to melting of the upper layers, even at temperatures of 40 % of $T_{m,\text{Au}} = 1337$ K. To determine the temperature rise of the boxes as different sizes were used, with a boundary condition on the last cell: temperature T $= T_{amb}$. This condition can represent a heat source at $T_{amb}$ placed at different distances from the object that radiates heat. This model can represent, for example, the presence of blood vessels in the proximity of a tissue in a real experiment of hyperthermia. It was found that the pulsed excitation temperature reached equilibrium depends by on the size of the simulation box, since increasing the distance from the source, increases the thermal capacity to storage heat in the irradiated volume.

The radial temperature evolution at different times (figure 5.29), shows temperature oscillations in the case of pulsed laser. Figure 5.27 shows transient temperature profiles for the duration of 200 ns, during which the nanorods are excited by several laser pulses arriving at 12.5 ns time intervals from an 80 MHz repetition rate laser system. Two considerations result from the calculations. First, both the temperatures of the electron and lattice of the particle and that of the water on the particle surface equilibrates before the arrival of the next pulse. This result is rather trivial, considering the relaxation times of 50 and 500 ps for electron-phonon and phonon-phonon (across the particle and water interface) couplings, respectively. Second, the overall temperature rises rapidly during the first few pulses and thereafter no significant temperature increase is observed.

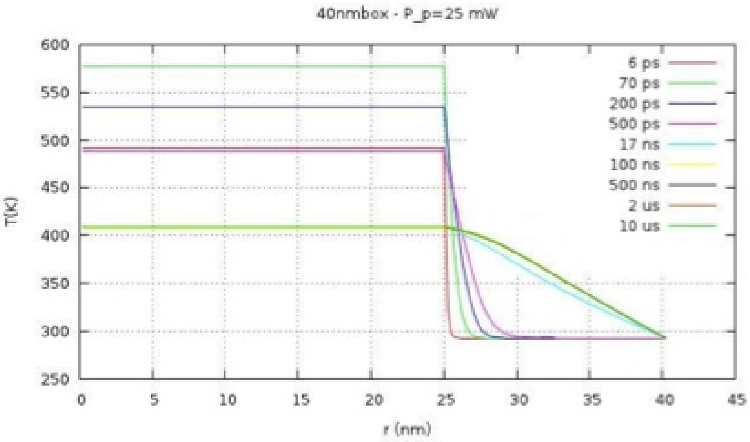

Figure 5.29: Temperature profiles at different times after laser exposure ( P = 25 mW) as a function of radial distance with box size 40 nm.

**Simulations double beam** We have also performed simulations with double excitation: a continuous laser to induce heating and pulse laser to measure lifetime of RhB. In particular, we have used a continuous power $P_{cw} = 18$ mW and a $P_p = 4$ mW, with a box size between 40 nm to 625 nm (table 5.13).

We have considered the case of a layer of adipose tissue, with different thickness and thermal conductivity ($k_{adi} = 0.2\,\mathrm{W\,m^{-1}\,K^{-1}}$) and specific heat ($c_{p,adi} = 2000\,\mathrm{J\,Kg^{-1}\,K^{-1}}$) lower than water. For example, considering a 1 $\mu m$ lipid layer sandwiched between a layer of 1 $\mu m$ of water and GNR, at 50 $\mu s$ of experiment with only continuous beam $P_{cw} = 90$ mW the temperatures reached are the same (fig. 5.30).

The contribution of the two types of excitation is thus determined by the detailed process of heating. The continuous beam provides steadily energy for all time, during of the experiment, as opposed to the pulsed beam. In this case, $\dot{Q}_W$ follows the fluctuating

Table 5.13: Temperature of NR as function of box size, with $P_{cw} = 18$ mW + $P_p = 4$ mW.

| box size (nm) | T (K) |
|---|---|
| 40 | 410 |
| 55 | 570 |
| 145 | 830 |
| 625 | 1210 |

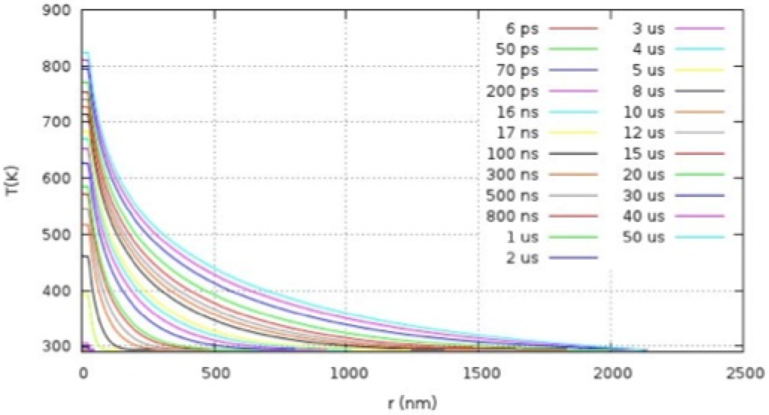

Figure 5.30: Temperature profiles at different times after laser exposure ( $P_{cw} = 90$ mW) as a function of radial distance with box size 2 $\mu m$

temperature of the lattice, until to level around the stationary value, while in continuous excitation, the rate of heat flow follows an asymptotic behavior to thermodynamic equilibrium. In the case of only pulsed excitation there is the cooling of the NR in successive pulses, contrary to what happens when there is the continuous excitation because the efficiency of dissipation of the absorbed energy, reaches an equilibrium value higher than in the case of pulsed excitation. In conclusion, for better performance to induce heat and then measure lifetime of Rhodamine B we need two laser sources: a continuous laser to induce heating and pulse laser to measure lifetime of RhB. However, the single-beam simulations show that the increase obtained is more than enough to perform thermal therapy and for this reason (for the moment) the experimental measurements were conducted on the single beam.

# Bibliography

[1] Van der Zee. Annals Oncol., 13, 1173-1184, 2002.

[2] Rowe-Horwege. Encyclopedia of Medical Devices and Instrumentation. John Wiley and Sons; New York, 42-46, 2006.

[3] M. H. Falk and R. D. Issels. Int. J. Hyperthermia, 17(1), 1-18, 2001.

[4] M. W. Dewhirst, E. J. Ozimek and J. Gross. Radiology, 137(3), 811-817, 1980.

[5] M. W. Dewhirst, F. A. Gibbs and R. B. Roemer. Clinical Radiation Oncology. Churchill Livingstone; New York, 2000.

[6] P. Wust, B. Hildebrandt, G. Sreenivasa, B. Rau, J. Gellermann, H. Riess, R. Felix and P. M. Schlang. Lancet Oncol., 3, 487, 2002.

[7] W. Andra, C. G. d'Ambly, R. Hergt, I. Hilger and A. Kaiser. J. Magn. Magn. Mater., 194, 197, 1999.

[8] A. Jordan, R. Scholz, P. Wust, H. Fahling and R. Felix. J. Magn. Mag. Mater., 201, 413, 1999.

[9] I. Hilger, R. Hergt and W. A. Kaiser. Invest. Radiol., 35, 170, 2000.

[10] R. Hiergeist, W. Andra, N. Buske, R. Hergt, I. Hilger, U. Richter and W. Kaiser. J. Magn. Magn. Mater., 201, 420, 1999.

[11] L. Neel. C. R. Acad. Sci., 228, 664, 1949.

[12] D. C. F. Chan, D. B. Kirpotin and P. A. Bunn. J. Magn. Magn. Mater., 122, 374, 1993.

[13] I. Hilger, K. Fruhauf, W. Andra, R. Hiergeist, R. Hergt and W. A. Kaiser. Acad. Radiol., 9, 198, 2002.

[14] R. E. Rosensweig. J. Magn. Magn. Mater., 252, 370, 2002.

[15] P. Ciarlet. The Finite Element method for Elliptic Problems. North Holland, 1978.

[16] T. M. Hagstrom and H. B. Keller. Mathematics of Computation, 48, 449-470, 1987.

[17] D. Pissuwan, M. S. Valenzuela and M. B. Cortie. Biotechnology and Genetic Engineering Reviews, 25, 93-112, 2008.

## Chapter 6

# Conclusion

> Recitar! Mentre preso dal delirio,
> non so piú quel che dico, e quel
> che faccio!
>
> R. Leoncavallo, Pagliacci
> R. Leoncavallo

This thesis has shown some potential applications of nanoparticles in the biomedical field. Gold nanorods have a variety of real or potential applications in medical diagnosis and therapeutic treatments as a result of their particularly attractive combination of optical, physical and chemical properties. A specificity of effect and a selective targeting can be achieved generally by functionalization of the gold nanorods with a biomolecule. In principle, antibody-conjugated gold nanorods can be used to target specific cell lines, or even invading organisms, either for diagnostic of therapeutic purposes. According to these considerations I have developed our project on three lines related to the use of gold nanoparticles for sensing and non linear imaging.

## 6.1 Summary of Results

I have tested the possibility to use a hybrid nanodevice composed of spherically symmetric gold NPs (10 and 5 nm diameter) functionalized with specific antibodies to detect tiny amounts of proteins. Focusing on the p53 wt recognition and using fluorescein isothiocyanate (FITC) dyes (ratio [Ab]:[FITC] = 3:1), I have shown that p53 in vitro detection can be performed by this device by exploiting the linear decrease of the FITC excited state lifetime, measured on the fluorescence bursts, with the p53 concentration and the detection until 5 pM, better of the ELISA test. The nanodevice proposed has been also tested for recognition specificity again some model globular proteins BSA (bovine serum albumin), Lysozyme and BLG (beta-lattoglobuline)) and applied to p53 detection in p53 positive and p53 null cell lines. The analysis reported here proves that the gold NP-FITC-$Ab_{p53}$ nano-constructs can be used to detect the presence of traces of p53 proteins in TCEs (Total Cell Extracts) opening the way to their application to in-vivo studies. In particular, an original way to analyze the data has been proposed which to take into account the observed anti-correlation between the burst size and the FITC lifetime value in order to single out the p53-( NP-FITC-$Ab_{p53}$) complexes from auto-fluorescence and un-bound NP-FITC-$Ab_{p53}$ crystals, and to measure the fraction of the small lifetime events to get an estimate of the p53 concentration in the TCEs (Total Cell Extracts).

A second line of interest has been the characterization of non spherically symmetric gold nanoparticles, in order to exploit their luminescence properties for cellular imaging. In particular, I have studied asymmetric branched gold nanoparticles obtained by using for the first time a zwitterionic surfactant, laurylsulphobetaine (LSB), in the seed growth method approach. LSB concentration in the growth solution allows to control the dimension of the NPs and the LSPR (longitudinal surface plasmon resonance) position, that can be tuned in the 700-1100 nm Near Infrared range. The samples have been analyzed with several techniques to obtain a complete characterization: by counting the data obtained through the absorption spectra in the UV-Visible region, the TEM images of the solutions, FCS (Fluorescence Correlation Spectroscopy) and DLS (Dynamic Light Scattering) experiments, I achieved an exhaustive picture of the nanoparticles shape and dimensions (length $\sim$ 50 - 100 nm, width $\sim$ 8 nm). In particular, three different populations have been found: nanospheres with diameter lower than 20 nm, nanostars characterized by large trapezoidal branches, and asymmetric branched nanoparticles with high aspect ratio ($\approx$ 4-5). For comparison, the same properties have been followed in the case of gold nanorods obtained by CTAB synthesized (length $\sim$ 50 nm, width $\sim$ 12 nm) The dependence of the luminescence intensity on the incident light intensity for samples realized with LSB and CTAB was studied, checking the quadratic dependence and therefore the two photon nature of the observed luminescence (TPL). By measuring the luminescence spectra for different excitation wavelengths with a spectral CCD camera, it has been possible to obtain the excitation spectra of the NPs, very similar to the extinction spectra: this result is indicative of the role played by surface plasmons in TPL. As a further characterization, the dependence of the TPL on polarization angle of the incident radiation was checked.

The use of gold anisotropic nanoparticles as bright contrast agents for two-photon luminescence (TPL) imaging of cells was also explored. I have detected the toxic concentration; by viability $> 80$ % we find $\sim 80$ $\mu g$/ml for 0.35 M LSB, $\sim 5$ $\mu g$/ml for 0.5 M LSB and $\sim 100$ $\mu g$/ml for 0.2 M CTAB. I have therefore investigated the ability of the NPs to permeate cell membranes, by measuring the cellular uptake from HEK (Human Embryonic Kidney) and macrophages cells, at the conditions of minimum toxicity obtained above. NPs has been internalized in the cytoplasm of HEK and macrophages cells but not in the nuclei; otherwise pegylated gold NPs are invisible to the immune system and none cellular uptake was detected.

Finally, I have demonstrated the potential use of NPs, gold nanorods and magnetic nanoparticles (MNPs), for selective thermal therapy of cancer cells using a near-infrared low energy laser and an AC magnetic field, respectively. I have first evaluated the increase in temperature of NR and MNP solutions, using a direct visualization by means of a sensitive thermocamera. I have developed a novel hybrid metal-organic system, based on NPs complexed to RhB by electrostatic adsorption on multiple poly-electrolyte layers, in order to detect the local temperature around the NP induced by the laser heating. RhodamineB-NPs assay is able to play the role of molecular thermometer and can be tested in-vivo to evaluate the damage temperature of tumoral cells. The hybrid sensor in fact can be used for imaging and photothermal purposes at the same time: the infrared laser radiation can excite both Rhodamine-B and TLP from the gold NRs in order to visualize the internalization of the sensor in cells and the same radiation can heat the NRs, damaging the tumor cell.

This study has revealed the properties of local heating and global gold nanoparticles and magnetic nanoparticles and allows us to evaluate the benefits and limitations of both. The nanorods at concentrations of a few nM causes a temperature increase sufficient to induce apoptosis ($\Delta T \sim 7\,^{\circ}$C at $P_{exc} = 100$ mW ). However, it is necessary to take into consideration the length of penetration of laser light, in our case I have a penetration depth in epithelial tissue of 200 $\mu m$. So now the use of NRs can be applied to superficial tumors (melanoma); to bring the laser deeper into is resorting to the use of microendoscopic gradient index. The use of MNPs does not present problems instead of the magnetic field penetration into the tissues, because the frequencies used are $10^6$ times lower compared to those of infrared light. These frequencies, however, transfer less power, and this translates into the need for greater concentration ([NR]:[MNP] $\approx$ 1: $10^5$) to obtain a sufficient rise in temperature ($\Delta T \sim 13\,^{\circ}$C at $B_{exc} = 0.032$ T).

## 6.2 Future Developments

Multifunctionality is the key advantage of nanoparticles over traditional approaches. Targeting ligands, imaging labels, therapeutic drugs, and many other functional moieties can all be integrated into the nanoparticle conjugate to allow for targeted molecular imaging and molecular therapy of cancer. Gold nanoparticles are unique because of its intriguing optical properties which can be exploited for both imaging and therapeutic applications. The future of nanomedicine lies in multifunctional nanoplatforms which combine both therapeutic components and multimodality imaging. The ultimate goal is that nanoparticle-based agents can allow for efficient, specific in vivo delivery of drugs without systemic toxicity, and the dose delivered as well as the therapeutic efficacy can be accurately measured noninvasively over time.

# Collaborations and Manuscripts

List of the collaborations that have made possible this PhD work:

- General Chemistry Department, University of Pavia, Pavia, Italy In particular the group of Prof. P.Pallavicini
- Environment and Territory Department, University of Milano-Bicocca, Milan, Italy. In particular Dr. P.Mantecca, Dr. G.Soncini and Dr. Maurizio Gualtieri (Polaris Project)
- CE.RI.COL., CEntro RIcerche COLorobbia, Vinci (FI), Italy. In Particular Dr. Baldi and Dr. Mazzantini.

List of the manuscripts related to this PhD work:

- S. Freddi, L. D'Alfonso, M. Collini, M. Caccia, L. Sironi, G. Tallarida, S. Caprioli, and G. Chirico. "Excited-state lifetime assay for protein detection on gold colloids-fluorophore complexes.", J. Phys. Chem. C, 113:27222730, Jan 2009.
- L.Sironi, S.Freddi, L.D'Alfonso, M. Collini, T. Gorletta, S.Soddu, G.Chirico. "P53 detection by fluorescence lifetime on a hybrid fluorescein-isothiocyanate gold nanosensor", J.Biomedical nanotechnology, 5: 683-691, 2009.
- L. Sironi, S. Freddi, L. D'Alfonso, M. Collini, T. Gorletta, S. Soddu, G. Chirico. "In-vitro and in-vivo detection of p53 by fluorescence lifetime on a hybrid FITC-gold nanosensor", Proceedings of the SPIE, 7574:757403, 2010
- P. Pallavicini, G. Chirico, M. Collini, G. Dacarro, A. Dona', L. D'Alfonso, A. Falqui, Y. A. Diaz-Fernandez, S. Freddi, B. Garofalo, A. Genovese, L. Sironi and A. Taglietti. "Synthesis of branched gold nanoparticles with tunable Near-InfraRed Localized Surface Plasmon Resonance using a zwitterionic surfactant for the seed-growth method", Chem. Commun., 2011, doi: 10.1039/C0CC02682D

- R. Bacchetta, N. Santo, U. Fascio, E. Moschini, S. Freddi, G. Chirico, M. Camatina and P. Mantecca. Nano-sized CuO, $TiO_2$ and ZnO affect Xenopus laevis development. Nanotoxicology, 201, doi:10.3109/17435390.2011.5796341

Appendix **A**

# Appendix

During the experiments we employed basically two excitation sources and two types of photo-detectors depending on the applications. We briefly discuss some of the technical details.

## A.1 Laser sources

The sources used are pulsed infrared lasers from Spectra Physics (Mountain View, CA): the Tsunami passive cavity and the Mai Tai infrared laser. Both are femtosecond pulsed lasers with a spectral range between 700 and 1000 nm and in both cases a 532 nm CW laser (Millennia X, Spectra Physics, CA) is used as a pump. The characteristics of the two optical resonant cavities are almost identical because the Mai Tai is the compact and fully automatized version of the combination of a Millennia solid state laser and a Tsunami cavity. Hereafter, there is the description of the main components of these excitation systems. Both are equipped with an active modelocking system that guarantees the production of pulses nominally 100 fs width at a repetition rate of 80 MHz (i.e. at the output of the cavity one measures a pulse every 12.5 ns).

### A.1.1 Millennia

The Millennia laser is based on two diode lasers whose emission is used to pump a solid state laser based on Nd$^{3+}$ ions crystalline matrix doped with yttrium vanadate (Nd:YVO4). The output wavelength is 1064 nm and is converted to a 532 nm green beam by means of a second harmonic generation process that takes place in a lithium triborate (LBO) non-linear crystal. The output is composed by a unique transverse mode (equivalent to the $TEM_{00}$ of a conventional laser) with a pseudo-Gaussian intensity profile characterized by an high ellipticity that has to be corrected before entering the IR mode-locked cavity. This is made by means of a couple of anamorph prisms mounted to an angle near to the Brewster angle with respect to incident beam (figure A.1a). The emission from the diode laser is perfectly superimposed to the absorption band of the Nd$^{3+}$ ion allowing a good coupling between the pump and the active medium (figure A.1b).

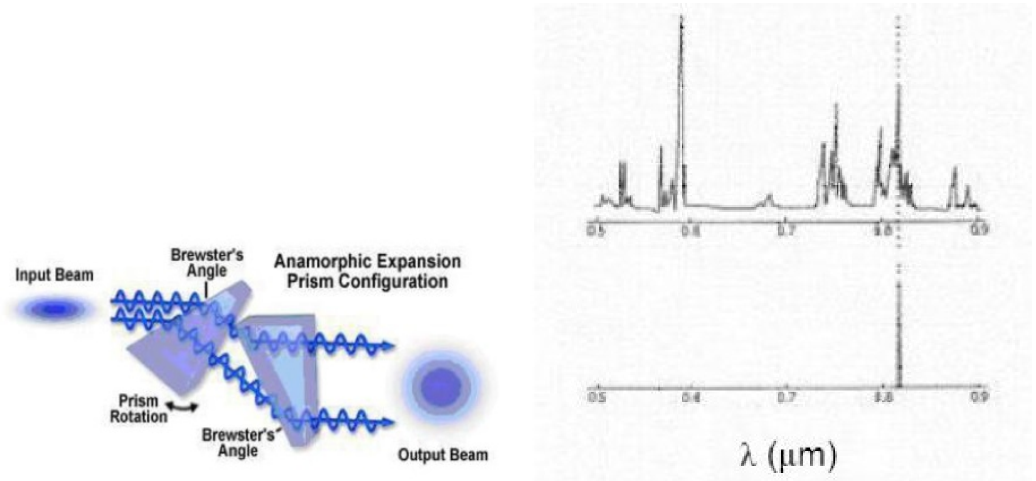

(a) *Correction of the beam ellipticity by means of two prism at the Brewster angle.*

(b) *Panel up: Absorption spectum for the* Nd$^{3+}$ *ion. Panel down: Emission spectrum of the diode pump laser.*

Figure A.1: Properties of Millennia.

The active medium neodymium has the principal absorption band in the red and near infrared region of the electromagnetic spectrum. The generation of the 532 nm green pump beam is made by means of the second harmonic generation process that takes place in a LBO crystal. This material is preferred to others with higher non-linear coefficient, because it is possible to optimize the conversion efficiency of LBO simply varying the working temperature. A dichroic mirror reflects back in the cavity the first harmonic from the solid state laser and allows the 532 nm beam to be sent in the Tsunami optical cavity. Since the intensity of the second harmonic radiation depends on the square of the first harmonic power it is possible to obtain a high conversion efficiency increasing the power of pump.Unluckily a solid state pumped by a diode laser gives rise to a chaotic emission characterized by high intensity fluctuations that avoid the application of the source to scientific experiments. These instabilities are mainly due to the non-linear coupling of the axial modes in the sum frequency (i.e. second harmonic generation) process. In the Tsunami and Mai Tai the problem is overcome by adopting the so called QMAD (Quiet Multi Axial Mode Doubling) solution: that employs many axial modes allowing the oscillation of more than 100 longitudinal modes. In this way the power of each axial mode is o low that none of them reaches the pick power needed to induce high non-linear loses. The non-linear coupling terms are therefore mediated with the effect that the second harmonic emission presents a very low noise (figure A.2).

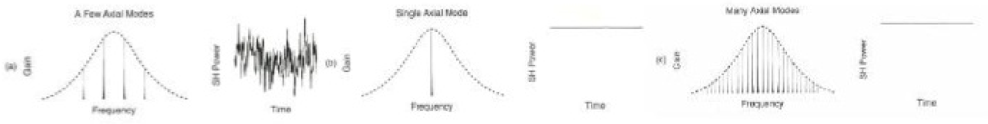

Figure A.2: Quiet Multi-Axial mode-Doubling (QMAD). Panel (a): intracavity frequency doubling in a laser with a few axial modes produces large amplitude fluctuations in the second harmonic output resulting from non-linear coupling of the modes through sum frequency mixing. Panel (b): single frequency solution forces oscillation on a single axis mode to eliminate mode coupling. Panel (c): QMAD solution produces oscillation on many axial modes, effectively averaging the non-linear coupling terms to provide highly stable second harmonic output.

### A.1.2 Titanium-Sapphire (TI-Sa) optical resonant cavity

The 532 nm beam from the Millennia is used to pump a Titanium-Sapphire (Ti-Sa) rod that gives rise to the IR output of the laser system. The Ti-Sa is a crystalline solid obtained introducing $Ti_2O_3$ into a solution of $Al_2O_3$ allowing the substitution of a little amount of $Al^{3+}$ ions with $Ti^{3+}$ ions. The $Ti^{3+}$ electronic configuration can be represented as two distinct energy levels with a great broadening caused by the presence of many vibrational levels (figure A.3).

The result is a broaden absorption band between 400 and 600 nm. The fluorescence emission is within 600 and 1000 nm and is due to the fact that the transition occur between vibrational levels whose energy lies between that of the excited and that of the ground state. However the laser coherent emission is possible only for wavelength $\lambda > 670$ nm since for $\lambda < 670$ nm the emission band is superimposed to the absorption one giving rise to auto-absorption processes that reduce the efficiency of the fluorescence emission.

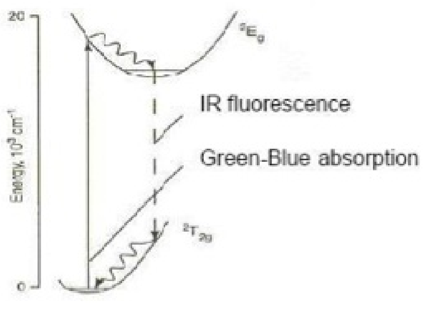

Figure A.3: Energy level structure for $Ti^{3+}$ ion in Sapphire.

### Wavelength selection

Since the Ti-Sa rod is birefringent, lasing is obtained when the c-axis of the rod is aligned coplanar to the polarization of the electric field in the cavity. The chamber that hosts the rod orients the rod surfaces at Brewster's angle and allows the c-axis to be coplanar to the electric field vector. The output $\lambda$ is variable within 690-1000 nm by means of a system of four prisms and a slit. The prisms create a region in the cavity where the different $\lambda$ are separated and provide also the compensation of the group velocity dispersion. The slit, located in the central part of the four prisms arrangement, allows to select the desired $\lambda$.

### Pulse width

The temporal duration or the pulses depends principally on three factors:

1. the properties of the Ti-Sa rod
2. the size of the optical cavity
3. the selected wavelength

It is possible to control the pulse width by changing the Group Velocity Dispersion (GVD) in the optical cavity. The material refraction index depends on $\lambda$, thus every color component travels along a particular direction with slightly different speed, giving rise to a temporal separation of the wavelength components present in the pulse: this phenomenon is called GVD dispersion. For GVD $\geq 0$ the red colors travel faster than the blue ones (figure A.4)

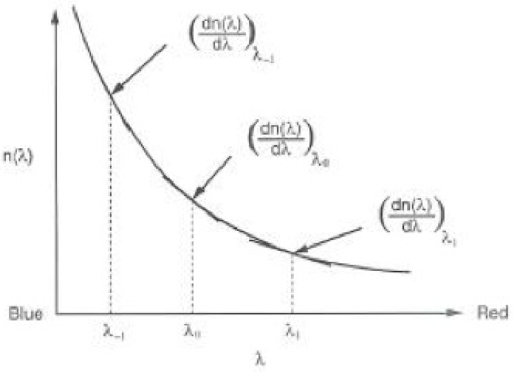

Figure A.4: Typical wavelength dependence of the refractive index of a material.

The GVD is related directly to the change of the group velocity versus the wavelength. By a simple computation one can demonstrate that the GVD is directly proportional to the second derivative of the refraction index versus the wavelength, $d^2n(\lambda)/d\lambda^2$. In the more general case we must refer to the change in the optical path instead to compute simply the change of the group velocity. For normal dispersion, the term $d^2n(\lambda)/d\lambda^2$ is positive and so is the GVD. The optical refractive components inside the resonant cavity create a positive GVD giving rise to a spread of the pulse. A compensation for the pulse spreading must be searched by thinking in terms of the optical path instead of the group velocity. The GVD is then defined as $d^2L(\lambda)/d\lambda^2$, where L is the optical path of the various wavelength components of the laser beam. The normal dispersion introduces a positive GVD, therefore, in order to keep the pulse short, it is necessary to introduce a negative GVD. Usually the negative GVD is obtained by means of an arrangement of two or four prisms. Varying the distance between the prisms, while keeping at a minimum the thickness of glass passed through by the beam, it is possible to have pulses with a time duration close to the minimal width $\cong$ 100 fs (Figure A.5). The minimum pulse width is limited by the width of the laser spectrum.

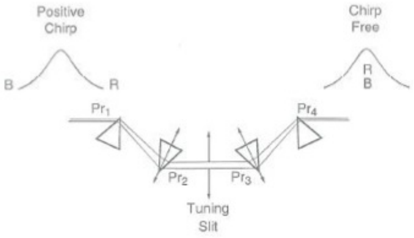

Figure A.5: Prisms sequence used for dispersion compensation. An input pulse with a positive chirp (red frequencies at the leading edge of the pulse) experiences a positive GVD (red frequencies have longer group delay time) in the prisms sequence. The net effect is that the prisms sequence compensates for the positive GVD and produces a pulse that has no chirp.

For the Tsunami optical resonant cavity the selection of output wavelength and the temporal characteristics of the pulses have to be checked by the operator while for the Mai Tai they are driven by a CVI written control program. This is the main difference between the two laser sources.

## A.2 Microscopes

The Tsunami and Mai Tai infrared laser are coupled to Nikon TE300 and Olympus BX51 microscopes, respectively. The firs is principally devoted to FCS and lifetime measurements, the second microscope has been employed for imaging experiments.

### A.2.1 Nikon TE300

The Nikon TE300 is an inverted optical microscope that collects the signal in epifluorescence geometry; the sample is placed on an (x,y) translational stage equipped with two DC electrical motors that allow macroscopic movements until 25 mm with a minimum $\Delta$ of 50 $\mu m$ and an accuracy of 0.1 $\mu m$. The sample stage has been modified in order to install a piezo-electric translator (x, y, z) cube (Figure A.6a) that allows micro-positioning on the sample with an accuracy of 50 nm and a maximum excursion of 100 $\mu m$.

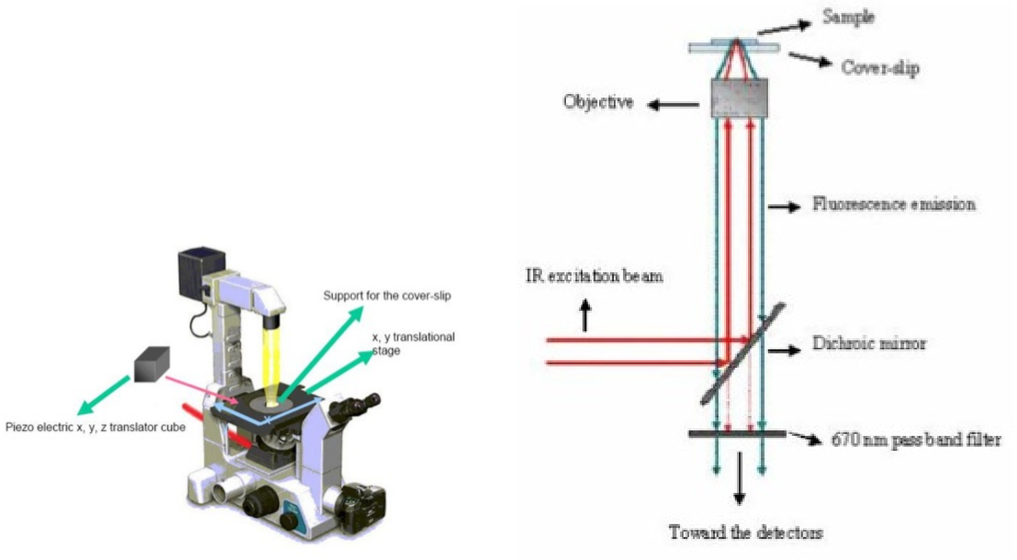

(a) *In the figure are underlined the modifications took in the experimental set-up: the position of the piezo electric translator cube, the translational stage and the support for the cover-slip.*

(b) *This simplified scheme explains the role of the dichroic mirror mounted.*

Figure A.6: Nikon TE300 microscope.

While conventional instruments (i.e. a spectrometer) collect the signal at 90° with respect to the direction of the excitation beam, in an epifluorescence microscope the objective has the double function of focusing the excitation beam and of collecting the fluorescence signal arising from the sample (Figure A.6b). In details: the excitation IR light enters the back aperture of the microscope and than encounters a dichroic mirror, mounted at 45° respect to the objective, (see Figure A.6b) that reflects the light toward the objective that focuses it on the sample. The fluorescence signal from the sample, once collected by the objective, passes through the dichroic and is sent to the detectors. In order to remove unwanted residual components of the IR excitation beam (due to reflections on the mechanical part of the TE300 and to the non-ideal behaviour of the dichroic mirror) and to select the desired detection wavelength, $\lambda_{em}$, the signal from the sample passes through a short pass filter with transmission T(%) 4-6 OD for $\lambda > 670$ nm and a pass band filter centered at the emission wavelength of the dye under investigation (for example employing Rhodamine 6G that present an emission maximum at 560 nm it is necessary to mount a filter centered at 560 nm with a full width at half maximum not higher than 40 nm, i.e. at 560 ± 40). The most important component of a microscope is the objective that is characterized by three parameters: the magnification, M, the immersion medium and particularly by the Numerical Aperture, N.A., defined as:

$$N.A. = ncos(\theta) \tag{A.1}$$

where n is the refractive index of the immersion liquid and $\theta$ is the semi-angle defined by the collection lens of the objective (Figure A.7); the larger is N.A., the better are the focusing and the collection efficiency of the signal.

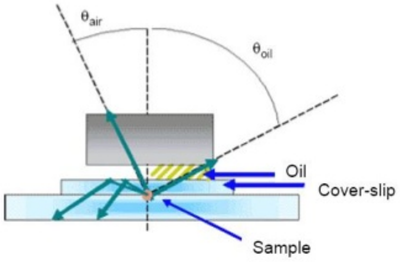

Figure A.7: Role of the immersion medium in order to achieve the index matching condition. In this figure are compared an air an oil immersion objectives.

This means that the $V_{ex}$ results smaller and the S/N ratio is enhanced. The immersion medium, usually water or oil (n = 1.33 and 1.5 respectively), is used to guarantee the correct index matching between the cover-slip and the sample in order to avoid total reflection of the fluorescence light along the optical path (Figure A.7). If total reflection happens, the collection efficiency results degraded because the effective numerical aperture is lower than the nominal N.A.. Our TE300 can be equipped with an oil immersion objective Nikon M = 100X, N.A. = 1.3 or with a water immersion Nikon objective M = 60X, N.A. = 1.2. Both guarantee a good collection efficiency and a good index matching with the cover-slip (n = 1.5) and the sample, usually water solutions or biological samples that present an index of refraction close to n = 1.33. Moreover it must be considered that it is of crucial importance to correctly fill the back aperture of the objective; in fact the divergence of a Gaussian beam apart from the beam waist is (FIgure A.8):

$$\theta = 2arctan\left(\frac{\omega(z)}{z}\right) \approx 2arctan\left(\frac{\lambda}{\pi\omega_0}\right) \tag{A.2}$$

will match $2\theta$ only if the back aperture is completely filled, otherwise $\theta$ and $\Theta$ result smaller and as a consequence the N.A. of the objective is not completely used and $V_{ex}$ results bigger with a lost of S/N ratio.

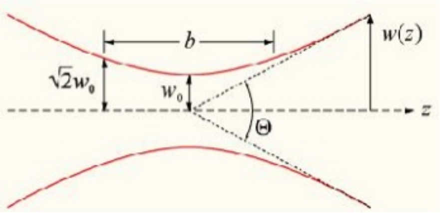

Figure A.8: Axial profile of a Gaussian beam in the proximity of the beam waist.

### A.2.2 Olympus BX51

The Olympus BX51 is an upright microscope that, as the Nikon TE300, collects the signal in epifluorescence (see Figure A.6) geometry. In our experimental set-up, the BX51 is equipped with a confocal scanning head (FV300) (see Figure A.9) modified in order to allow TPE. It mounts low pass filters in front of its PMT in order to clear the signal from the residuals of the excitation beam and the larger pin-hole was removed from the pin-hole wheel because TPE is intrinsically confocal. The scanning head has been used through the external PTM devices.

Figure A.9: Axial profile of a Gaussian beam in the proximity of the beam waist.

The IR incoming laser light enter the FV300 at right angle with respect to the visible lasers. All the laser beams are then sent to the galvo scanning mirrors that are mounted in front of the side aperture of the BX51. Before entering the main BX51 housing through the scanning lens, a visible/IR dichroic mirror can be mount to switch between the visible (confocal) and the IR (TPE) scanning mode. Once reflected in the microscope by the galvos, the excitation light may:

1. be directly focused onto the sample by means of the objective lens or
2. pass through a second visible/IR dichroic mirror and focused onto the sample by the objective lens.

The signal arising from the focus plane is collected by the same objective and the emission light is reflected by the second dichroic mirror and sent to the non-descanned unit where t is detected by the PTM devices external to the FV300 unit. The BX51 is equipped with a water immersion Olympus objective M = 20X, N.A. = 0.95 chosen because of its large working distance ($\cong$ 2 mm) and its relatively high numerical aperture. The galvo mirrors enables to collect image of maximum area of $720 \times 720$ $\mu m$ with different scanning modes and speeds.

## A.3 Detectors

The choice of the detectors depends on the experimental conditions. FCS relies on small fluctuations of the fluorescence signal around an average value and since each photon contributes to the whole statistics, it becomes very important to detect as many photons as possible. Single Photon Avalanche Diodes (SPAD) guarantee high single-photon detection efficiency and low dark current. Since they work close to the the breakdown bias, they allow each photon-generated carrier to be amplified by an avalanche current, resulting in an internal gain within the photo-diode, which increases the effective responsivity of the device making the SPAD very suitable for photo detection at low count rate (i.e. single photon regime). In MPM the main issue is to collect high resolution 3-dimensional images limiting the residence time per pixel in order to minimize the photo-damage. In scanning probe microscopy, where one wants to scan wide sample in few seconds, the Photo-Multiplier Tubes (PMT) are the most suitable detectors since they have typically large sensitive areas and allow therefore to collect simultaneously the signal coming from the whole scanned area. Hereafter we give some additional features of SPAD that has been used in this PhD report for the analysis of the fluctuations in terms of the correlation functions and of the histogram of the photon counting. The general characteristics of PMT can be found in several text-book and technical publications, and will not be discussed here.

### A.3.1 Single Photon Avalanche Diode (SPAD)

When a photon of enough energy hits the depletion zone of a photo-diode, practically an inversely biased p-n junction (Figure A.10), this zone may be the source of an electron-hole couple. The generated charge carriers will move in opposite directions under the influence of the electric field. Macroscopically the two current flows, generated by the electrons and the holes, have the same direction and they sum to generate a unique net current that once amplified gives a measure of the number of detected photons. We have to underline that a generic Photo-Diode (also known as PD) does not present a multiplication process: its gain is 1 and therefore it works well in situations where the flux of the incoming photons on the cathode is high.

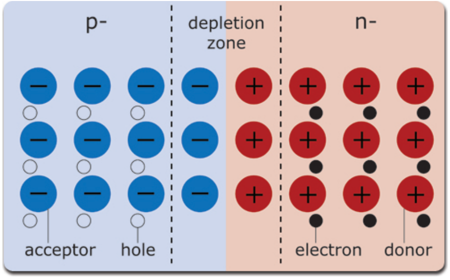

Figure A.10: Schematic representation of a p-n junction.

Unluckily in most applications high quantum efficiencies (30%), very low dark count levels ( $<$ 50 Hz) and high temporal resolutions (FWHM Å 1 ns) are required. The Avalanche Photo-Diode (APD) satisfies the first two requests because the electric field (the inversion polarization voltage is close to and less, in modulus, than the break-down value) applied to the couple of charge carriers generated by the photon is very high: during their migration toward the electrodes the electrons and the holes take a kinetic energy that enable them to create new couple of carriers just by collision. Since the empty zone in the p-n junction is wide enough also the two new carriers generated by the collision can create another couple giving rise to a process called avalanche multiplication. The macroscopic current generated by this process will be proportional to the flux of detected photons. In the case of experiments where one wants to reach the limit of the single detected photon, a time resolution and a single photon sensitivity as high as possible are needed. For this purpose the most suitable detector is the SPAD (Single Photon Avalanche Diode). These devices use an inversion polarization voltage larger than the breakdown one. Therefore the current growth after one photon detection is exponential and not controlled leading to an infinite gain. Due to this feature the SPAD can be considered similar to a Geiger detector because its output is not proportional to the input; the SPAD are just events' detector.

Modern SPAD modules are endowed with an active quenching circuit that is able to lower the output current after each count (i.e. the so called dead-time). It can be sketched as a large load resistance ($\cong$ 500 k$\Omega$) in series with the diode output circuit. The large voltage drop that occurs when the pulse current drops on this load resistance lowers reverse bias at the leads of the PD, the avalanche process is stopped and the system is brought back to the initial condition. The Perkin Helmer SPAD model SPCM-AQR-14 (Figure A.11) have a circular silicon photodiode of 180 $\mu m$ of diameter; because the gap between the conduction and valence bands is 1.12 eV, these SPADs enable to detect photons with $\lambda$ < 1100 nm.

Figure A.11: A Perkin Helmer SPAD model SPCM-AQR-14.

The two most important characteristics of the SPAD are the photo-sensitiveness, S, and the quantum efficiency, QE, defined respectively as the ratio between the produced photo-current, I, and the incident radiant power, P, and the ratio between the number of photons at the anode, $N_{anode}$, and the incoming photons, $N_{incoming}$:

$$S = \frac{I}{R} \tag{A.3}$$

$$QE = \frac{dN_{anode}}{dN_{incoming}} \tag{A.4}$$

Since the radiant power at the cathode is:

$$P = \frac{dN_{incoming}E}{dt} \tag{A.5}$$

where E is the energy of any incident photon and t is the time they need to reach the detector, and since the photo-current:

$$I = \frac{dN_{anode}e^{-}}{dt} \tag{A.6}$$

where $e^{-}$ is the electron charge, these two parameters are strictly connected as:

$$QE = \frac{SE}{e^{-}} \tag{A.7}$$

The QE for the Perkin Helmer SPCM-AQR-14 can be considered constant overall the sensitive area with a numerical value ≅ 70% (Figure A.12, panel A). It depends also on the detected (Figure A.12, panel B) and guarantees good performance in the range 400 - 1060 nm with its best at 700 nm. The typical maximum rate of the SPCM-AQR-14, certified by the company is ≅ 15 - 16 MHz (however non-linearity occurs already at 2 MHz) and the dark current is ≅ 50 Hz. The dead-time is ≅ 50 ns and the time resolution is limited by a jitter ∼ 350 ps. Finally, as can be see from Figure A.12, panel C, the QE of a SPAD is higher than that of a PMT in the green-red region and this is the reason that make us to prefer SPADs instead of PMTs.

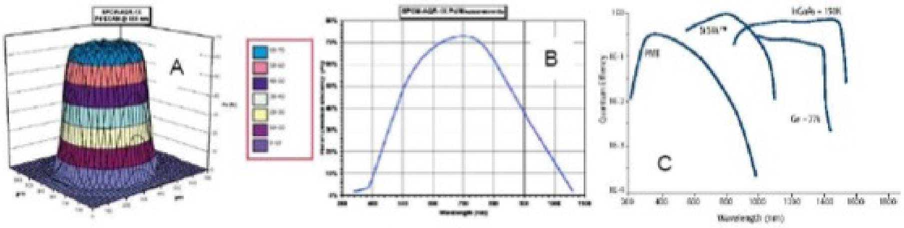

Figure A.12: Panel A: detection efficiency as a function of the position in the sensible area. Panel B: quantum efficiency as a function of $\lambda$. Panel C: comparison within the quantum efficiency of SPAD (indicated as Si-slik), PMT, Ge based detectors and InGaAs based detectors.

## A.4 TimeHarp and Symphotime softwares

Fluorescence lifetime measurements in the time domain are commonly performed by means of Time-Correlated Single Photon Counting (TCSPC). This is a histogramming technique based on precise timing and time binned counting of single photons emitted on pulsed laser excitation. However, in many fluorescence applications it is of great interest not only to obtain the fluorescence lifetime(s) of the fluorophore(s) but to record and use more information on the fluorescence dynamics. This is most often the case when very few or even single molecules are observed.For instance,single molecules flushed through capillaries (e.g in DNA analysis applications) will emit short bursts of fluorescence, that are of interest for further analysis. The resulting fluorescence intensity dynamics on a time scale of milliseconds can be used to identify single molecule transits and to discriminate these events against background noise. The desired capturing of the complete fluorescence dynamics can be achieved by recording the arrival times of all photons relative to the beginning of the experiment (time tag), in addition to the picosecond TCSPC timing relative to the excitation pulses. This is called Time-Tagged Time-Resolved (TTTR) mode [2]. Figure 6.49 shows the relationship of the time figures involved. As in conventional TCSPC, a picosecond timing between laser pulse and fluorescence photon is obtained. In addition to that, a coarser timing is performed on each photon with respect to the start of the experiment. This is done with a digital counter running at typically 50 or 100 ns resolution. Even though this is much higher than what most applications mentioned above would require, modern hardware provides this resolution at no extra cost. Since the TCSPC timing typically covers the time scale just below 100 ns, it is indeed sensible to chose a time tag resolution just above that range, thereby covering the whole time range for ultimate exibility in further data analysis. The two timing figures (TCSPC time and Time Tag) are stored as one photon record. In order to work efficiently with current host computers, the photon record is typically chosen as a 32 bit structure. A hardware First In First Out (FIFO) buffer for 128 k events is used to average out bursts and deliver a moderate constant data rate to the host interface. This way sufficient continuous sustained transfer rates are possible in real-time. Each single photon is recorded with its global arrival time and the 'microscopic' delay time with respect to the corresponding laser pulse. While the microscopic delay time is evaluated in lifetime related analyses, the global arrival time can be used to form a fluorescence intensity time trace, making all related analyses possible, like FCS, on / off analysis etc. In addition this global arrival time can be synchronized with external trigger pulses, for example the line or frame clock of LSMs, which is used to extract imaging information. Intensity traces over time, as traditionally obtained from Multi-Channel-Scalers (MCS), are obtained from TTTR data by evaluating only the time tags of the photon records.

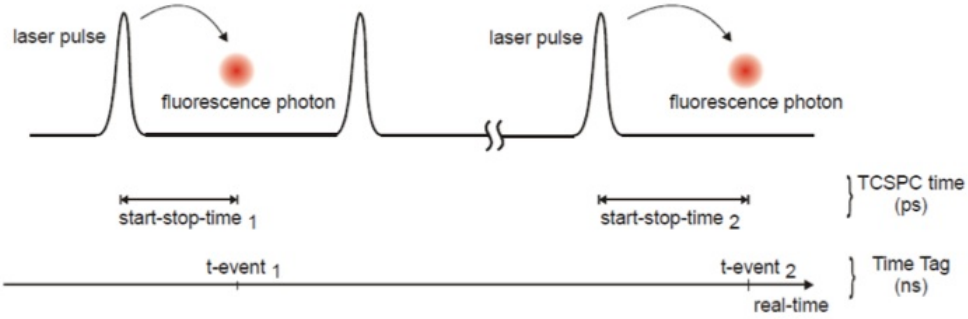

Figure A.13: Timing figures in TTTR data acquisition.

Sequentially stepping through the arrival times, all photons within the chosen time bins (typically milliseconds) are counted. This gives access to e.g. single molecule bursts (in flow) or to blinking dynamics. The bursts can be further analyzed e.g. by histogramming for burst height and frequency analysis. Fluorescence lifetimes can be obtained by histogramming the TCSPC (start-stop) times and fitting of the resulting histogram, as in the conventional approach. In single molecule applications with very few counts per histogram, faster algorithms based on maximum likelihood criteria may be used. Lifetime fitting can either be done using iterative reconvolution, taking into account the influence of the instrument response function (IRF), or as a tailfit, neglecting this influence. Decay models up to four exponential components can be applied. A Maximum Likelihood Estimator (MLE) method can be used to account for regions with low signal intensity. The strength of the TTTR format is used when both time figures are used together. For instance, one can first evaluate the MCS trace to identify single molecule bursts, and then use the TCSPC times within those bursts, to evaluate fluorescence lifetimes for individual bursts.

## A.5 Method of Cumulants

Finding the precise functional form for the distribution of decay rates G($\Gamma$) is problematic because the correlation function is measured discretely only over an incomplete range of lag times and there is always Poisson noise associated with the data. There are several ways of using DLS data to characterize G($\Gamma$), but one of the simplest is the method of cumulants first proposed by Koppel[8]. This method is based on two relations: one between g(1)($\tau$) and the moment-generating function of the distribution, and one between the logarithm of g(1)($\tau$) and the cumulant-generating function of the distribution. It is appropriate only for use in cases in which G($\Gamma$) is monomodal [8][9]. In fact, the form of g(1)($\tau$)

$$g(1)(\tau) = \int_0^\infty G(\Gamma) exp(-\Gamma\tau) d\Gamma \tag{A.8}$$

is equivalent to the definition of the moment-generating function $M(-\tau,\Gamma)$, of the distribution $G(\Gamma)$:

$$M(-\tau,\Gamma) = \int_0^\infty G(\Gamma) exp(-\Gamma\tau) d\Gamma \equiv g^{(1)}(\tau) \tag{A.9}$$

The mth moment of the distribution $m_m(\Gamma)$ is given by the mth derivative of M($-\tau,\Gamma$) with respect to $\tau$:

$$m_m(\Gamma) = \frac{d^m M(-\tau,\Gamma)}{d(-\tau)^m}|_{-\tau=0} = \int_0^\infty G(\Gamma)\Gamma^m exp(-\Gamma\tau) d\Gamma|_{-\tau=0} \tag{A.10}$$

Similarly, the logarithm of the field-correlation function is equivalent to the definition of the cumulant generating function K($-\tau,\Gamma$)

$$K(-\tau,\Gamma) = ln[M(-\tau,\Gamma)] \equiv ln[g^{(1)}(\tau)] \tag{A.11}$$

where the mth cumulant of the distribution $\kappa_m(\Gamma)$ is given by the mth derivative of K$(-\tau,\Gamma)$:

$$\kappa_m(\Gamma) = \frac{d^m K(-\tau,\Gamma)}{d(-\tau)^m}|_{-\tau=0} \tag{A.12}$$

By making use of the fact that the cumulants, except for the first, are invariant under a change of origin, one can write the cumulants in terms of the moments about the mean as

$$\kappa_1(\Gamma) = \int_0^\infty G(\Gamma)\Gamma d\Gamma \equiv \bar{\Gamma} \tag{A.13}$$

$$\kappa_2(\Gamma) = \mu_2 \tag{A.14}$$

$$\kappa_3(\Gamma) = \mu_3 \tag{A.15}$$

where $\mu_m$ are the moments about the mean, as defined by

$$\mu_m = \int_0^\infty G(\Gamma)(\Gamma - \bar{\Gamma})^m d\Gamma \tag{A.16}$$

The first cumulant describes the average decay rate of the distribution. The second and the third cumulants correspond directly to the appropriate moments about the mean: the second moment corresponds to the variance, and the third moment provides a measure of the skewness or asymmetry of the distribution. The first two cumulants must be positive, but the third cumulant can be positive or negative. The basis of the cumulant expansion that is tipically used in the analysis of DLS data lies in expanding the logarithm of $g^{(1)}$ in terms of the cumulants of the distribution. This relation follows from the fact that mth cumulant is the coefficient of $(-\tau)^m/m!$ in the Taylor expansion of K$(-\tau,\Gamma)$, about $\tau = 0$, as given by

$$ln[g^{(1)}(\tau)] \equiv K(-\tau,\Gamma) = -\Gamma\tau + \frac{\kappa_2}{2!}\tau^2 - \frac{\kappa_3}{3!}\tau^3 + \ldots \tag{A.17}$$

To take advantage of this form and use linear least squares methods to fit this function to the data requires that a key assumption be made about the data: the baseline must be assumed to be exactly one. Then a fit can be made to

$$ln[g^{(1)}(\tau) - 1] = ln\frac{\beta}{2} - \Gamma\tau + \frac{\kappa_2}{2!}\tau^2 - \frac{\kappa_3}{3!}\tau^3 + \ldots \tag{A.18}$$

Equation A.18 is the traditional fitting function that is described in many DLS text. Although most modern correlators do an excellent job of measuring the baseline, small amounts of noise can lead to small deviations from unity. Nonlinear fitting routines permit the possibility of fitting the data to $g^{(2)}$ directly. From eq. A.18, we obtain

$$g^{(2)} = B + \beta exp(-2\bar{\Gamma}\tau + \kappa_2\tau^2 - \frac{\kappa_3}{3}\tau^3) \tag{A.19}$$

where $\bar{\Gamma}$ is the average decay rate and $\kappa_2/\bar{\Gamma}^2$ is the second order polydispersity index. The first cumulant is directly proportional to some average diffusion coefficient, $\bar{D}$, called z average diffusion coefficient,

$$\bar{D} = \bar{\Gamma}/q^2 = D_z \tag{A.20}$$

with

$$D_z \equiv \frac{\sum_i c_i m_i D_i}{\sum_i c_i m_i} \tag{A.21}$$

where $m_i$ is the molecular weight and $c_i$ the weight concentration.

## A.6 Memexp program

The program MemExp uses the maximum entropy method (MEM) and either nonlinear least squares (NLS) or maximum likelihood fitting to analyze a general time-dependent signal in terms of distributed and discrete lifetimes. One or two distributions of effective log-lifetimes, g(log$\tau$) and h(log$\tau$), plus an optional polynomial baseline (up to a cubic) can be extracted from the data. The h distribution is used to account for signals opposite in sign to those described by the g distribution when analyzing data that rise and fall. Both distributions are obtained numerically from the data and are not restricted to any functional form. Simultaneously, MemExp performs a series of fit by discrete exponentials in which exponentials are added one at a time and are initialized based on the emerging structure in the MEM distribution. The amplitude and log-lifetime of each exponential, plus any optional baseline parameters utilized, are varied using either NLS (for Gaussian noise) or ML (for Poisson noise) fitting. MemExp automatically recommends one distributed and one discrete description of the kinetics as optimal. The graphical summary plotted by MemExp permits a through evaluation of the results. Multiple MEM 'prior models' are supported, facilitating a comprehensive analysis of the kinetic data[12]. The hybrid MEM/NLS analysis is applicable to a general time-dependent signal. A continuous description that evolves according to the MEM is used to guide a series of discrete NLS fits during which one exponential is added at a time. Thus, the hybrid algorithm provides an automated and objective approach to the multiple-minimum problem that plagues conventional parametric fitting (NLS and ML) when many kinetic processes are present. Consequently, MemExp is particularly useful when a large number of discrete processes is an appropriate kinetic description. By interpreting kinetics simultaneously from the complementary perspectives of discrete exponentials and continuously distributed lifetimes, a comprehensive assessment of the data can be performed conveniently. Also, the use of several different priors is supported to improve the fidelity of the distributions recovered. In the next section, the MemExp algorithm is described[12][13].

## A.7 MemExp: a MEM/NLS algorithm

Kinetics measured at times $t_i$ can be fit by

$$F_i = D_0 \int_{-\infty}^{\infty} dlog\tau[g(log\tau) - h(log\tau)]e^{-t_i/\tau} + \sum_{k=0}^{3}(b_k - c_k(t_i/t_{max}))^k \tag{A.22}$$

where g(log$\tau$) and h(log$\tau$) are the lifetime distributions that correspond to decaying and rising kinetics, respectively, and a polynomial accounts for the baseline. The constant $t_{max}$ is approximately the longest time measured and prevents baseline coefficients from differing greatly in magnitude. Formally, Laplace transforms involve an integral over the rate coefficient k = $1/\tau$, but when analyzing data that span several decades in time, it is more convenient to express the underlying distribution as a function of log$\tau$[14]. Upon discretizing eq. 3.1 for a computer, the g and h distributions become vectors. All g, h, b, and c parameters may be restricted to positive values without loss of generality. The normalization constant $D_0$ can be estimated from the data, provided that the temporal window spanned by the measurement is sufficient to include all kinetic processes. In the presence of experimental uncertainties, the unconstrained numerical inversion of eq. 3.1 is known to be an ill-posed problem; infinitely many solutions exist that fit the data to within the noise. Alternatively, a fit can be done by $n_e$ exponentials:

$$F_i = D_0 \sum_{j=1}^{n_e} A_j e^{-t_i/\tau_j} + \sum_{k=0}^{3} B_k (t_i/t_{max})^k \tag{A.23}$$

where $A_j$ and $\tau_j$ are the amplitude and lifetime of the jth exponential respectively, and $B_k$ is the kth coefficient in the polynomial approximation of the baseline. The MEM part of MemExp is an extension of the previous work and is based on the algorithm of Cornwell and Evans. It fits eq. 3.1 to kinetics by an iterative, second-order optimization of the entropy S,

$$S(\vec{P},\vec{F}) = \sum_{j=1}^{M}[P_j - F_j - P_j ln(P_j/F_j)] \tag{A.24}$$

subject to constrained values of $\chi^2$ :

$$\chi^2 = \frac{1}{N}\sum_{i=1}^{N}\left(\frac{F_i - D_i}{\sigma_i}\right)^2 \tag{A.25}$$

and, optionally, the normalization I,

$$I = \Delta\left(\sigma_{j=1}^{M_1} g_j - \sigma_{j=1}^{M_2} h_j\right) \tag{A.26}$$

The constrained optimization is achieved by maximizing the function Q,

$$Q \equiv S - \lambda\chi^2 - \alpha I \tag{A.27}$$

where $\lambda$ and $\alpha$ are Lagrange multipliers. The natural logarithm in eq. 3.3 requires that all elements of the desired image P be positive. Here, P is the concatenation of up to four vectors: g, h, b and c. $M_1$ and $M_2$ pixels are used to discretize the g and h distributions, respectively, and $\Delta$ is the spacing in log$\tau$. Implicit in the use of $\chi^2$ is the assumption that the standard errors $\sigma_i$ in the measured data, $D_i$, can be assumed Gaussian. Note also that, if P is normalized and if all $F_j$ are set equal to a constant, then maximizing S is the same as maximizing a more familiar expression for the entropy

$$S = -\sum_{j=1}^{M} P_j ln(P_j) \tag{A.28}$$

Unconstrained maximization of S ($\lambda = \alpha = 0$) with respect to $P_j$ yields $P_j = F_j$ . That is, F is the prior image that is defaulted to in the absence of good data. The ability to manipulate F lends flexibility to MEM inversions not available to other regularization methods. In contrast, this added flexibility requires that F be chosen wisely. The MEM calculation is iterative, starting with an initial image having maximum entropy: P = F (initially, a constant); $\lambda \sim \alpha \sim 0$. Newton Raphson optimizations of Q at fixed values of and are followed by automatic adjustments of the Lagrange multipliers. The multipliers are changed gradually enough to ensure that the gradient of Q remains sufficiently small [16]. Thus, P evolves from a flat distribution (with very large $\chi^2$) into a series of maximum-entropy distributions that become increasingly structured as $\chi^2$ and I approach the desired values. Whenever the prior F is derived from P, P is set equal to the new prior and the Lagrange multipliers are reset to near zero. The optimization of Q and multiplier updating are iterated until $\chi^2$ stops changing appreciably. When $\chi^2$

reaches a specified value (e.g., 1.2), the current P distribution is written to a file, and MemExp performs the first NLS fit with one exponential included for each MEM peak having an appreciable area and a mean within a specified log$\tau$ range. Because distributions produced by the MEM are quite smooth and noiseless, simple identification of minima and maxima in P is sufficient to detect peaks in the lifetime distribution. Let $i_-$ and $i_+$ denote the location of the minima immediately preceding and following the ith local maximum in P, respectively. Then the area and mean of this MEM peak are obtained by numerical integration, as in

$$Area_i = \Delta \sum_{j=i_-}^{i^+} g_j \tag{A.29}$$

$$Mean_i = \frac{\Delta}{Area_i} \sum_{j=i_-}^{i^+} g_j log\tau \tag{A.30}$$

For the outermost MEM peaks (fastest and slowest processes), the range of integration extends to the distribution edge. The initial amplitude and log lifetime of the ith exponential in the NLS fit are then taken as $Area_i$ and $Mean_i$, respectively. During NLS optimization of the discrete parameters, the lifetimes are free to stray outside the specified log$\tau$ range. This range is used to exclude exponentials from the NLS fit that correspond to undesirable ripples in the MEM distribution at either end of the log$\tau$ axis. The analysis of local maxima performed by MemExp also serves to identify relatively sharp, well-resolved peaks. In addition to the area and mean, two ratios are calculated for each local maximum in the lifetime distribution. The value of P at the local maximum is divided by each of the values of P at the adjacent minima. For a small ripple superimposed on a broad peak, at least one of these ratios is approximately unity. For a well-resolved peak, both ratios are large, perhaps exceeding 100. For a narrow peak partially overlapping a broad peak, one ratio will be rather large (e.g., 100) and the other will be smaller (e.g., 2), depending on the extent of overlap. If the ith MEM peak is found to be sufficiently large and sufficiently well resolved, then it is subtracted from P in the range from $i_-$ to $i_+$. After all such peaks are subtracted, the remainder of P is blurred uniformly. Then each subtracted peak is accounted for, either by adding it to F unchanged or by adding a Gaussian with the same area and a reduced FWHM. As the MEM convergence continues, this analysis (and storage) of the P distribution is repeated periodically to determine the current number of MEM peaks n, the peak means and areas, and the maximum-to-minimum ratios. If n has not changed since the last time the image was analyzed, the MEM calculation is resumed. If n has increased by one, the areas and means of the current MEM peaks are characterized and a new NLS fit is performed with one more exponential than was used in the previous NLS fit. If n has increased by more than one, the n+1 MEM peaks of largest area are introduced as exponentials in an NLS fit. Then, the next largest MEM peak is accounted for in an additional NLS fit, and so on. Thus, the MEM is used to introduce one exponential at a time into a series of NLS fits; as features are resolved in the continuous kinetic description, exponentials are added to the discrete description.

In chapter 3 the autocorrelation functions were analyzed by means of the MEM method: the acquired second order autocorrelation functions (ACFs) of the scattering light were first converted into the first order ACFs, G (t), and the first order ACFs were analyzed by means of the Maximum Entropy method obtaining the distribution of relaxation times according to the relation:

$$G(t) = A \int_{-\infty}^{\infty} dlog(\tau) P_{\tau}(log(\tau)) exp[-t/\tau] \tag{A.31}$$

The relaxation time $\tau$ is inversely proportional to the particle diffusion coefficient, D, and the exchanged wave vector, Q, by the relation $\tau = 1/(DQ^2)$. The diffusion coefficient is related to the particle average hydrodynamic radius, $R_h$, as, $D = k_B T/6\pi\eta R_h$. Therefore, the linear relation between the relaxation time and the hydrodynamic radius, $\tau = R_h(6\pi\eta)/(k_b T Q^2) = R_h/\rho$, can be used to compute the number distribution of particles with radius $R_h$ by fitting the $P_R(R_h) = P_{\tau}(log(\tau))\frac{1}{\tau}$ distribution to a sum of log-normal functions of the type:

$$P_R(log(R_h)|_{R_h=\rho\tau} = \rho A \sum_j \alpha_j < R >_j^5 exp\left[\frac{(log(R_h) - log(< R >_j))^2}{2\sigma_j^2}\right] \tag{A.32}$$

where $< R >_j$ and $\sigma_j$ are the average values of the hydrodynamic radius and the width of the distribution component and $\alpha_j$ is the number fraction of the jth component in the distribution.

# Acknowledgments

E' notte fonda e sto iniziando a scrivere la parte piú difficile di questa tesi di dottorato: ovvero i ringraziamenti. Non é facile iniziare, soprattutto quando le persone da ringraziare sono tante . . . almeno quante le stelle in cielo questa notte e come per un semplice marinaio, mi sono servite da guida durante questi 3 anni. Ogni giorno numerose persone hanno ruotato vorticosamente intorno all'ufficio del 4 piano, poco piú di una scialuppa di nome LABS, scandendo le giornate in modo quasi sempre imprevedibile. Navigando di bolina nell'immenso oceano della ricerca ho avuto bisogno di un punto di riferimento o meglio sette, come le stelle dell'Orsa Minore. Ringrazio infinitamente Giberto, Maddalena, Laura, Piersandro, Paride, Alice e Maurizio per l'aiuto e la disponibilitá dimostratami.

Ci sono state due persone veramente speciali che hanno illuminato tante e tante splendide giornate. La mia Croce del (profondo) Sud Rocco, il miglior compagno di lavoro "pugliese" che potessi avere: grazie di cuore. Ringrazio infinitamente il magnetico Diego, una Fornace di idee, dal piccolo museo delle cere, al laboratorio di falegnameria, fino al nostro miglior successo cioé il set cinematografico infrarosso. Rimarrete per sempre i miei tesisti preferiti. Grazie mille a Laura (la Sairon), l'Orione del LABS, sempre a caccia di qualcosa da fare, di qualcuno da aiutare o all'occorrenza, da uccidere. Ringrazio Mic, la Lira e non solo per la sua grandissima bravura compositiva e la sua immensa conoscenza, ma anche per avermi fatto conoscere il miglior gruppo rockabilly di tutti i tempi: Sam, the Sham and the Pharaohs. Se vi é capitato di trovare enormi Crateri sparsi per il LABS o gente con torce e forconi, molto probabilmente avete appena scampato uno degli scherzi del vulcanico SDaglio; un ottimo compagno di scrivania, soprattutto visto che non mi ha mai reso oggetto di un suo scherzo.

Grazie mille Saretta, la miglior ex-tesista di tutti i tempi; purtroppo non esiste la Costellazione dell'uragano, ma ne esiste una che ha problemi di spazio . . . un pó come te: la Costellazione dell'Idra. Non farti ingannare dalla mostruositá dell'animale, rimarrai per sempre tra le mie preferite. Sirio é la stella piú luminosa del cielo notturno; allo stesso modo c'é qualcuno che ha illuminato molte giornate nel LABS semplicemente con il suo affetto, la sua dolcezza, il suo sorriso e la sua immensa avidigia nel mangiare Nutella:

grazie di cuore Gio. Grazie Pozz, l'Argonauta della situazione; non so se troverai mai il vello d'oro in quel di Pavia, ma so per certo che la tua mancanza si fará sentire.

Nel mese del Capricorno é apparsa in LABS una persona inizialmente emarginata, portatrice di un pesante fardello: essere un fisico teorico. In realtá ti sei dimostrato una grande persona e uno splendido amico; grazie mille Nic, certo rimarrai sempre un ibrido, insomma ne capra ne pesce. E circa 7 mesi dopo arriva ... il Leone (Simba, figlio di Mufasa) una bellissima new entry, una persona generosa e di gran cuore. Grazie a te ho scoperto il sapore della conquista, potenziando il LABS (all'ufficio di fronte) da semplice gozzo a galeone a quattro ponti. Ad un certo punto ha iniziato ad orbitare intorno al LABS un buco nero chiamato Silvienji; un vero tunnel spazio-temporale capace di scomparire in un batter d'occhio e di ritrovarsi senza sapere come in Piazza San Babila. Ha attratto tutto e tutti con la sua simpatia e imprevedibilitá.

All'anagrafe risulto figlio unico, ma nella sostanza ho un gemello fantastico; grazie Kata, sei veramente unico. Mi dispiace di aver perso un pó della tua fiducia dopo averti fatto conoscere la Cry Cry (il granchio), una ragazza bella e dolce ma sempre pronta a mordere. Porta pazienza Brother, tanto siamo giá Santi! Ringrazio Margaux, lo Scorpione, il piú delle volte in versione dolce e raggiante come la costellazione, ma a volte nella versione piú pericolosa di animaletto temibile e pungente.

Se pensate che possa essere difficile avere un teorico in LABS, figuratevi avere un Darietto, una specie di Big Bang napoletano, sempre pronto a farti ridere; e di questo ti saró per sempre grato. E non c'é due senza tre. A Ricky avrei dovuto dare la tessera fedeltá; é sempre un piacere avere la tua compagnia. E con questo il Triangolo teorico é completo. Ringrazio la pulsar del LABS Mary che appari e scompari in maniera ciclica, ma capace di donare affetto con un semplice abbraccio. Grazie infinite a Cecco lo Scudo, sei stato il miglior guardiano della porta del LABS ma soprattutto una splendida persona con cui ridere e giocare ... in ufficio. Alberto l'Aquila del MEF Utd, il Messi di Bergamo Alta, grazie per la compagnia e la grinta dimostrata in campo. Grazie mille Tullia, la mia personal stylist, sempre pronta a punzecchiarmi come una Freccia, soprattutto nel campo dell'abbigliamento. Ringrazio Frodo Fede Botta Baggins un'autentica supernova, una persona veramente fantastica, dispensatrice di affetto ed energia.

Grazie Ago l'Indiano (nonostante tu sia un ingegnere), é stato un piacere conoscerti e conoscere la tua grande maestria nello sfornare torte. In un laboratorio di Biofisica non poteva mancare il Microscopio (Ema), una fonte inesauribile di domande e di consigli pratici fondamentali. Ringrazio Fede, l'artista del LABS, una persona veramente squisita. Infine non potrei non ringraziare le ultimissime due arrivate nel LABS: Vale e Lucy. La prima simpatica e dolce come una Colomba, la tesista modello; la seconda una specie di catastrofe ultravioletta che prevedo giá sará fonte di disastri ... Queste sono solo alcune delle persone che maggiormente hanno lasciato il segno durante questi anni. Ci sono poi persone che hanno fatto sporadiche apparizioni, un po' come le Perseidi. Faizan e Ste, (i due amanti di Nick), Gianlu (temibile avversario teorico), Pier (l'amanuense di Teorica), Carlo (il gemello di Pozz), Nic di Vara (l'All Black della Bicocca), Davide (un Re Magio portatore di lecornie), Corti (il broccolatore per eccellenza), Ely (la mia amica "bionda"), Fede & Fede (una splendida coppia), Francy (semplicemente grandissima), Gaia (la nuova compagna di scrivania), Fuda (con il vestito che avevi alla laurea sei diventato il Boss), Vale Q. (la mia preferita), Melis (l'oriundo). Ci sono inoltre una serie di persone che non hanno vissuto le mirabolanti avventure in L.A.B.S., ma con cui ho trascorso momenti fantastici: Salvi, Sonia, Cesko, Kikka, Alby, Dani, Espo, Lorena,Teo, Dana, Jessica, Krizia, Lolly, Emy. Sono stati i miei genitori a permettermi di avere tutto questo, quindi non ci sono parole per esprimere la mia eterna gratitudine e il mio amore per loro.

Infine non potrei non ringraziare le 2 potentissime stufette elettriche, i veri soli del LABS, fonti di calore (e salate bollette elettriche) nelle gelide giornate invernali. Questo é l'universo in cui ho vissuto e vivo tutt'ora, pieno di luci e di colori. Non c'é stato giorno in cui ognuna di queste persone non mi abbia fatto sorridere, che poi si sa . . . un giorno senza un sorriso é un giorno perso.